Microwave Studies of Van der Waals Complexes

A thesis submitted for the degree of Doctor of Philosophy
at the University of Oxford

by

James Patrick Connelly
Exeter College
Hilary Term 1993

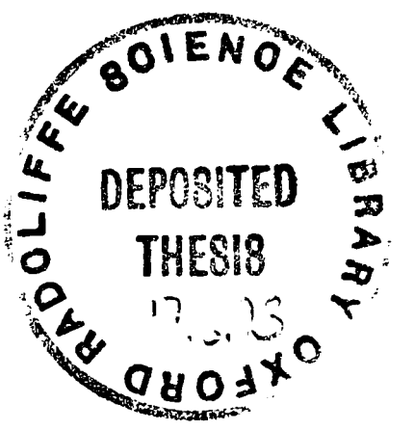

Abstract

Microwave Studies of Van der Waals Complexes

A thesis submitted for the degree of Doctor of Philosophy
at the University of Oxford.

James Patrick Connelly
Exeter College
Hilary Term, 1993

This thesis describes the commissioning and development of a pulsed supersonic nozzle, Fourier-transform microwave spectrometer and its application to the study of several weakly bound van der Waals complexes.

A pulsed supersonic expansion, Fourier-transform microwave spectrometer based on the Flygare design with a number of modifications has been constructed with an operating range of 6-18 GHz. A homodyne detection circuit mixing signals to modulus values between dc and 1 MHz is used, requiring two measurements to determine absolute transition frequencies. Transition frequencies are measured from the power spectrum by determining the first derivative zero crossing point in a least squares fitting procedure. Semiautomation of many of the spectrometer operations has been achieved allowing unattended data collection over scans of up to 300 MHz.

The microwave spectrum of Ar_2-OCS and Ar_2-OC^{34}S has been observed and analysed using conventional Watson S reduction hamiltonian parameters. Effective structural parameters are derived and used in a harmonic force field analysis, based on the centrifugal distortion constants, to compare the trimer interations with a model based on the sum of dimer interactions.

A series of complexes containing the nitrogen molecule undergoing tunnelling motions have been studied. Hyperfine matrix elements for the first order nuclear quadrupole interaction are derived for the coupled identical nuclei case appropriate to the rapid tunnelling motions observed.

The microwave spectrum of N_2-OCS is described. Tunnelling and nuclear spin statistical effects for two symmetry states are observed arising from the interchange of nitrogen nuclei. Rotational and quadrupole constants are derived; an accidental near degeneracy of two rotational levels allows the off-diagonal quadrupole coupling constant to be determined from second order effects. A tunnelling hamiltonian fitting the quadrupole coupling constants to an angular potential has been used to calculate the tunnelling frequency and barrier to N_2 rotation.

The microwave spectrum of N_2-O_3 and a preliminary spectrum of N_2-SO_2 have been observed. Rotation-inversion motions of the O_3 and SO_2 moieties must be considered in addition to the N_2 tunnelling to fit the spectrum. Tunnelling frequencies for the O_3/SO_2 and geared motions with the N_2 are derived as well as structural parameters.

Modifications for production of refractory molecules and complexes by laser ablation have been made. A modified nozzle employing rods of material is used with the ablation process taking place in the nozzle throat. Modifications to obtain an expansion along the axis of the microwave cavity employ a hemispherical Fabry-Perot cavity configuration. The system has been tested on a number of diatomic molecules including PbS and CuCl.

Acknowledgements

A large number of people have contributed to the successful completion of this thesis. First and greatest thanks must go to my supervisor, Dr. Brian Howard who has provided an endless supply of ideas, enthusiasm and encouragement. In addition the advice and assistance given by Andrew Auty in all matters experimental, especially the ozone experiments, was greatly appreciated. Professor John Muenter was instrumental in assembling the spectrometer and obtaining the first spectra and has since provided many useful suggestions.

Several Part II students have contributed to the work described in this thesis. Simon Duxon and Sharon Kennedy contributed to the work on N_2-OCS and Jason Tuckley to work on Ar_2-OCS. In addition, I must also thank all the users of my 'spectrometer computer control programs' and Matthew Brookes in particular, for their patience in the use of computer programs conforming to the rule 'if the program was hard to write, it should be hard to use'.

I would also like to thank John Freeman who produced many of the figures and diagrams for this thesis at short notice, improving the presentation immensely.

Finally I must thank the members of my family for their love and support and all the members of the Howard and Brown groups for helpful advice and friendly banter.

Contents

Chapter 1

Van der Waals Complexes

1.1 Introduction

Van der Waals complexes are aggregates of molecules and atoms held together by weak forces rather than formal chemical bonds. The electrostatic nature of the van der Waals forces results in the properties of such complexes depending on the interaction of charge distributions and polarizabilities of the component molecules. Correspondingly, van der Waals complexes are characterized by low bond energies of the order of thermal energy at room temperature and long bond lengths relative to chemical bonds. The contribution of these intermolecular forces to physical and chemical phenomena and in maintaining condensed phases is of considerable importance. An understanding of the molecular processes involved in collisional energy transfer, reaction dynamics, condensed phase behaviour and macromolecule folding is one approach to calculating chemical properties on the laboratory scale. To this end, a large amount of research has been directed towards the determination of the structure and dynamics of van der Waals complexes, in particular dimeric complexes and the analytical form of intermolecular pair potentials.

Early work on intermolecular forces used the data available from bulk phenomena. Discrepancies in the ideal gas equation of state led J. D. van der Waals to account for the increase in gas volume due to repulsive forces and the effective reduction in pressure due to attractive interactions between molecules in a modified equation of state. Constants introduced in the van der Waals gas equation and subsequently in transport property expressions for fluids could be related through kinetic theory to the form of averaged isotropic intermolecular potential. The potentials obtained from bulk properties are averaged over orientation, velocity distribution and many body interactions and thus give information on the radial part of the potential. Experimental techniques and methods for extracting potential information are comprehensively reviewed by Maitland *et al.*[1]

1.2 Weakly bound complexes

Low density, low temperature gas phase conditions reduce the study of intermolecular interactions to effects between isolated molecules and small van der Waals complexes and clusters.

These are much more sensitive to orientation and offer a more manageable approach to many-body interactions. At room temperature and pressure, the concentration of gas phase binary complexes, with binding energies of a few hundred cm^{-1} or less, is typically less than 0.01% and the lifetime, corresponding to the time between collisions[2], is $\sim 10^{-10}$s. Improvements can be made by decreasing the temperature to increase the complex concentration although this is countered by decreasing the pressure sufficiently[3] to enable measurements to be made within the equilibrium lifetime of the complex. Research into binary complexes has expanded rapidly in cooperation with methods employing molecular beams and supersonic expansions under vacuum conditions. Supersonic expansion methods produce localised regions of high gas density with low temperatures, low collision rates, lifetimes of the order of 100μs-1ms and typically 10% conversion to binary complexes. In spectroscopy of van der Waals complexes, supersonic expansion methods have all but supplanted static cell techniques. Static cell experiments are generally used to provide high temperature measurements which are very difficult to achieve in supersonic expansions. The analysis of structure and dynamics and the development of intermolecular potentials by this route has been based upon the results of scattering experiments and high resolution spectroscopy of van der Waals dimers.

Scattering experiments between gas phase molecular beams to measure differential scattering cross sections provide a sensitive means to sample pair potentials[1]. These experiments are most suitable for collisions between a target molecule and light, small, rare gas atoms or molecules such as H_2 to obtain the greatest degree of scattering with highest resolution without the analytical complications of many degrees of freedom contributing to very inelastic collisions[4]. In a few cases such as Na-Hg a very precise form of potential can be extracted by direct inversion of the data[5].

1.3 Spectroscopy

A profusion of spectroscopic techniques have been employed to study intermolecular dynamics, potentials and structure of van der Waals dimers. Early measurements relied on bulk properties influencing both infra-red (IR) line broadening[6] and NMR relaxation rates. Matrix isolation studies have provided one means to study weak interactions[7]. However, in addition to the intermolecular interactions of interest, the influence of the matrix must also be taken into account. A matrix can be used to stabilize thermodynamically less favourable complexes such as HF-HCN as well as the more favourable HCN-HF[8].

High resolution gas phase spectra of van der Waals complexes, in regions of the spectrum from microwave to ultra-violet (UV)[9], have been obtained using many techniques. These types of study have delivered very accurate structural information of weakly bound dimers and trimers[10]. With the equilibrium structure well determined, the dipole moment[11] and hyperfine constants can

be used in elucidating the dynamics of the complex as demonstrated for N_2-OCS in this thesis. Study of single vibrational modes and combination bands can give very specific information on the nature of the intermolecular potential near the potential minimum as well as the effect of dynamics such as vibrational predissociation on line shapes. Introducing sufficient energy to dissociate the complex by intermolecular vibrational relaxation the vibrational predissociation dynamics can be studied by monitoring the product monomer states. As only the ground electronic state is involved, these systems are quite amenable to accurate dynamical calculation. This can be extended to use weakly bound dimers and trimers as prototype systems of photochemical processes[12].

This thesis is concerned mainly with high resolution, gas phase data obtained for weakly bound dimers and trimers using the well established Fourier transform microwave spectroscopy technique[13]. However, recent methods employed in developing potentials and dynamics[14] require complementary data from several techniques and a review of general spectroscopic techniques is given here.

1.3.1 Microwave spectroscopy

Microwave and radiofrequency data collection has relied heavily on two techniques, both employing molecular beams or expansions. Molecular beam electric resonance (MBER) and Fourier transform microwave spectroscopy (FTMW) both offer resolution of $\leq$10kHz enabling the measurement of hyperfine features as well as rotational and centrifugal distortion constants. The MBER spectroscopy technique employs a continuous or pulsed molecular beam to produce complexes. Complexes are selected in a particular rotational state using Stark effects in an inhomogeneous electric field and deflected around a stop wire. This selection procedure ensures an adequate population difference before microwave radiation induces transitions in a parallel plate Stark field. A second field refocusses the selected beam into a mass spectrometer. The technique allows an extensive tuning range, radiofrequency (500 MHz) to mm wave (50 GHz) but is experimentally intricate. A number of complexes have been studied by this technique such as $(HF)_2$[15] and Ar-SO_2[16], both of which exhibit tunnelling motions and many rare gas (Rg)-molecule complexes[17]. A recent modification using only one refocussing region and bolometric detection has been employed to study rotational-tunnelling transitions in $(H_2O)_2$[18].

Pulsed supersonic expansion, Fourier transform microwave spectroscopy (FTMW) developed by Flygare[19] and others[20] has superseded MBER in sensitivity and resolution although not in operating range and ease of scanning. A supersonic expansion of gas is pulsed into an evacuated microwave cavity and polarized by a narrow bandwidth of microwave frequencies from a coherent source. Coherent emission is detected using superheterodyne detection and Fourier transformed to

give spectra covering the polarizing bandwidth of a few MHz. The use of pulsed nozzles, which can generate greater concentrations of larger complexes per pulse than observed in continuous flow nozzles has enabled the study of weakly bound trimers and larger complexes such as Ar_n-HF with $n \leq 4$[21] and $(HCN)_2$-X where X=HF, H_2O, HCN, *etc*[22]. Exploitation of the high sensitivity has allowed the measurement of very weakly polar complexes such as Ar-N_2[23] where the dipole moment estimate is $\sim$0.01D. A large area of interest has been the study of hydrogen bonded interactions as exemplified by $(H_2O)_2$ [24]. This area is reviewed by Legon and Millen[25].

An additional level of sophistication is introduced by the use of double resonance techniques. A few examples of microwave-radiofrequency, microwave-microwave and microwave-infrared double resonance experiments have been reported. In combination with Fourier-transform microwave spectroscopy, a number of 2-dimensional techniques analogous to NMR methods have been developed[26].

The rotational constants provided by the microwave techniques are used primarily to determine precise vibrationally averaged structures. The centrifugal distortion constants provide information on the vibrational modes of the complex but in the absence of direct vibrational data are sufficient only for simplified potential modelling, for example, by normal coordinate analysis as in the case of Ar-ClCN[27]. Both MBER and FTMW techniques resolve hyperfine structure due to nuclear quadrupole and magnetic dipole interactions[22] as well as internal motion and tunnelling effects to a few kHz. Dipole measurements in both methods have been made employing Stark fields and in the case of FTMW also estimated using pulsed microwave methods[21]. These data provide angular information which in a few cases have been used to calculate internal dynamics[10,14,15].

1.3.2 Infrared spectroscopy

The behaviour of weakly bound complexes with excited vibrational modes can be investigated using infra-red techniques. These methods deliver rotational and centrifugal distortion constants of the ground and excited state but with lower resolution ($\sim$ 10 MHz or less) than microwave. The vibrational excitation is often accompanied by vibrational predissociation of the weak intermolecular bond. This effect can be studied by observing lifetime induced broadening of transition linewidths. The weak van der Waals interaction is ideal as a model system for studying the dynamics of vibrational predissociation and intermolecular vibrational relaxation[12]. Energy transfer within the complex not resulting in dissociation will be evident in large changes in the van der Waals bond length and consequently changes in the rotational constants.

Vibrational modes of van der Waals complexes can generally be classified as either slightly perturbed internal modes of the monomer constituents or modes corresponding to the intermolecular

stretches and bends. The force constants associated with these two classifications differ by a factor greater than 100. Corresponding transitions will be in different parts of the IR spectrum with the van der Waals modes in the less accessible far infra-red (FIR), < 200 cm^{-1}.

Early measurements in the mid-infrared were made using absorption in multiple-pass, long path, static gas cells at low temperature. Improvements have subsequently been made by increasing path lengths, employment of lasers, decreasing the gas density and temperature to about 20 K, incorporation of the absorption cell into a Fourier transform spectrometer and extension into the far infrared spectrum. Hydrogen dimers and rare gas-H_2 complexes exhibiting very weak bonding ($D_0(H_2..H_2) \sim 2.9$ cm^{-1}) with few van der Waals vibrational levels have been extensively studied using this method by McKellar *et al.*[28]. Other studies have taken advantage of the higher vibrational and rotational temperatures to augment the abundant lower temperature data available from supersonic expansion techniques. Ar-HCl measured in a static cell at 127 K showed direct rotational predissociation with no rotational transitions seen for $J > 60$[29].

Supersonic expansion methods in the IR and FIR spectrum are characterized by the use of lasers. Sensitivity is improved by passing the laser light through the expansion many times and employing slit nozzles to increase the interaction path length[35]. Detection as a function of wavelength is either by direct absorption, where the transmitted laser power is recorded, or by monitoring the molecular beam using, for example, bolometric detectors.

Optothermal techniques using a liquid helium cooled bolometer measure the energy associated with the flux from the expansion reaching the detector. Energy absorbed appears as an increase in energy at the detector, predissociation with the fragments recoiling out of the beam appears as a decrease in signal at the detector. By using a collimated molecular beam, the Doppler profile can be reduced giving very high resolution. Application of this technique to rovibrational IR spectroscopy using a tunable colour centre laser has been reviewed by Miller[30]. Complexes studied include HCN-HF where substantially different vibrational predissociation rates, measured using linewidths, are observed on exciting the C-H and F-H stretches[31]. N_2O-HCN has also been observed[32] where the rotational structure indicates both a slipped parallel and the higher energy linear hydrogen bonded geometry complexes are present in the molecular beam.

A few other methods have been used to monitor the molecular beam. Scattering, using a second beam of helium, has been used to study the infra-red induced dissociation of CH_3OH-H_2O[33]. Mass spectrometers have also been used to study alkane-OCS complexes[34].

Several direct absorption techniques have been developed differing mainly in the type of laser source used. Small differences in the intensity of light, transmitted perpendicularly through an expansion, due to absorption require very sensitive gated detection methods to maintain sensitivity.

The development of the technique employing an infrared diode laser with a multipass cell and axisymmetric expansion is reviewed by Hayman[35]. A number of rare gas-molecule complexes have been observed by this method including Ne-CO and Ar-SiH_4[36] complexes where the spectra are complicated by the high degree of internal motion. More recently colour centre lasers and difference frequency lasers with higher stability have been used in place of diode lasers. Nesbitt[37] and Beaudet[38] have incorporated slit nozzles to decrease the Doppler profile and increase the path length giving up to two orders of magnitude improvement in sensitivity. The spectra of HF-X complexes where X=He, N_2 and CO_2 [33] and O_2-N_2O[34] have been recorded in this way. In a few cases, infrared data has been complemented by results from Raman spectroscopy as in the case of $(C_6H_6)_2$[39].

The infrared studies of vibrations corresponding to perturbed monomer modes sample only regions of the intermolecular potential near the minimum. In order to develop more complete potential surfaces, data corresponding to the van der Waals vibrational interactions are desirable.In the case of Ar-HCl, this has been achieved by observing combination bands or hot bands involving the low frequency modes[32]. Alternatively, the spectra can be measured directly in the far infrared region. Tunable lasers in the FIR region have proved to be technologically demanding. Fixed frequency lasers with Stark tuning of transitions have been used to observe Ar-HCl. Recently developed tunable lasers employ pumped fixed frequency FIR lasers which are mixed with microwave radiation to obtain tunable sidebands[40]. The development and results for Ar-H_2O and $(H_2O)_2$ are reviewed by Saykally[41].

1.3.3 Electronic spectroscopy

Electronic spectroscopy of van der Waals complexes has been mainly involved in structure determination in different electronic states and dissociation. There has been some limitation on the chromophores available so studies have been limited to certain groups of complexes. Levy *et al.*[42] have studied the structure and predissociation dynamics of complexes based on tetrazine and similar aromatic/rare gas combinations using laser induced fluorescence experiments. Results for Ar_n-aminotetrazine[43] indicate that the dissociation dynamics are very sensitive to the excited vibrational state. Long dissociation lifetimes are observed illustrating the energy sink behaviour expected in larger molecules. A series of rare gas-metal atom complexes[44], produced by laser ablation, have also been observed by LIF to give dissociation energies and bond lengths. An alternative approach employs two laser experiments such as resonance enhanced multiphoton ionization and pump-probe techniques. This has been applied to rare gas complexes of dihalogens as reported by Janda[45]. Ar_n-C_6H_6 where $n \leq 2$[46] has been similarly observed employing a mass selection technique to separate

the rare gas complex from $(C_6H_6)_2$. Most recently these techniques have been applied to the burgeoning field of radical and ion complexes of the type Ne-OH[47] and Ne-N_2O^+ [48].

1.4 Intermolecular potentials

Several allusions to intermolecular potentials have been made in this discussion. In the simplest form, intermolecular pair potentials are considered to consist of interactions between rigid molecules[1] with two contributions. Long range attractive forces with contributions from electrostatic, dispersion and induction forces, which in many cases determine the angular minimum and the intermolecular orientation. Short range repulsive forces arising from exchange interactions determine the intermolecular separation[49]. In a number of complexes, the orientation giving minimum separation and most effective 'packing' arrangement determines the structure. This is illustrated by $(CO_2)_2$[50]. Methods for calculating energies using multipole expansions and hard sphere separations have been formulated and reviewed by Buckingham *et al.*[51] These types of calculation have proved useful in the prediction of structure. Although the factors influencing structure are more complicated quantitatively, the generalization is reminiscent of the bulk phase correction terms in the van der Waals gas equation of state.

More sophisticated methods of calculating potentials have been employed to make general use of the spectroscopic data. Harmonic force field calculations allow the use of vibrational and centrifugal distortion data in determining parameterized potentials with harmonic force constants[52]. However, these types of calculations are not wholly appropriate for weakly bound complexes with large amplitude internal motion. More elaborate general hamiltonian methods are extensively reviewed by Hutson[53]. Perhaps the most illustrative example of the goal in developing potentials is given by Ar-HCl. Pair potentials for Ar-HCl[54] have been developed utilizing bulk and spectroscopic data. Subsequent developments using the recent spectroscopic data for Ar-HCl and Ar_2-HCl have resulted in a description of the pair potential suitable as a foundation for calculating three body contributions in the observed spectra of Ar_2-HCl[55].

Acknowledgements

I would like to thank Dr. Richard Barrow for providing a preprint of his review article on recent advances in high resolution spectroscopy[56] and Dr. J. M. Hutson for providing a preprint of the Ar_2-HCl paper[55].

References

[1]G. C. Maitland, M. Rigby, E. B. Smith., W. A. Wakeham, *Intermolecular Forces,* Oxford University Press, Oxford, 1987.

[2]K. Laidler, *Chemical Kinetics,* McGraw-Hill, New York, 1965.

[3]D.E. Stogryn, J. O. Hirschfelder, *J. Chem. Phys.* **31**, 1531 (1959); *ibid.* **33**, 942 (1960).

[4]R. B. Bernstein, *Atom-Molecule Collision Theory,* Plenum Press, New York, (1979).

[5]U. Buck, H. Pauly, *J. Chem. Phys.* **51**, 1929 (1971).

[6]D. A. Rank, B. S. Rao, T. A. Wiggins, *J. Chem. Phys.* **37**, 2511 (1962).

[7]W. Klemperer, D. Yaron, D. D. Nelson, *Faraday Discuss Chem. Soc.*, **86**, 261 (1988)

[8]L. Andrews, *J. Chem. Phys.* **88**, 2940 (1984).

[9] *Structure and Dynamics of Weakly Bound Molecular Complexes,* ed. A. Weber, NATO ASI series C, Vol 212 Reidel, Dordrecht, 1987.

[10]S. E. Novick, K. R. Leopold, W. Klemperer, *Atomic and Molecular clusters,* ed. E. R. Bernstein, Elsevier, New York, pg 359, 1990.

[11]G. T. Fraser, A. S. Pine, R. D. Suenram, *J. Chem. Phys.*, **88**, 6157 (1988).

[12]R. E. Miller, *Science,* **24**, 447 (1988).

[13]A. C. Legon, *Ann. Rev. Phys. Chem.* **34**, 275 (1983).

[14] J. M. Hutson, *Dynamics of Polyatomic van der Waals Complexes*, eds. N. Halberstadt, K. C.Janda, Plenum Press, New York, 1990

[15]B. J. Howard, T. R. Dyke, W. Klemperer, *J. Chem. Phys.*, **81**, 5417 (1984).

[16]J. S. Muenter, R. L. DeLeon, A. Yokozeki, *Farad. Discuss. Chem. Soc.*, **73**, 63 (1982).

[17]T. R. Dyke, *Topics Current Chem.*, **120**, 86 (1984).

[18]G. T. Fraser, R. D. Suenram, L. H. Coudert, *J. Chem. Phys.*, **90**, 6077 (1989).

[19]T. J. Balle, W. H. Flygare, *Rev. Sci. Instrum.*, **52**, 33 (1981).

[20]J. U. Grabow, W. Stahl, *Z. Naturforsch.*, **45a**, 1043 (1990).

[21]H. S. Gutowsky, C. Chuang, T. D. Klots, T. Emilsson, R. S. Ruoff, K. R. Krause, *J. Chem. Phys.*, **88**, 2919 (1988).

[22]T. D. Klots, H. S. Gutowsky, *J. Chem. Phys.*, **91**, 63 (1989).

[23]W. Jäger, M. C. L. Gerry, *Chem. Phys. Lett.*, **196**, 274 (1992).

[24]G. T. Fraser, R. D. Suenram, L. H. Coudert, *J. Chem. Phys.*, **90**, 6077 (1989).

[25]A. C. Legon, D. J. Millen, *Chem. Rev.*, **86**, 635 (1986).

[26]B. Vogelsanger, A. Bauder, *J. Chem. Phys.*, **92**, 4101 (1990).

[27]M. R. Keenan, D. B. Wozniak, W. H. Flygare, *J. Chem. Phys.*, **75**, 631 (1981).

[28]A. R. W. Mckellar, *Farad. Discuss. Chem. Soc.*, **73**, 89 (1982); A. R. W. McKellar, J. Schaefer, *J. Chem. Phys.*, **95**, 3081 (1991); A.R.W McKellar, *ibid.* **92**, 3261 (1990).

[29]B. J. Howard, A. S. Pine, *Chem. Phys. Lett.*, **122**, 1 (1985).

[30]R. E. Miller, *Science*, **240**, 447 (1988).

[31]D. C. Dayton, R. E. Miller, *Chem. Phys. Lett.*, **143**, 181 (1988).

[32]D. C. Dayton, L. G. Pedersen, R. E. Miller, *J. Chem. Phys.*, **96**, 1087 (1992).

[33]F. Huisken, M Stemmler, *Chem. Phys. Lett.*, **180**, 332 (1991).

[34]M. A. Hoffbauer, C. F. Giese, W. R. Gentry, *J. Chem. Phys.*, **79**, 192 (1983).

[35]G. D. Hayman, *D. Phil. Thesis*, Oxford University, 1985.

[36]R. W. Randall, *D. Phil. Thesis*, Oxford, 1991.

[37]D. J. Nesbitt, *Chem. Rev.*, **88**, 843 (1988).

[38]S. W. Bunte, Y. Lin, C. Wittig, R. A. Beaudet, *Ohio State University, 47^h International Molecular Spectroscopy Symposium*, 1992.

[39]B. F. Henson, G. V. Hartland, V. A. Venturo, R. A. Hertz, P. M. Felker, *Chem. Phys. Lett.*, **176**, 91 (1991).

[40]G. A. Blake, K. B. Laughlin, R. C. Cohen, K. L. Busarow, D-H. Gwo, C. A. Schmuttenmaer, D. W. Steyert, R. J. Saykally, *Rev. Sci. Instrum.*, **62**, 1693 (1991).

[41]R. J. Saykally, *Acc. Chem. Res.*, **22**, 295 (1989).

[42]D. H. Levy, *Annu. Rev. Chem. Phys.*, **31**, 197 (1980).

[43]J. C. Alfano, S. J. Martinez III, D. H. Levy, *J. Chem. Soc., Faraday Trans.*, **86**, 2503 (1990).

[44]M. J. McQuaid, J. L. Gole, M. C. Heaven, *J. Chem. Phys.*, **92**, 2733 (1990).

[45]C. R. Bieler, K. E. Spence, K. C. Janda, *J. Chem. Phys.*, **95**, 5058 (1991).

[46]T. Weber, H. J. Neusser, *J. Chem. Phys.*, **94**, 7689 (1991).

[47]B. C. Chang, L. Yu, D. Cullin, B. Rehfuss, J. Williamson, T. A. Miller, W. M. Fawzy, X. Zhang, S. Fei, M. C. Heaven, *J. Chem. Phys.*, **95**, 7086 (1991).

[48]A. M. Soliva, E. J. Bieske, J. P. Maier, *Chem. Phys. Lett.*, **179**, 247 (1991).

[47]B. J. Howard, *Structure and Dynamics of Weakly Bound Molecular Complexes,* ed. A. Weber, NATO ASI series C, **212**, Reidel, Dordrecht, 1987

[50]M. A. Walsh, T. H. England, T. R. Dyke, B. J. Howard, *Chem. Phys. Lett.*, **142**, 265 (1987).

[51]A. D. Buckingham, P. W. Fowler, *Canad. J. Chem.* **63**, 2018 (1985).

[52]S. Li, E. R. Bernstein, *J. Chem. Phys.*, **95**, 1577 (1991).

[53]J. M. Hutson, *Annu. Rev. Phys. Chem.*, **41**, 123 (1990); J. M. Hutson, *Advances in Molecular Vibrations and Collision Dynamics,* **1**, 1 (1991); M. L. Dubernet, D. Flower, J. M. Hutson, *J. Chem. Phys.*, **94**, 7602 (1991).

[54]J. M. Hutson, *J. Chem. Phys.*, **89**, 4550 (1988).

[55]A. R. Cooper, J. M. Hutson, *J. Chem. Phys.*, in press (1993).

[56]R. Barrow, P.Crozet, *Annual Reports of the Royal Society of Chemistry,* to be published 1993.

Chapter 2

The pulsed supersonic expansion, Fourier-transform microwave spectrometer

2.1 Introduction

Pulsed supersonic expansion microwave Fourier-transform spectroscopy has become a well established technique since first reported by Balle and Flygare in 1979[1]. A number of similar spectrometers have been constructed and modified in other laboratories for example by Driezler[2] and coworkers, Legon[3], Bauder[4] and Lovas[5]. These more recent spectrometers incorporate technological improvements, computer control[6] and automation[2].

The recently assembled apparatus in Oxford follows the design of Flygare with some modification. Figure 2.1 illustrates the main features of the spectrometer consisting of microwave frequency generation, Fabry-Perot cavity, pulsed supersonic nozzle and a low noise heterodyne detection circuit. Gas from a pulsed supersonic nozzle ($\sim$300 μs pulse length) is expanded into an evacuated chamber with large dimensions so not to perturb the expansion dynamics. The gas expands between the two spherical mirrors of the Fabry-Perot cavity, either along the cavity axis or perpendicular to it. A microwave pulse is generated from a coherent tunable low noise source and introduced into the cavity tuned to resonance at the microwave frequency of choice. The microwave pulse, which is $\sim 1\mu$s in length, is timed to coincide with the gas pulse and optimize absorption and emission processes. Transient absorption by the molecules occurs if a rotational transition falls within the bandwidth of the cavity and the microwave pulse. After a delay to avoid detector saturation, the spontaneous coherent emission is detected using a heterodyne detection system which beats, phase coherently, the signal down to low ≤ 1 MHz offset frequencies. The down converted beat frequencies can then be sampled digitally during the time taken for the phase coherent signal to decay to noise level. By repeating the process in the absence of a gas expansion and subtracting the result from the emission data, coherent instrumental noise can be removed. Cycling this procedure N times with averaging results in an increase in signal to noise (defined as peak height to root mean square height of noise) of $\sqrt{(\frac{1}{2}N)}$. The averaged decay signal, termed the free induction decay (abbreviated to FID), can then be Fourier-transformed to give the frequency spectrum.

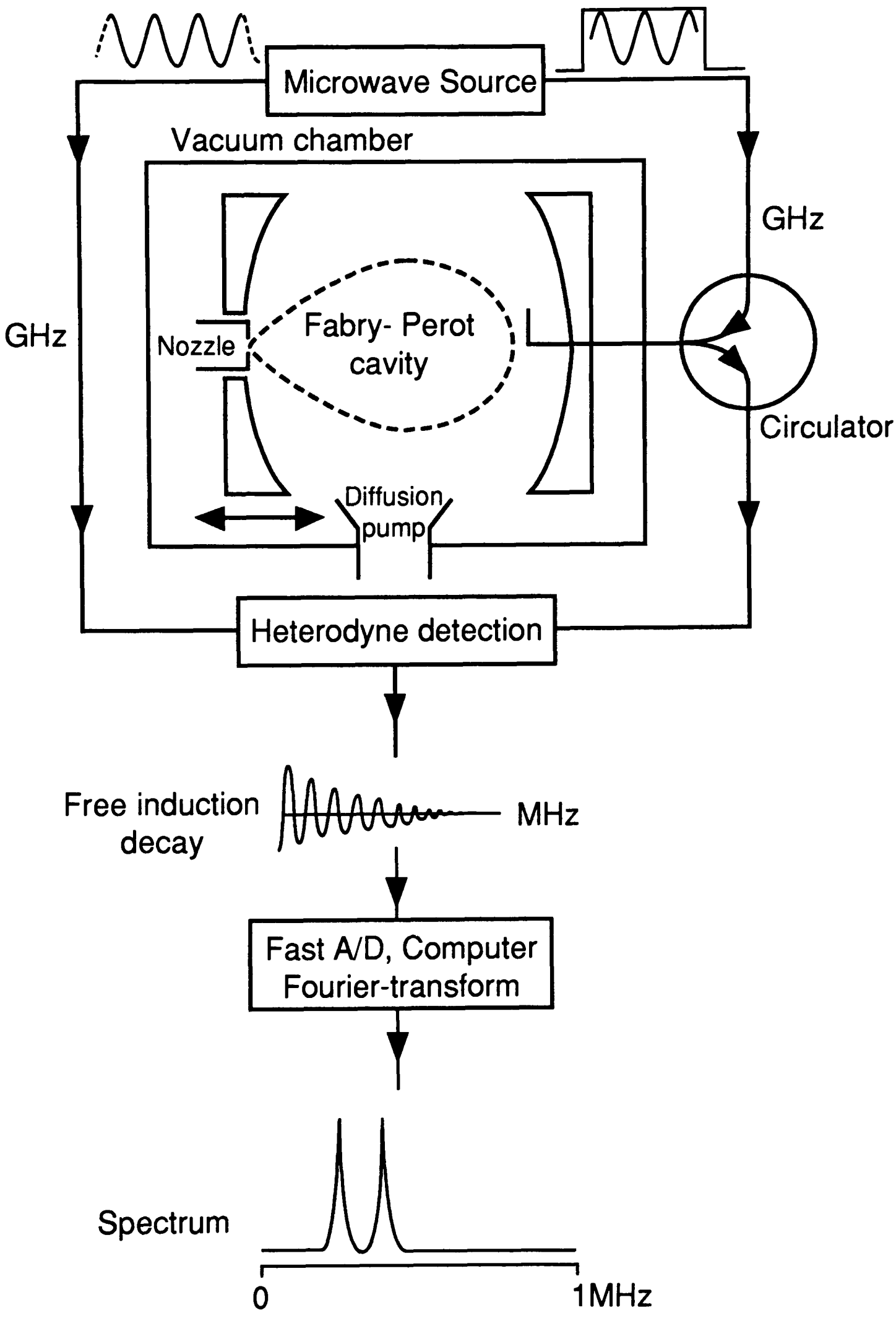

Figure 2.1; Schematic diagram of the pulsed supersonic expansion, Fourier-transform microwave spectrometer.

Extension of the technique with the application of electric (Stark) fields has allowed dipole moment measurement[7]. Laser ablation[7], heated[8] and extended channel nozzle[9] arrangements have enabled the generation of relatively involatile molecules and the study of rotational spectra in excited vibrational states. Electric discharge nozzles[10], together with Helmholz coils to control homogeneous experimental magnetic fields, have recently opened up the field of open shell molecules to high resolution study[11].

2.2 The spectrometer

Before describing the operation of the spectrometer in detail, the properties of cavities, supersonic expansions and the theoretical background of the technique are considered.

2.2.1 Fabry-Perot cavities

The high power stored in high reflection, low loss (corresponding to a high Q, equation 2.3) resonant microwave cavities, compared with the low power input to the cavity, improves the efficiency of interaction between the radiation and molecular species. Figure 2.2 illustrates the essential features of a general Fabry-Perot cavity combined with a supersonic expansion in arrangements used in the spectrometer. Flygare employed the cavity properties by expanding gas through a Fabry-Perot cavity at 90° to the cavity axis (figure 2.2b). Subsequently Stahl *et al.*[12] obtained a more efficient overlap of the spatial properties of the cavity and the supersonic expansion by directing the expansion along the cavity axis (figure 2.2c).

Fabry-Perot cavities provide a number of properties[13] useful in the study of supersonic expansions by microwave Fourier-transform methods. The open design of such cavities allows ease of access and easy pumping under vacuum conditions and can be made large enough so as not to disturb the dynamics of a supersonic expansion during the few hundred μs emission of a typical experiment. The high intensity localized fields supported between the mirrors give improvements in sensitivity and can be exploited to sample reduced regions of the expansion and improve resolution.

Spherical mirror Fabry-Perot cavities have the advantage over planar or parabolic cavities in not requiring the axis of the mirror to be well aligned for optimum use. Provided the mirror is large relative to the field pattern (to minimize diffraction losses) and approximately correctly orientated, a high Q field pattern can be established although not necessarily with optimum use of the mirror area. This feature allows the mirrors to be moved using a simple drive mechanism without great attention to alignment being necessary and fulfils an additional requirement for scanning the resonant frequency, that the cavity be easily and rapidly retuned (by translating one mirror by Δ mm, changing the mirror separation, d) while retaining the high Q factor.

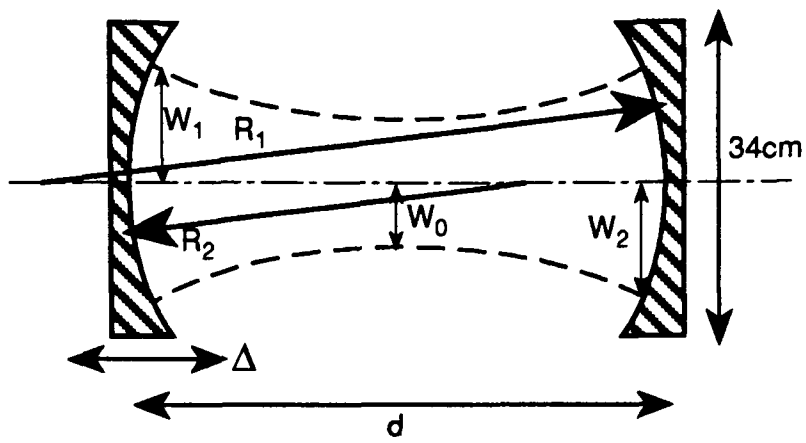

2.2a; General near-confocal spherical cavity defining the radii of curvature, $R_{1,2}$, the beam waist $W_{0,1,2}$ (and indicated by dashed line), mirror separation d ~ $\frac{1}{2}R_1 + \frac{1}{2}R_2$ and tuning displacement Δ.

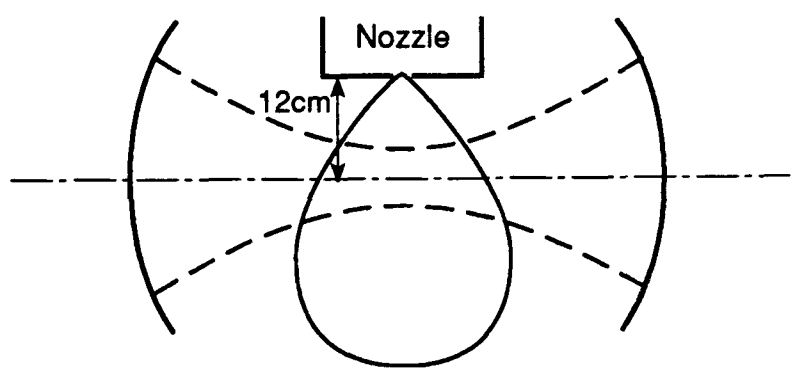

2.2b; Cavity with a perpendicular expansion.

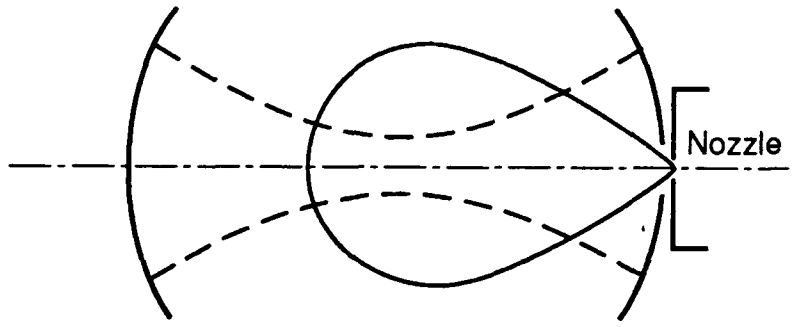

2.2c; Cavity with parallel expansion.

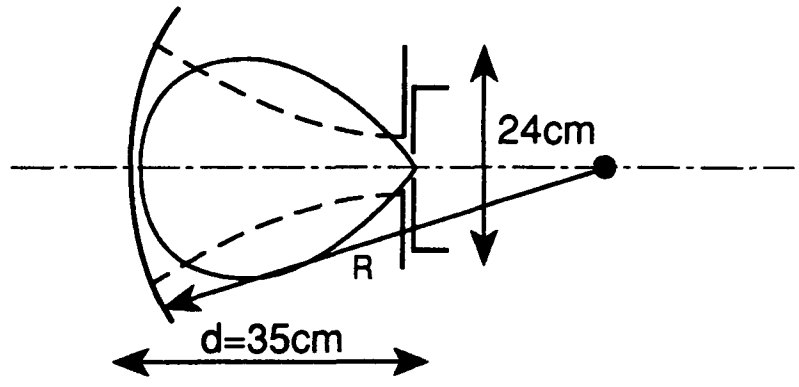

2.2d; Hemispherical cavity for use with a laser ablation nozzle giving an axial expansion. Mirror separation d ≈ ½R.

Figure 2.2; Various Fabry-Perot cavity arrangements.

To design a suitable microwave Fabry-Perot cavity, the nature of the fields supported between the mirrors must be considered. Extensive reviews on the theory of electromagnetic fields in Fabry-Perot cavities derived for lasers, masers and optical systems are given elsewhere[14]. Field distributions in spherical mirror Fabry-Perot cavities have been calculated by considering constant phase wavefronts propagating between mirrors and equivalent lens systems with propagating rays. Field distribution solutions for standing-waves in the cavity are Hermite-Gaussian wavefunctions labelled TEM_{mnq} where m and n refer to the order of the Hermite polynomial in the transverse plane and q to the number of half wavelengths between the mirrors (*cf.* Hermite polynomials are also solutions to the harmonic potential Schrödinger equation). Linear polarization patterns for the lowest order TEM modes illustrating the position of field nodes are shown in figure 2.3[15]. The beam waist, ie the point at which the field intensity falls to 1/e of its equivalent phase axial value, is often used to characterize the fundamental mode field distribution. In figures 2.2a-d, the beam waist is indicated by the dashed line. General expressions[14] for the beam waist (w_1 and w_2) at mirrors of radius of curvature R_1 and R_2, separation d (figure 2.2a) are given by

$$\left(\frac{w_1}{w_2}\right)^2 = \frac{R_1}{R_2}\frac{R_2-d}{R_1-d} \qquad (w_1w_2)^2 = \left(\frac{\lambda}{\pi}\right)^2 \frac{R_1R_2d}{R_1+R_2-d} \tag{2.1}$$

and resonant frequencies(ν) by,

$$\nu = \frac{c}{2d}\left[q+\frac{1}{\pi}(1+m+n)\cos^{-1}\sqrt{\left(1-\frac{d}{R_1}\right)\left(1-\frac{d}{R_2}\right)}\right] \tag{2.2}$$

c is the speed of light. Equation 2.2 gives rise to resonant conditions depending on transverse(m,n) and axial (q) modes as illustrated in figure 2.4. In the confocal configuration, the transverse modes are degenerate. In addition, the comb of resonance frequencies is tunable by varying the mirror separation, d in figure 2.2a.

Flygare *et al.*[1] give expressions for the power and Q factors of the Fabry-Perot cavity and antenna by an equivalent circuit treatment. The Q or ratio of total energy stored in the cavity (and/or the input/output couplings) to the energy dissipated per cycle defines a number of important characteristics. An approximate Q can be calculated by estimating the fractional power loss per cycle(α) of a beam between the mirrors.

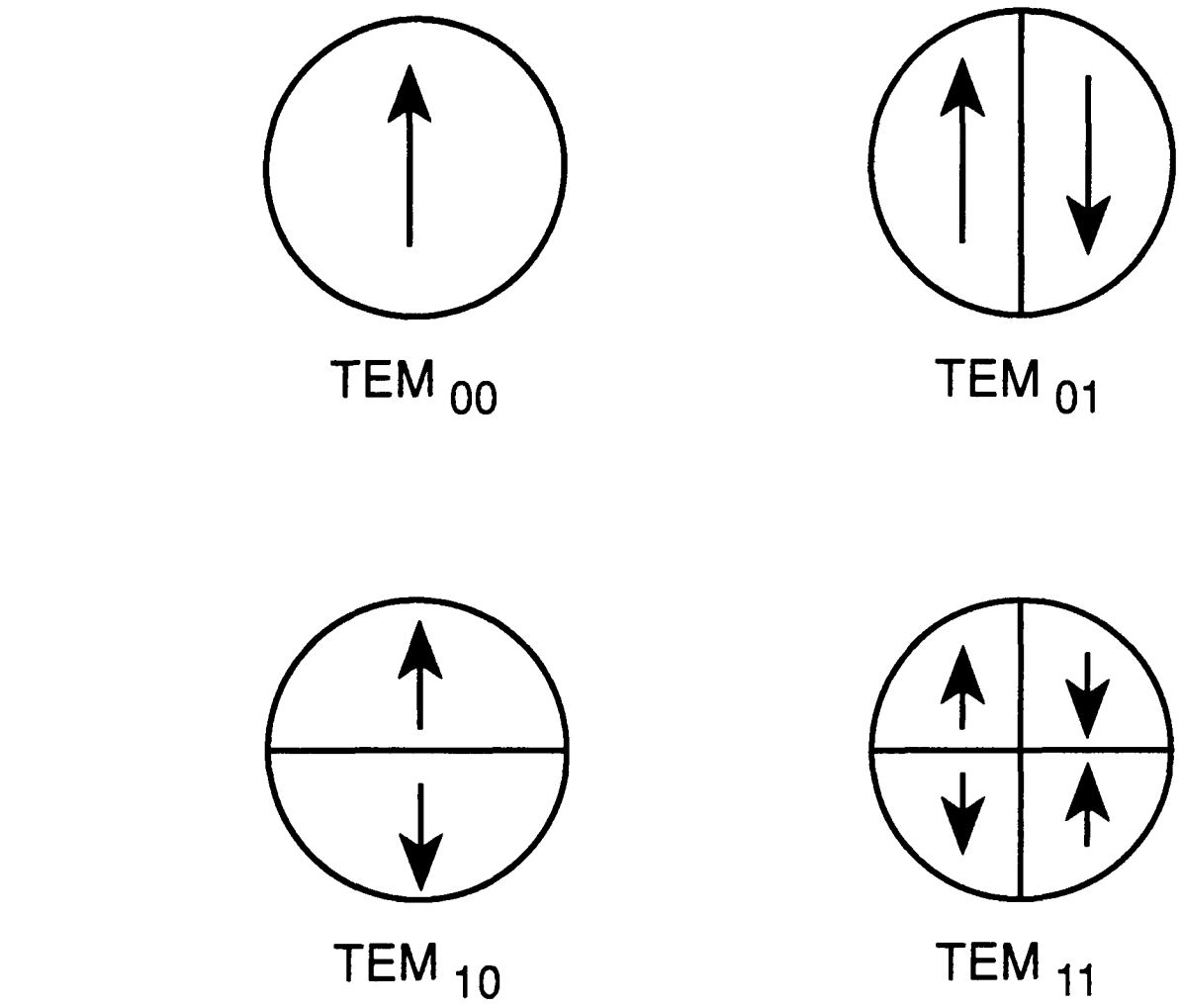

Figure 2.3; Schematic diagram of the variation of linear polarization and field node positions across some low order transverse TEM_{mn} modes in a spherical Fabry-Perot cavity[15].

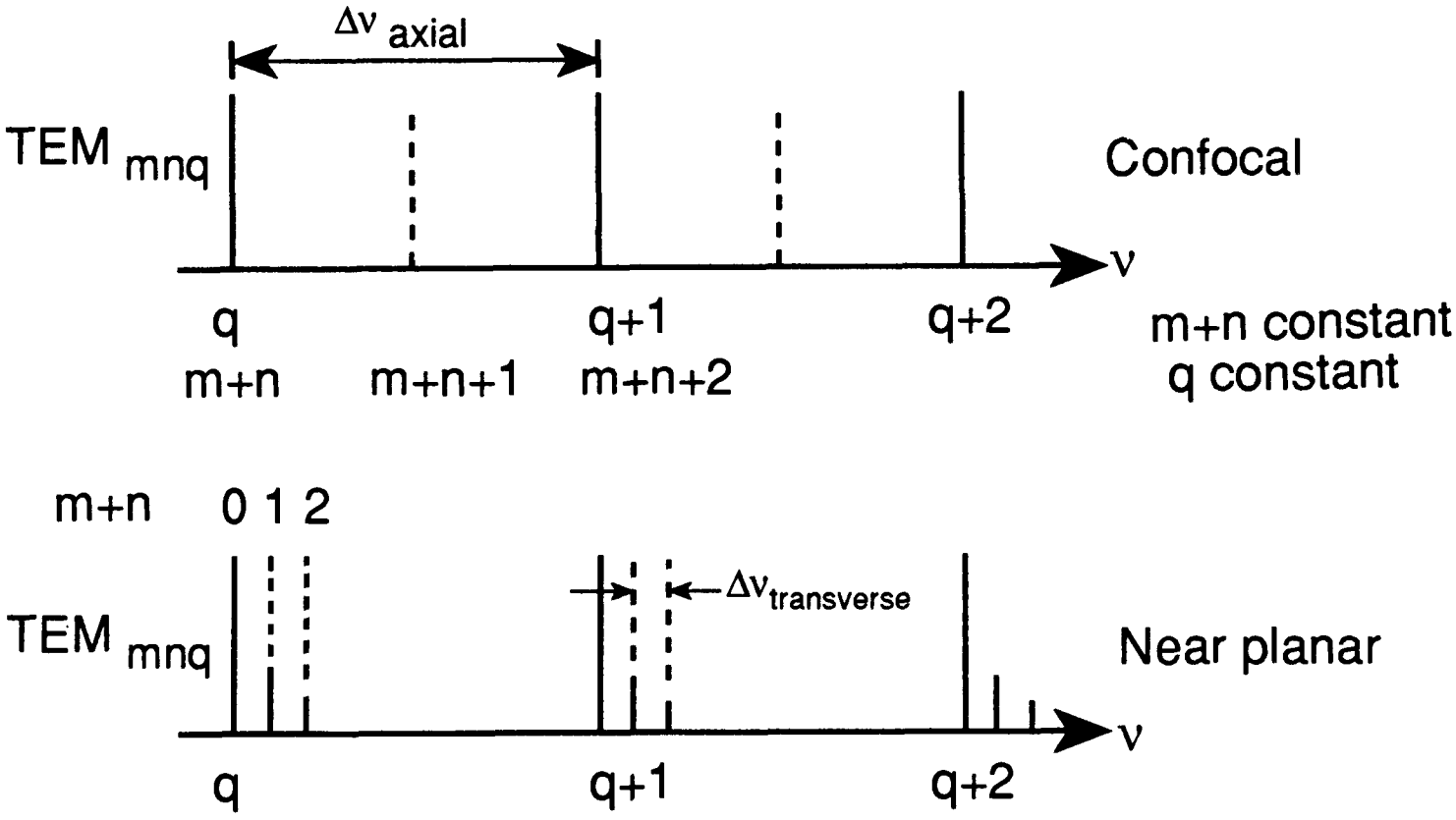

Figure 2.4; Pattern of axial and transverse mode resonant frequencies for confocal and near-planar ($R \gg d$) Fabry-Perot cavity configurations[15].

$$Q = \frac{2\pi d}{\alpha\lambda} = \frac{\nu}{\Delta\nu} = 2\pi\nu\tau_c \qquad (2.3)$$

τ_c is the cavity decay time constant, λ the wavelength, ν frequency and $\Delta\nu$ the cavity resonance lineshape full width at half height.

For reflection losses only, the Q can be expressed in terms of the mirror material skin depth (δ) and the mirror separation[1]. For aluminium mirrors separated by 50 cm at 10 GHz the Q is approximately 3 x 10^5. This can be compared with the general operating Q estimated directly via $Q=\nu/\Delta\nu$ to be $\leq 10^4$, where $\nu=10$ GHz and the cavity Lorentzian resonance curve full-width at half height $\Delta\nu \geq 1$ MHz. Also important is the cavity decay time constant τ_c which must be much less than the molecular polarization decay time constant, T_2, in order to avoid introducing additional noise into the detection process. τ_c is calculated from $\tau_c=Q/2\pi\nu$ to be 0.16μs at 10 GHz and considerably shorter than the $\sim$200μs polarization decay time observed for axial expansions.

An approximately confocal cavity was used for initial experiments with a perpendicular supersonic expansion, as depicted in figure 2.2b. Two 50 cm centre of curvature, circular aluminium mirrors of diameter 35cm were employed giving a beam waist at the mirror of 8.9-5.1 cm for 6-18 GHz. In the confocal arrangement, the beam waist(w) is at a minimum and the transverse modes are degenerate in frequency (figure 2.4a). For the spectroscopic application, it is most desirable to support the fundamental transverse mode TEM_{00q}(fig. 2.3) in the absence of higher order modes to eliminate non-degenerate transverse mode resonances(fig. 2.4b) which can result in spurious signals. This also ensures the highest field density at the cavity axis with the narrowest field distribution, suitable for sampling a reduced Doppler component of an axial expansion. Due to the open structure of the cavity, higher more spatially divergent transverse modes are automatically suppressed by spilling off the mirrors. Lower order modes, for example TEM_{10q}, TEM_{01q} which become more prevalent at higher frequencies, can be suppressed by fixing annuli of microwave absorbent foam[16] of suitable radii to one mirror to selectively degrade the Q of the higher modes. The Q of the lowest mode can also be adjusted, either by increasing the mirror separation to improve the Q or by degrading the Q with foam, to give a convenient cavity resonance bandwidth. The separation of axial modes or free spectral range of the cavity is approximately 300 MHz from equation 2.2.

Subsequently, a nozzle was installed at the centre of a 70 cm radius of curvature(R_1), 35 cm diameter mirror to allow axial expansions[12] and used in conjunction with a 50 cm (R_2) mirror (see figure 2.2c). It was found that cavity mode characteristics were most useful with a mirror spacing

(d) of ~40 cm, ie less than confocal. Under these conditions at 6 GHz the beam waist at the 70 cm mirror is 6.7 cm, 9.9 cm at the 50 cm mirror and the axial mode separation ~375 MHz. Theory based on equivalent sequences of lenses suggests that for mixed focal length mirrors the cavity is unstable, ie the beam waist increases rapidly with mirror separation and diffraction losses become important, for separations $R_2 > d > R_1$ and $d > R_1+R_2$.

A hemispherical cavity employing a flat mirror, diameter 24 cm, with a centrally mounted laser ablation nozzle and a 70 cm radius of curvature(b) mirror with a cavity separation(d) of ~34 cm (see figure 2.2d and chapter 7) was also used. This cavity has characteristics equivalent to the near confocal two b=70 cm mirror cavity but with half the mirror movement resolution. Theory suggests that the cavity becomes unstable when the mirror separation equals or exceeds the radius of curvature(b).

2.2.2 Antennas

The coupling of microwave power into the Fabry-Perot cavity is of primary concern. As expressed by the reciprocity theorem for antennas[17], the radiation pattern properties of an antenna in transmitting and receiving are the same. This feature is exploited by using the same antenna by way of a circulator to perform the polarization and detection processes.

There are a number of requirements to be considered in the selection of a suitable antenna. The antenna must be broadbanded, preferably operating from 6 to 18 GHz without modification. For a coaxial application a dipole (monopole) or loop antenna is most suitable[18] providing linearly polarized radiation. The radiation pattern, ie the angular power distribution, of the antenna should optimally match the power distribution of the lowest cavity transverse mode, TEM_{00}. For a dipole antenna, that requires the dipole to be half the transmitted wavelength which at 12 GHz is ~2.5 cm. At longer dipole lengths, nodes are introduced into the radiation pattern along the cavity axis and are more likely to excite higher cavity modes. In practice it was found that dipoles, with one pole removed, of length 1.5 cm or less were most effective with shorter antennas appearing to be more broadbanded.

The influence of the mirror on the antenna field pattern is also of importance. Mirrors are used in many antenna applications to improve the directionality although usually in free space rather than in a cavity arrangement. However, the qualitative free space results are similar to what is observed in the cavity and are summarized here. The flat mirror configuration, as used in the laser ablation system, is considered for simplicity and in such an arrangement the effect of the mirror can be considered as equivalent to an image antenna with a phase reversal. The result is an increased directionality of the field pattern dependent on the antenna-mirror distance. Free space mirror-

antenna calculations[18] suggest that the optimum antenna-mirror separation is between 0.1 and 0.25 λ, where the bandwidth of the antenna increases with smaller separation. Again this is generally found to be the case in practice with the cavity.

All these considerations result in a requirement for the antenna to be positionally adjustable, preferably while the system is under vacuum. This was achieved by using a length of semirigid coaxial cable, with the central conductor forming a 1 cm single-pole antenna, passing through a single O-ring bulkhead feedthrough and connecting directly with the microwave circuit.

2.3 The supersonic expansion

Supersonic expansions generated in low pressure systems through small commercially available nozzle systems have been used extensively in the spectroscopy and study of weak intermolecular forces and clustering. Such expansions achieve low temperatures, narrow velocity distributions and directed flow. A substantial degree of clustering is also observed. The low relative velocities in the beam reduce the collisional broadening while the localized gas density remains high. By pulsing the nozzle the background pressure can be maintained low enough so that the expansion is not perturbed significantly by background collisions. As a result, higher localized concentrations of longer lived van der Waals complexes are observed than in low pressure, low temperature static cells. There is also an improvement in sensitivity to be gained by using a pulsed nozzle. A signal to noise improvement of $\sqrt{N}$, where N is the number of pulses, is gained compared with the analogous experiment using a continuous flow nozzle[1]. This field has been the subject of much research and is comprehensively reviewed by Scoles[19].

Properties of a gas flow through a nozzle are dependent on the size of the nozzle aperture(D) relative to the mean free path(λ) of the gas behind the nozzle and the pressure difference across the nozzle. Supersonic flow requires $\lambda \ll D$ where, for conditions typical of the experiments in this thesis, a backing pressure of 1.5 atm, the mean free path is of the order of 10^{-8} m compared with a nozzle diameter of 0.5mm. Under these conditions, many molecular collisions occur during the expansion through the nozzle aperture with the effect of collimating the molecular velocities and redistributing internal energy into directed flow. The effect is a narrowed distribution of molecular speeds and a corresponding drop in associated translational temperature. Simulated velocity distributions[22] are illustrated in figure 2.5. Collisions continue down stream of the nozzle with decreasing frequency until the decreasing density of the expansion results in a diverging, almost collision-free molecular flow. Down stream of the nozzle, flow velocities(v) are greater than the local speed of sound(a), hence the term 'supersonic'.

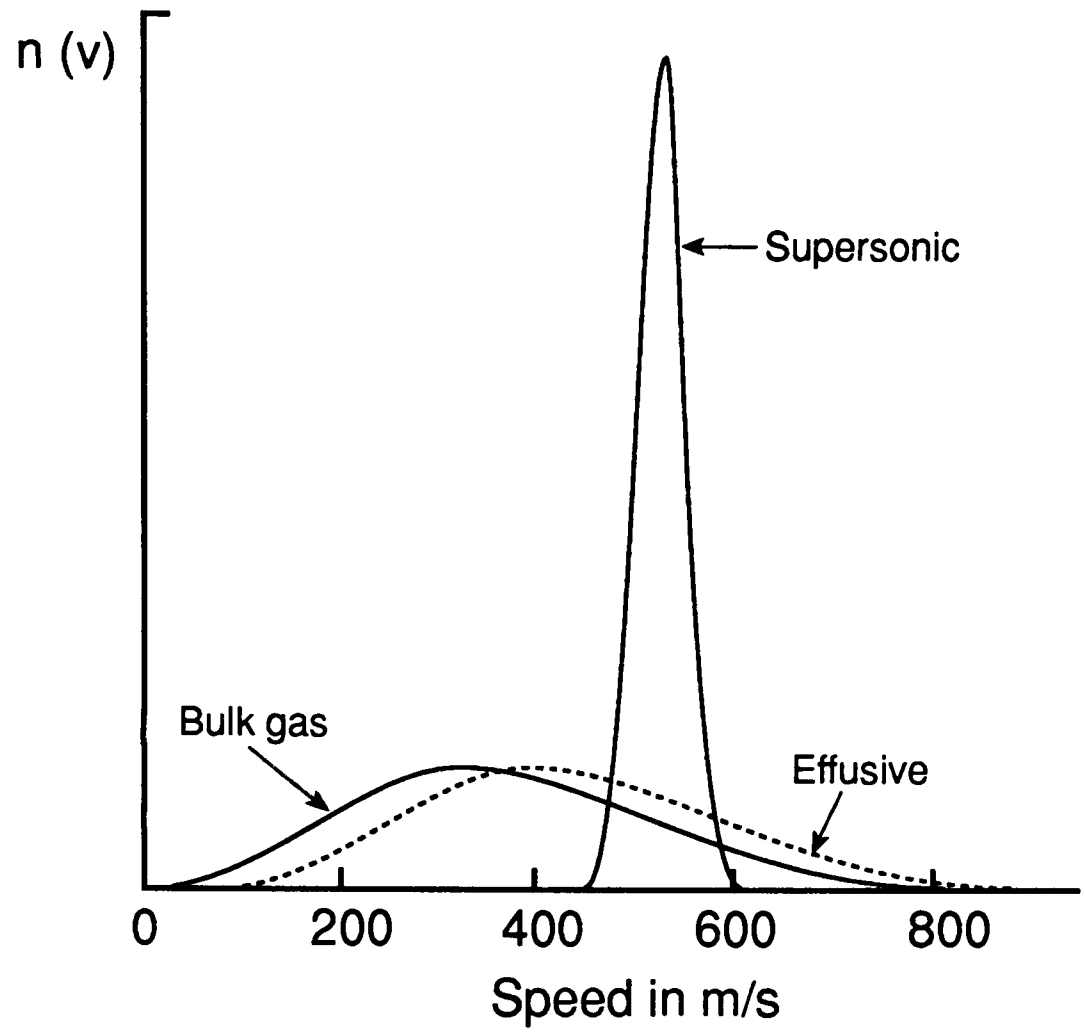

Figure 2.5; Molecular speed distributions in the bulk gas, effusive and supersonic expansions[22].

The ratio of the flow velocity (V) to the local speed of sound(c) or Mach number(M) is used to characterize the speed of the expansion[19],

$$V = Ma = M\left(\frac{\gamma kT}{m}\right)^{\frac{1}{2}} \tag{2.4}$$

m is the mass of the gas particle, T is the local temperature, k the Boltzmann constant and γ the ratio of specific heat capacities.

For an adiabatic and isentropic expansion of a perfect gas, thermodynamic expressions for a supersonic expansion can be derived for the temperature(T), pressure(P) and gas density(ρ) in terms of γ and the Mach number(M)[19,1].

$$\left(\frac{T}{T_0}\right) = \left(\frac{\rho}{\rho_0}\right)^{\gamma-1} = \left(\frac{P}{P_0}\right)^{\frac{\gamma-1}{\gamma}} = \left(1+\frac{\gamma-1}{2}M^2\right)^{-1} \tag{2.5}$$

Parameters with subscript 0 refer to the conditions behind the nozzle. An expression for the flow

velocity in terms of the temperature can also be written,

$$V = \left[\frac{2\gamma}{\gamma-1}\frac{kT_0}{m}\left(1-\frac{T}{T_0}\right)\right]^{\frac{1}{2}} \qquad (2.6)$$

Various expressions have been derived to determine the Mach number as a function of distance downstream measured in nozzle diameters[19]. By the same analysis, the terminal Mach number, M_T, where continuous flow can be thought to convert to free molecular flow can be determined by the source pressure, P_0/atm, and nozzle diameter, D/cm. For an argon expansion, M_T is given by[20],

$$M_T = 133(P_0 D)^{0.4} \qquad (2.7)$$

This can be used with equations 2.5 and 2.6, to determine the terminal flow velocity and translational temperature. For a typical argon expansion from a reservoir at 298 K with a backing pressure of 2 atm and 0.5mm nozzle diameter, the terminal Mach number is $\sim$53 corresponding to a translational temperature of 0.3 K and a terminal flow velocity of 556 m s^{-1}(eqn 2.6). This is not usually achieved in practice, due to beam warming by cluster formation. The presence of a low concentration of a molecular species also influences the temperature.

For non-ideal expansions, several additional effects must be considered. The expansion occurs into a finite volume at low pressure defining the boundary conditions. Interactions between the background gas and the expansion result in shock wave regions of local compression. Such regions are expected to be several mean free path(λ) distances in depth which at pressures of 10^{-4} mbar, $\lambda \approx 0.5$m are expected to be quite diffuse. More perturbing effects are expected in the event of collision with fixings and the cavity walls. For an axial expansion with a 50 cm mirror separation and a terminal flow velocity of 550 m s^{-1}, the leading edge of a 200μs gas pulse, after collecting the emission signal for 300μs, will have travelled 27.5 cm. This suggests that by increasing the mirror separation (with the main result of increasing the Q) a nozzle could be mounted in each mirror with up to a factor of 2 increase in sensitivity.

The effect of introducing a low concentration of a molecular gas into an argon expansion can be considered as causing perturbations of the properties discussed. As well as translational cooling, collisions result in the cooling of the internal degrees of freedom of the molecule, with different degrees of efficiency for rotations and vibrations. Smaller quanta of energy are more efficiently redistributed by collision with the result that translational cooling is greater than rotational cooling

which in turn is greater than vibrational cooling. In addition, a non-thermal equilibrium population distribution between the rotational states occurs, which is observed in the line intensity distribution in infra-red absorption spectra[21]. As the collisional energy decreases with time, the efficiency of cooling the rotational states decreases more rapidly for the higher rotational states than the lower states and the distribution is preserved in the free molecular flow region.

2.3.1 Cluster formation

With the decrease in temperature as the supersonic expansion proceeds, deviations from the isentropic assumption occur when the mean thermal energy becomes significantly less than the binding energy of the van der Waals interactions. The result is the formation of clusters which can undergo further cooling or aggregation through collisions before free molecular flow occurs. The mechanisms by which the cooling occurs are reviewed elsewhere[20] although generally, the success of any particular mechanism is related to the availability of efficient pathways for redistributing energy. An example is the greater efficiency of neon than argon in cooling vibrations because the shorter collision time scale for neon results in higher energy relaxation pathways[21]. Typical vibrational temperatures in argon expansions are of the order of a few hundred kelvin or less[21]. Rotational temperatures, calculated by fitting a Boltzmann distribution to rotational intensities for van der Waals dimers observed by infra-red absorption spectroscopy are typically 5K or less[24].

The processes involved in complex formation have been modelled based on the formation of dimers by three body collisions leading to higher clusters by binary collisions[22]. Calculated rates for the dissociation of dimers decrease rapidly with distance downstream of the nozzle. The forward rate constant for cluster formation is a weak function of the temperature(T) and therefore the rate is largely determined by decrease in monomer density which is roughly proportional to $1/r^2$ (r is distance from the nozzle). The predicted behaviour for the formation of dimer early in the expansion is an initial decrease as a result of the expansion density (ρ,eqn 2.5) decreasing while the more slowly cooling temperature is too high to stabilize complexes. This is followed by a rapid increase once the mean thermal energy is less than the complex dissociation energy $\sim 100 cm^{-1}$ ($< 144K$). With the formation of dimers dependent on termolecular collisions, the rate of formation decreases as the density cubed ($1/r^6$). The bimolecular removal of dimer to give trimer and higher clusters, decreasing with a density squared ($\sim 1/r^4$) dependency, becomes dominant further down stream diminishing the dimer concentration and increasing higher clusters concentration.

Higher initial pressure, to increase the number of collisions, is expected to increase the size and the rate at which higher clusters form. A larger nozzle diameter will result in a higher gas density, less rapid decrease in rate of binary collisions facilitating complex formation. Without

detailed rate constants it is difficult, especially for higher order complexes, to predict the optimum gas mixture and conditions.

2.3.2 Lineshapes

The density of gas as a function of polar angle away from the expansion axis, θ and distance (r) from the nozzle can be modelled for a monatomic gas by[23],

$$\rho(r,\theta) = \rho_0 \left(\frac{D^2}{r^2}\right) \cos^b\theta \qquad (2.8)$$

D is the nozzle diameter and b is between 2 and 3 for an argon expansion. ρ_0 is the gas density behind the nozzle.

The angular distribution has a number of effects. Gas travelling in stream lines away from the axis have velocity components perpendicular to the flow. If the expansion is observed using a cavity perpendicular to the expansion flow a symmetrical Doppler distribution will contribute to the line shape. It is found that the lineshape observed by FTMW spectroscopy is determined, almost exclusively, by the Doppler profile and thus the line width increases with frequency.

Equation 2.8 must be modified to take account of cluster formation. The previous section described the dependence of clustering rates on the density. It is clear that with density decreasing more rapidly off axis, the degree of clustering will be less than on the expansion axis. As a result, under most clustering conditions, a low order complex will be depleted on the axis relative to concentrations away from the axis due to higher cluster formation on the axis[22,24]. This is observed as a dip in the lineshape as illustrated in figure 2.6b. This effect is also observed in infra-red spectra discounting Doppler dephasing, described by Campbell *et al.*[1], as the dominant factor determining the dipped lineshape.

When the expansion axis is parallel with the cavity axis, the flow velocity contributes directly to the Doppler shift[1]. With radiation in the cavity travelling both parallel and antiparallel to the expansion, the line shape is split into two Doppler components symmetrically disposed about the true transition frequency (ν_0) with a shift for each component ($\nu_{\pm\text{Doppler}}$) given by

$$\nu_{\pm Doppler} = \nu_0 \left(1 \pm \frac{V}{c}\right) \qquad (2.9)$$

V is the speed of gas flow (flow velocity), c is the speed of light.

Figure 2.6a; Parallel expansion lineshape

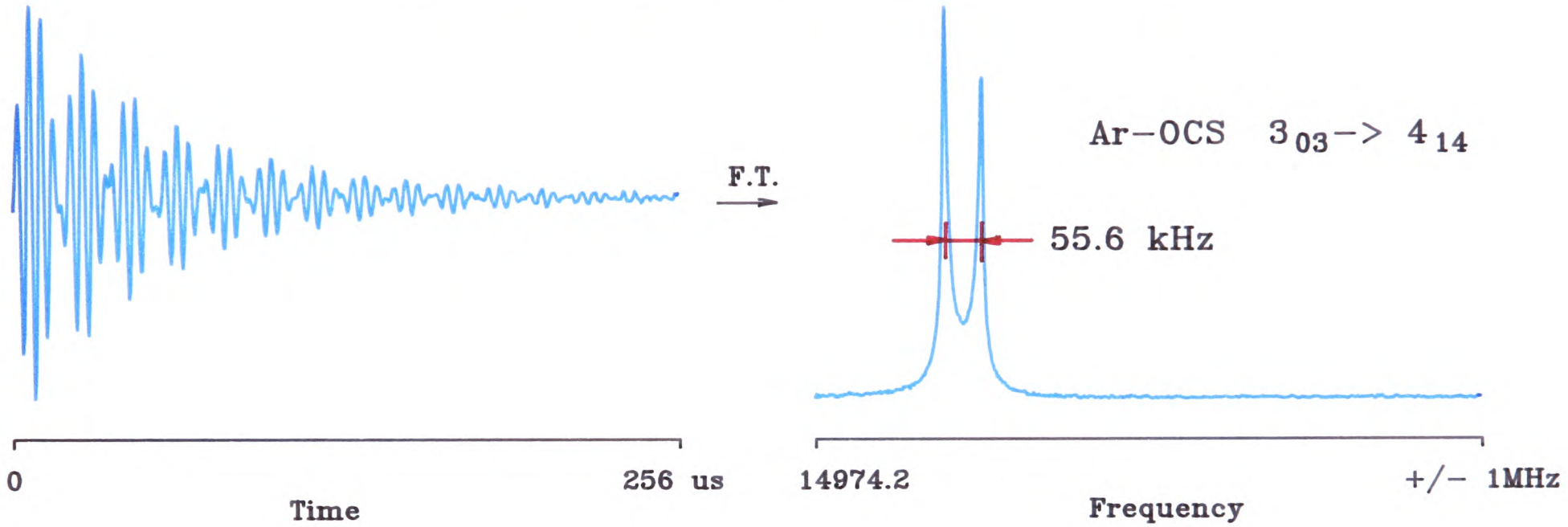

Figure 2.6b; Perpendicular expansion lineshape

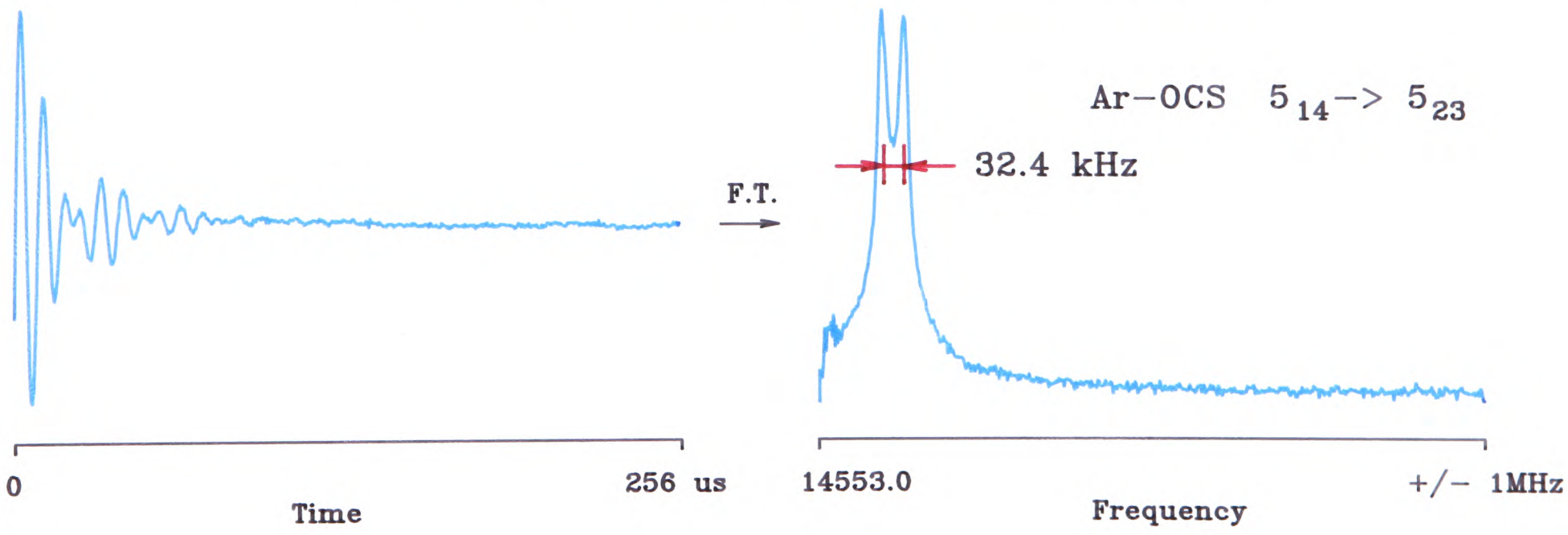

Molecules or complexes with velocity components perpendicular to the flow have transition frequencies closer to ν_0 and hence reduced intensity in the line shape is observed at frequencies between the Doppler doublets. An additional influence on the line shape due to the cavity field 'skimming' effect must be considered. The field pattern in the cavity is localized along the cavity axis(see section 2.2, fig. 2.2c). This has the effect of sampling complexes which are confined to the field volume along the axis and down weighting the contribution due to complexes with large perpendicular velocity components. Observed signals therefore have a narrower Doppler profile and decay more slowly. The cavity beam waist decreases with frequency, counteracting the corresponding increase in Doppler profile so that line widths are roughly constant at 8 kHz over the 6-18 GHz range. An example spectrum for Ar-OCS in an argon expansion is shown in figure 2.6a. The measured Doppler splitting (at 14974 MHz) is 55.6 KHz corresponding to a flow velocity of 556.6 m s^{-1}. This corresponds very closely to the predicted 556 m s^{-1} flow velocity (equations 2.7, 2.4).

2.4 Theory

Detailed theory for the electric dipole-electric field interactions for rotational systems has been developed by Flygare *et al.*[25,1] and reviewed by Dreizler[26]. Only a summary of the salient features of the analysis are given here and attention is drawn to the similarity with pulsed nuclear magnetic resonance.

The resonant frequencies of the Fabry-Perot cavity correspond to standing waves or integral numbers of half wavelengths between the mirrors (equation 2.2). As a result, reflected radiation in the cavity interferes constructively to build up in the field intensity to a steady state value characterized by the cavity quality factor or Q. The field intensity rise and decay is characterized by the time constant τ_c. During the experiment, a short pulse of radiation, τ_p, is applied to a supersonic expansion in the cavity. The pulse, τ_p is of sufficient length to allow the cavity field to reach a steady state but short enough ensuring molecular translational motion is negligible during the excitation. The molecules experience the high intensity phase coherent field and are thus coherently excited as an ensemble. The coherent ensemble electric dipole moment is therefore much larger than the molecular electric dipole moment in the corresponding process without a cavity. These results reduce the spontaneous emission lifetime and make an emission based experiment viable. With a suitable microwave pulse, the coherent emission process begins with optimum coherent polarization following the transient absorption. However, with time the molecular motion relative to the standing wave phase becomes significant. The initial coherence decays as molecular translation resulting in dephasing causes destructive interference. As a result of the diminishing coherence the observed radiation due to the oscillating macroscopic dipole decays more rapidly than might otherwise be

expected. On Fourier-transformation, this decay results in the Doppler broadened line profile. The analogous decay in NMR is characterized by the T_2 relaxation time.

The semi-classical model is convenient but to obtain a complete account of the absorption and emission processes, expressions using time dependent quantum mechanical operators must be obtained. For ensembles of two level systems this requires the use of the statistically based density matrix formalism[27]. By this method, analogues of the NMR Bloch equations[28] for the electric field-electric dipole interaction can be developed[1]. These express the rate of change of polarization induced by the electric field and population difference(ΔN) as a function of time where the polarization (P) is given by a complex function with real(P_r) and imaginary(P_i) parts (corresponding to a 90° phase shift).

$$\begin{aligned} P(r,v,t) &= (P_r(r,v,t) + iP_i(r,v,t))\, e^{i\omega t} \\ &\quad + (P_r(r,v,t) + iP_i(r,v,t))e^{-i\omega t} \end{aligned} \tag{2.11}$$

r is the position vector from the centre of the cavity, **v** is the velocity and t is time. Solutions to the Bloch type equations when the exciting frequency (ω) is the same or very close to the transition frequency (ω_0), ie $\Delta\omega=0$, are appropriate for the narrow bandwidth cavity. Expressions for the polarization and population difference at the end of the excitation pulse, where the pulse length (τ_p) is very short, are given by,

$$\begin{aligned} p_r(r,t) &= 0 \\ p_i(r,t) &= \frac{-\kappa\hbar\Delta n_0}{4}\sin(\kappa\mathscr{E}_0\tau_p f_c) \\ \Delta n(r,t) &= \Delta n_0\cos(\kappa\mathscr{E}_0\tau_p f_c) \end{aligned} \tag{2.12}$$

- p_r ,p_i and Δn are derived from terms in equation 2.10 by integrating over the velocity stream lines for molecules emanating from the nozzle ie $N(\mathbf{r},t)p_r(\mathbf{r},t)= \int d\mathbf{v}P_r(\mathbf{r},\mathbf{v},t)$, similarly for p_i and Δn.
- $\kappa=2\hbar^{-1}|\langle a|\mu|b\rangle|$ where $\langle a|\mu|b\rangle$ is the electric dipole transition moment connecting a and b levels.
- f_c is a function determined by the field distribution of the cavity mode. In the lowest order case, TEM_{00}, $f_c=1$.
- $\mathscr{E}$ is the electric field oscillation amplitude.

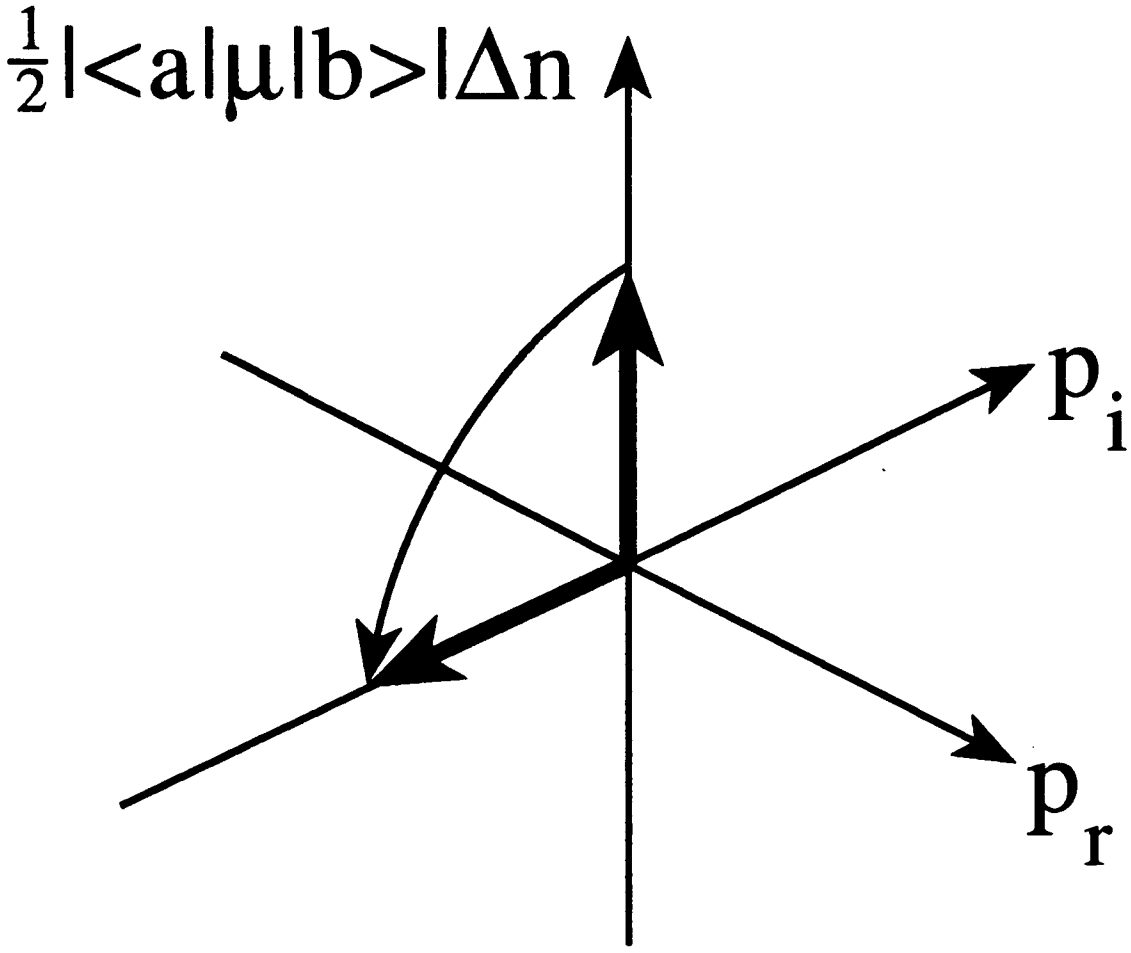

Figure 2.7; Vector model of on-resonance polarization induced by a ½π microwave pulse. Axis system is in polarization space. p_i, p_r and ½ |⟨a|μ|b⟩| Δn are defined in equation 2.11.

Again the analogy with NMR is useful and a vector model analogous to that describing magnetization in NMR can be employed[28]. The ensemble can be pictured as defining a vector sum of contributing electric dipole moments in p_r, p_i and ½|⟨a|μ|b⟩|Δn space as illustrated in figure 2.7. Optimum excitation corresponds to a 90° rotation of the vector into the polarization plane equalizing the population difference (Δn=0), figure 2.7. From equation 2.12, the 90° pulse condition corresponds to

$$\frac{2}{\hbar}|\langle a|\mu|b\rangle|\,\mathscr{E}_0\tau_p = (2n+1)\,\frac{\pi}{2}, \quad n=0,\ 1,.... \tag{2.13}$$

For a given molecular dipole, the pulse can be achieved by varying either the microwave power (related to $\mathscr{E}_0$) or the pulse length, τ_p. Generally the microwave pulse length (time) is set by the required pulse bandwidth (frequency) so that power is variable. Transitions with smaller transition dipole moments, ⟨a|μ|b⟩ require greater microwave power to achieve 90° polarization. Excitation

on resonance ($\Delta\omega=0$) results in the vector along the p_i axis, off resonance excitation ($\Delta\omega\neq0$) rotates the vector towards the p_r axis (see figure 2.7). It should be noted that unlike NMR, the microwave polarization process does not induce uniform 90° polarization for all molecules in the sample because the power density varies across the cavity modes.

Expressions for the time evolution of the emission process, in terms of p_r, p_i and Δn, are treated in the same way where the electric field in the cavity is developed by the polarized gas. Additional terms similar to the NMR T_1 and T_2 decay constants are introduced to account for the population difference and coherence relaxation processes during emission. Doppler dephasing with the decay of coherence can be considered in figure 2.7 as the diminution in the length of the vector component in the p_r-p_i plane. This occurs simultaneously with the relaxation in population difference although not at the same rate. Electric field solutions for the cavity Bloch equations must account for the expansion velocity, density distribution and observed decay by including terms for Doppler dephasing and any other relaxation effect within the confines of the cavity boundary conditions. This has been reviewed by Flygare *et al.*[1] and used to predict time domain beat patterns and spectral lineshapes.

2.4.1 Sensitivity

In detecting the effect of microwave radiation on supersonic expansions in resonant cavities, emission with time domain[29] and Fourier-transform techniques have been universally used. There are several reasons for this choice.

The multiplex or Fellgett gain in sensitivity, estimated by comparing the time required to measure a spectral line by conventional absorption and Fourier transform emission methods[30,1] is approximately a factor of 20.

As a function of frequency, the sensitivity of the Fourier transform microwave spectrometer[1] increases more rapidly with frequency than an equivalent transient absorption instrument[22]. Opposing this is the inefficiency of spontaneous emission (compared with absorption) at microwave frequencies, although this is partially alleviated by the coherence effects in the Fabry-Perot cavity. While only a fraction of the absorbed radiation is detected in emission, source noise is eliminated and superheterodyne detection reduces the detector noise. An additional increase in sensitivity results from the dependence of the detected signal on the coherent addition of molecular emitters with a population squared dependency as compared with the linear dependence for absorption. However, with increasing frequency, the cavity beam waist (section 2.2.1) diminishes and fewer molecules (approximately $\propto$ 1/frequency) are polarized.

The low temperatures(T) provided by the supersonic expansion result in large low rotational level population differences. This is very important in the emission experiment due to the T^{-2} dependence of the population and thereby the electric vector. As a result, the power spectrum has a T^{-4} dependence. A severe requirement is put on methods to increase the population of higher J levels while maintaining the sensitivity. This can be done by seeding the expansion with a large percentage of a molecular gas, such as nitrogen, to warm the expansion although usually not to great effect.

Nuclear magnetic resonance and electron spin resonance have become far more versatile by the use of pulsed Fourier transform techniques. Analogous pulse sequence[31] and two dimensional[32] techniques have been applied to the microwave experiment but with less general applicability.

2.5 Microwave circuit.

The experimental system and microwave circuit is based on the Balle-Flygare design[1]. Most circuit modifications are due to improvements in the characteristics of components[33] and can be generally summarized as follows.

- Computer controlled, broadbanded microwave synthesizers.
- low-loss broadbanded flexible and semi-rigid coaxial cable.
- Miniaturized semiconductor components with broadbanded, low noise specification.
- Single side-band generating systems and the elimination of the requirement for a second r.f. oscillator.
- Low noise and high gain microwave amplifiers.
- Use of microprocessor control in interfacing and general microcomputer usage.

The circuit used for the collection of data presented in this thesis is shown as a block diagram in figure 2.8. Component specifications are listed in table 2.1. Approximately 20mW (13 dBm) of monochromatic microwave radiation between 6 and 18 GHz is generated using a microwave synthesizer(1). The output is divided in a power divider(2) with each output passing through a broadbanded isolator(3). One output is used directly as the local oscillator input to the microwave mixer(11). Power in the other output is varied using a voltage controlled variable attenuator(4) and optional amplifier(5) combination.

Microwave pulses of $\sim 1\ \mu s$ duration are generated from the continuous output by a pin diode switch(7) and then coupled in to the cavity via a circulator(9) and antenna (section 2.2.2). The continuous wave power delivered to the cavity is $\sim$ dBm so the typical energy delivered per pulse is $\leq$?J. The pulses are carefully timed relative to the pulsed gas expansion to obtain optimum polarization and emission. In order to obtain a standing field in the Fabry-Perot cavity, the mirror separation is tuned so that the resonant frequency coincides with the input microwave frequency.

Power returned from the cavity, due either to molecular emission or reflection is coupled out through the antenna and directed via a circulator into the detector circuit. From the circulator, the output is amplified using a low noise microwave amplifier(6), with a typical noise figure of 4 dB and passed through a directional coupler(10). -6dB of the input power is rectified in a crystal diode detector(12) and used in monitoring the reflected power from the cavity. The major part of the signal continues through a second pin diode switch(8) which serves to prevent cavity ring down and other saturation effects from overloading the analogue to digital converter. A short delay ($< 10\mu s$) is set between the microwave pulse and the detector switch after which the output passes through a phase shifter (line extender)(13), an isolator(9) and into the double balance microwave mixer(11). With a difference in phase between the local oscillator input and the signal input to the mixer, a dc offset is superimposed on the output signal. The phase shifter is used to eliminate the dc offset and the down converted signal is amplified and filtered to remove frequencies greater than a few MHz.

A number of problems are associated with mixing the signal to dc. Any signal observed may be due to a transition either above or below the polarizing microwave frequency but appear at the modulus frequency in the spectrum. As a result two measurements are required to determine the position and where many transitions are close together eg hyperfine splittings, the spectrum may become very congested. Similarly the noise present both above and below in frequency will reinforce in the spectrum with a loss of $\sqrt{2}$ in signal to noise. Two methods to overcome this effect have been reported. The first is to use quadrature detection as routinely employed in NMR[28]. The second method is to mix the signal to a low intermediate frequency, suitable for digitizing eg 2 MHz, with the downconverted exciting pulse bandwidth not encompassing d.c. Such a procedure is described elsewhere based upon generating a suitable phase coherent sideband frequency to mix to 2.5 MHz[2]. An alternative method can be proposed where by the synthesizer frequency is changed by a few MHz without disrupting the phase in the period between the microwave pulse and the detection process so that down conversion occurs at a slightly offset frequency. Neither process has been used in the collection of data presented in this thesis.

In the original Flygare design, no detector circuit microwave amplifier was used and hence in order to achieve suitable amplification of the emitted signal, a superheterodyne system based on 30 MHz sidebands with narrow banded amplification at 30 MHz was used. In the circuit described above, the use of the microwave amplifier allows the 30 MHz heterodyne system to be removed simplifying the circuit. This could be done without significant reduction in signal to noise for the complexes reported in this thesis. However, there is some indication[34] that amplitude noise produced by microwave synthesizers is significant such that mixing to a more stable fixed intermediate frequency followed by amplification may improve sensitivity for weaker transitions.

Table 2.1; Microwave components

No	Component	Specification
1	Wiltron microwave synthesizer 6737A-20	Range 2-20 GHz Output 1-18 dBm
2	Reactive power divider μlab FXR D2-9FF	6-18 GHz 3 dB ins. loss
3	Isolator. M/A-COM ML 2J718	7.5-18 GHz 1.3 dB ins. loss min. isol. 10 dB
4	Var. absortive attenuator. M/A-COM ML 6560-117	Bandwidth 8-16 GHz Attenuation 9-53 dB
5	Amplifier Avantek APT 18649	Bandwidth 6-18 GHz Gain 41 dB,noise 8.3 dB
6	Low noise amplifier Avantek AWT 18675	Bandwidth 6-18 GHz Gain 34 dB,noise 4.1 dB
7	Pin diode switch General microwave F9114	Bandwidth 1-18 GHz Isol^n 78dB, Ins loss 2.6dB
8	Pin diode switch General microwave F9113	Range 1-18 GHz Isol^n 63dB, Ins loss 2.3dB
9	Circulator. M/A-COM ML 3G6100 ML 3G9700 ML 3G15200	Ins loss 0.6dB,isol. 20dB. 4-8 GHz 7-12.4 GHz 12-18 GHz
10	directional coupler μlab FXR CB-86F/106F	6 dB coupling, 6-18 GHz Ins. loss 2 dB.
11	Double balance mixer R.H.G. DM1-18A	Range 1-18 GHz,Conv. loss 6dB Isol^n 24dB, LO power $\geq$ 8.5dB
12	Point contact diode detector Omni-Spectra 20790	Range 0.01-18 GHz Max power 100mW
13	Coaxial phase shifter. Radiall	dc-18 GHz. Ins loss 0.5dB max φ 60° at 6 GHz

Numbers refer to the text and figure 2.8
Isol^n = isolation, Ins. loss = insertion loss

Pulsed Supersonic Nozzle Microwave Fourier Transform Spectrometer

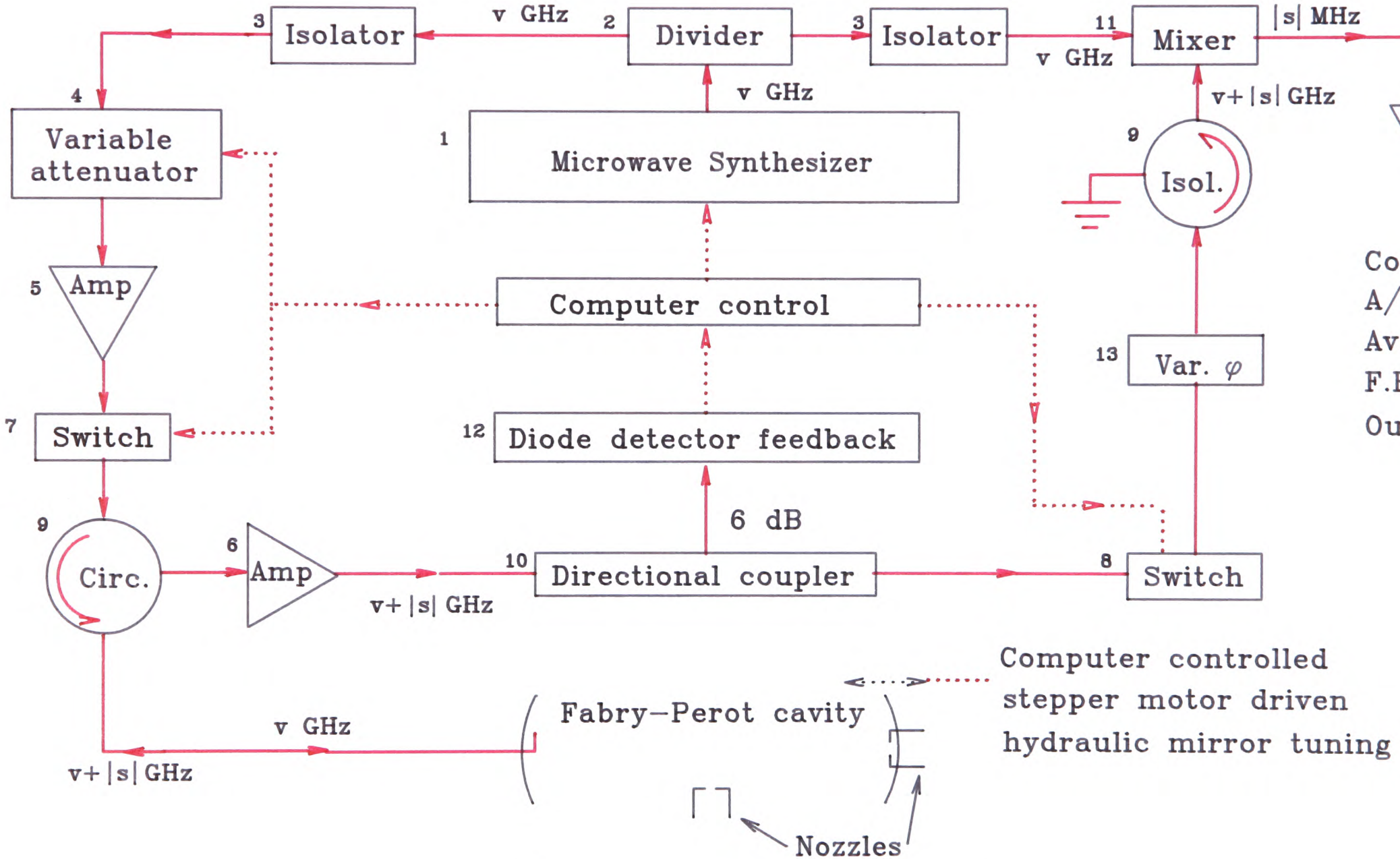

Figure 2.8; Microwave circuit diagram.

(1–12 component numbers refer to table 2.1)

2.6 Pulse sequence and averaging process

The timing between the events involved in the experiment must be carefully controlled to obtain i) optimum production and polarization of the sample and ii) the greatest resolution and sensitivity in detection. Figure 2.9 shows the typical pulse sequence used in experiments involving van der Waals complexes. The initial computer generated pulse triggers the entire process and determines the repetition rate used in averaging, usually set at 25 Hz. The nozzle is opened on alternate cycles and flow sustained for typically 200-400 μs. Subtraction of the cycles with and without the gas pulse removes any coherent noise although with the expense of reduced signal to noise.

A microwave pulse is generated by the use of a pin diode switch to modulate the output of the preamplifier. The delay time, relative to the computer initiated trigger pulse, is determined by the time required for the nozzle to function (μs for a solenoid General valve, ns for a piezo crystal LaserTechnics valve) and gas pulse to reach optimum concentration and polarization conditions for the sample to be observed. The microwave pulse width is determined by the required bandwidth of frequencies to be generated, ie equivalent to the bandwidth of the cavity($\sim$1MHz) or less, and the power to be delivered to the sample.

From the Fourier transform of a top hat function and given the width at half height, $\Delta\nu$, of the required frequency distribution (sinc function) the width of the microwave pulse ,τ_p, is given by $\tau \approx 0.9/\Delta\nu$[35]. Using the vector model of section 2.4, optimum polarization of the sample is obtained with a $\pi/2$ pulse which can be calculated as a function of microwave power and dipole moment (equation 2.13). Once the transition dipole moment is established, the microwave power required can be delivered using a suitable combination of pulse length and microwave power. With the undetermined frequency response of the microwave circuit and antenna, it is easiest to determine the optimum pulse length and microwave power by analogy with a known transition of a species with similar dipole moment present in similar concentrations.

It was found that the optimum operating bandwidth was 2MHz or less depending on the dipole moment of the molecular species and the required cavity Q. With greater bandwidths, shorter pulse widths and higher powers are required and the optimum $\pi/2$ polarization is less closely achieved. Consequently, greater averaging is required to recover the loss in signal to noise and the main gain is in diminished cavity retuning time. In addition, the requirement that $\tau_c < \tau_p < T_2$ (τ_c is the cavity decay time constant, T_2 is the characteristic molecular emission decay time) to achieve a steady state condition in the cavity following the microwave pulse imposes a lower time limit ($\tau_c \approx 0.16$ μs).

Experimental pulse sequence and timing

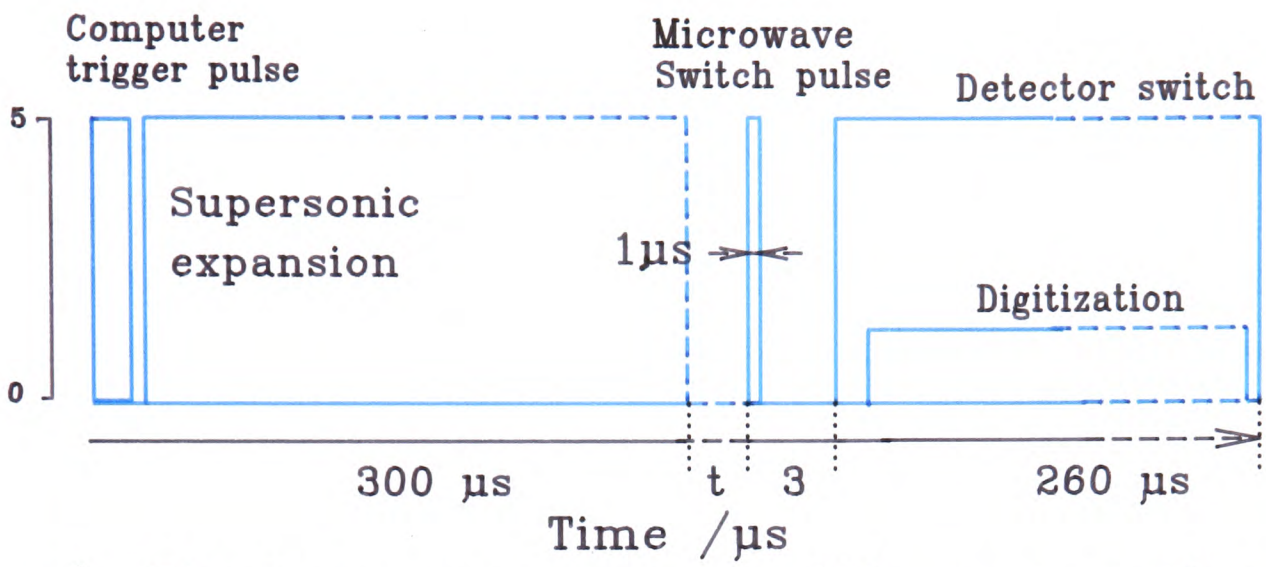

a) Timing sequence with gas pulse

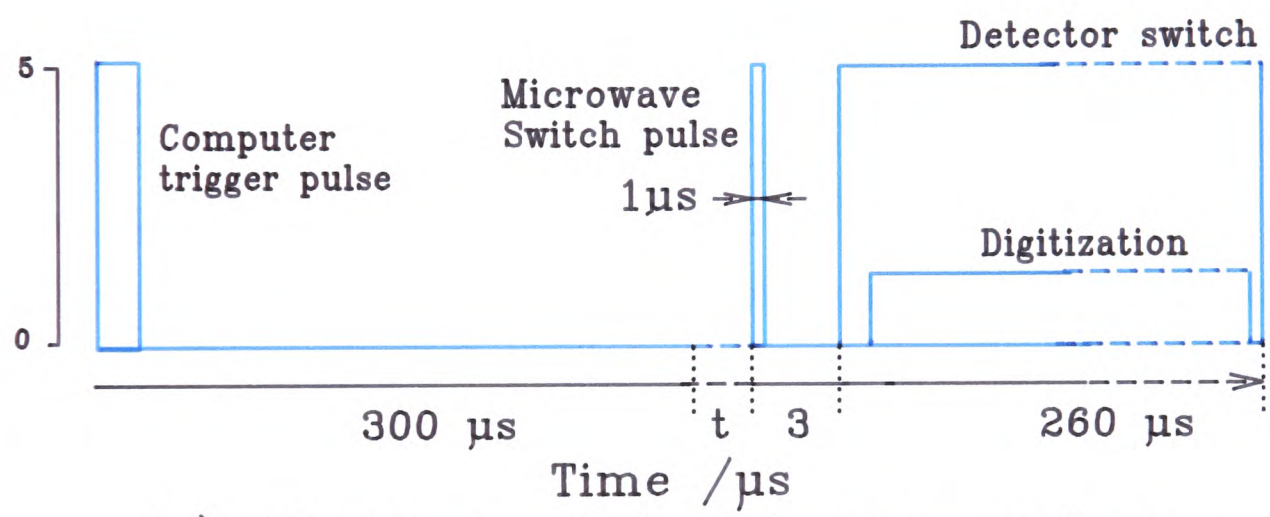

b) Timing without gas pulse

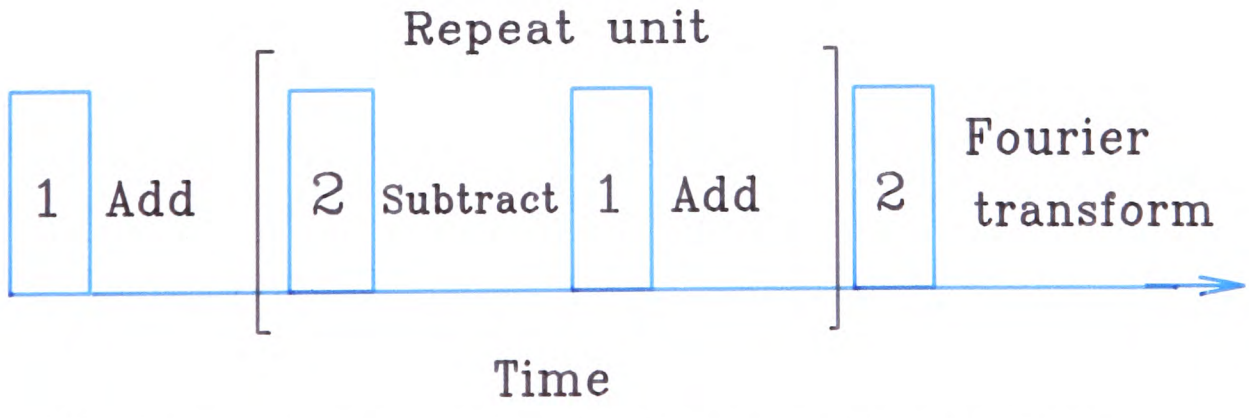

Computer averaging sequence

Figure 2.9

A delay period of typically 3-15 μs between the microwave pulse and the detector switch opening allows for decay of saturation effects and coherent signals which do not effectively cancel, such as switching transients occurring in the laser/gas pulse cycle. For the same reason, a delay of 1-5 μs is made between the detector switch closing and initiating the digitization process. This combined delay is long compared to the characteristic decay time of the cavity, $\tau_c \sim 0.16$ μs. The cavity ring down following the microwave pulse is the major source of coherent noise and hence it is possible, in the absence of other sources of coherent noise, to dispense with the alternating gas pulse sequence. A more reliable method is to use a 180° phase modulation cycle as proposed by Dreizler[26]. Neither method was employed in the collection of data presented.

Implicit to the averaging cycle is the requirement that the frequency mixing processes occur with the same phase relationship on each cycle and that timing jitter and digitization errors are minimized. Signal digitization occurs at 20 MHz whereas the trigger timers are based on 10 MHz clocks. Therefore the maximum digitization error of $\pm$ ½ clock cycle combined is not significant compared with the data collection at 2 MHz.

2.7 Computer control and data collection.

With the high resolution and narrow bandwidth of the spectrometer, any spectrum which involves a search problem is dependent on a repetitive sequence of retuning and data collection. Most processes involved in the data collection and retuning can be controlled by computer and an obvious aim is to semi-automate the scanning process to achieve greater efficiency. Control and interface software has been developed where necessary using Fortran and assembler code with the result that the spectrometer is able to scan several hundred MHz without user intervention.

The spectrometer-computer interface, illustrated in figure 2.10, is based around a fast analogue to digital (A/D) converter card and two interface cards onboard the controlling 12 MHz 286 computer. The general purpose interface bus (GPIB) card provides direct interactive control of the synthesizer. Programmed sequences using supplied routines allow setting/reading of the oscillator frequency, output power and switching between single frequency and sweep modes.

All remaining processes except the digitization of the signal are controlled by an Amplicon PC-30AT general purpose interface card based on the Intel 8255 programmable peripheral interface chip and front ended by a BNC conversion box. Of the 24 I/O TTL lines, 10 are used in pulse or logic level sequences in the experiment. Two lines are required for each stepper motor controller governing the mirror translation (2 stepper motors)(and the laser ablation rod mechansism). One pulse line and one logic line is used to initiate timed pulse sequences from the trigger box. The trigger box consists of five delay counter circuits based on 10 MHz clocks which allow independently

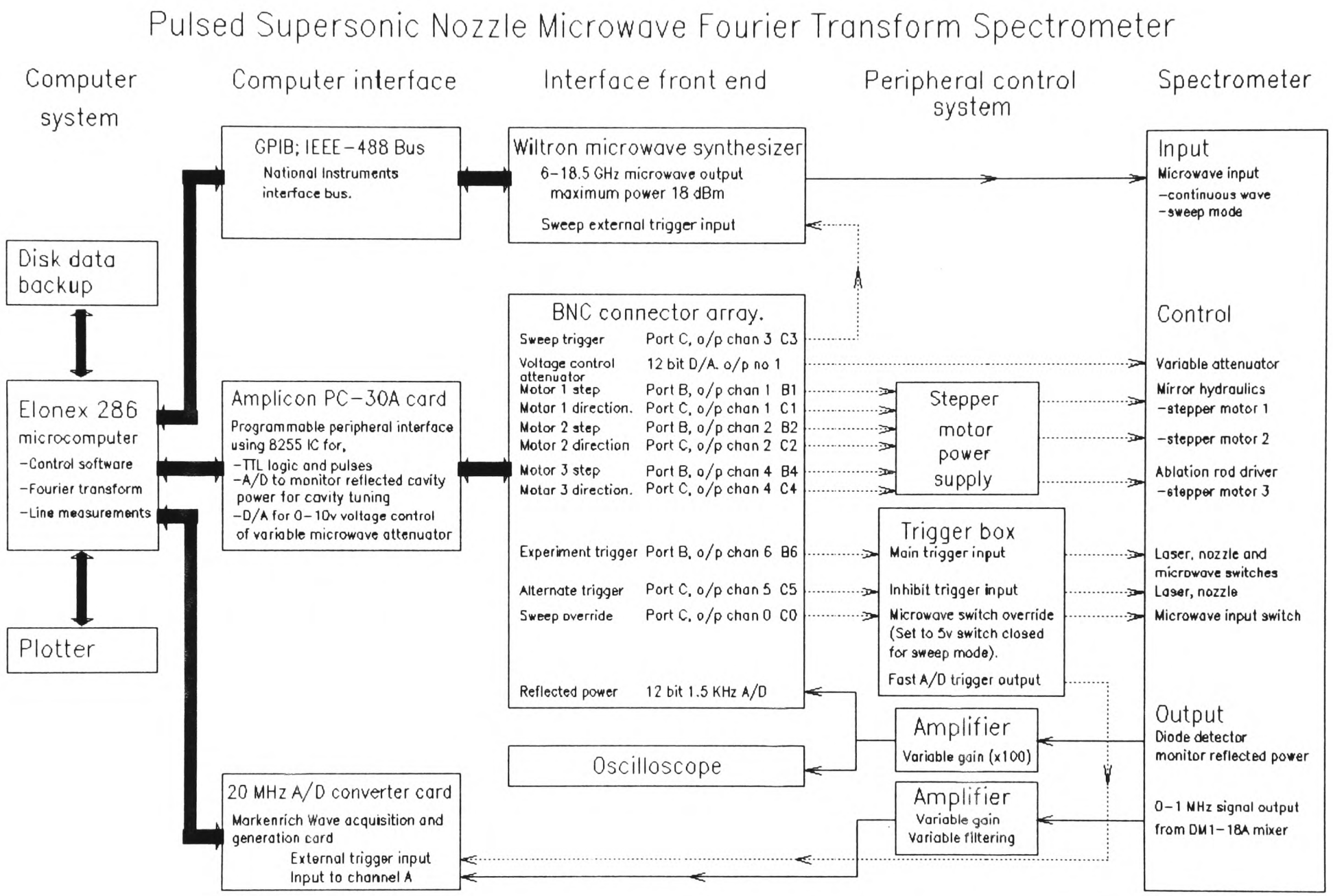

Figure 2.10; Control circuit block diagram

variable delayed triggering of the nozzle (and laser), microwave pulse, opening of the detector switch and triggering of the data collection (figs 2.9 and 2.8). The logic input to the trigger box cancels the nozzle (and laser) outputs.

While tuning the cavity, a logic line is used to close the microwave switch and a pulsed output line is used to trigger the synthesizer in sweep mode. The reflected microwave power from the cavity is detected by a diode detector (fig 2.8 component 12) and sampled using the PC30AT A/D converter. In addition, the microwave power input is controlled by the synthesizer power setting and by the use of a voltage controlled attenuator driven by a 12 bit digital to analogue converter. Control of the power is important both for obtaining the optimum polarization of the molecules and for controlling the input level to the various A/D converters.

2.7.1 Data collection

Data collection is based around a fast A/D card. The 8 bit resolution A/D card (Markenrich WAAG board) operates at 20 MHz with 16 Kbytes of onboard memory; this maps directly into system memory giving fast access. After software initialization, setting the number of data points and collection speed, data collection is started by a pulse from the trigger box initiated by the computer.

Signals are detected within $\sim \pm$ 1 MHz of the exciting microwave frequency. The bandwidth is determined primarily by the cavity bandwidth but also by the exciting pulse length and by subsequent circuit filters. From the Nyquist condition the sampling rate must be at least twice the frequency of the maximum observed frequency, in this case at least 2 MHz. In order to minimize timing errors resulting from the clock speed, the data is collected at 20 MHz and every 10th point used. Strong signals occurring outside the 1 MHz bandwidth can still be observed due to the residual fields and the unsharp filter cut-off. As a result the signal is sampled at a subharmonic of the actual frequency and folds back or aliases onto the spectrum. This can be eliminated together with any noise folding back by using every 5th point and calculating the spectrum for a 2MHz bandwidth. Using this method, the actual spectrum bandwidth can be matched to the low pass filter cut-off point.

Several additional requirements must be considered in choosing the number of points to be collected. 2^n points are required for the numerical Fourier transform procedure although this can be achieved by completing the data set with zero values. The signal must not be truncated before becoming indistinguishable from the noise since this is equivalent to convolution with a step function[28] and results in ringing in the frequency spectrum with a reduction in resolution. Also there is no need to collect the signal after it falls significantly below the noise level as this increases the noise contribution to the signal to noise ratio. All the transition frequencies in this thesis were obtained from spectra of 512 data points corresponding to 256μs of data collection. This was suitable for scanning and gave suitable resolution for spectra containing several hyperfine components.

A limitation of the fast A/D card used in this experiment is the constraint to 8 bit (or 256 steps) resolution. This requires the input signal must be correctly centred within the dynamic range

to avoid clipping large signals. Problems also arise where very weak signals are observed in the presence of very strong signals. Clipping in the time domain appears as low frequency undulations in the spectrum. There are also trigger and memory limitations involved in collecting several sets of data per pulse cycle, precluding multiple data acquisitions per gas pulse as described by Chuang *et al.*[6]

2.7.2 Automated scan

The automated sequence requires the user to initially tune the cavity to an appropriate cavity resonance, optimally tune the antenna and ensure that all A/D inputs are suitably scaled and within specified dynamic ranges. The limits of the scan must be specified and usually do not exceed the free spectral range of the cavity ($\sim$300 MHz). The step size is determined by the cavity or microwave pulse bandwidth (usually set to 1 MHz). When the data collection at one frequency is complete, the free induction decay is saved to disk. A 10 MHz sweep centred on the synthesizer frequency is digitized through the diode detector and the minimum reflected power measured. The synthesizer frequency is subsequently stepped and the cavity retuned. By monitoring the reflected power with the diode, the mirror motors are stepped until the reflected power is diminished to a level similar to that measured in the initial sweep. This method tunes to about $\pm$ 100 kHz of minimum reflected power (there is a certain amount of hysteresis associated with wearing and leakage of the mirror hydraulic system) and fine tuning is achieved by tuning the frequency and monitoring the reflected power. The entire sequence requires about 15 s and hence a 100 MHz scan with averaging of 3000 FID signals, collected at 60 Hz and a step size of 1 MHz, requires $\sim$1 hour 50 minutes.

2.8 Fourier transform and data processing

Fourier transform procedures are well established in NMR and ESR[36] and many methods and techniques are also directly applicable to the microwave data. Using the discrete Fourier transform,

$$H_n = \sum_{k=0}^{N-1} h_k \exp\left(\frac{-i2\pi kn}{N}\right) \qquad (2.14)$$

N data points of the free induction decay data, h_k, are transformed to give N points in the frequency spectrum, H_n, where the number of data points defines the resolution. The discrete Fourier transform is analogous to the continuous infinite transform except that the transform function, H_n or h_k, sampled between convenient limits, is treated as a periodically repeating function. As a result, the spectrum outside the function range can fold (or alias) back into the range and must be eliminated by low pass filtering the free induction decay as described in section 2.7.1

Using a complex Fourier transform routine from Numerical recipes[37] based on the Cooley-Tukey algorithm, 512 FID data points were zero filled to expand the data set to 2048 real points with the corresponding 2048 imaginary points all set to zero. This data set was then transformed to give the complex spectrum. The power spectrum was calculated from the sum of the squares of the real and imaginary parts and used in line measurements. Although this is the simplest way of obtaining transition frequencies, it is standard practice in NMR to use the absorption or real component spectrum to measure frequencies. However, the absorption spectrum is only of value when the phase of the signal is such that it optimizes the real component as an even symmetric function and conversely the imaginary component as odd and antisymmetric. With these conditions, the real component spectrum line widths are narrower and the signal to noise ratio is improved[38]. Delaying the detection with respect to the microwave pulse and the effect of some active electronic components results in a phase offset and a linear, frequency dependent phase change across the spectrum. The result is a complicated conjugate mixture of the even and odd functions in both the real and imaginary spectra which, without phase correction, are most easily treated as the power spectrum (sum of the squares of the real and imaginary spectra). The microwave experiment differs from the NMR experiment in that the polarizing frequency is tunable. Hence the signal phase varies with frequency requiring compensating phase shifts to be recalculated for each new measurement[38].

To measure frequencies from the lineshapes obtained, a procedure based on measuring the position of the first derivative zero crossing is used. The first derivative is calculated using a least squares convolution (or filter) function method formulated by Savitzky and Golay[39,37]. A variable size cubic first derivative convoluting polynomial based on coefficients operating over 5 to 25 data points is stepped through the data point by point. The function consists of weighting coefficients calculated to least squares fit the central data point to the 1st derivative of the polynomial when convoluted with an equal number of data points either side of the central point[40]. As the function will not fit all features precisely, there is some smoothing effect and hence greatest efficiency, the number of points in the function is determined by the width at half height of the feature to be differentiated. Some care is required if there is close overlap or poor signal to noise to avoid distorting the derivative[37]. Following the calculation of the 1st derivative, data in the linear region about the zero crossing (corresponding to the transition maximum) are least squares fitted to a straight line and the zero crossing position calculated. From the zero crossing position a frequency offset in the 1MHz modulus spectrum is measured and hence an absolute frequency can be calculated by addition or subtraction from the initial microwave pulse frequency. When the expansion is along the cavity axis and the transition is split into two Doppler components (figure 2.6a), the average offset is used to calculate the frequency.

A number of alternative procedures for calculating the spectrum from the FID data can be conceived. Maximum entropy methods are well established in NMR and existing algorithms are probably suitable for fitting microwave data[28,37]. Time domain fitting has proven useful for fitting

hyperfine data where the Fourier-transform power spectrum introduces distortions[41] in closely overlapping lineshapes. Neither method has been used in fitting the data presented in this thesis.

2.9 Vacuum system

The Fabry-Perot cavity is mounted in a chamber constructed of 1/2" stainless steel sheet with 1/4" overlap to give internal dimensions of 15½" × 15½" x 34½". Three central 9" diameter port fittings of ¾" aluminium are used to mount a laser ablation window, a quadrupole mass spectrometer and adjustable nozzle fixings. The fourth port connects to an Edwards Diffstak MK.2 250/2000 diffusion pump with a pumping speed of 2000 l s^{-1} at 10^{-4} mbar backed by an Edwards E2M80 rotary pump with a pumping speed of 80 m^3 h^{-1}. The minimum cavity chamber pressure achieved is $\sim 1.4 \times 10^{-5}$ mbar rising to $\leq 1.4 \times 10^{-4}$ mbar during optimized pulsed expansion operation. This correspond to a mean free path for hard collisions of ~50cm.

The cavity mirrors, which are of aluminium both for lightness and high microwave reflectivity, are fixed to supports which move on tracking fixed to the chamber floor. One mirror can be fixed, the other mirror position can be adjusted using a spring retained hydraulic drive system. This is controlled by two stepper motor driven micrometers giving a minimum step size of 2.5 μm, easily suitable for fine tuning cavity resonances. The total mirror movement is 30mm, more than adequate to tune 25mm between successive cavity resonances at 6GHz. For the flat mirror / spherical mirror cavity with separation 35 cm, a resolution of ~50KHz per step is obtained at 6 GHz. Apiezon C non-silicone oil is used in the hydraulic and diffusion pump systems.

Two supersonic nozzle systems have been employed. A laserTechnics LPV valve employs a piezo-crystal driver to operate the nozzle. Very fast response times are achieved although long pulses do not give consistent even flow due to poor damping of the mechanism 'bounce'. Deflection of the nozzle plunger is also very small giving different effective pressures at the nozzle compared with the gas reservoir. A General valve series 3 solenoid valve has also been used. This has a slower response time but provides a more consistent flow with better opening characteristics.

Acknowledgements.

A number of people have contributed to the commissioning of the Fourier-transform spectrometer. Mr C. Jones built the vacuum chamber, mirrors, hydraulic systems and many sundry items. The electronics workshop provided most of the power supplies, nozzle drivers and low frequency amplifiers. Professor John Muenter was instrumental in assembling the spectrometer and obtaining the first spectrum. In addition, Stephen Ashworth and Mark Jackson provided useful advice on programming and hardware interfacing.

References

[1]T. J. Balle, E. J. Campbell, M. R. Keenan, W. H. Flygare, *J. Chem. Phys.*, **71**, 2723 (1979); *ibid.*, **72**, 922 (1980); T. J. Balle, W. H. Flygare, *Rev. Sci. Instrum.*, **52**, 33 (1981).

[2]U. Andresen, H. Dreizler, J. U. Grabow, W. Stahl, *Rev. Sci. Instrum.*, **61**, 3694 (1990).

[3]A. C. Legon, *J. Mol. Struct.*, **266**, 21 (1992).

[4]R. M. Spycher, P. M. King, A. Bauder, *Chem. Phys. Lett.*, **191**, 102 (1992).

[5]R. D. Suenram, G. T. Fraser, F. J. Lovas, *J. Mol. Spectrosc.*, **148**, 114 (1991).

[6]C. Chuang, C.J. Harley. T. Emilsson, H. S. Gutowsky, *Rev. Sci. Instrum.*, **61**, 1629 (1990).

[7]R. D. Suenram, F. J. Lovas, G. T. Fraser, K. Matsumura, *J. Chem. Phys.*, **92**, 4724 (1990).

[8]M. Iida, Y. Ohshima, Y. Endo, *J. Chem. Phys.*, **94**, 6989 (1991).

[9]A. C. Legon, D. Stephenson, *J. Chem. Soc. Faraday Trans.*, **87**, 3325 (1991).

[10]J. U. Grabow, N. Heineking, W. Stahl, *Z. Naturforsch.*, **46**, 914 (1991).

[11]R. D. Suenram, G. T. Fraser, F. J. Lovas, *J. Mol. Spectrosc.*, **148**, 114 (1991).

[12] J. U. Grabow, W. Stahl, *Z. Naturforsch.*, **45a**, 1043 (1990).

[13] J.M.Vaughan. *The Fabry-Perot Interferometer.* Adam Hilger, Bristol, 1989.

[14]G. D. Boyd, H. Kogelnik, *Bell Sys. Tech.*, **41**, 1347 (1962).

[15]A. Yariv, *Introduction to Optical Electronics,* Holt, Rinehart and Winston, New York, 1976; P. W. Milonni, J. H. Eberly, *Lasers,* Wiley Interscience, New York, 1988.

[16]Emerson & Cuming (U.K.) Ltd. Eccosorb AN-73 foam sheet.

[17]F. R. Connor. *Antennas.* Edward Arnold, London, 1979.

[18]J. D. Kraus. *Antennas.* McGraw-Hill, New York, 1988.

[19]G. Scoles, *Atomic and Molecular Beam methods,* Oxford University Press, New York, 1987.

[20]G. M. McClelland, K. L. Saenger, J. J. Valentini, D. R. Herschbach, *J. Phys. Chem.*, **83**, 947 (1979).

[21]G. D. Hayman, *D. Phil. Thesis,* Oxford University, 1985.

[22] P. J. F. Gandy, *Part II Thesis.* Oxford, 1991.

[23]H. Ashkenas, F. S. Sherman, *Proceedings of the 4th International Symposium on Rarefied Gas Dynamics, Vol. 2,* ed. J-H. de Leeuw, Academic Press, New York, 1965.

[24]F. Lovas, R. D. Suenram, *J. Chem. Phys.*, **87**, 2010 (1987).

[25]E. J. Campbell, L. W. Buxton, T. J. Balle, W. H. Flygare, *J. Chem. Phys.*, **74**, 813 (1981); *ibid.* **74**, 829, (1981).

[26]H. Driezler, *Mol.Phys.*, **59**, 1 (1986).

[27]W. H. Flygare, *Molecular Structure and Dynamics,* Prentice-Hall, New Jersey, 1978.

[28]R. Freeman, *A Handbook of Nuclear Magnetic Resonance,* Longman Scientific, Harlow, 1987.

[29]J. Haekel, H. Mäder, *Z. Naturforsch.*, **43a**, 203 (1988).

[30]J. Ekkers, W. H. Flygare, *Rev. Sci. Instrum.*, **47**, 449 (1976).

[31]B. Vogelsanger, A. Bauder, *Z. Naturforsch.*, **44a**, 726 (1989).

[32]B. Vogelsanger, A. Bauder, *J. Chem. Phys.* **92**, 4101 (1990).

[33]T. K. Ishii, *Microwave Engineering.* Harcourt Brace Jovanovich (1989).

[34]A. Bauder, Private communication.

[35]H. J. Pain, *The Physics of Vibrations and Waves,* John Wiley and Sons, Chichester, 1979

[36]A. G. Marshall, *Fourier, Hadamard and Hilbert Transforms in Chemistry,* Plenum Press, New York, 1978.

[37]W. H. Press, B. P. Flannery, S. A. Teukolsky, W. T. Vetterling, *Numerical Recipes,* Cambridge University Press, Cambridge, 1992.

[38]N. Heineking, H. Dreizler, *Z. Naturforsch.*, **44a**, 573 (1989).

[39]A. Savitzky, M. J. E. Golay, *Analytical. Chem.*, **36**, 1627 (1964).

[40]J. Steiner, Y. Termonia, J. Deltour, *Analytical Chem.*, **44**, 1906 (1972).

[41]I. Merke, H. Dreizler, *Z. Naturforsch.*, **43a**, 196 (1988).

Chapter 3

The microwave spectrum and harmonic force field of Ar_2-OCS

3.1 Introduction

Van der Waals complexes involving more than two molecules or atoms are potentially of interest as intermediates between condensed phases and dimeric species[1]. It might be expected that the properties of such complexes, for example the low frequency van der Waals vibrational modes, form the basis of condensed phase properties. For small clusters, it is convenient to approach the analysis of properties using the addition of pair potentials deduced for the corresponding binary complexes and then to adjust empirically or otherwise for the many body interactions. Ar_2-HCl has been successfully analysed in this way using the detailed potentials available for Ar-HCl[2]. However, for the majority of dimers, potentials are either not available or are calculated using restrictive assumptions e.g. harmonic force field calculations and hence only trends and qualitative comparisons can be made.

In the microwave spectrum a number of higher complexes have been observed, often falling into two categories which can perhaps be considered as molecular scale limiting cases of solvent/solute and surface/adsorbate interactions. The first involves hydrogen bonded species, for example $(HCN)_2$-X where X is HF,HCl,N_2,Ar,HF-CO[3] *etc* and $(H_2O)_2$-CO_2[4] where the hydrogen bond dominates the interactions and determines the geometry. The second category involves complexes of argon clusters with aromatic species or acids, for example Ar_2-C_4H_4O[5] and Ar_n-H/DX[6] where X is Cl,Br,CN, n up to 4.

The interest in Ar_2-OCS resulted from the observation of a number of unassignable lines in argon expansions while searching for O_2-OCS. The lines were not present in an equivalent neon expansion. Following the elimination of transitions due to Ar-OCS isotopomers[7] and discounting transitions due to OCS clusters, although there is some evidence for transitions due to $(OCS)_n$ in higher concentration OCS/Ar mixtures[8], complexes due to clusters of argon with OCS appeared most likely. A previous study by Leopold and Klemperer[9] using molecular beam electric resonance

(MBER) spectroscopy yielded six weak unassigned rf and microwave transitions. These were attributed to Ar_2-OCS on the basis of mass spectroscopic evidence. Five of the transitions have been confirmed in this study. In the absence of detailed potentials for Ar-OCS, comparisons between Ar_2-OCS, Ar_2 and Ar-OCS have been made on the basis of harmonic force field analyses using the centrifugal distortion constants for several Ar_n-OCS (n=1, 2) isotopomers[7] to calculate force constants. Although the application of this method to large amplitude van der Waals modes is limited[10], general trends and comparisons with similar analysis of Ar_n-HX complexes can be made.

3.2 The rigid asymmetric rotor

Predictions of the structure of Ar_2-OCS suggest that the complex is quite asymmetric and hence a suitable hamiltonian, to take account of the asymmetry and possible distortions of the complex due to rotation, must be used in the prediction and analysis of the rotational spectrum. The various and commonly used rotational hamiltonians are reviewed elsewhere[11] and only the essential features pertinent to the analysis are described here.

An asymmetric top has no component of the total angular momentum conserved along any molecular fixed axis and as such the rigid rotor hamiltonian in the principal inertial axis system is given by,

$$H_{rigid} = A\hat{J}_a^2 + B\hat{J}_b^2 + C\hat{J}_c^2 \qquad (3.1)$$

- $\hat{J}_a$, $\hat{J}_b$, $\hat{J}_c$ are components of the total rotational angular momentum operator, $\hat{J}$.
- A, B, C are rotational constants given by $\hbar/4\pi I_{a,b,c}$ Hz and I_a etc are principal moments of inertia.
- By convention A > B > C and in the symmetric top limits, A > B = C for a prolate symmetric top and A = B > C for an oblate symmetric top. Methods of treating the problem depend on the degree of asymmetry or deviation from symmetric top behaviour where a measure is given by,

$$\kappa = \frac{2B-A-C}{A-C} \quad , \quad b_p = \frac{C-B}{2A-B-C} \quad , \quad b_o = \frac{A-B}{2C-B-A} \qquad (3.2)$$

- κ is the Ray asymmetry term ranging from -1 to 1 in the prolate and oblate symmetric top limits.
- b_p is the Wang prolate asymmetry parameter ranging from 0 for a prolate top to -1 for an oblate top. b_o is the corresponding parameter for an oblate top.

The hamiltonian in equation (3.1) can be rewritten in terms of a symmetric top expression and an asymmetry term, which for a near prolate symmetric top is given by,

$$H_{rigid} = \left(\frac{B+C}{2}\right)\hat{J} + \left(A-\frac{B+C}{2}\right)\hat{J}_a^2 + \left(\frac{B-C}{4}\right)\left(\hat{J}_+^2+\hat{J}_-^2\right) \qquad (3.3)$$

$\hat{J}^2=\hat{J}_a^2+\hat{J}_b^2+\hat{J}_c^2$ and $\hat{J}_\pm=\hat{J}_b\pm i\hat{J}_c$. Exact expressions for the symmetric top energies can be calculated in terms of two rotational constants, A and ½(B+C), the total angular momentum quantum number J and its projection quantum number along the molecular symmetry axis, K. The symmetry axis is chosen to minimize the asymmetry term, ie the A axis in the prolate limit (as in equation (3.3)) or the C axis in the oblate limit corresponding to the I^R and III^R representations respectively for a right handed axis system. Unlike the symmetric top terms, the asymmetry term removes the degeneracy in +K and -K levels by mixing K levels differing by 2. By convention the 2J+1 non-degenerate K levels are labelled J_{KaKc} where K_a and K_c are the corresponding values of K in the prolate and oblate symmetric top limits. For small asymmetries, perturbation theory gives adequate energy expressions with the largest splitting occurring between the degenerate $K=\pm1$ levels, given by 1/2(B-C)J(J+1). The second order terms in other states can be expanded in terms of the asymmetry parameters b_p or b_o (equations (3.2)); coefficients are tabulated elsewhere[12]. The general solution is obtained by diagonalizing the hamiltonian matrix created using appropriate symmetric top basis functions $|JK\rangle$. The non zero matrix elements, corresponding to the near prolate asymmetric top hamiltonian in equation 3.3, are given by[11],

$$\langle J,K \mid H_{rigid} \mid J,K \rangle = \left(\frac{B+C}{2}\right)J(J+1) + \left(A-\frac{B+C}{2}\right)K^2$$

$$\langle J,K\pm2 \mid H_{rigid} \mid J,K \rangle = \left(\frac{B-C}{4}\right)[J(J+1)-K(K\pm1)]^{\frac{1}{2}} \qquad (3.4)$$
$$\times\,[J(J+1)-(K\pm1)(K\pm2)]^{\frac{1}{2}}$$

By considering the symmetry of the system, the matrix can be split into four submatrices. The hamiltonian is invariant to 180° rotations about a, b and c axes and hence belongs to the D_2 symmetry group. Wave functions can similarly be classified by their symmetries relative to the D_2 group operations. The symmetric top wavefunctions belong to the D_∞ group with an undefined symmetry for rotation about the symmetry axis. Using the Wang transformation a new set of

symmetrized basis functions, $|J,K^{\pm}\rangle$ appropriate to the D_2 group are generated from the symmetric top functions,

$$\begin{aligned} K = 0 \;&:\; |\, J,0^{+}\,\rangle = |\, J,0\,\rangle \\ K > 0 \;&:\; |\, J,K^{\pm}\,\rangle = \frac{1}{\sqrt{2}}\left(|\, J,K\,\rangle \pm |\, J,-K\,\rangle \right) \end{aligned} \tag{3.5}$$

This separates the matrix into two submatrices since there are no elements connecting $|J,K^{+}\rangle$ and $|J,K^{-}\rangle$ basis functions. In addition no elements connect K even with K odd allowing further separation of the matrices into two. The resulting four matrices can be labelled according to the parity of K and the sign of the symmetrized wavefunction ie E^{+},E^{-},O^{+},O^{-} and diagonalized separately.

The selection rules for microwave transitions can be deduced from the symmetry properties of the asymmetric wave functions and the components of the dipole moment under operations of the D_2 point group. Classification of the wavefunctions are given by the change in symmetry resulting from rotation about the prolate (a) and oblate (c) axes and can be related to the evenness or oddness of K_a and K_c. The inertial axis dipole moment components transform as the direction cosines connecting the space fixed and inertial axes and the symmetry species are as follows;

Symmetry	Dipole moment	Rotational wavefunction	
D_2	component	K_a	K_c
A		even	even
B_A	μ_a	even	odd
B_B	μ_b	odd	odd
B_C	μ_c	odd	even

Hence, for a non zero matrix element of the type

$$\langle\, J',K_a',K_c' \mid \mu_i \mid J'',K_a'',K_c''\,\rangle \neq 0 \tag{3.6}$$

with a permanent dipole moment μ_i component along the relevant inertial axis, i, the selection rules are given by $\Delta J = 0, \pm 1$ (section 3.2.1) and the following selection rules for K_a and K_c,

Transition	symmetry[a]	K selection rule
a-type $\mu_a \neq 0$	ee ⟷ eo	$\Delta K_a = 0, \pm 2, \ldots$
	oo ⟷ eo	$\Delta K_c = \pm 1, \pm 3, \ldots$
b-type	ee ⟷ oo	$\Delta K_a = \pm 1, \pm 3, \ldots$
$\mu_b \neq 0$	eo ⟷ oe	$\Delta K_c = \pm 1, \pm 3, \ldots$
c-type $\mu_c \neq 0$	ee ⟷ oe	$\Delta K_a = \pm 1, \pm 3, \ldots$
	eo ⟷ oo	$\Delta K_c = 0, \pm 2, \ldots$

[a] even and odd symmetry to π rotation about a and c axes abbreviated to e,o.

3.2.1 Transition strengths

The strength of a transition between two asymmetric top levels described by $|J''K_a''K_c''M\rangle$ and $|J'K'K'M'\rangle$ is proportional to $A_{J''K''}$ given by,

$$I \propto A_{J''K''} = |\langle J' K_a' K_c' M' | \mu_Z | J'' K_a'' K_c'' M'' \rangle|^2 \tag{3.7}$$

μ_Z is the electric dipole operator referred to the same space fixed axis system as the exciting microwave radiation. The asymmetric top eigenfunction can be expanded in terms of the contributing symmetric top basis functions. A summation over the contributions of each symmetric top Hönl-London factor[13] in upper and lower states then gives the asymmetric top factor A_{JK} as,

$$A_{J''K''} = \left[\sum_{K''}\sum_{K'} c_{J''K''} c^*_{J'K'} |\langle J' K' M' | \mu_Z | J'' K'' M'' \rangle|\right]^2 \tag{3.8}$$

c_{JK} are the coefficients of the symmetric top basis functions $|J\ K\ M\rangle$ appearing in the asymmetric top eigenfunction. In the near prolate top case, $K=K_a$. Evaluation of this term is more convenient when transformed to the inertial axis system in which the dipole moment has constant components along each axis. This can be done using angular momentum theory described in standard texts[14] to give expressions for A_{JK} in J and K, where for a dipole moment of unity (or relative intensity)

$$A_{JK} = (2J'+1)(2J''+1) \left| \sum_{K'}\sum_{K''} c_{J'K'} c^*_{J''K''} \begin{pmatrix} J'' & 1 & J' \\ K'' & K'-K'' & -K' \end{pmatrix} \right|^2 \tag{3.9}$$

The relative intensities are therefore determined by the properties of the three-j symbol (:::). The three-j symbol triangle rule requires $\Delta J = 0, \pm 1$. Transitions for a prolate top involving ΔK_a, $\Delta K_c = 0, \pm 1$ are found to be strongest. In addition to the Hönl-London factor, the rotational level populations and population differences also affect the absolute intensity. Predictions based on the Hönl-London factors and a Boltzmann population distribution (although this is not totally appropriate for supersonic expansions) for temperatures of 1 K proved to be useful in predicting observable intensities of transitions for Ar_2-OCS. There are however, a number of problems associated with measuring absolute line intensities using Fourier transform microwave spectroscopy. Variations in the response of the spectrometer over the frequency range are difficult to quantify and generally only relative intensities can be estimated.

3.3 Centrifugal distortion

In the case of a non-rigid molecule, rotation will result in centrifugal distortion of the molecular structure. The effect can be expressed in terms of the rotation-vibration interaction[14] and the magnitude of such distortion will depend on the rotational angular momentum and the degree of coupling between vibrational levels. Therefore additional terms are added to the rigid rotor hamiltonian to account for the effect. Higher order terms are generated either as a power series in components of **J** or by second and higher order perturbation treatment of the vibration-rotational hamiltonian. The rotational hamiltonian including quartic centrifugal terms[15] is given by

$$H_{rot} = H_{rigid} + H_{cent} = \frac{1}{2}\sum_{\alpha,\beta} \mu_{\alpha\beta}\hat{J}_\alpha\hat{J}_\beta + \frac{1}{4}\sum_{\alpha,\beta,\gamma,\delta} \tau_{\alpha,\beta,\gamma,\delta}\hat{J}_\alpha\hat{J}_\beta\hat{J}_\gamma\hat{J}_\delta \qquad (3.10)$$

The nine rotational terms are reduced to three by transforming to the principal axis system. Similarly, the possible 81 terms in $\tau_{\alpha\beta\gamma\delta}$ can be reduced by using commutation relations to reduce terms in $\hat{J}_x\hat{J}_y\hat{J}_x\hat{J}_z$ to lower order terms giving a power series of the form,

$$H_{rot} = \sum_{p,q,r} h_{pqr}(\hat{J}_a^p\hat{J}_b^q\hat{J}_c^r + \hat{J}_c^r\hat{J}_b^q\hat{J}_a^p) \qquad (3.11)$$

Due to the invariance of the energy (hamiltonian) to symmetry operations of the D_2 point group and Hermitian conjugation, the sum p+q+r is even and the coefficients h_{pqr} are real. The hamiltonian is also totally symmetric in the molecular point group. These considerations allow reduction in the number of terms of degree n=p+q+r to ⅛(n+2)(n+4) and generate the three rotational constants when n=2 and six quartic constants for n=4. The series can be continued to give ten sextic

centrifugal distortion constants and so on. One consequence of the reduction (eqn 3.10) is to redefine the rotational constants to incorporate some centrifugal distortion character and hence the reduced rotational constants are not true rigid rotor constants. It is possible to perform a further unitary transformation to reduce the quartic expansion to five and the sextic to seven terms. This can be done in several ways where two commonly used reductions are the Watson symmetric (S) top and antisymmetric (A) top reductions. The A reduction has no terms off diagonal in K by more than 2 and hence has the same tridiagonal form as the rigid rotor hamiltonian. However, several terms contain functions of the inverse of the asymmetry parameter b_p or b_o (eqn 3.2) which tend to infinity in the limit of a symmetric top. This can be overcome be choosing a representation where the near-symmetry axis does not correspond to the z axis but at the expense of increased correlation between rotational and centrifugal constants. In the case of van der Waals dimers which, as a result of the long intramolecular distance, tend to be near prolate symmetric tops the symmetric top (S) reduction is preferable. The S reduction hamiltonian up to sextic centrifugal distortion terms has the form[11]

$$H_{rot}^{S} = \left(\frac{B+C}{2}\right)\hat{J}^2 + \left(A-\frac{B+C}{2}\right)\hat{J}_a^2 + \left(\frac{B-C}{4}\right)(\hat{J}_+^2+\hat{J}_-^2)$$
$$-D_J\hat{J}^4 - D_{JK}\hat{J}^2\hat{J}_a^2 + D_K\hat{J}_a^4 + d_1\hat{J}^2(\hat{J}_+^2+\hat{J}_-^2) + d_2(\hat{J}_+^4+\hat{J}_-^4) \qquad (3.12)$$
$$+H_J\hat{J}^6 + H_{JK}\hat{J}^4\hat{J}_a^2 + H_{KJ}\hat{J}^2\hat{J}_a^4 + H_K\hat{J}_a^6$$
$$+h_1\hat{J}^4(\hat{J}_+^2+\hat{J}_-^2) + h_2\hat{J}^2(\hat{J}_+^4+\hat{J}_-^4) + h_3(\hat{J}_+^6+\hat{J}_-^6)$$

Coefficients of terms with the same difference in powers in $\hat{J}$ and $\hat{J}_a$ form a diminishing geometric sequence if the semi-rigid model converges correctly. It may be necessary for weakly bound complexes, with correspondingly large quartic centrifugal distortion constants, to include some of the sextic terms in order to fit the data to measurable resolution. In addition, the information available from the observed transitions will limit the number of distortion terms that can be determined.

The matrix elements for the S reduction hamiltonian, excluding the sextic H_K, h_1, h_2 and h_3 terms, are given in equation 3.13. For the complexes detailed in this thesis, too few transitions are observed to determine H_K, and h_1, h_2 and h_3 contributions are significantly smaller than the experimental precision. Computer programs employing the S reduction matrix elements have been used to predict spectra and a general non-linear least squares routine[16] was used to fit S reduction parameters to observed transition frequencies.

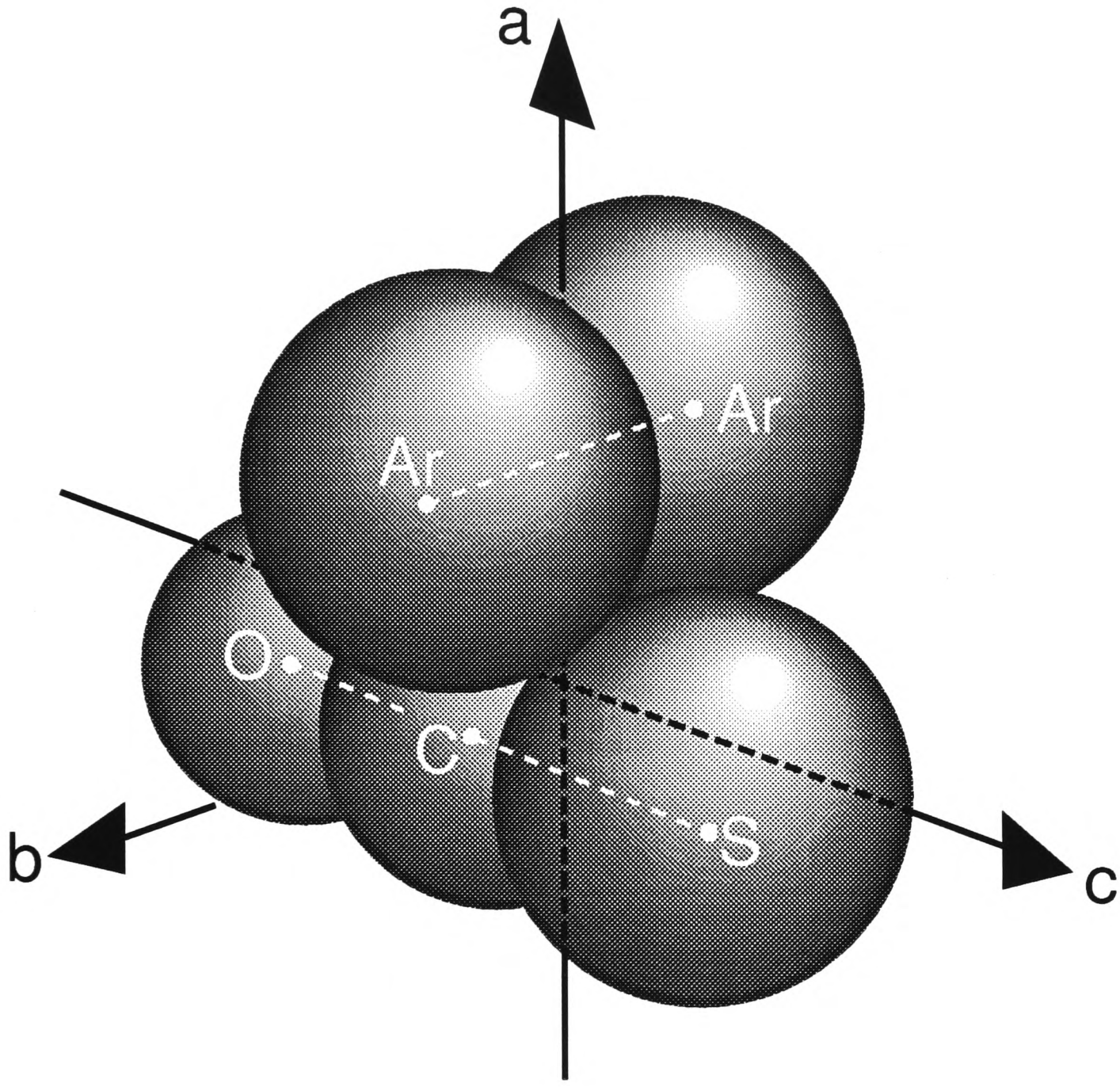

Figure 3.1; The Ar_2-OCS trimer structure.
Approximate billiard ball model in the inertial axis system,
spheres based on van der Waals radii (not to scale)

Equation 3.13; Matrix elements for the I^R Watson S reduction hamiltonian.

$$\begin{aligned}
\langle J,K \mid H^S_{rot} \mid J,K \rangle &= \left(\frac{B+C}{2}\right)J(J+1) + \left(A-\frac{B+C}{2}\right)K^2 \\
&\quad - D_J J^2(J+1)^2 - D_{JK}J(J+1)K^2 - D_K K^4 \\
&\quad + H_J J^3(J+1)^3 + H_{JK}J^2(J+1)^2K^2 + H_{KJ}J(J+1)K^4 \\
\langle J,K\pm2 \mid H^S_{rot} \mid J,K \rangle &= \left[\left(\frac{B-C}{4}\right) + d_1 J(J+1)\right] \\
&\quad \times [J(J+1)-K(K\pm1)]^{\frac{1}{2}}\,[J(J+1)-(K\pm1)(K\pm2)]^{\frac{1}{2}} \\
\langle J,K\pm4 \mid H^S_{rot} \mid J,K \rangle &= d_2[J(J+1)-K(K\pm1)]^{\frac{1}{2}}[J(J+1)-(K\pm1)(K\pm2)]^{\frac{1}{2}} \\
&\quad \times [(J(J+1)-(K\pm2)(K\pm3)]^{\frac{1}{2}}[(J(J+1)-(K\pm3)(K\pm4)]^{\frac{1}{2}}
\end{aligned} \tag{3.13}$$

3.4 Experimental

Sections of the Ar_2-OCS spectrum were recorded between 7 and 18 GHz. A LaserTechnics piezo-crystal driven valve with a 0.6mm nozzle was mounted to give a perpendicular expansion (figure 2.2b) through a 50 cm radius of curvature confocal Fabry-Perot cavity. A 1% OCS argon gas mixture at a backing pressure of 1 atm and gas pulse lengths of 300μs gave adequate signal to noise to measure the weaker a-type transitions on averaging 5000 FID signals. The 4% natural abundance Ar_2-$OC^{34}S$ spectrum was measured using an axial expansion employing a 0.5mm nozzle General Valve solenoid valve mounted in a 70 cm radius of curvature mirror paired with a 50 cm curvature mirror. The LaserTechnics valve has a lower opening efficiency than the General valve and hence a lower backing pressure than used with the LaserTechnics valve would be expected to give the equivalent effective pressure conditions at the General Valve nozzle exit. However, the optimum gas conditions were found to be 1.5 atm backing pressure for a 0.25% OCS/argon expansion. C-type transitions only were recorded for Ar_2-$OC^{34}S$ with suitable signal to noise with 5000-10000 averaged FID signals. The perpendicular expansion measurements gave Doppler (frequency) dependent measurement uncertainties of between 1 and 4 kHz. Axial measurements were only a weak function of the Doppler profile and were measured with an uncertainty of 1 kHz.

3.5 Results and analysis

Predictions were based on a structural model employing the Ar-OCS structure with the two argon atoms placed in equivalent positions to reflection and separated by the Ar-Ar dimer distance[17]. This structure, illustrated in figure 3.1 and 3.2, corresponds to a very asymmetric (oblate) top with $\kappa \sim 0.4$ (equation 3.2) . The dipole moment due to OCS would be resolved along the a and c axes with c-type transitions expected to be a factor of three times stronger than a-type transitions. As a result of the high asymmetry, significant intensities were predicted for all possible $\Delta K_a = 1$ c-type R branch transitions giving a recognisable pattern over 1 GHz for transitions of the same ΔJ.

Observed transitions proved to be quite close to those predicted. 60 transitions were assigned to Ar_2-OCS and are listed in appendix I. Following similar predictions for Ar_2-$OC^{34}S$ using structural parameters deduced for Ar_2-OCS, 32 c-type transitions due to Ar_2-$OC^{34}S$ were observed (appendix I). A I^R Watson S reduction hamiltonian with quartic centrifugal distortion constants was sufficient to least squares fit the separate isotopic data to the estimated experimental accuracy of 1 kHz (2kHz in the case of a perpendicular expansion); the fitted constants are given in table 3.1 and residuals tabulated in appendix I.

No lines corresponding to b-type transitions were observed suggesting that the OCS dipole lies in the ac plane (figure 3.1). Additional confirmation is provided by the planar moment P_b, given by $\frac{1}{2}(I_a+I_c-I_b)$, which gives the moment of inertia due to mass out of the ac plane.

$$P_b(Ar_2\text{-}OCS) = 294.795 \text{ amu Å}^2$$

$$P_b(Ar_2\text{-}OC^{34}S) = 294.803 \text{ amu Å}^2$$

$$P_b(Ar_2\text{-}^{18}OCS)^{19} = 294.785 \text{ amu Å}^2$$

$$I_0(Ar_2) = 291.756 \text{ amu Å}^2$$

P_b does not change significantly for the isotopic forms of OCS and has a value similar to the moment of inertia of Ar_2. Based upon these observations it is assumed that the argon atoms occupy equivalent positions either side of the plane of symmetry (figure 3.1, 3.2). In order to fit three structural parameters (defined in figure 3.2a) to the rotational constants, it is necessary to assume that the structure of OCS is unperturbed by the weak interaction with the argon atoms; a reasonable assumption based on results for other rare gas complexes. Hence, using known OCS bond distances[18], the Ar-Ar (R) and Ar-C ($r_1 = r_2$) distances and the Ar-C-S bond angle ($\theta_1 = \theta_2$) can be calculated and are given in table 3.2.

The structure of Ar_2–OCS in the principal inertial axis system

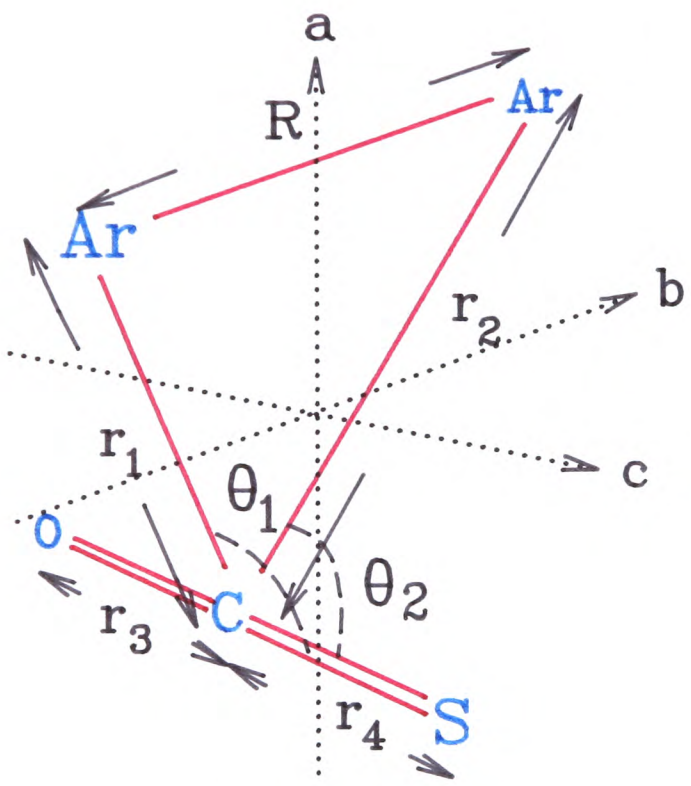

Figure 3.2a
Definition of internal coordinates

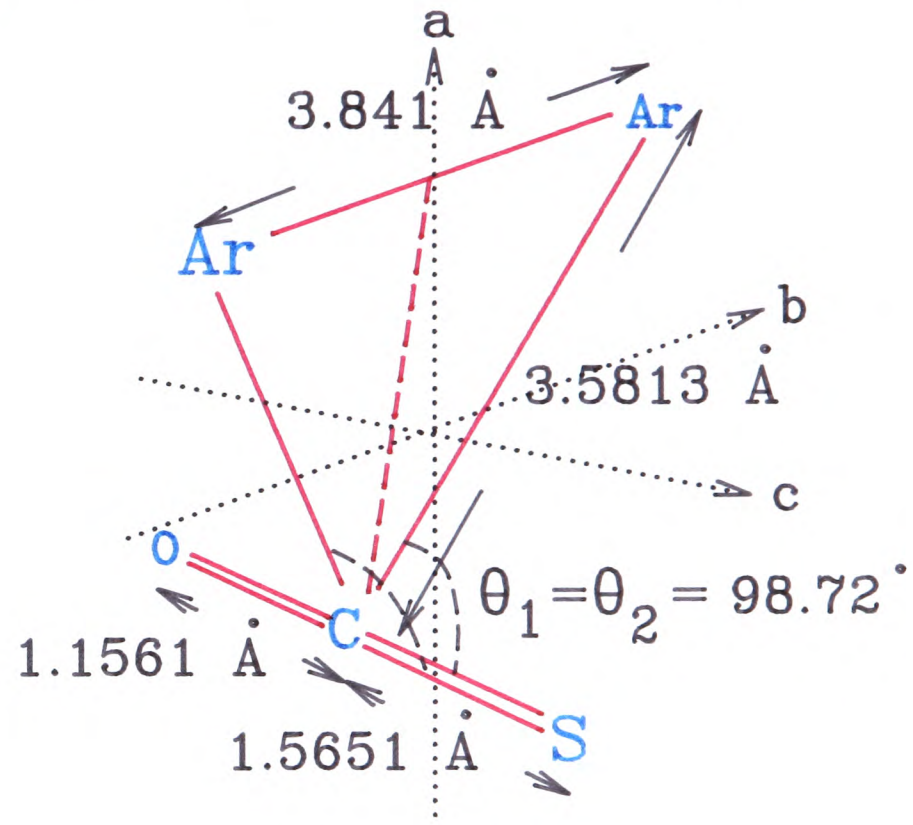

Figure 3.2b
Derived and assumed structural parameters

Table 3.1: Spectroscopic constants of Ar_2-OCS isotopomers.

Parameter[a]	Ar_2-OCS	Ar_2-$OC^{34}S$	Ar_2-^{18}OCS[b]
A/MHz	1381.55489(18)	1376.90889(15)	1360.68859(11)
B/MHz	1188.27861(16)	1159.15789(16)	1166.16627(13)
C/MHz	778.59565(14)	767.40515(23)	775.68678(45)
D_J/kHz	3.9114(18)	3.7134(33)	3.847(12)
D_{JK}/kHz	-0.4606(87)	-0.039(12)	-0.982(19)
D_K/kHz	9.8360(81)	9.4466(94)	9.6717(94)
d_1/kHz	-1.2089(9)	-1.1390(20)	-1.0927(95)
d_2/kHz	-0.0059(4)	0.0203(6)	0.0419(38)
σ_{Fit}/kHz	1.6	1.2	0.5

[a] Watson S reduction parameters, I^R representation.
[b] Data provided by Y. Xu, M. C. L. Gerry[19].

Table 3.2: Effective structural parameters

Structural parameter	Ar_2-OCS[a]	Ar-OCS	Ar_2[c]
$r_{(CO)}$ Å	1.1561(12)[d]	1.1561(12)[d]	
$r_{(CS)}$ Å	1.5651(9)[d]	1.5651(9)[d]	
$r_{(Ar\text{-}C)}$ Å	3.5813	3.586(6)[b]	
$R_{(Ar\text{-}Ar)}$ Å	3.8410		3.821(10)
$\theta_{(\angle Ar\text{-}C\text{-}S)}$ °	98.72	98.6(5)[b]	

[a] Parameters derived from fit to Ar_2-OCS rotational constants defined in figure 3.2
[b] Structural data from reference 20
[c] Bond length from reference 17
[d] OCS bond lengths from reference 18

3.5.1 Harmonic force field analysis

The simplest form of potential analysis for Ar_2-OCS is by the harmonic force field method[21] based around the treatment of vibrational modes of the complex as harmonic oscillators. By ignoring the anharmonicity, a reasonable assumption for small amplitude motions, a set of orthogonal internal coordinates can be derived where motions are described by 3n-6 (n nuclei) orthogonal simple harmonic oscillators. The potential is then only a function of force constants and displacements. Harmonic force constants for Ar-OCS and Ar_2 have been calculated[7,17] and hence a comparison with a model for Ar_2-OCS based on pair potentials is possible. It is a well established means of analysis to use infra-red vibrational data to obtain harmonic force constants for internal displacement coordinates such as bond stretches, bends and torsions. In addition the five centrifugal distortion coefficients can be used to refine force constant information or, if the first derivatives with respect to the force constants are favourable[22], determine upto five force constants. This treatment is extensively reviewed[24,21] and only briefly discussed here.

It is expected that there is an inverse relationship between centrifugal distortion coefficients and force constants complicated by the requirement that the force constants be referred to internal coordinates rather than cartesian coordinates used in centrifugal distortion. By separating rotations and vibrations in the molecular frame (and incorporating the Coriolis interaction into the rotational part) a hamiltonian for the vibrating, rotating polyatomic molecule can be written with the potential energy term approximated by harmonic potentials for each displacement coordinate ($R_{i,j}$),

$$H = \frac{1}{2}\sum_{\alpha,\beta} \mu_{\alpha\beta}\hat{J}_\alpha\hat{J}_\beta + \frac{1}{2}\sum_{i,j} G_{ij}\, p_i\, p_j + \frac{1}{2}\sum_{i,j} f_{ij}\, R_i\, R_j \qquad (3.14)$$

- $\mu_{\alpha\beta}$ is an element of the inverse moment of inertia matrix.
- $P_{\alpha\beta}$ are components of the rotational angular momentum (note; $J^{(i)}_{\alpha\beta}$ conventionally used to indicate $\partial I_{\alpha\beta}/\partial R_i$ rather than angular momentum).
- G_{ij} is an element of the G matrix, dependent on masses and geometric factors.
- $p_{i,j}$ is the momentum associated with vibration of internal displacement coordinate $R_{i,j}$.
- f_{ij} are harmonic force constants.

Averaging the effects of vibration in equation 3.14, a rotational hamiltonian analogous to equation 3.9 can be written with the centrifugal distortion term expressed in terms of internal displacement coordinate ($R_{i,j}$) harmonic potentials. By averaging over vibrational effects, $-\partial H_{Rot}/\partial R_i = 0$ and equation 3.14 can be differentiated and rearranged to give R_j. For small

displacements in R_i, $\partial\mu_{\alpha\beta}/\partial R_i$ is approximated to linear terms in a series expansion about the equilibrium value.

The displacement coordinate R_j is then given by

$$R_j = -\frac{1}{2}\sum_i (f^{-1})_{ij}\left(\frac{\partial \mu_{\alpha\beta}}{\partial R_i}\right)_e \hat{J}_\alpha \hat{J}_\beta \qquad (3.15)$$

Reexpressing the derivatives of elements of the inverse moment of inertia matrix, $\mu_{\alpha\beta}$, in terms of derivatives of the moment of inertia matrix elements $I_{\alpha\beta}$ via,

$$\left(\frac{\partial \mu_{\alpha\beta}}{\partial R_i}\right)_e = -\frac{1}{I^e_{\alpha\alpha} I^e_{\beta\beta}}\left(\frac{\partial I_{\alpha\beta}}{\partial R_i}\right)_e \qquad (3.16)$$

and substituting for R_i and R_j in equation 3.14, the hamiltonian assumes the form of equation 3.9 where the distortion constants are given by,

$$\tau_{\alpha\beta\gamma\delta} = -\frac{1}{2}\frac{1}{I^e_{\alpha\alpha} I^e_{\beta\beta} I^e_{\gamma\gamma} I^e_{\delta\delta}}\sum\left(\frac{\partial I_{\alpha\beta}}{\partial R_i}\right)_e (f^{-1})_{ij}\left(\frac{\partial I_{\gamma\delta}}{\partial R_j}\right)_e \qquad (3.17)$$

The Watson S reduction rotation and centrifugal distortion constants can be written as linear functions of $\tau_{\alpha\beta\gamma\delta}$ which are tabulated elsewhere[15]. Expressions for $\partial\tau_{\alpha\beta\gamma\delta}/\partial F_{mn}$ can be formulated[23,24] and hence procedures can be devised to least squares fit force constants using experimentally determined distortion constants. This was done for Ar_2-OCS using a standard program[23] designed primarily to fit force constants to infra-red data using the **FG** matrix formalism of Wilson[21]. A summary of the processes involved in refining the Ar_2-OCS force constant estimates and calculating van der Waals vibrational frequencies is given here. A comprehensive exposition is given by Califano[24].

Internal displacement coordinates are defined for Ar_2-OCS as shown in figure 3.2a. These coordinates are chosen so that the motions of the constituent atoms can be expressed in terms of the molecular structure and deduced force constants can be directly associated with bonding. Vectors in internal displacement coordinates (**s**) are related to cartesian displacement coordinates (**x**) through a transformation matrix (**B**)

$$s = Bx \tag{3.18}$$

The **B** matrix is calculated using the structural parameters given in table 3.2. Expressions for the kinetic and potential energy can then be written in terms of internal coordinates defining the **F** and **G** matrices (cf equation 3.14)

$$\begin{aligned} 2T &= \dot{x}M\dot{x} = \dot{s}B^{-1}MB^{-1}\dot{s} = \dot{s}G^{-1}\dot{s} \\ 2V &= \tilde{x}M^{\frac{1}{2}}fM^{\frac{1}{2}}x = \tilde{s}Fs \end{aligned} \tag{3.19}$$

The internal coordinates can be further combined into groups of symmetry coordinates corresponding to the symmetry species of the molecular point group, which in the case of Ar_2-OCS is the C_s point group. This results in block diagonalisation of each matrix into submatrices corresponding to the symmetry species of the point group and a reduction in the size of the problem. Interactions between vibrational states of different symmetry are not allowed in order to maintain the indistinguishability of energy with respect to the symmetry operations. Therefore only matrix elements (force constants) between modes of the same symmetry are non zero. By separating the effects of vibration and rotation, the vibrational energy is given by the hamiltonian in equation 3.14 with the influence of rotation ignored (ie the equilibrium structure). 3n (n=number of atoms) coupled second order differential equations of motion can be formulated for which the solutions are harmonic oscillator functions corresponding to normal modes of oscillation. This can be reexpressed using the Lagrangian form of the equations of motion to give a matrix eigenvector equation in terms of **F** and **G** matrix elements. Solutions are obtained by diagonalizing the determinant to give 3n-6 normal (independent) modes of internal motion and associated vibrational frequencies (and 3 translational, 3 rotational modes with zero frequency) .

$$\begin{aligned} GFL &= L\Lambda \\ |GF - E\lambda| &= 0 \end{aligned} \tag{3.20}$$

Λ is the matrix of vibrational frequencies and **L** the normal modes in terms of the original coordinate system. By incorporating a least squares fitting procedure, the **FG** matrix method can be employed to determine force constants from vibrational and rotational data.

3n-6 symmetry coordinates for Ar_2-OCS, where n=5, are defined according to the A_1 and A_2 symmetry species of the C_s point group. These are illustrated in figure 3.3.

Force constants associated with these coordinates appear on the force constant matrix diagonal. In addition, as the coordinates do not represent the normal mode solutions, there are cross terms off the diagonal. In order to reduce the problem to five unknown force constants to fit to the five centrifugal distortion constants, OCS monomer force constants are used for modes f_{11}, f_{22}, f_{33}, f_{77}, and f_{13}[25]. The van der Waals modes are quite insensitive to the OCS molecular force field, therefore errors due to the use of OCS constants are unlikely to be important. There are no cross terms between coordinates of different symmetry. The cross term between the Ar-C stretch and bend modes in both symmetry species f_{46}, f_{89} can be estimated from the equivalent term in Ar-OCS, $k_{r\theta}$ by assuming negligible three-body contributions to these interactions. The Ar_2-OCS potential can be written in terms of the van der Waals symmetry modes defined in figure 3.3,

$$\begin{aligned} 2V_{Ar_2\text{-}OCS} = {} & \frac{f_{44}}{2}(\Delta r_3+\Delta r_4)^2+f_{55}(\Delta\theta_1+\Delta\theta_2)^2+\frac{f_{45}}{\sqrt{2}}(\Delta r_3+\Delta r_4)(\Delta\theta_1+\Delta\theta_2) \\ & + \frac{f_{88}}{2}(\Delta r_3-\Delta r_4)^2+f_{99}(\Delta\theta_1-\Delta\theta_2)^2+\frac{f_{89}}{\sqrt{2}}(\Delta r_3-\Delta r_4)(\Delta\theta_1-\Delta\theta_2) \\ & + f_{66}R^2 + V_{OCS} \end{aligned} \tag{3.21}$$

f_{nn} are force constants corresponding to symmetry modes defined in figure 3.3. f_{nm} are cross terms.

The Ar_2-OCS potential derived from Ar-OCS and Ar_2 pair potentials is given by

$$2V_{Ar_2\text{-}OCS} = k_r(\Delta r_3^2+\Delta r_4^2)+k_R\Delta R^2+k_\theta(\Delta\theta_1^2+\Delta\theta_2^2)+k_{r\theta}(\Delta r_3\Delta\theta_1+\Delta r_4\theta_2)+V_{OCS} \tag{3.22}$$

k_R is the Ar_2 force constant, k_r the Ar-C stretch, k_θ the $\angle$Ar-C-O bend force constants and $k_{r\theta}$ the bend-stretch cross term of Ar-OCS.

Internal coordinate coefficients can be equated, in the absence of all but two body interactions, to relate the force constants as follows,

$$\begin{aligned} &\textit{Ar-C stretch} && f_{44} = f_{88} = k_r \\ &\textit{Ar-C-O } \angle \textit{ bend} && f_{66} = f_{99} = \frac{k_\theta}{2} \\ &\textit{Stretch-bend cross-term} && f_{46} = f_{89} = \frac{k_{r\theta}}{\sqrt{2}} \\ &\textit{Ar-Ar stretch} && f_{44} = k_R \end{aligned} \tag{3.23}$$

Figure 3.3; Ar_2–OCS harmonic force field analysis coordinates

A_1 symmetry displacement coordinates

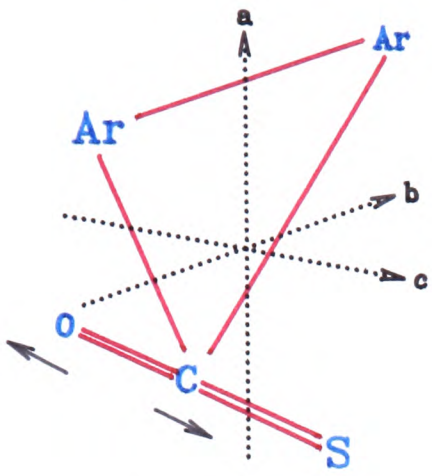

$S_1 = \Delta r_3$

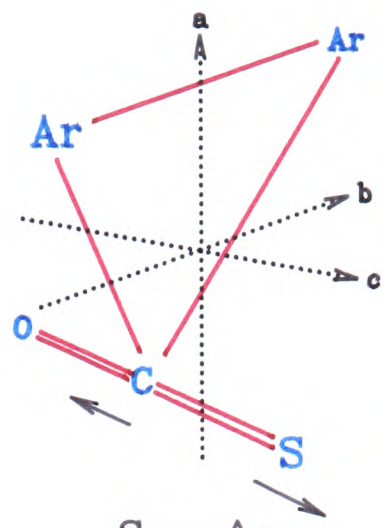

$S_2 = \Delta r_4$

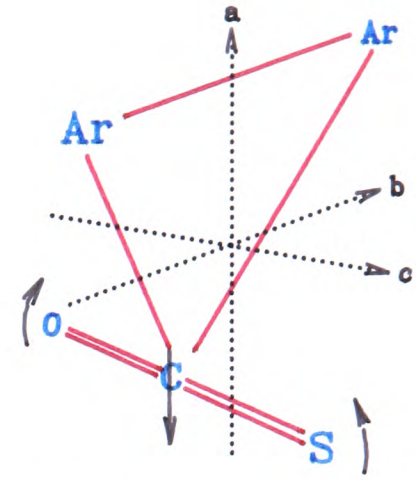

S_3 = in–plane OCS linear bend

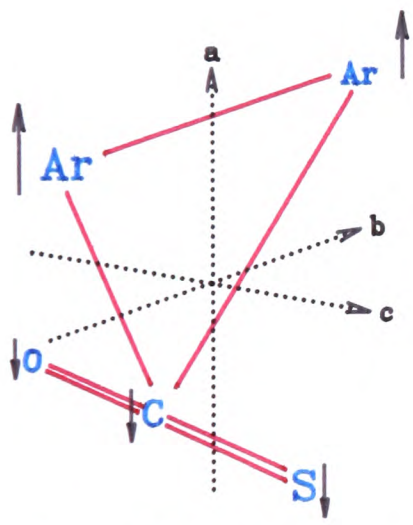

$S_4 = \frac{1}{\sqrt{2}}(\Delta r_1 + \Delta r_2)$

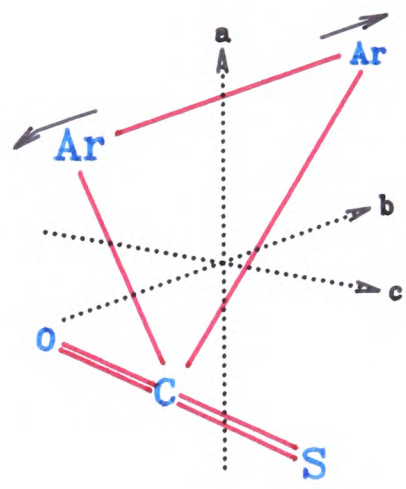

$S_5 = \Delta R$

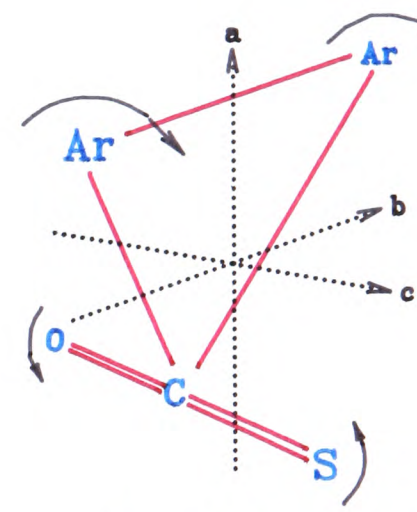

$S_6 = \Delta\theta_1 + \Delta\theta_2$

A_2 symmetry displacement coordinates

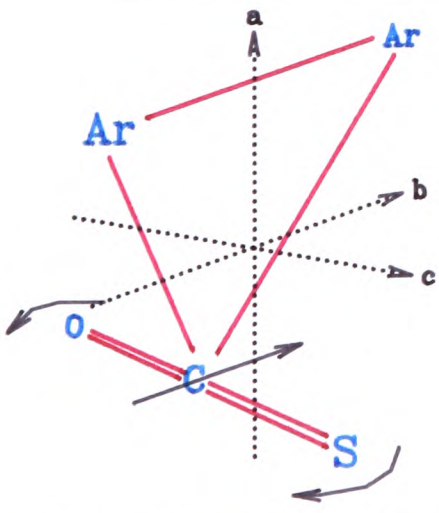

S_7 = out–of–plane OCS linear bend

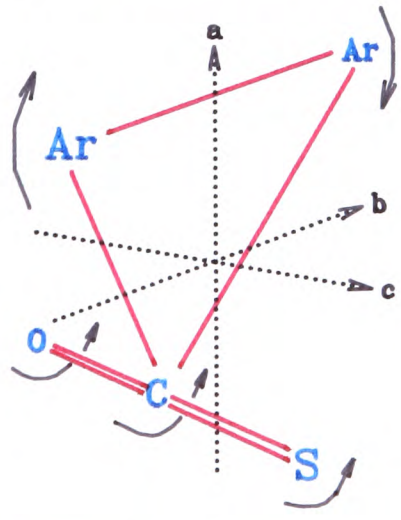

$S_8 = \frac{1}{\sqrt{2}}\Delta\theta_1 - \Delta\theta_2$

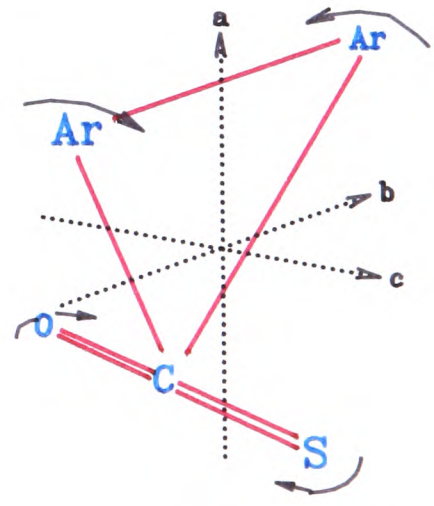

$S_9 = \Delta\theta_1 - \Delta\theta_2$

Table 3.3; Harmonic force constants derived from centrifugal distortion data for three Ar_2-OCS isotopomers[c].

Ar_2-OCS force constants		Ar-OCS, Ar_2 force constants		
f_{11}	16.14[a]	$f_{c\text{-}o}$	16.14[a]	mdyn/Å
f_{12}	1.040[a]	$f_{o\text{-}c,c\text{-}s}$	1.040[a]	mdyn/Å
f_{22}	7.443[a]	$f_{c\text{-}s}$	7.443[a]	mdyn/Å
f_{33}	0.6513[a]	$f_{\Delta ocs}$	0.6513[a]	mdyn Å/rad^2
f_{44}	0.01989(34)	k_r	0.0226[d]	mdyn/Å
f_{55}	0.00831(6)	k_R	0.0078[e]	mdyn/Å
f_{46}	-0.00110[b]	$k_{r\theta}/\sqrt{2}$	-0.00110[d]	mdyn/rad
f_{66}	0.0126(10)	$k_\theta/2$	0.0127[d]	mdyn Å/rad^2
f_{77}	0.6513[a]	$f_{\Delta ocs}$	0.6513[a]	mdyn Å/rad^2
f_{88}	0.02169(31)	k_r	0.0226[d]	mdyn/Å
f_{89}	-0.00110[b]	$k_{r\theta}/\sqrt{2}$	-0.00110[d]	mdyn/rad
f_{99}	0.01145(24)	$k_\theta/2$	0.0127[d]	mdyn Å/rad^2

[a] Constrained to values in reference 24.
[b] Constrained to $k_{r\theta}$(Ar-OCS)/$\sqrt{2}$ as in text.
[c] Simultaneous least squares fit to Ar_2-OCS, Ar_2-$OC_{34}S$ and Ar_2-^{18}OCS data.
[d] Ar-OCS force constants from reference 7.
[e] Ar_2 force constant from reference 17.

Table 3.4; Predicted vibrational frequencies of van der Waals modes in Ar_2-OCS.

mode	Ar_2-OCS	Ar_2-$OC^{34}S$	Ar_2-^{18}OCS
ν_4 cm^{-1}	44.9	44.9	44.0
ν_5 cm^{-1}	29.6	29.3	29.1
ν_6 cm^{-1}	23.3	23.2	23.3
ν_8 cm^{-1}	36.9	36.9	36.4
ν_9 cm^{-1}	18.4	18.2	18.1

The cross terms, f_{46} and f_{89} are therefore estimated to have the value -0.0011 mdyn rad^{-1} where $k_{r\theta}$=-0.0015(2) mdyn rad^{-1}.[7] Inclusion of these cross term constants improves the fit to the distortion constants. The remaining cross term contributions are taken to be smaller and neglected.

Five diagonal force constants due to van der Waals modes remain to be determined. The distortion coefficients for Ar_2-OCS, Ar_2-$OC^{34}S$ and Ar_2-^{18}OCS (Gerry et al.[19]) were weighted according to their standard deviations and fitted simultaneously. Results and predictions of the van der Waals vibrational frequencies, obtained using the ASYM20 normal coordinate program[23], are given in table 3.3 and 3.4.

3.6 Discussion

Although quite successful in predicting the rotational and centrifugal distortion constants for Ar_2-OCS, the pair interaction model overestimates the rotational constants by $\sim$1 to 2% and the centrifugal distortion by up to 20%. In the trimer the Ar-Ar(R) distance is found to have increased compared with Ar_2, as might be expected through induced dipole repulsions and is similarly observed in most Ar_2-HX complexes. There is also an increase in the Ar-C(r_1,r_2) distance compared with the dimer, a trend also observed for Ar_2-HCl/F.

Further comparisons between complexes based on the small differences in results of force field analyses must be treated with some care. Assumptions implicit to the method that data refer to small amplitude (or harmonic) motions of the equilibrium molecular structure are not particularly applicable to wide amplitude van der Waals modes using the effective ground vibrational state structure. It is notable that the general behaviour of force constants predicted from the pair interaction model (equation 3.23) $f_{44} \approx f_{88}$ and $f_{66} \approx f_{99}$ is roughly reproduced suggesting a near negligible degree of mixing by non-pairwise interactions. The Ar-C stretch force constants f_{44},f_{88} are slightly less than the equivalent Ar-OCS stretch, the reverse of what is observed in Ar_n-HCl/F. In terms of the force constant corresponding to the Ar-Ar stretch, the value for Ar_2-OCS is slightly larger than that for Ar_2. For Ar_2-HX the reverse is observed although it should be noted that a cross term between the Ar-Ar stretch and symmetric stretch in Ar_2-HCl/F is included and found to be quite large whereas similar terms, f_{45} and f_{56}, are ignored in the Ar_2-OCS analysis.

The more detailed analysis of Ar_2-HCl by Cooper et al[2] concludes that three body interactions make a significant contribution to the intermolecular potential of which the exchange quadrupole moment, on the Ar_2 moiety, interaction with the HCl dipole is dominant. In the case of Ar_2-OCS, the angular orientation is such that the dipole-exchange quadrupole interaction is probably quite small and possibly repulsive. However, with the large quadrupole moment on the OCS, the quadrupole-exchange quadrupole interaction may well be significant. Analysis of the type for Ar_2-HCl is not

possible without a more accurate potential for Ar-OCS. The pair potentials used for Ar_2-HCl are estimated to be good to 1% and reproduce observed quantities to 0.1%. An alternative method would be to extend the normal mode analysis to allow the use of simple non-harmonic empirical intermolecular potentials as formulated by Bernstein et al[26] although this would require vibrational data.

The prediction of the Ar_2-OCS structure based on pairwise additive forces giving a close packed equilibrium structure has been shown to be quite successful. In addition, considerations based on orbital interactions with the electropositive centre on OCS also give a similar result. Any formal donation of charge to OCS acting as a π^* acceptor would however, constrain the Ar-C-Ar angle to $\sim 90°$ and is unrealistic. These considerations were extended in an attempt to identify a number of unassigned transitions as Ar_3-OCS or OCS_n. The prediction of the Ar_2-OCS structure was extended to Ar_3-OCS by placing the third argon atom on the same radius about the OCS axis with the same Ar-Ar distance. No transitions corresponding to predictions from this model were observed suggesting the model is incorrect. A similar result is inferred by Janda *et al*[27] for the argon atom positions in Ar_2-Cl_2 and Ar_3-Cl_2. It can be postulated that the three argon atoms form a triangular cluster although there are several possible orientations relative to the OCS. One possibility is where the argon cluster three-fold symmetry axis is aligned with the OCS axis to form a symmetric top analogous to Ar_3-HX. In a second possibility, two Ar atoms occupy positions as in Ar_2-OCS with the third occupying a position in the symmetry plane, with an orientation relative to the other argon atoms similar to that calculated for the argon dimer in Ar_2-C_4H_4O[5].

Acknowledgements

Concurrent with the study described here, Y. Xu and M. C. L. Gerry recorded similar spectra for three isotopomers of Ar_2-OCS using the same technique. I would like to thank Professor Gerry for providing the Ar_2-^{18}OCS results and Professor W. Klemperer for providing the MBER data. In addition I would like to acknowledge the assistance of Dr. C. Pulham in using the ASYM20 normal coordinate analysis program and Jason Tuckley in collecting part of the Ar_2-OCS data.

References

[1]T. L. Beck, J. Jellinek, R. S. Berry, *J. Chem. Phys.*, **87**, 545 (1987).

[2]A. R. Cooper, J. M. Hutson. *J. Chem. Phys.*, in press (1993).

[3]R. S. Ruoff, T. Emilsson, C. Chuang, H. S. Gutowsky. *J. Chem. Phys.*, **93**, 6363 (1990).

[4] K. I. Peterson, R. D. Suenram, F. J. Lovas. *J. Chem. Phys.*, **94**, 106 (1991).

[5] R. M. Spycher, P. M. King, A. Bauder. *Chem. Phys. Lett.*, **191**, 102 (1992).

[6]T. D. Klots, H. S. Gutowsky. *J. Chem. Phys.*, **91**, 63 (1989).

[7]Y. Xu, W. Jager, M. C. L. Gerry. *J. Mol. Spectrosc.*, **151**, 206 (1992).

[8]J. S. Muenter. Private communication and unpublished results.

[9]K. R. Leopold. *Ph.D thesis*, Harvard University, 1983.

[10]S. Li, E. R. Bernstein, *J. Chem. Phys.*, **95**, 1577 (1991).

[11]W. Gordy, R. L. Cook, *Microwave Molecular Spectra.* Wiley, 1984; J. M. Hutson, *Dynamics of Polyatomic Van der Waals Complexes.* Plenum Press, New York, 1990.

[12]C. H. Townes, A. L. Schawlow, *Microwave Spectroscopy*, Dover Publications, New York, 1975.

[13]G. Herzberg, *Molecular Spectra and Molecular Structure, Vol II.* Krieger, Malabar, 1991.

[14]R. N. Zare, *Angular Momentum*, Wiley Interscience, New York, 1988.

[15]J. K. G. Watson, *Vibrational Spectra and Structure*, ed J. R. Durig. Elsevier, Amsterdam, 1977.

[16] W. E. Wentworth, *J. Chem. Educ.*, **42**, 96 (1965); D. W. Callahan, J. S. Muenter, *An uncorrelated nonlinear least squares data fitting program written in Fortran.* 1982.

[17]E. A. Colbourn, A. E. Douglas, *J. Chem. Phys.*, **65**, 1741 (1976).

[18]J. K. G. Watson, *J. Chem. Phys.*, **46**, 1935 (1967).

[19]Y. Xu, M. C. L. Gerry, J. P. Connelly, B. J. Howard. *J. Chem. Phys.*, **98**, 2735 (1993).

[20]F. J. Lovas, R. D. Suenram, *J. Chem. Phys.*, **87**, 2010 (1987).

[21]E. B. Wilson, J. C. Decius, P. C. Cross, *Molecular Vibrations: The Theory of Infra-red and Raman Vibrational Spectra.* McGraw-Hill, 1955.

[22]M. R. Aliev, J. K. G. Watson, *J. Mol. Spectrosc.*, **74**, 282 (1979).

[23]L. Hedberg, I. Mills, *ASYM20 normal coordinate analysis Fortran program.* 1990; *J. Mol. Spectrosc.*, to be published 1993.

[24]S. Califano, *Vibrational States.* Wiley, New York, 1976.

[25]Y. Morino, T. Nakagawa, *J. Mol. Spectrosc.*, **26**, 496 (1968).

[26]S. Li, E. R. Bernstein, *J. Chem. Phys.*, **95**, 1577 (1991).

[27]D. D. Evard, F. Thommen, K. C. Janda, *J. Chem. Phys.*, **84**, 3630 (1986).

Chapter 4

Nuclear Hyperfine Interactions

4.1 Introduction

The high resolution and low rotational temperatures afforded by the pulsed nozzle Fourier transform microwave technique are particularly well suited to resolving hyperfine and internal motion effects. As a result, a number of complexes containing molecular nitrogen (N_2) have been studied using both infra-red and microwave spectroscopy. Used as a probe of van der Waals interactions, N_2 provides several extra degrees of freedom over rare gas complexes. Firstly, the properties of N_2 can be resolved parallel and perpendicularly to the molecular axis allowing two possible configurations. Secondly, the nuclear hyperfine interactions due to the nitrogen (I = 1) nuclear electric quadrupole and magnetic dipole moments perturb the rotational spectra providing additional structural data and, under some favourable circumstances, information on electric field gradients and charge distributions[1].

Two limits of complexation for the nitrogen molecule can be considered. One where the nitrogen atoms are inequivalent and the other where the atoms are equivalent, either by symmetry or through internal motion. Most nitrogen complexes reported so far have been of the former type and involve quite strong interactions such as end on hydrogen bonding, for example N_2-HX where X=F,Cl[2],Br[3],CN,CCH[1] and weak Lewis acid/base interactions as reported for N_2-BF_3 and N_2-SO_3[4]. In a few cases, the effects due to zero point motions and the difference in field gradient experienced by the two nitrogen nuclei on complexation has been deconvoluted using microwave data in conjunction with ab initio calulations. This has allowed the calculation of the induced dipole moment and the free nitrogen coupling constant[1]. A few complexes of the second type have been reported including Ar-N_2[5] which is T shaped, N_2-C_6H_6 [6] where the nitrogen undergoes internal rotation in a plane parallel to the benzene plane and N_2-H_2O[7] which, although assuming a structure as if hydrogen bonded, undergoes a concerted tunnelling motion resulting in rotation of the N_2 and permutation of hydrogen nuclei.

A series of three complexes involving the nitrogen molecule complexed with OCS, O_3 and SO_2 have been studied using the apparatus already described (chapter 2). In the complexes of N_2 with OCS and O_3 it was clear from the features in the spectra that the patterns were best explained by

symmetry effects resulting from equivalent nitrogen nuclei. This was further confirmed in the third case by the predictions of a suitable hamiltonian for near prolate asymmetric top complexes where the nitrogen molecule rotates through a tunnelling process and the nitrogen nuclei experience equivalent environments. The hamiltonian used to analyse the nitrogen complexes consists of the sum of two contibutions. The rotational energy is calculated using the Watson S reduction hamiltonian used to fit the Ar_2-OCS rotational data and discussed in section 3.12. Additional smaller energy terms, which are observed as splittings of the rotational transitions, are expressed collectively as the hyperfine hamiltonian and discussed in the following sections.

4.2 The hyperfine hamiltonian

The hyperfine features for complexes without electronic angular momentum and in the absence of significant external magnetic or electric fields arise due to interactions between the nucleus and surrounding electronic charge and between the nuclei themselves. The hamiltonian can be written as,

$$H_{hyper} = H_Q + H_{SR} + H_{SS} \qquad (4.1)$$

- H_Q is the nuclear quadrupole hamiltonian,
- H_{SR} is the nuclear spin-rotation hamiltonian,
- H_{SS} is the the nuclear magnetic dipole-dipole hamiltonian.

Implicit to the hamiltonian is any symmetry effect arising from internal motions and tunnelling. Detailed theory for each of these interactions has been developed and described elsewhere[8] so only the analysis necessary to study the effects expected in complexes containing the N_2 molecule is reviewed here.

4.3 Nuclear quadrupole hyperfine interactions

A non-spherical distribution of nuclear charge, as found for nuclei of spin greater than ½, has associated electric and magnetic moments. The charge distribution can be written as a multipole expansion where the order lowest terms are electric charge, the magnetic dipole moment and the electric quadrupole moment. These moments will interact with magnetic and electric fields generated by the angular momentum associated with electron and nuclear charges. The coulombic interaction has no direct bearing on the rotational spectrum. However, higher order interactions do influence the spectrum and give rise to electric and magnetic hyperfine perturbations in the rotational spectrum. The influence of the largest contribution due to the electric quadrupole hyperfine interaction is considered first.

In a non-uniform electric field, the electric quadrupole moment will experience a torque and as a result of the nuclear spin angular momentum will precess about the principal axis of the electric field gradient. In a rotating molecule the principal field gradient axis will depend on averaging over the rotational state. For a single nucleus, the result is a coupling of the nuclear spin angular momentum to the rotational angular momentum and a perturbation of the rotational energies. An expression for the quadrupole interaction can be derived from the general multipole expansion by considering the potential energy, V due to the interaction between i nuclear charges and j electronic charges (cgs units),

$$V = \sum_{i,j} \frac{e_i e_j}{r_{ij}} \tag{4.2}$$

The separation r_{ij} in a space fixed coordinate system with angular orientation θ, ϕ can be expanded in terms of spherical harmonics , Y_{LM} to give,

$$V = \sum_{L=0}^{\infty} \sum_{M=-L}^{L} \left[\left(\frac{4\pi}{2L+1} \right)^{\frac{1}{2}} \sum_i e_i (r_i)^L Y^*_{LM}(\theta_i,\phi_i) \right] \times \left[\left(\frac{4\pi}{2L+1} \right)^{\frac{1}{2}} \sum_j \frac{e_j}{(r_j)^{L+1}} Y_{LM}(\theta_j,\phi_j) \right] \tag{4.3}$$

In quantum mechanical terms, the first part of the equation represents the multipole moment operator of the nucleus whereas the second part is due to the surrounding charge. Two criteria[9] limit the expansion in L. The first requires L to be even in order to retain the same symmetry with coordinate inversion. The second criterion limits L to 2^{2I}, the consequence of an angular momentum rule. Hence expanding the summation in terms of L, the L=0 term reproduces the Coulombic interaction and the L=2 expression is the interaction due to the nuclear electric quadrupole moment(Q) and the electric field gradient(∇E) generated by the surrounding electronic charge. Reexpressed in terms of irreducible spherical tensor operators[10], the quadrupole interaction can be written as,

$$H_Q = Q^{(2)} \cdot \nabla E^{(2)} = \sum_{p=-2}^{2} (-1)^p \, T^{(2)}_p(\nabla E) \, T^{(2)}_p(Q) \tag{4.4}$$

where $T^{(2)}_p(X)$ are components of a second rank tensor in a space fixed axis system.

There are a number of ways to evaluate the terms in equation 4.4. When there are several nuclei contributing to the quadrupole effect, a suitable representation of the angular momentum must be chosen in order to define a convenient basis set. In the case of nitrogen complexes, it is expected that the electric field gradient is dominated by the charge distribution of the nitrogen molecule and that only small perturbations arise due to complexation. For an extreme case such as the non-tunnelling hydrogen bonded N_2-HCN[11] complex, the difference in coupling constants for the N_2 nitrogen nuclei is 226 kHz compared with the free N_2 coupling constant of -5.07(8) MHz[1]. In a coupled angular momentum representation, used to reduce the size and number of off-diagonal matrix elements, neither nuclear spin is coupled much more strongly than the other to the rotation. Indeed for the repidly interchanging nitrogen nuclei, they are equivalent. Therefore, it is convenient to couple the spin angular momentum of the nitrogen nuclei ($\mathbf{I}_1$,$\mathbf{I}_2$) together to give a total spin angular momentum (**I**). The total spin angular momentum, **I**, is then coupled to the rotational angular momentum **J** to give a total angular momentum **F**, ie

$$\begin{aligned} \mathbf{I}_1 + \mathbf{I}_2 &= \mathbf{I} \\ \mathbf{I} + \mathbf{J} &= \mathbf{F} \end{aligned} \qquad (4.5)$$

Basis functions for solving the quadrupole hamiltonian in the coupled representation are therefore given by $| JKI_1I_2IFM_F \rangle$ and matrix elements can be evaluated using angular momentum theory. Details of such methods can be found in standard texts[12]. The procedure for deriving matrix elements for the two equivalent or nearly equivalent coupled nuclei is reviewed by Cook and DeLucia[10] and discussed below for the derivation of near-prolate asymmetric top elements.

The derivation of the quadrupole hamiltonian demonstrates that the interaction can be separated into two parts, one, $T_p^{(2)}(Q)$ associated with the nuclear angular momentum and the $| I_1I_2I \rangle$ basis and the other, $T_p^{(2)}(\nabla E)$, associated with the rotational angular momentum and the $| J\ K \rangle$ basis. Provided the irreducible tensors commute, the hamiltonian can be expanded in terms of reduced matrix elements dependent on the separate quantum numbers, $\langle l \| T^{(2)} \| l' \rangle$ as follows,

$$\begin{aligned} \left\langle JKIFM_F \middle| H_{Q_1} + H_{Q_2} \middle| J'K'I'FM_F \right\rangle &= (-1)^{J'+I'+F} \begin{Bmatrix} J & I & F \\ I' & J' & 2 \end{Bmatrix} \langle J \| T^{(2)}(\nabla E) \| J' \rangle \\ &\times \left\langle I_1I_2I \| T^{(2)}(Q_1) + T^{(2)}(Q_2) \| I_1I_2I' \right\rangle \end{aligned} \qquad (4.6)$$

where formulae for evaluating the six j symbol, {:::}, are tabulated elsewhere[13]. F, the total angular momentum quantum number, is conserved and H_Q is independent of the projection M_F.

4.3.1 Reduced quadrupole tensor matrix elements

The reduced quadrupole tensor matrix elements, in terms of the coupled spin I, can be evaluated in terms of the individual uncoupled reduced matrix elements for $T^{(2)}(Q_1)$ of nucleus 1 and similarly for nucleus 2, $T^{(2)}(Q_2)$ via[10,14]

$$\langle I_1\ I_2\ I \parallel T^{(2)}(Q_1) \parallel I_1\ I_2\ I' \rangle = (-1)^{I_1+I_2+I+2}\ [(2I+1)(2I'+1)]^{\frac{1}{2}} \times \begin{Bmatrix} I_1 & I & I_2 \\ I' & I_1 & 2 \end{Bmatrix} \langle I_1 \parallel T^{(2)}(Q_1) \parallel I_1 \rangle \tag{4.7}$$

The observable nuclear quadrupole moment, eQ is defined as the maximum projection of the uncoupled single nucleus quadrupole moment (M_I) along a space fixed axis, corresponding to $M_I = I_{1,2}$.

$$\langle I_1\ M_{I_1}=I_1 \mid T_0^{(2)}(Q_1) \mid I_1\ M_{I_1}=I_1 \rangle = \frac{eQ_1}{2} \tag{4.8}$$

Therefore, determining the reduced matrix element for the maximum projection by the Wigner-Eckart theorem[13] and substituting for the observable quadrupole moment, the reduced matrix element can be evaluated,

$$\left\langle I_1\ M_I=I_1 \mid T_0^{(2)}(Q_1) \mid I_1\ M_I=I_1 \right\rangle = \frac{eQ_1}{2} = \begin{pmatrix} I_1 & 2 & I_1 \\ -I_1 & 0 & I_1 \end{pmatrix} \langle I_1 \parallel T^{(2)}(Q_1) \parallel I_1 \rangle \tag{4.9}$$

For equivalent nitrogen nuclei, $I_1 = I_2 = 1$, and $Q_1 = Q_2 = Q(N_2)$. The three J symbol (:::) can be evaluated to give,

$$\langle I_1 \parallel T^{(2)}(Q_1) \parallel I_1 \rangle = \langle I_2 \parallel T^{(2)}(Q_2) \parallel I_2 \rangle = \sqrt{\frac{15}{2}}\ eQ \tag{4.10}$$

Substituting equation 4.10 into equation 4.7 for nucleus 1 and 2 gives the coupled spin reduced matrix element.

$$\langle I \parallel T^{(2)}(Q) \parallel I' \rangle = (-1)^I\ [(2I+1)(2I'+1)]^{\frac{1}{2}} \begin{Bmatrix} 1 & I & 1 \\ I' & 1 & 2 \end{Bmatrix} \left[(-1)^I + (-1)^{I'}\right] \sqrt{\frac{15}{2}}\ eQ \tag{4.11}$$

4.3.2 Reduced field gradient tensor matrix elements

To calculate the field gradient in the space fixed axis system the effect of rotation must be considered. The field gradient at a particular nucleus is determined by the charges external to the nucleus in orbitals that are fixed in the molecular frame. In first order, rotation will average components of the field gradient perpendicular to the axis of rotation so that the field gradient becomes symmetrical about the rotational axis. As a result, the quadrupole interaction has a **J** dependence with the size of the hyperfine splitting decreasing with increasing J. By convention, the field gradient is defined as the value corresponding to the maximum projection of **J** on to the space fixed axes system ($M_J=J$). In space fixed spherical tensor terms this corresponds to the expectation value of the $T_0^{(2)}(\nabla E)$ component operator. Evaluation of the field gradient reduced matrix element is by means of the Wigner-Eckart theorem in the prolate symmetric top basis $| J\ M_J\ K \rangle$ for the maximum projection of M_J, the space fixed projection. K is the molecule fixed projection quantum number,

$$\left\langle J\ M_J{=}J\ K \mid T_0^{(2)}(\nabla E) \mid J'\ M_J'{=}J'\ K' \right\rangle = (-1)^{J-J'} \begin{pmatrix} J & 2 & J' \\ -J & 0 & J' \end{pmatrix} \langle J \parallel T^{(2)}(\nabla E) \parallel J' \rangle \tag{4.12}$$

In order to evaluate this term further, the field gradient tensor term is transformed from the space fixed frame, $T_0^{(2)}(\nabla E)$, to the molecular frame principal inertial axes[14], $T_q^{(2)}(\nabla E)$, via

$$T_0^{(2)}(\nabla E) = \sum_{q=-2}^{2} D_{0q}^{2*}(\alpha\beta\gamma)\ T_q^{(2)}(\nabla E) \tag{4.13}$$

where $D_{pq}^{(2)*}(\alpha\beta\gamma)$ are elements of the Wigner rotation matrices and α,β,γ are Euler angles. In the molecule fixed system the components of the field gradient are constants independent of the rotational state in the absence of significant centrifugal distortion effects. Matrix elements in the molecular frame are then given by

$$\sum_{q=-2}^{2} \langle J\ M_J{=}J\ K \mid D_{pq}^{2*}\ T_q(\nabla E) \mid J'\ M_J'{=}J'\ K' \rangle =$$

$$\sum_{q=-2}^{2} (-1)^{M_J-K} [(2J+1)(2J'+1)]^{\frac{1}{2}} \begin{pmatrix} J & 2 & J' \\ -K & q & K' \end{pmatrix} \begin{pmatrix} J & 2 & J' \\ -J & 0 & J' \end{pmatrix} \langle \eta \mid T_q^{(2)}(\nabla E) \mid \eta \rangle \tag{4.14}$$

The final matrix term, $\langle \eta | T_q^2(\nabla E) | \eta \rangle$, expresses the field gradient expectation value, in the molecular frame and in spherical tensor form, with η representing vibrational and electronic wavefunctions. Converting between the spherical and cartesian tensor forms allows the expression to be written in terms of the conventional experimentally observable coupling constants along the inertial axes. The first order quadrupole energy is proportional to the expectation values of the diagonal components of the field gradient tensor in the rotational state of interest. The off-diagonal field gradient tensor component expectation values average to zero over the rotation and contribute only in second order. For the nitrogen complexes reported in this thesis, each complex has a plane of symmetry which eliminates all off-diagonal coupling constants except the term corresponding to the symmetry plane. Therefore, the field gradient tensor components for a molecular system where the ab plane is a plane of symmetry are given by,

$$\begin{bmatrix} q_{aa} & q_{ab} & 0 \\ q_{ba} & q_{bb} & 0 \\ 0 & 0 & q_{cc} \end{bmatrix} \qquad (4.15)$$

$$where\ q_{ij} = \left\langle \frac{\partial^2 V}{\partial i \partial j} \right\rangle$$

At this stage, it is convenient to multiply the field gradient tensor component, q_{ij}, by the quadrupole moment eQ to define the conventional quadrupole coupling constants χ_{ij}. The quadrupole coupling constants in the spherical tensor notation ($T_q^{(2)}(\chi)$) can be related to cartesian coupling constants by[15]

$$\begin{aligned} 2\chi_0 &= \chi_{zz} \\ 2\chi_{\pm 1} &= \mp\sqrt{\frac{2}{3}}(\chi_{xz} \pm i\chi_{yz}) \\ 2\chi_{\pm 2} &= \sqrt{\frac{1}{6}}(\chi_{xx} - \chi_{yy} \pm 2i\chi_{xy}) \end{aligned} \qquad (4.16)$$

The field gradient($\nabla^2 V$) at the nucleus is due to charge external to the nuclear volume so the Laplace equation, $\nabla^2 V = 0$ applies with the result that the sum of diagonal terms in the coupling tensor is zero. As a consequence, only two diagonal coupling constants can be defined. For a near prolate asymmetric top the constants are chosen to be χ_{aa} and $\Delta\chi = \chi_{bb} - \chi_{cc}$ in order to minimize the off-

diagonal terms in K, where $\chi_{ii} = eQ \langle \partial^2 V/\partial i^2 \rangle$, i=a,b,c and eQ, the quadrupole moment, is defined in equation 4.7.

By transforming to the inertial axis system, the form of the field gradient reduced matrix element becomes similar to that of the rigid asymmetric rotor problem where analogous functions in J and K to those given by $\langle J\ K \mid H_{rigid} \mid J\ K' \rangle$ are given by the numerator of the 3-J symbol in terms of J and K in equation 4.14. This is more clearly illustrated by the first order quadrupole energy expression derived by Bragg[16] which includes the rotational expectation term as,

$$H_Q = (\chi_{aa} \hat{J}_a^2 + \chi_{bb} \hat{J}_b^2 + \chi_{cc} \hat{J}_c^2)\, f(I,J,F) \tag{4.17}$$

f(I,J,F) is a function in terms of I,J,F quantum numbers arising from the coupling of nuclear spin and rotational angular momenta. The f(I,J,F) expression given by Bragg refers to coupling for a single nucleus and is not directly applicable to the two coupled nuclear spin case discussed here. The equivalent f(I,J,F) factor for the two coupled nuclei case is developed in equations 4.19 and 4.21. However, the factor dependent on the rotational expectation values is the same in both cases. This can be derived from the direction cosines between space fixed and molecular inertial axes corresponding to the transformation in equation 4.13. The familiar asymmetric rotor hamiltonian form (equation 3.3) can be obtained by expanding equation 4.17 in terms of χ_{aa}, $\Delta\chi$ and noting that $\Sigma\chi_{ii} = 0$,

$$H_Q = \frac{1}{2}\left[\chi_{aa}(3\hat{J}_a^2 - \hat{J}^2) + \Delta\chi(\hat{J}_+^2 + \hat{J}_-^2)\right] f(I,J,F) \tag{4.18}$$

where $\hat{J}_\pm = \hat{J}_b \pm i\hat{J}_c$. This illustrates that the first order quadrupole hamiltonian matrix includes elements between terms differing in K by 0 or ± 2 in the symmetric top basis. The angular momentum expectation values along each inertial axis are calculated as part of the rigid rotor hamiltonian problem. Therefore, provided the eigenvectors of the diagonalized rotational hamiltonian are known the quadrupole hamiltonian can be calculated in the diagonal K_aK_c basis rather than constructing and diagonalizing matrices in K for each F value. The expectation values, $\langle \hat{J}_P^2 \rangle = \langle \partial H_{rot}/\partial P \rangle$, where P = A,B,C rotational constants are calculated using the rotational eigenvectors and the Hellmann-Feynman theorem. The quadrupole dependence on the rotational expectation values is then given by multiplying these terms by the coupling constants, χ_{aa} and χ_{bb}-χ_{cc}.

4.3.3 Quadrupole hyperfine matrix elements

Using the expressions derived for the reduced matrix elements and noting that the quadrupole hamiltonian can be written as the sum of the contributions of nucleus 1 and 2, the quadrupole interaction hamiltonian matrix elements (equation 4.6) are given by,

$$\begin{aligned}\langle J\ K\ I\ F \mid H_{Q_1}+H_{Q_2} \mid J'\ K'\ I'\ F \rangle = \\ (-1)^{J'+I+F}\begin{Bmatrix} J & I & F \\ I' & J' & 2 \end{Bmatrix}\langle \eta \mid T_q^{(2)}(\nabla E) \mid \eta \rangle \\ \times (-1)^{J-K}\,[(2J+1)(2J'+1)]^{\frac{1}{2}}\begin{pmatrix} J & 2 & J' \\ -K & q & K' \end{pmatrix} \\ \times \left[(-1)^{I'}\,eQ_1+(-1)^{I}\,eQ_2\right][(2I+1)(2I'+1)]^{\frac{1}{2}}\begin{Bmatrix} 1 & I & 1 \\ I' & 1 & 2 \end{Bmatrix}\sqrt{\frac{15}{2}}\end{aligned} \tag{4.19}$$

Before deriving explicit matrix elements several simplifications can be considered. In the expression above, terms mixing J with J$\pm$1 and J$\pm$2 arise which result in a second order perturbation contribution to the rotational energy by the quadrupole interaction and therefore J is not a perfectly good quantum number. In the case of nitrogen the molecular quadrupole coupling constant of $\sim$-5 MHz is very small compared with the typical rotational energy splitting in the complexes studied. Only in the case of accidental near degeneracy of the rotational levels are the second order effects expected to be significant compared with the experimental resolution of 1 kHz. Therefore, J can be treated as a good quantum number, only matrix elements of the same J (diagonal) need be calculated and any near degenerate rotational levels can be treated separately by including a second order perturbation term. The second order energy term is given by

$$\Delta E_Q^{(2)} = \pm\sum_{J,I,K}\frac{|\langle J\ I\ K\ F \mid H_Q \mid J'\ I'\ K'\ F \rangle|^2}{E - E'} \tag{4.20}$$

where the energy separation E_2-E_1 is between rotational levels and is generally 4 GHz or more. The squared matrix element is dependent on the nitrogen coupling constant, $\sim$-5MHz, and a matrix element numerical factor which is of the order 0.2. The total perturbation is then 0.25 kHz which is less than the experimental uncertainty of $\sim$1 kHz.

When the nuclei are equivalent, the term $[(-1)^{I'}eQ_1+(-1)^{I}eQ_2]$ in the hamiltonian is non-zero only when $I'=I,I\pm2$. This is a result of permutation symmetry where the total nuclear spin wavefunction is symmetric to permutation when I is even and antisymmetric when I is odd. As a result there are no matrix elements connecting even I and odd I so the overall matrix can be factored into two submatrices. The total nuclear spin of N_2 can take the values 2,1,0 so there are no $I'=I\pm2$ terms mixing with $I=1$ and the odd submatrix is diagonal. The even submatrix is also diagonal except for terms with $F=J$ where mixing of $I=0$ and 2 occurs. These elements form a two by two submatrix which can be solved generally and the even submatrix can also be made diagonal.

Matrix elements calculated from equation 4.19 for the coupled equivalent nitrogen nuclei case, diagonal in F, J and I for $I=0,1,2$ are given by

$$\langle J\ K\ I\ F \mid H_Q \mid J\ K'\ I\ F \rangle =$$

$$\frac{3I(I+1)-11}{4(2I-1)(2I+3)} \times \frac{3C(C-1)-4J(J+1)I(I+1)}{(2J-1)(2J+3)4J(J+1)} \times g(J,K,K')$$

$$\text{where } g(J,K,K') = \begin{cases} 2[3K^2 - J(J+1)]\ \chi_{aa} & \text{for } K'=K \\ [J(J+1) - K(K\pm1)]^{\frac{1}{2}} & \\ \times[J(J+1) - (K\pm1)(K\pm2)]^{\frac{1}{2}}\ \Delta\chi & \text{for } K'=K\pm2 \end{cases} \qquad (4.21)$$

$$\text{also } C = J(J+1) + I(I+1) - F(F+1)$$

The two by two matrix mixing terms in $I=0$ and 2 for $F=J$ is given by

H_Q	$\mid J\ K\ I=0\ F=J \rangle$	$\mid J\ K\ I=2\ F=J \rangle$
$\langle J\ K\ I=0\ F=J \mid$	0	$\frac{[2(2J-1)(2J+3)2J(2J+2)]^{\frac{1}{2}}}{2(2J-1)(2J+3)2J(2J+2)}$
$\langle J\ K\ I=2\ F=J \mid$	$\frac{[2(2J-1)(2J+3)2J(2J+2)]^{\frac{1}{2}}}{2(2J-1)(2J+3)2J(2J+2)}$	$\frac{-(2J+5)(2J-3)}{2(2J-1)(2J+3)2J(2J+2)}$

(4.22)

where each element is also to be multiplied by the J and K dependent term g(J,K,K') in brackets in equation 4.21.

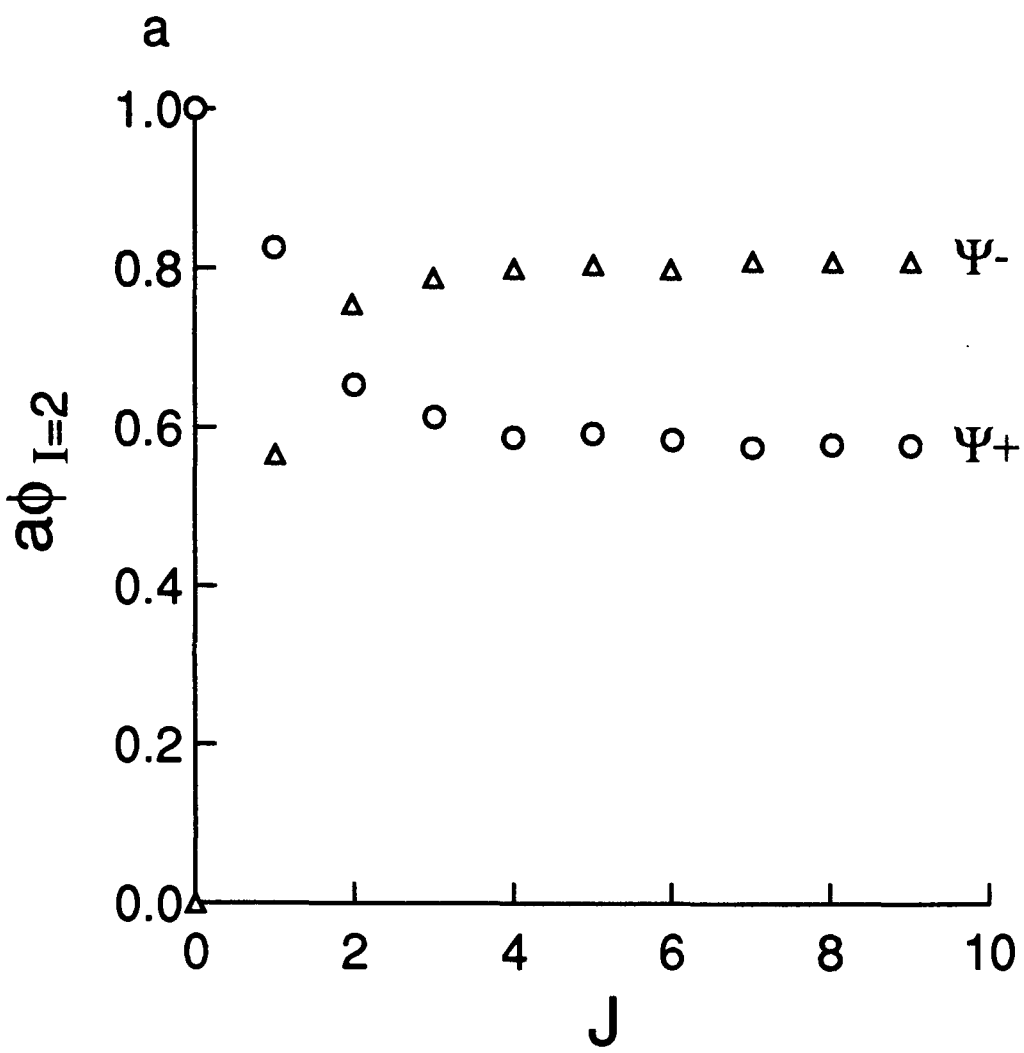

Figure 4.1; Graph of the contribution of the I=2 basis function to the mixed F=J state. $\Psi_{\pm}$ refers to equation 4.24. Contribution from I=0 given by $1-a^2_{I=2}$.

The solution to the 2x2 matrix, obtained using the standard quadratic formula is

$$E_{\pm} = g(J,K,K') \times \frac{-(2J+5)(2J-3) \pm \sqrt{(2J+5)^4(2J-3)^2+8(2J)(2J+2)(2J-1)(2J+3)}}{4(2J)(2J+2)(2J-1)(2J+3)} \tag{4.23}$$

The contribution of each basis function (ie I=0 and 2) to the mixed eigenfunction can be deduced by parameterizing the contribution of each basis function in terms of an angle β to give[17]

$$\Psi_{+} = \varphi_{I=0}\cos\beta + \varphi_{I=2}\sin\beta$$

$$\Psi_{-} = -\varphi_{I=0}\sin\beta + \varphi_{I=2}\cos\beta$$

$$\cos\beta = \left[\frac{1}{2}\left\{1 + \left(\frac{-(2J+5)(2J-3)}{\left[\{(2J+5)(2J-3)\}^2 + 8(2J-1)(2J)(2J+2)(2J+3)\right]^{\frac{1}{2}}}\right)\right\}\right]^{\frac{1}{2}} \tag{4.24}$$

Figure 4.1 shows a graph of the contribution of each basis function as a function of rotational quantum number.

Transitions between levels of mixed nuclear spin, I

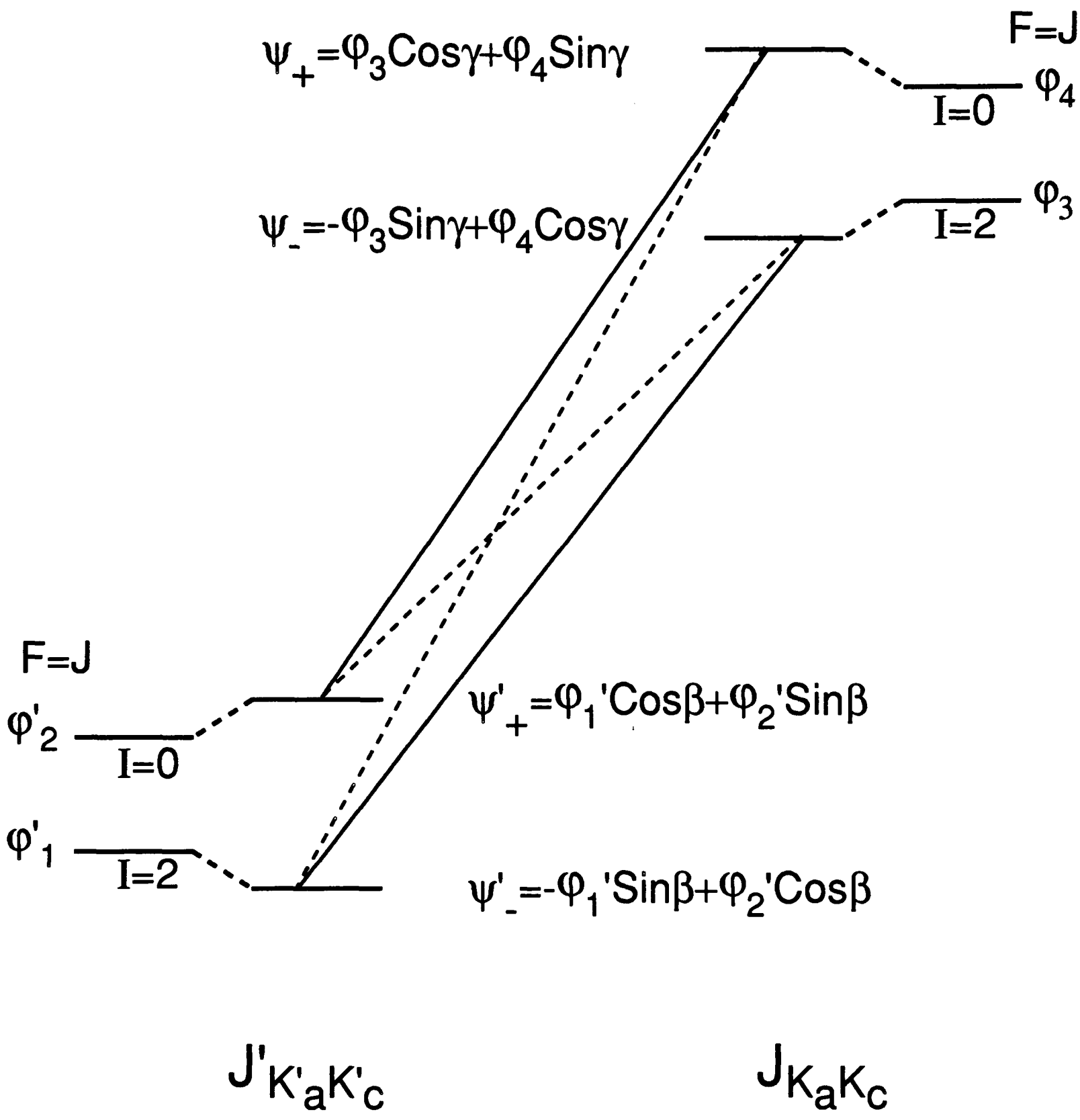

Figure 4.2; Energy level diagram showing the effects of mixing symmetric I=0,2 nuclear spin states. Strong transitions are indicated by a solid line, weak by a dotted line. $\Psi\pm$ are defined in equation 4.24.

With the strong mixing between I=0 and I=2 levels, transitions of the type $\psi_+ \longleftrightarrow \psi_-$ are expected to be weak. The effects of mixing and expected transitions are indicated in figure 4.2.

To summarize, the quadrupole hamiltonian for asymmetric top complexes with equivalent nitrogen nuclei can be calculated in a diagonal form to give energies with a precision better than the 1 kHz experimental measurement uncertainty. This disregards second order effects which become significant if there are perturbing energy levels with separations less than 1 GHz. The quadrupole interaction energy of any particular hyperfine level can be calculated directly provided the eigenvectors of the rotational hamiltonian are known. A computer program to fit data for such complexes need only diagonalize the asymmetric top rotational hamiltonian in order to calculate the rotational energies and then use the rotational expectation values to calculate the first order quadrupole and total energies.

4.3.4 Nuclear quadrupole structural information

The nuclear quadrupole coupling constants provide useful structural information. In the free nitrogen molecule, the nuclear quadrupole interaction is characterized by one coupling constant corresponding to the coupling along the molecular axis, $\chi(N_2)$=-5.39 MHz[18]. In dinitrogen complexes, the observed coupling constants correspond to projections of the molecular constant on to the inertial axes which in general do not coincide with the N_2 molecular axis system. As discussed earlier, the coupling constants in a molecule or van der Waals complex are derived from spherical harmonic functions and hence have the same $P_2(\cos\theta)$ - Legendre polynomial functional form. It must also be remembered that the actual angles are the ground vibrational state averaged expectation value angles, indicated by enclosing the expression in angled brackets, $\langle P_2(\cos\theta) \rangle$. When converted into cartesian coordinates, the coupling constants have an angular functional form in θ and ϕ analogous to the atomic d orbitals. By convention, θ is the angle between the nitrogen molecular axis and the z cartesian axis. ϕ is the angle of rotation from the x axis of the projection of the nitrogen in the xy plane. This is illustrated in figure 4.3. Expressions for projections in a near prolate asymmetric top containing a plane of symmetry in the ab plane, as observed for N_2-OCS are given in equation 4.25[15,10]. The a,b,c inertial axes correspond to z,x,y axes of figure 4.3.

$$\chi_{aa} = \chi_0 = \chi_{N_2}\left\langle \frac{1}{2}(3\cos^2\theta - 1)\right\rangle \qquad (d_{z^2})$$

$$\chi_{bb} - \chi_{cc} = \sqrt{\frac{3}{2}}(\chi_{-2} + \chi_{+2}) = \chi_{N_2}\left\langle \frac{3}{2}\sin^2\theta\cos 2\phi\right\rangle \qquad (d_{x^2-y^2}) \qquad (4.25)$$

$$\chi_{ab} = \sqrt{\frac{3}{2}}(\chi_{-1} - \chi_{+1}) = \chi_{N_2}\langle \sin\theta\cos\theta\cos\phi\rangle \qquad (d_{zx})$$

The analogy with d atomic orbitals which have identical angular behaviour is indicated in parenthesis.

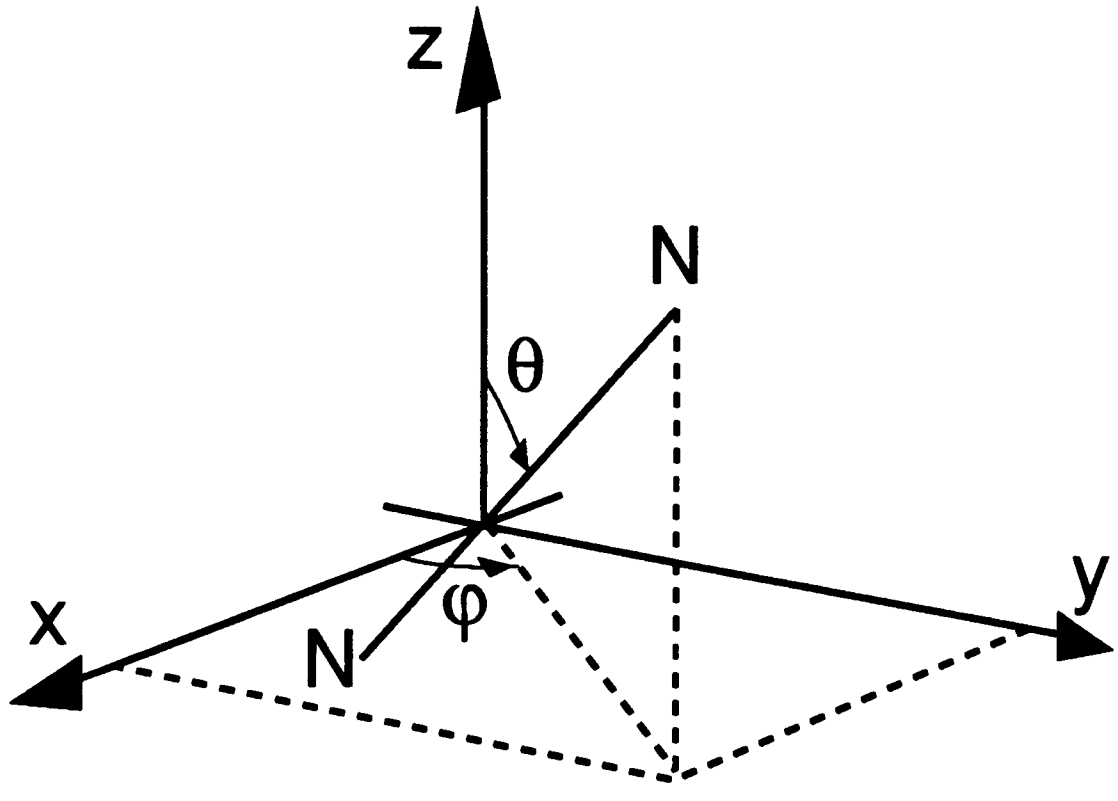

Figure 4.3; Coordinate system for N_2 in the molecular frame of N_2-X complexes. Z corresponds to the a inertial axis.

4.3.5 Centrifugal Distortion

Centrifugal distortion of the complex will result in slight changes in structure. Consequently, the projections of the nuclear quadrupole moment onto the inertial axes will change slightly with increasing rotational angular momentum. Equations 4.17 and 4.18 show the similarity between the quadrupole and rotational hamiltonian dependence on the rotational expectation values. As a result, an analogous power expansion in $\hat{J}^2$, $\hat{J}_a^2$ and $(\hat{J}_b^2 - \hat{J}_c^2)$ angular momentum operators to that discussed in section 3.3 for the Watson S and A reduction hamiltonians is a convenient representation for the quadrupole distortion. It is therefore convenient to expand the two effective quadrupole coupling constants as,

$$\begin{aligned} \chi_{aa}^{effective} &= \chi_{aa} + D_{\chi_{aa}}^{K} J_a^2 + D_{\chi_{aa}}^{J} J^2 \\ \Delta\chi^{effective} &= \Delta\chi + D_{\Delta\chi}^{K} J_a^2 + D_{\Delta\chi}^{J} J^2 \end{aligned} \qquad (4.26)$$

Terms involving $(\hat{J}_b^2 - \hat{J}_c^2)$ are expected to be considerably smaller than the observable resolution (*cf.* d_1 and d_2 distortion constants) and are ignored. D^K constants are expected to be largest although with near prolate asymmetric tops, only the lowest K_a levels are populated so the contribution may be small. D^J constants are smaller but gain prominence with higher J.

Rotational and centrifugal distortion constants form a decreasing geometric series in functions of $\hat{\mathbf{J}}$ and $\hat{\mathbf{J}}_a$ so that the distortion constants are considerably smaller than the rotational constants; this is illustrated with Ar_2-OCS (chapter 3) where distortion constants are $\sim 10^{-5}$ times the rotational constants. A similar pattern is expected with the quadrupole distortion although the ratio is expected to be $\sim 10^{-4}$ for the less rigidly bound nitrogen complexes[19]. The nitrogen quadrupole coupling constant is -5.39 MHz[18] giving possible distortion constants of <0.5 kHz for D_χ^K.

4.4 Spin-rotation interaction hamiltonian

In addition to the electrostatic interaction, further effects must be considered resulting from the magnetic interactions induced by the motion of charges associated with the nucleus and the surrounding electronic charge. The resulting nuclear magnetic interactions induced can be expressed generally as a multipole expansion[8] analogous to electronic multipole expansion in equation (4.2). By replacing the nuclear charge distribution e_n by $(-\nabla_n \cdot m_n)$ and the molecular charge distribution e_m by $(-\nabla_m \cdot m_m)$ the magnetic multipole expansion is obtained. $-\nabla_{m,n} \cdot m_{m,n}$ is derived from the curl of the vector magnetic potential(m) associated with the current density. The extent of the expansion is limited to odd order terms, as there is a change in parity with coordinate reversal and no terms of greater order than 2^{2I}. Corresponding to the lowest order is the magnetic dipole interaction which can be written in terms of 1st order spherical harmonics/irreducible tensors and a hamiltonian given by,

$$H_{SR} = m^{(1)} \cdot \mu^{(1)} \tag{4.27}$$

Although it is expected that significant magnetic interactions will be observed in molecules or complexes with electronic angular momentum in their ground states, small effects are also observed in high resolution microwave spectra of ostensibly $^1\Sigma$ ground state molecules[20,21]. This arises from first order contributions due to the nucleus rotation which is very much smaller than the electronic effects observed for open shell systems. Small second order effects give rise to an electronic contribution resulting from the mixing between the ground and excited electronic states induced by the molecular rotation. Effective constants which account for both effects are generally used[22].

A similar procedure to that used to calculate the quadrupole energy is employed to calculate the spin-rotation energy. The hamiltonian in the coupled basis is expanded in terms of reduced matrix elements

$$\langle J\ I\ F\ M_F \mid H_{SR} \mid J\ I'\ F\ M_F \rangle = (-1)^{J+I'+F} \begin{Bmatrix} J & I & F \\ I' & J & 1 \end{Bmatrix} \times \langle J \parallel T^{(1)}(m) \parallel J \rangle \langle I \parallel T^{(1)}(\mu) \parallel I' \rangle \quad (4.28)$$

The reduced matrix elements can be related to observable quantities and are derived by Cook and De Lucia[7]. The reduced matrix element for the magnetic moment of nitrogen in the coupled basis, $I_1=I_2=1$, $I_1+I_2=I$ is given by

$$\langle I_1=1\ I_2=1\ I \parallel T^{(1)}(\mu) \parallel I_1=1\ I_2=1\ I' \rangle = \{(-1)^I+(-1)^{I'}\} [(2I+1)(2I'+1)]^{\frac{1}{2}} \times \begin{Bmatrix} 1 & I & 1 \\ I' & 1 & 1 \end{Bmatrix} \sqrt{6}\ g_I\ \mu_N \quad (4.29)$$

μ_N is the nuclear magneton and g_I the nitrogen nuclear g factor. For identical nuclei, interactions between even and odd I states vanish. In addition since $m^{(1)}$ and $\mu^{(1)}$ are vectors, interactions between states differing in I by 2 vanish.

For a $^1\Sigma$ ground state complex, the magnetic field is a result of the rotation and hence the field components in the inertial axis system can be taken to be proportional to a coupling constant C_{ii} where i=a,b,c and the rotational angular momentum expectation value along each axis. An expressions for C_{ii} in terms of first order nuclear and second order electronic contributions is given by Flygare et al[22]. In general the magnetic susceptibility tensor principal axis system will not coincide with the principal inertial axis system and off-diagonal terms will result. However, in first order the expectation values of the off-diagonal terms average to zero. As a result, the reduced matrix element is given by

$$\langle J \parallel T^{(1)}(m) \parallel J \rangle = (g_I\ \mu_N)^{-1} [J(J+1)(2J+1)]^{\frac{1}{2}} \frac{(C_{aa}\hat{J}_a^2 + C_{bb}\hat{J}_b^2 + C_{cc}\hat{J}_c^2)}{J(J+1)} \quad (4.30)$$

Substituting equations 4.28 and 4.29 into 4.30, the spin rotation matrix elements are given by,

$$\langle J\ I\ F\ M_F \mid H_{SR} \mid J\ I\ F\ M_F \rangle = \frac{(C_{aa}\hat{J}_a^2 + C_{bb}\hat{J}_b^2 + C_{cc}\hat{J}_c^2)}{2J(J+1)} \times [F(F+1) - J(J+1) - I(I+1)] \quad (4.31)$$

The expression involving $C_{ii}\hat{J}_i^2$ again has the form of the asymmetric rotor hamiltonian and can be evaluated using the solutions to the asymmetric top rotational hamiltonian giving $\hat{J}_i^2$. Note that there are no matrix elements between I=0 and 2 states but account must be taken of fact that quadrupole has already mixed states of different I when J=F. For the mixed states, only the I=2 basis function will have a spin-rotation contribution and hence the corresponding eigenfunction is evaluated for the I=2 contribution only. This is multiplied by the square of the I=2 basis function coefficient evaluated in equation 4.24.

$$\langle a_1\varphi_{I=0} + a_2\varphi_{I=2} \mid H_{SR} \mid a_1\varphi_{I=0} + a_2\varphi_{I=2} \rangle = 0 + a_2a_2 \langle \varphi_{I=2} \mid H_{SR} \mid \varphi_{I=2} \rangle \quad (4.32)$$

The a coefficients correspond to the normalized basis function coefficients in equation 4.24

4.5 The Nuclear magnetic dipole-dipole hamiltonian

The nuclear magnetic dipole-dipole interaction arises from the interaction between two nuclear dipole moments. The classical interaction energy for two dipoles, μ_1, μ_2 separated by vector **r** is given by[15],

$$U = \frac{1}{r^3}\left[\mu_1\mu_2 - \frac{3(\mu_1 r)(\mu_2 r)}{r^2}\right] \quad (4.33)$$

The quantum mechanical hamiltonian can be obtained from this expression[23] by replacing μ_1 and μ_2 by the nuclear spin angular momentum operators $g_N\mu_N\mathbf{I}_1$ and $g_N\mu_N\mathbf{I}_2$. μ_N is the nuclear magneton and g_N the ^{14}N nuclear g factor. Equation 4.33 can be written in a more compact form, in terms of $\mathbf{I}_1$, $\mathbf{I}_2$ and a cartesian coupling tensor $\mathbf{D}_{NN}$[24],

$$H_{SS} = I_1 \cdot D_{NN} \cdot I_2 \quad (4.34)$$

The $\mathbf{D}_{NN}$ tensor is determined by geometric factors involving the dipole separation, angular orientation and a coupling constant given by $d = g_N^2\mu_B^2/r^3$ which for the nitrogen molecule has the value, d_0=0.471(6) kHz[18] (equilibrium nuclear separation). Evaluation of the H_{SS} matrix elements is most conveniently done by transforming the cartesian $\mathbf{D}_{NN}$ tensor, which is both symmetric and traceless, into second order irreducible spherical tensor form with reduced matrix elements dependent on J. Continuing the spin coupling scheme used so far, the two spin operators can be combined to give 0, 1st and 2nd order tensors of which only the second order interaction with the coupling tensor needs to be considered. Therefore the hamiltonian can be written as a product of two 2nd order spherical tensors with an analogous form to the quadrupole problem. However, two points can be considered. Firstly, the dipole-dipole interaction is determined by known nuclear quantities and geometric factors so that when the structure is known, the contribution can be calculated. Secondly, the coupling constant is small, less than the FT microwave spectrometer experimental measurement uncertainty. The energy perturbation will be reduced relative to the characteristic d_0 constant by matrix elements generally less than 1. In addition, the nitrogen molecule in the complex is not in the principal axis system of the $\mathbf{D}_{NN}$ tensor and projections along the inertial axes appear in expressions for the energy. For these reasons, the dipole-dipole interaction has been excluded from the calculation and it is noted that the deduced quadrupole constants will have contributions from the dipole-dipole interaction of approximately 0.5 kHz or less.

4.6 Relative transition intensities

The difficulty in maintaining the same instrument response, or quantifying variations in response, over the operating frequency range of the Fourier transform microwave spectrometer means that measured line intensities are quite uncertain. However, where several transitions occur within the bandwidth of the Fabry-Perot cavity resonance, relative intensities can be roughly estimated. This is the case with nitrogen complexes, where the hyperfine splitting is expected to be of the order of 1 to 2 MHz for low rotational transitions[2].

Explicit expressions for the relative intensities of hyperfine transitions involving two coupled nuclear spins have been derived[10] and are given by

$$S_{(J\,I\,K\,F \to J'\,I'\,K'\,F')} = |\langle J\ I\ K\ F \parallel \mu^{(1)} \parallel J'\ I'\ K'\ F' \rangle|^2$$

$$= \sum_I \left| a_I'\, a_I\, (-1)^{J+I'+F'+1}\left[(2F+1)(2F'+1)\right]^{\frac{1}{2}} \begin{Bmatrix} J & F & I \\ F' & J' & 1 \end{Bmatrix} \right|^2 \qquad (4.35)$$

a_I are coefficients of each spin state contributing to the eigenfunction. Only in the case of the mixed I=0 and 2, J=F states will values of a_I be other than 1 or 0.

Equation 4.35 illustrates that the transition intensities are determined by the properties of a first order 6-j symbol and hence the selection rule in the total angular momentum quantum number F is $\Delta F = 0, \pm 1$. The relative intensities of all except the mixed spin I=0 and I=2, F=J transitions correspond to the values tabulated in standard microwave texts[6] so that transition intensities for $\Delta F = \Delta J > \Delta F = 0 > \Delta F = -\Delta J$ within the rotational transition. In the high J limit, the hyperfine spectrum is dominated by the $\Delta F = \Delta J$ transitions. In the case of transitions between the mixed spin levels, the coefficients a_I and a_I' take the values of the spin basis function coefficients given by equation 4.24.

References

[1]A. C. Legon, P. W. Fowler, *Z. Naturforsch.*, **47a**, 367 (1991).

[2]R. S. ALtman, M. D. Marshall, W. Klemperer, *J. Chem. Phys.*, **79**, 57 (1983).

[3]N. W. Howard, A. C. Legon, *J. Chem. Phys.*, **90**, 672 (1989).

[4]K. H. Bowen, K. R. Leopold, K. V. Chance, W. Klemperer, *J. Chem. Phys.*, **73**, 137 (1980).

[5]W. Jäger, M. C. L. Gerry, *Chem. Phys. Lett.*, **196**, 274 (1992).

[6]Y. Oshima, H. Koguchi, Y. Endo, *Chem. Phys. Lett.*, **184**, 175 (1991).

[7]H. O. Leung, M. D. Marshall, R. D. Suenram, F. J. Lovas, *J. Chem. Phys.*, **90**, 700 (1989).

[8]W. Gordy, R.L.Cook, *Microwave Molecular Spectra*. Wiley, New York, 1984 .

[9]N. F. Ramsey, *Molecular Beams*. Oxford 1956.

[10]R. L. Cook, F. C. De Lucia, *Am. J. Phys.*, **39**, 1433 (1970).

[11]E. J. Goodwin, A. C. Legon, *J. Chem. Phys.*, **82**, 4434 (1985).

[12]B. L. Silver, *Irreducible Tensor Methods*. Academic Press, New York, 1976.

[13]R. Zare, *Angular Momentum*. Wiley Interscience, New York, 1988.

[14]H. P. Benz, A. Bauder, H. H. Günthard, *J. Mol. Spectrosc.*, **21**, 156 (1966).

[15]M. Weissbluth, *Atoms and Molecules*. Academic Press, New York, 1978.

[16]J. K. Bragg, *Phys. Rev.*, **74**, 533 (1948).

[17]P. W. Atkins, *Molecular Quantum Mechanics*, 2nd Edition, Oxford University Press, New York, 1984. pages 100, 173.

[18]T. A. Scott, *Phys. Rep. C*, **27**, 89 (1976).

[19]M. A. Walsh, T. R. Dyke, B. J. Howard, *J. Mol. Struct.*, **189**, 111 (1988).

[20]Y. Xu, M. C. L. Gerry, D. L. Joo, D. J. Clouthier, *J. Chem. Phys.*, **97**, 3931 (1992).

[21]C. H. Townes, G. C. Dousmanis, R. L. White, R. F. Schwarz, *Diss. Farad. Soc.*, **19**, 56 (1955).

[22]M-K Lo, V. W. Weiss, W. H. Flygare, *J. Chem. Phys.*, **41**, 206 (1964); C. Styger, M. C. L. Gerry, *J. Mol. Spectrosc.*, **158**, 328 (1993).

[23]P. Thaddeus, L. C. Krishner, J. H. N. Loubser, *J. Chem. Phys.*, **40**, 257, (1964).

[24]R. M. Garvey, F. C. DeLucia, *J. Mol. Spectrosc.*, **50**, 38 (1974).

Chapter 5

The rotational and hyperfine spectrum of N_2-OCS

5.1 Introduction

Several nitrogen complexes involving planar, T-shaped structures have been reported by other workers using infra-red absorption spectroscopy. Examples are N_2-OCS[1], N_2-CO_2[2] and N_2-N_2O[3] where the $\sim$10 MHz resolution of the infra-red technique is insufficient to resolve the nitrogen nuclear hyperfine structure or small internal motion effects. The Ar-N_2 complex[4] shows effects in both the hyperfine and rotational spectra which can be attributed to large amplitude motions. Similar arguments are used to explain differences in the molecular quadrupole coupling constant for N_2 calculated from rotational spectra of various complexes[4,5] and NQR data[6]. Evidence for tunnelling motions of the nitrogen molecule in dimers with a non-linear molecule is provided by the microwave spectrum of N_2-H_2O where splittings due to both N_2 and H_2O tunnelling effects are observed[7]. A second complex which may show similar effects is N_2-NH_3. A limited MBER study of N_2-NH_3 has been made by Fraser *et al.*[8] and compared with CO-NH_3. Although these results are inconclusive, the results for CO-NH_3 suggest a long, quite weak van der Waals bond, large amplitude motions of the CO and possible NH_3 tunnelling-inversion effects.

N_2-OCS, with the moderate OCS dipole moment (0.715D)[9] and two quadrupolar nuclei is the simplest of the complexes observed in the infra-red for the study of the internal motions of the nitrogen moiety in the microwave spectrum. Analysis of the infra-red spectrum of N_2-OCS[1] indicates that the complex is T-shaped with the nitrogen axis oriented towards the electropositive carbon in OCS (figure 5.3). This is also confirmed by an electrostatic distributive multipole[10] (DMA) calculation[1] where the dominant interaction can be thought of as that between the molecular quadrupole moments. In the case of a complex where the nitrogen molecule undergoes wide amplitude libration motions without inversion, the spectral hyperfine features will correspond to that of an asymmetric top with two nitrogen nuclei possessing slightly differing coupling constants. The maximum observed difference between nitrogen coupling constants in linear hydrogen bonded complexes is 250 kHz for N_2-HCN[5] which can be taken as an upper limit. However, if tunnelling can occur at a sufficient rate, the nitrogen nuclei become effectively equivalent. In this case, nuclear hyperfine splitting with characteristic nuclear statistical intensity variations and tunnelling effects may be discernable in the spectrum.

Figure 5.1a; Antisymmetric hyperfine transitions in a neon expansion

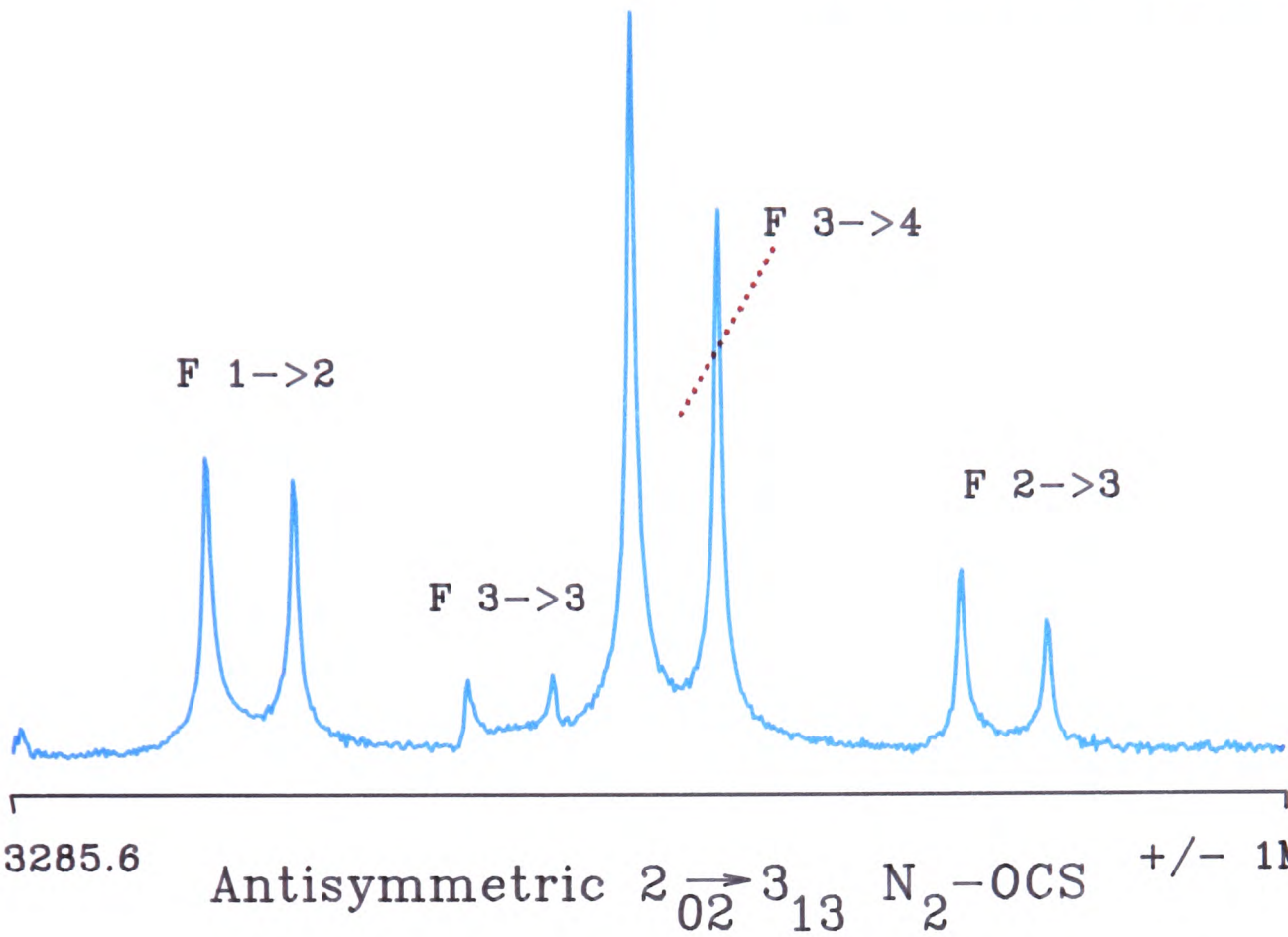

Figure 5.1b; Symmetric hyperfine transitions in an argon expansion

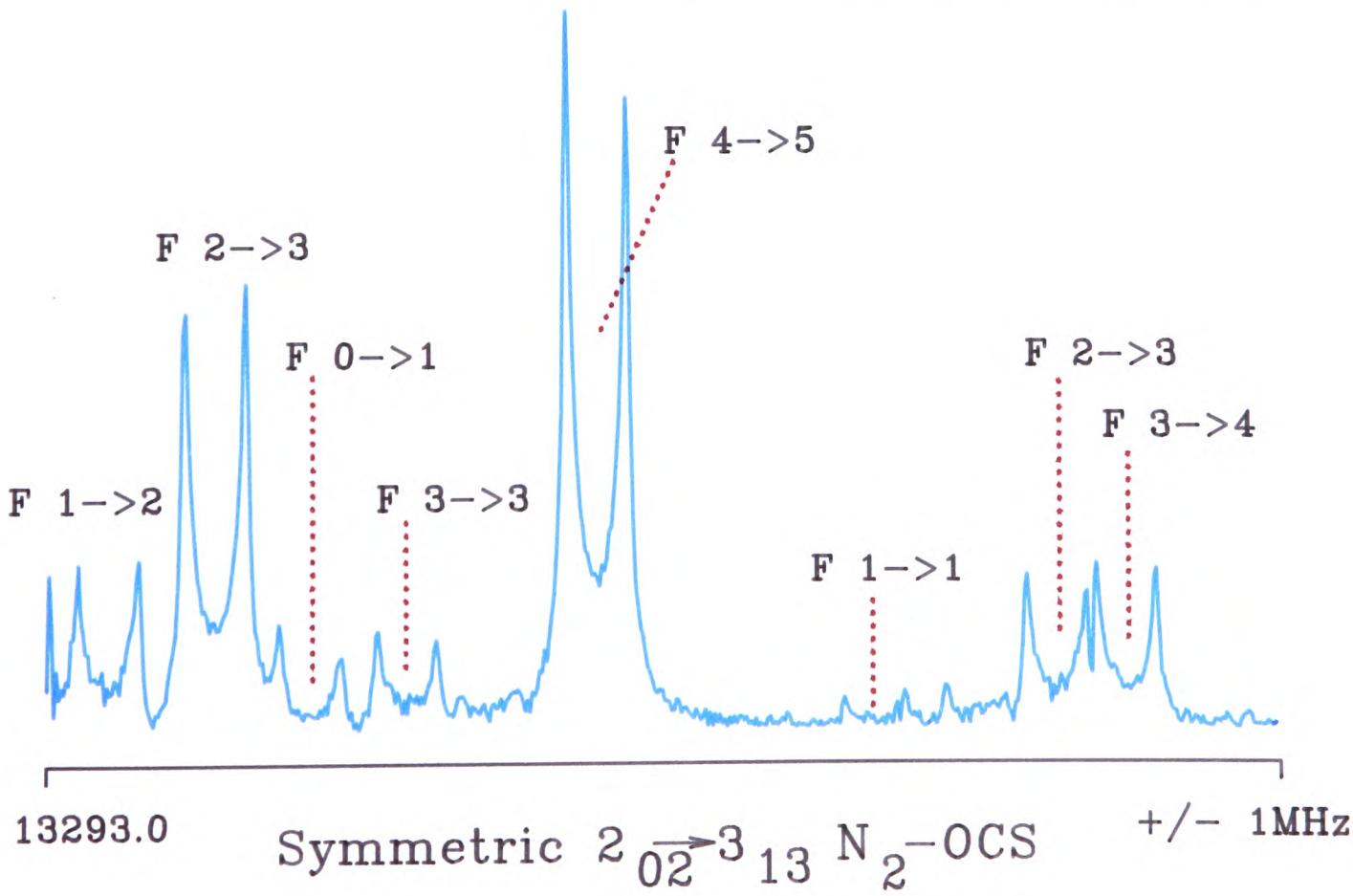

5.2 Experimental

The N_2-OCS spectrum was recorded between 6 and 18 GHz. Initial measurements were made using a perpendicular supersonic expansion generated by a LaserTechnics piezo-crystal valve with a 0.6mm nozzle. Later measurements employed an axial expansion with a corresponding improvement in signal to noise and measurement uncertainties of <2 kHz with fairly constant line widths of $\sim$ 8 kHz (full width at half height) over the entire range. In both cases a gas mixture of 0.5% OCS, 4% N_2 in Ar was used at 2 atm for the 0.6mm Laser Technics valve and 1atm for the 0.5mm solenoid valve. Further axial expansion measurements were made using 1% OCS, 5% N_2 in neon in order to resolve some of the overlapping Doppler doublets in several congested spectra. An example spectrum is given in figure 5.1 where the Doppler splitting corresponds to a flow velocity of 552.5 m s^{-1} in argon and 767.2 m s^{-1} in neon. The stronger b-type transitions were recorded averaging 2500 pulses, the a-type transitions were approximately a factor of 3 times weaker.

5.3 Results and analysis

Predictions based on the infra-red rotational constants[1] enabled observation of several low rotational state transitions without a search problem. Following the initial measurement of the 0_{00}-1_{11} transition it was not obvious from the hyperfine pattern which nitrogen model was appropriate and predictions for both the tunnelling and inequivalent[11] nitrogen nuclei were compared. The observed splittings for the two lowest $\Delta J=1$, $\Delta K_a=1$ transitions are illustrated in figure 5.2. Most other rotational transitions were observed to be split into two unequal groups of hyperfine patterns which in only a few cases were overlapping. It was found that separate rotational constants could be deduced for each series and that with increasing rotational quantum number J, one series converged to six strong hyperfine components, the other to three strong components (see figure 5.1). The relative spacing in the group of three lines were proportional to tabulated nuclear quadrupole splittings[12] for a nucleus of spin 1 and four of the six line group with a nuclear spin of 2.

The identification of the groups of hyperfine corresponding to different nuclear spin states and separate rotational constants is consistent with the symmetry effects associated with interchange of the N_2 nuclei. The T-shaped structure elucidated by the infra-red analysis is illustrated in figure 5.3 (and 5.7) with the nitrogen nuclei apparently occupying inequivalent positions. Therefore, the case where the nitrogen molecule is free to tunnel through the barrier to internal rotation, exchanging the two nuclei, is most consistent with the features observed in the spectrum.

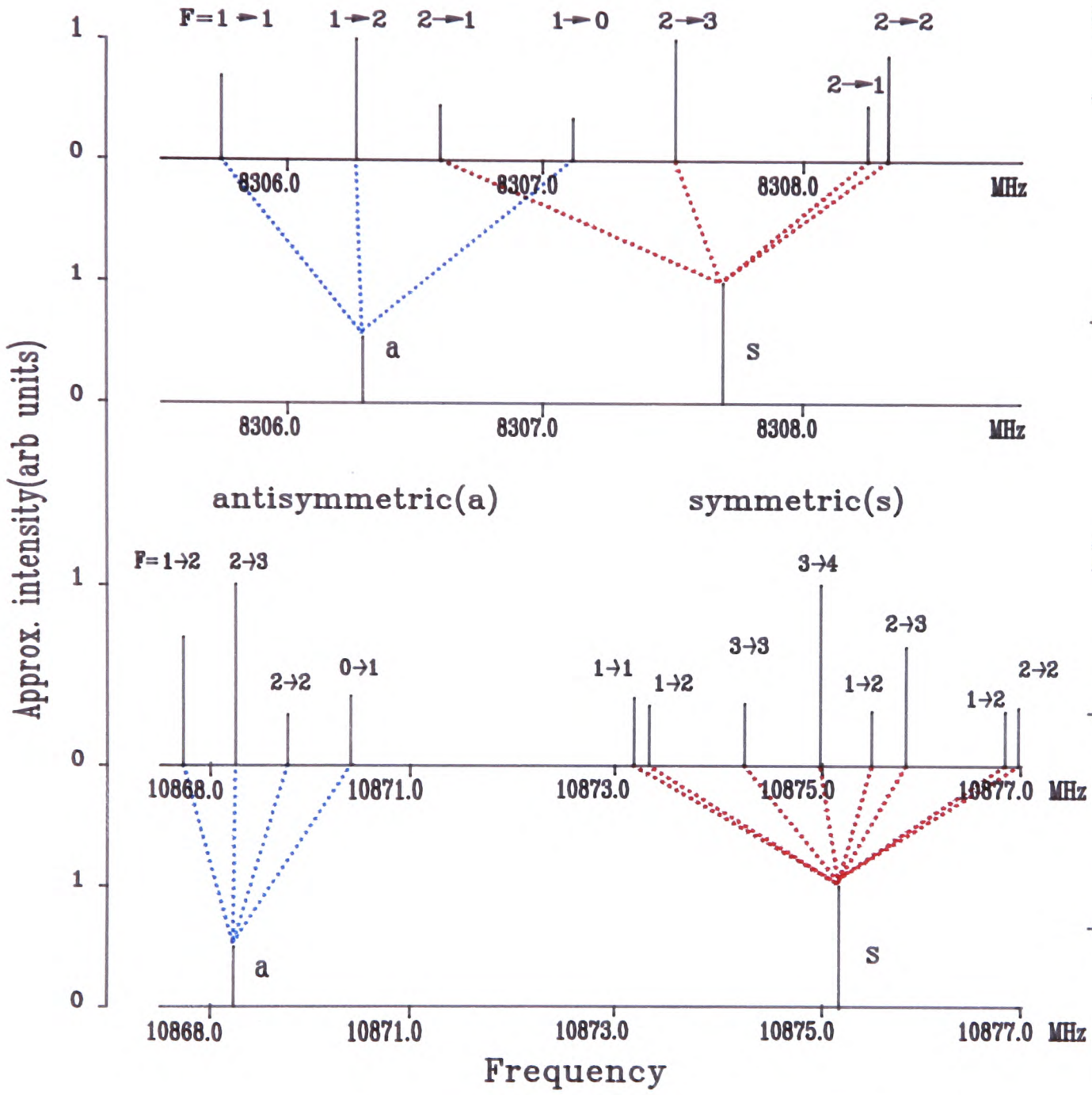

$0_{00} \rightarrow 1_{11}$ transition

- Observed spectrum

- Calculated hyperfineless symmetric/antisymmetric transition frequencies

$1_{01} \rightarrow 2_{12}$ transition

- Observed spectrum

- Calculated hyperfineless symmetric/antisymmetric transition frequencies

Figure 5.2; Assigned hyperfine and tunnelling states for two rotational transitions of N_2–OCS.

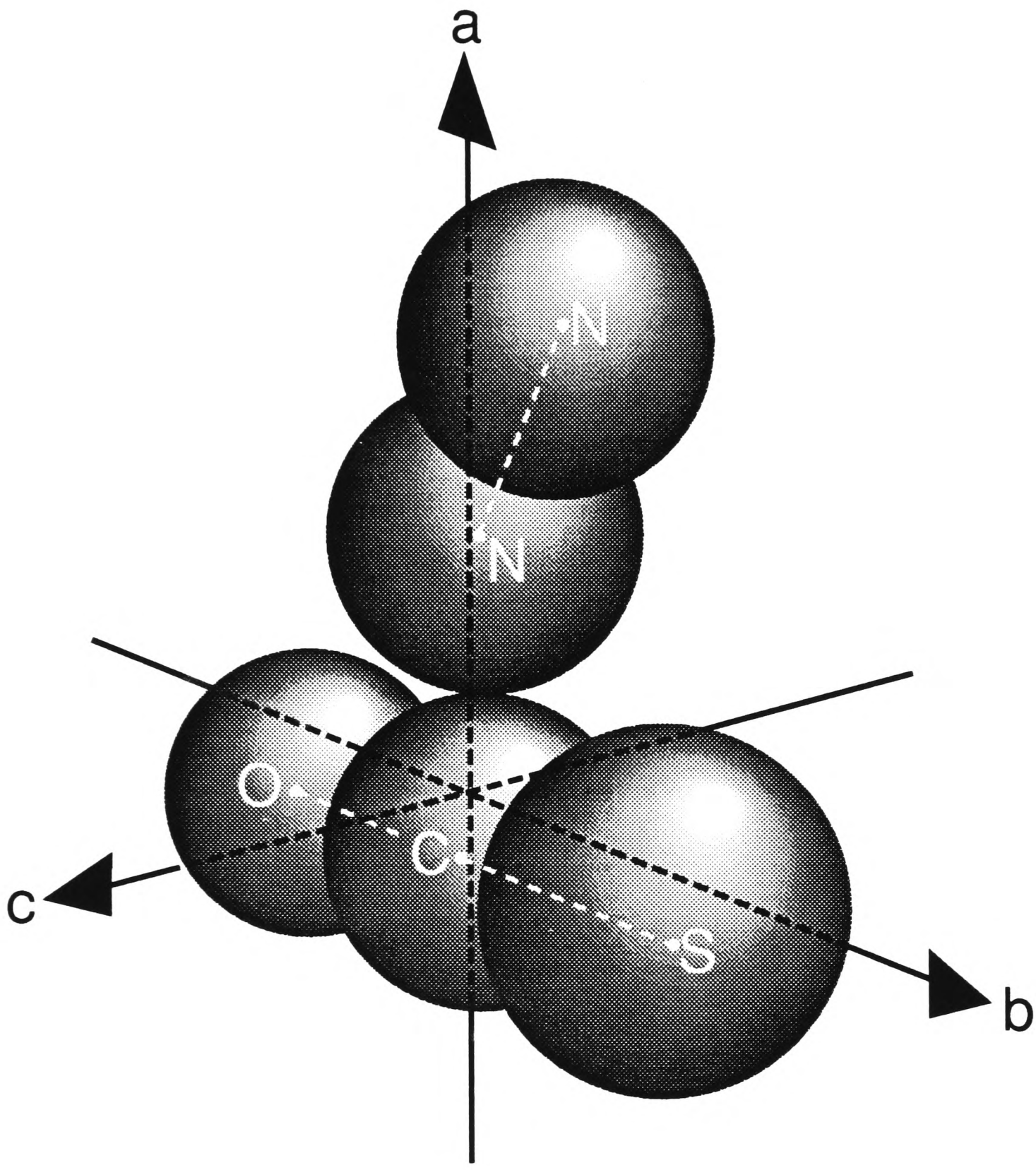

Figure 5.3; Billiard ball model of the N_2-OCS structure in the principal inertial axis system. Spheres based on van der Waals radii (not to scale).

The effect of tunnelling through the barrier to internal rotation is illustrated in figure 5.4. In the presence of a high barrier to inversion of the N_2, the librational wavefunctions corresponding to θ and $\theta+\pi$ orientations of the N_2 are effectively degenerate with no mixing (figure 5.4a). If the barrier is low enough to mix the degenerate nitrogen librational wavefunctions, rotation (inversion) of the nitrogen can occur although with considerably lower frequency than the N_2 monomer rotational frequency. The tunnelling model with the resulting non-degenerate energy levels is illustrated in figure 5.4b. Symmetric, $\psi_+ = \sqrt{1/2}(\phi_1+\phi_2)$, and antisymmetric, $\psi_- = \sqrt{1/2}(\phi_1-\phi_2)$, wavefunction combinations of the unmixed wavefunctions (fig 5.4a ϕ_1, ϕ_2) can be written to express the non-degenerate tunnelling states and the energies can be calculated from the 2 x 2 secular determinant (the same procedure as the mixed nuclear spin states in section 4.3.3, eqn 4.24).

$$\begin{array}{c|cc} & \phi_1 & \phi_2 \\ \phi_1 & E_{rot}-E & \Delta \\ \phi_2 & \Delta & E_{rot}-E \end{array} = 0 \qquad (5.1)$$

$$E_{\pm} = E_{rot} \pm \Delta = E_{rot} \pm \tfrac{1}{2} h\nu_N$$

The split energy levels are given by $E_{\pm}$, where the tunnelling frequency (energy level splitting) is given by $h\nu_N = -2\Delta$. The new states can be associated with slightly different nitrogen angular(θ, fig 5.7) expectation values and correspondingly slightly different rotational constants. An alternative explanation is that on rotation, centrifugal forces change the tunnelling barrier resulting in a change of tunnelling frequency. This effect will be slightly different for the symmetric and antisymmetric states and can be interpreted as different rotational constants for the two symmetry states. Provided the tunnelling frequency is sufficiently large, the effect on the rotational constants will be discernable. This identifies the source of the splitting of the hyperfine pattern into two groups (figure 5.2).

The influence of nuclear spin must also be considered. Using the analysis in section 4.3 and equation 4.5, the nitrogen nuclear spin angular momenta can be coupled together to give a total spin of 2,1 and 0 where, for equivalent nuclei, I=2,0 are symmetric and I=1 antisymmetric spin wavefunctions. Coupling the spin (**I**) with the rotational angular momentum (**J**), the total angular momentum (**F**) can take integral quantum number values J+I to |J-I|. The resulting states are labelled according to symmetry giving three antisymmetric levels (I=1) and six symmetric levels of which only the F=J, I=2,0 levels perturb each other. At high values of J, the strongest transitions are those for $\Delta F = \Delta J$ which leads to three strong antisymmetric and six strong symmetric transitions as observed in the spectrum.

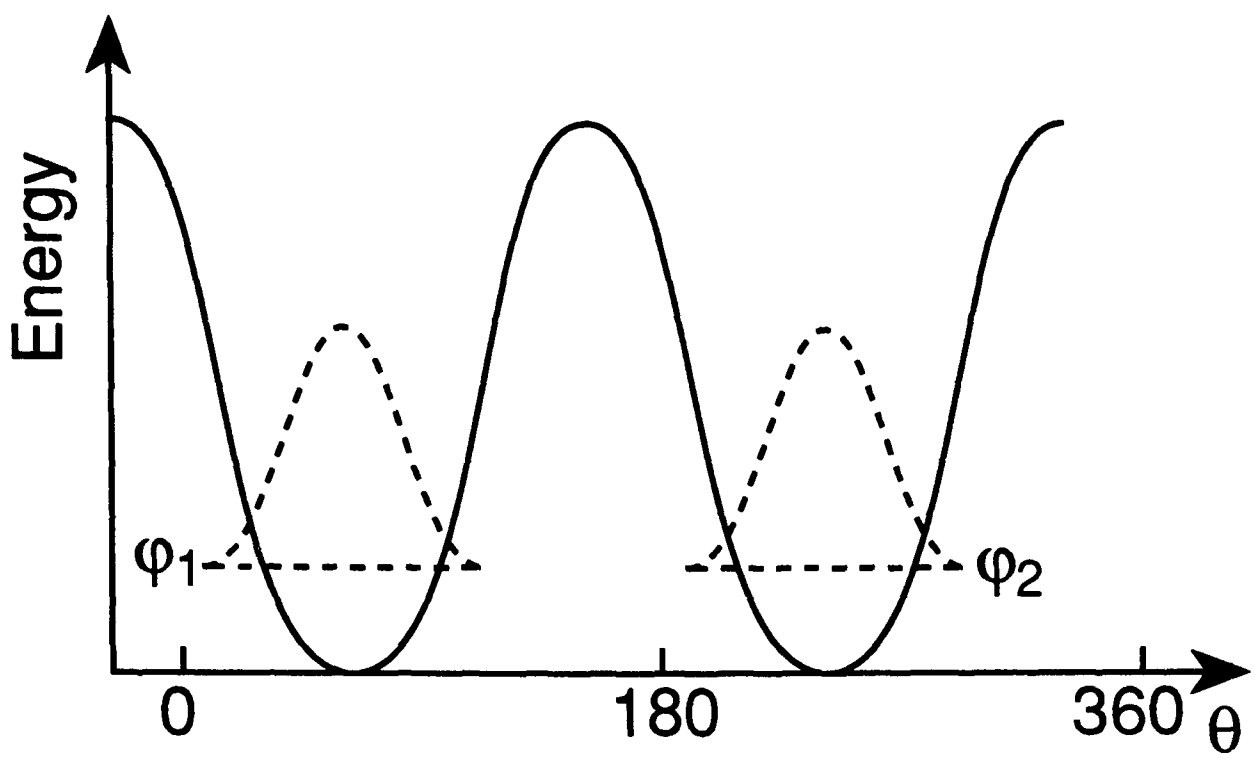

Figure 5.4a; Potential energy diagram for a large barrier to internal rotation of N_2 with negligible tunnelling. φ_1 and φ_2 (indicated by dotted lines) are librational wavefunctions, θ is the angle made by N_2 to the a inertial axis.

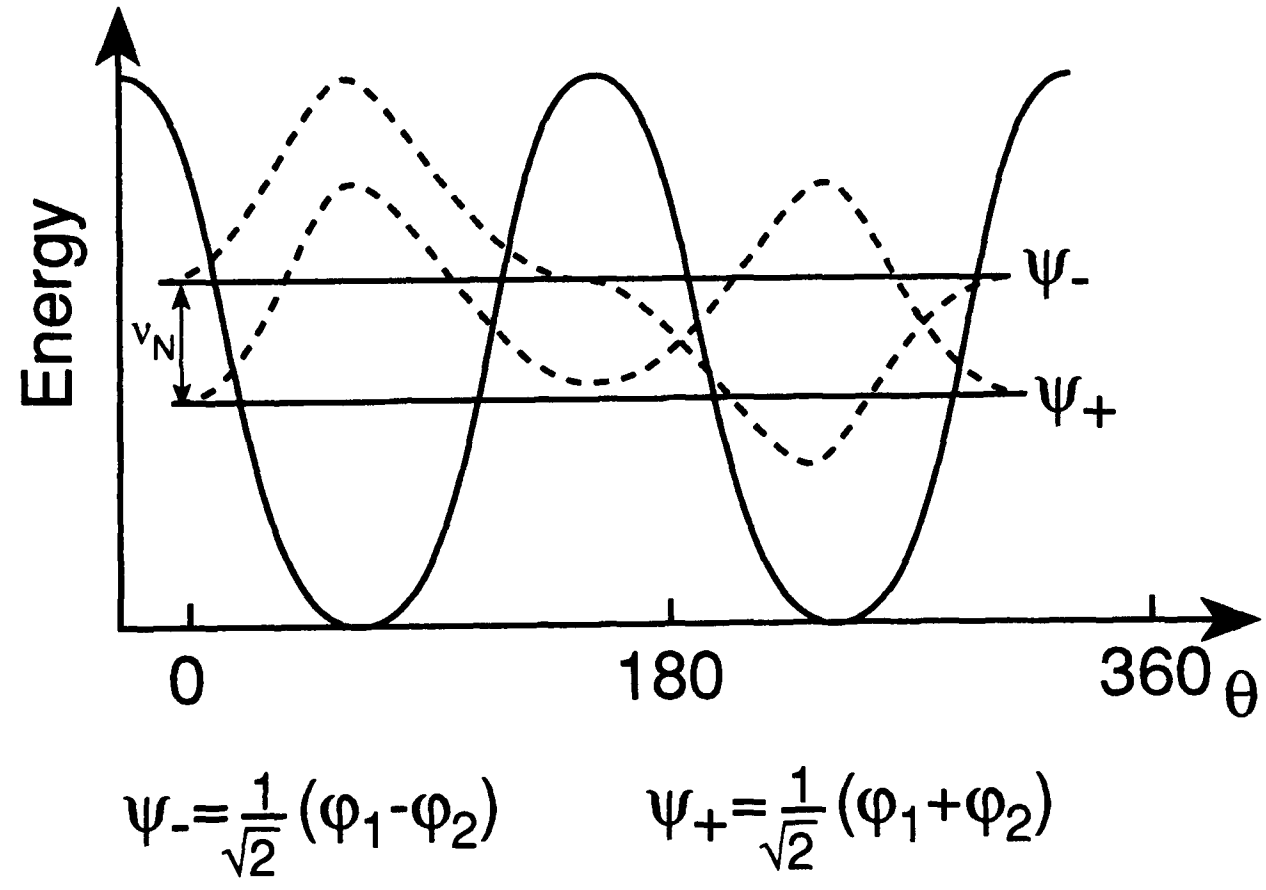

Figure 5.4b; Potential energy diagram with a low barrier to N_2 rotation illustrating the effects of tunnelling. ν_N is the tunnelling splitting, $\psi_\pm$ are tunnelling wavefunctions (indicated by dotted lines).

Exchange of the I=1 nitrogen nuclei requires the total wavefunction to remain symmetric so only combinations of tunnelling and nuclear spin wavefunctions of the same symmetry are allowed. Since the dipole moment operator does not change symmetry during a rotational transition, the allowed transitions are between tunnelling states of the same symmetry. The tunnelling frequency ν_N can not therefore, be measured directly from the microwave spectrum and the two symmetry states are effectively independent. An energy level diagram illustrated in figure 5.5 shows a- and b-type transitions expected for N_2-OCS with the differences in symmetric and antisymmetric rotational constants exaggerated. Combining nuclear spin statistics with the tunnelling effect, rotational transitions with statistical weights of 6 for symmetric and 3 for antisymmetric states are expected. However, the observed hyperfine transitions are reduced in intensity in proportion to the number of resolved splittings, so the relative intensities observed are roughly equal.

Twenty-one a- and b-type rotational transition with 148 symmetric and 75 antisymmetric hyperfine components were observed and are tabulated in appendix II. Hyperfine levels are labelled according to F and I quantum numbers where, when I is even and F=J, I is not a representative quantum number and serves only as a label. Using the notation of equation 4.24, + and - labels are used to indicate which of the ψ_+, ψ_- mixed nuclear spin eigenvectors contributes to the level involved. The symmetric and antisymmetric data sets were fitted separately to a hamiltonian consisting of the semi-rigid I^R Watson S reduction hamiltonian (section 3.3) including sextic H_J, H_{JK} and H_{KJ} centrifugal distortion terms (equation 3.12), the quadrupole hamiltonian for equivalent, coupled nuclei (section 4.3.3) and the spin-rotation hamiltonian (section 4.4). The tables in appendix II include calculated residuals.

Initial residuals for the fit of the symmetric set were found to be much larger than the experimental uncertainty. This was a result of the accidental near degeneracy of the 1_{10} and 2_{02} rotational levels. As discussed in section 4.3.3, the principal axis system of the N_2 quadrupole tensor does not coincide with the N_2-OCS principal inertial axis system except in the out of plane axis so there are off-diagonal tensor components which contribute only in second order to the energy. With the expected structure of N_2-OCS (figure 5.3) confined to the ab plane, symmetry allows only one non-zero off-diagonal coupling constant, in this case χ_{ab}. The second order effects for N_2 are generally expected be very small as a result of the small N_2 molecular quadrupole coupling constant (-5.39 MHz)[6] compared with the rotational energy level spacing and therefore not accounted for initially in the fit. However, the rotational energy splitting between the 1_{10} and 2_{02} levels is $\sim$2.6 MHz. A rough criterion introduced in section 4.3.3 estimated that rotational level separations should be $<$1 GHz for second order effects mixing $\Delta J=1$ or 2 levels to become significant compared with the experimental resolution. Levels separated by less than 1 GHz are listed in table 5.1

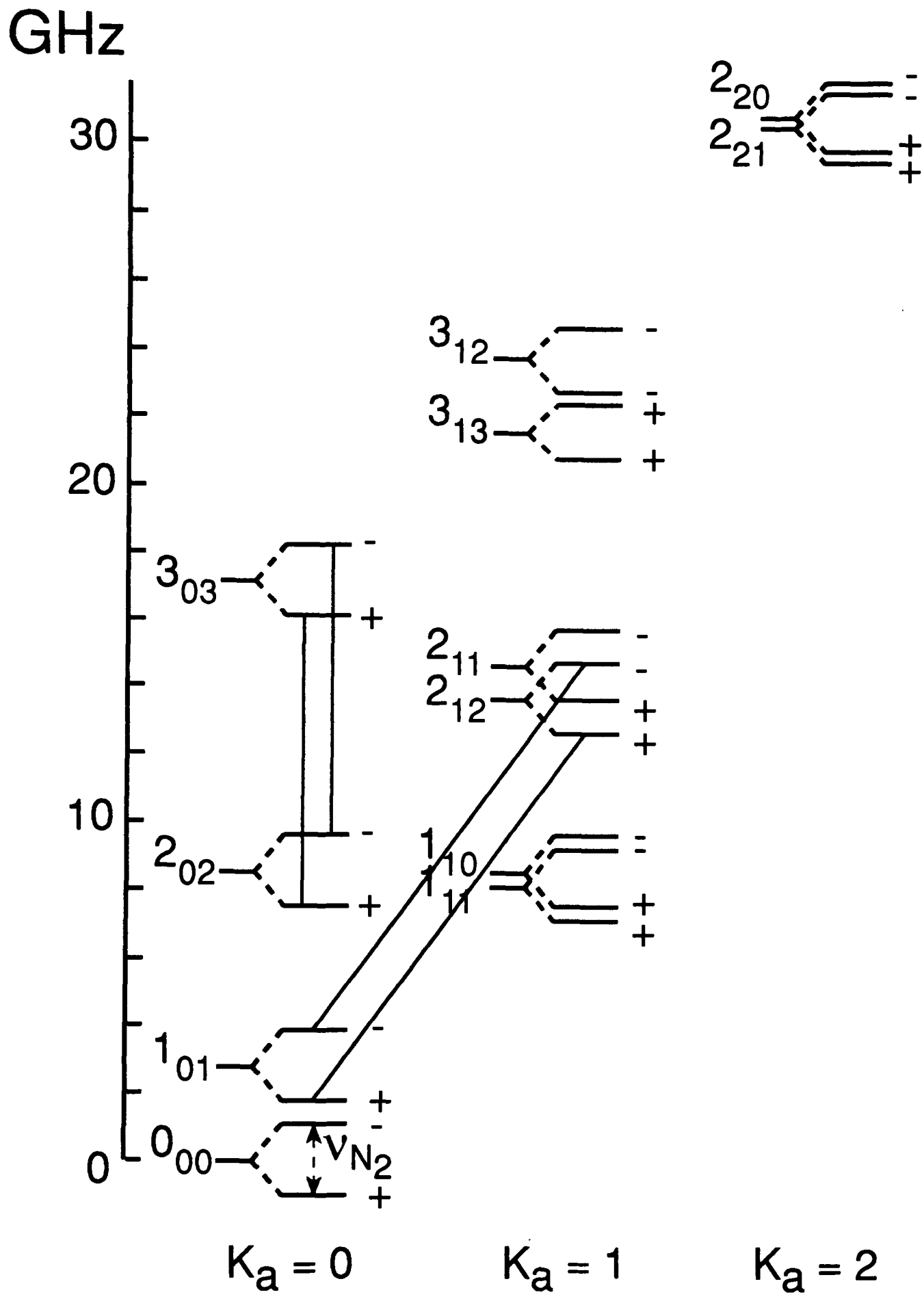

Figure 5.5; Energy level diagram for N_2-OCS showing the effects of tunnelling. Each level is split by the tunnelling frequency, ν_{N2}, where the $\pm$ notation indicates the symmetric(+) and antisymmetric(-) tunnelling states.

Table 5.1; Rotational energy level separations with significant second order quadrupole contributions.

Perturbed rotational levels		Symmetric separation/MHz	ΔE kHz[a]	Antisymmetric separation/MHz	ΔE kHz[a]
1_{10}	2_{02}	2.6	~70	220.2	0.6
4_{22}	5_{14}	346.6	<0.5	422.8	<0.5
4_{23}	5_{14}	160.6	0[b]	241.5	0[b]

[a] ΔE is the largest 2nd order energy correction.
[b] χ_{ac} connecting $\Delta K_a=1$, $\Delta K_c=1$ is zero by symmetry.

The second order effects perturb levels with the same F quantum number differing in J by ± 1 and ± 2. Changes in energy can be calculated using second order perturbation theory by evaluating

$$E_Q^2 = \frac{|\langle J\ K_a\ K_c\ I\ F \mid H_Q \mid J'\ K_a'\ K_c'\ I'\ F \rangle|^2}{E_{J_{K_a K_c}} - E_{J'_{K_a' K_c'}}} \qquad (5.2)$$

E_{JKaKc}-$E_{J'KaKc}$ is the energy separation between unperturbed levels. In addition, the symmetry of χ_{ab} limits perturbations to levels differing by $\Delta K_a=\pm 1$, and $\Delta K_c=0,\pm 2$ (*cf.* similar considerations to the asymmetric top transitions selection rules, section 3.2). The first two pairs of levels in table 5.1 conform to this rule. The explicit matrix elements for perturbed levels given by,

$$\langle J,K_a,K_c,I,F \mid H_Q \mid (J-1),(K_a+1),(K_c-2),I',F \rangle$$

are calculated using equation 4.19 and listed in table 5.2 for the 2_{02}(symmetric) level.

Of the levels listed in table 5.1, only transitions involving the 2_{02} and 4_{22} levels have been observed. With the exception of the 2_{02} F=0 and 4 hyperfine levels which are unperturbed, the 2_{02} hyperfine were removed and the symmetric set refitted. The appropriate unperturbed energy level separations were then calculated and the observed-calculated discrepancies equated with the second order perturbation energy. Only in the case of the symmetric 2_{02} level was the perturbation greater than the final standard deviation of the fit(~2.5 kHz). The effect of the perturbation is illustrated in figure 5.6 and the average values for the observed-uncorrected calculated frequencies for transitions involving the 2_{02} level (transitions to 3_{13}, 3_{03} and 2_{11} levels) are listed in table 5.2.

Perturbed levels in N_2OCS

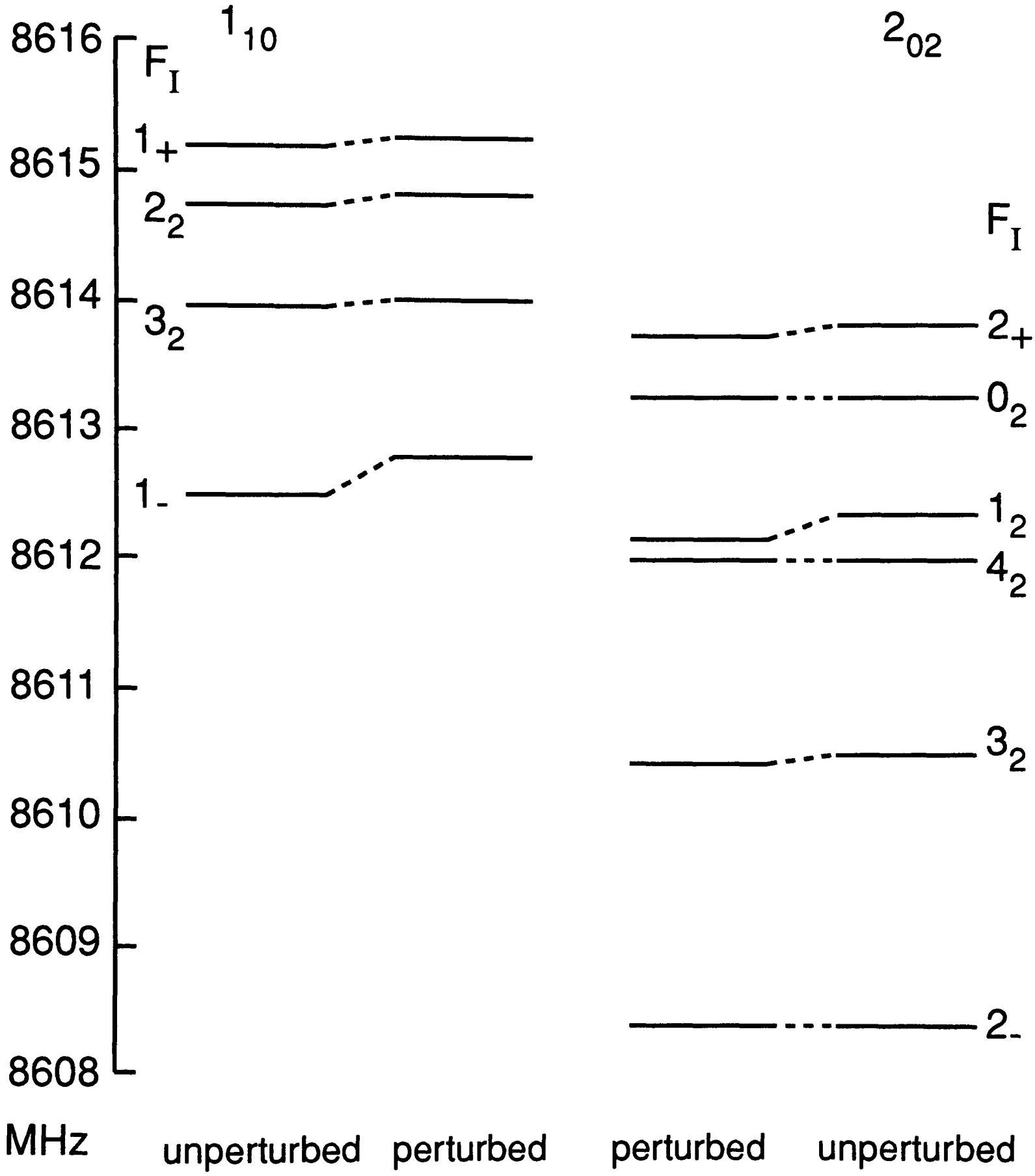

Figure 5.6; Energy level diagram of the perturbed hyperfine levels resulting from the accidental near degeneracy of the symmetric 1_{10} and 2_{02} rotational levels. The labelling system for F and I is detailed in section 4.3.3.

Table 5.2; Observed shifts in the symmetric 2_{02} level due to 2nd order quadrupole interactions

F_1	obs-calc/kHz[b]	matrix element[c]	(calc) χ_{ab} /MHz
1_2	67.1	0.717692	0.551
2_+[a]	41.0	0.531470	0.550
2_-[a]	1.2	0.0698	[d]
3_2	9.3	0.320473	0.562

[a] +,- notation refers to the mixed spin states occurring for I=0,2, J=F. See section 4.3
[b] Standard deviation is 2kHz.
[c] The matrix element is the entire factor multiplying χ_{ab}.
[d] obs-calc less than measurement uncertainty, χ_{ab} not determined.

Using equation 5.2, values of χ_{ab} were calculated for each F_1 level. The discrepancy for the 2_- level is within the standard deviation of the initial data fit and not used. An unweighted average value of χ_{ab} is taken as 0.554 MHz. Using this value, corrections for the symmetric and antisymmetric perturbed transitions were calculated before refitting the data. The second order contribution to the energies of the other levels in table 5.1 is estimated to be <0.5 kHz and assumed negligible.

The parameters obtained by fitting the symmetric and antisymmetric data sets are given in table 5.3. The rotational and nuclear quadrupole parameters are well determined in each case. However, the quality of the fit is not very good; the standard deviations of the symmetric and antisymmetric fits exceeds the experimental uncertainty of ~ 1 kHz. The source of the discrepancies is in fitting the hyperfine transitions, which in some cases give residuals of up to 8 kHz. These effects can not be accounted for by second order, spin-rotation or spin-spin effects, which are expected to contribute by less than 1kHz (sections 4.3.3, 4.4, 4.5). Inclusion of terms for the centrifugal distortion of the quadrupole parameters, of which $D_J^{\chi_{aa}}$ only is well determined, also only account for effects of less than 2kHz. The rapid N_2 tunnelling motions, indicated by the difference in symmetric and antisymmetric rotational constants may give rise to effects not accounted for in the treatment described here. Similar discrepancies are reported by Leung *et al.*[7] for the N_2-H_2O spectrum but with a measurement uncertainty of 4 kHz. However, in N_2-H_2O, the H_2O also undergoes rapid tunnelling. The spectrum of Ar-N_2[4] also gives discrepancies although these can be attributed to inadequacies in the semi-rigid model used to fit the data.

Table 5.3; Fitted Spectroscopic constants of N_2-OCS.

Parameter	Symmetric	Antisymmetric
Rotational constants[a]		
A /MHz	7024.9413(83)	7025.6843(12)
B /MHz	1590.6604(4)	1584.4174(5)
C /MHz	1284.2069(3)	1281.9942(3)
Quartic centrifugal distortion constants[a]		
D_J /kHz	14.886(17)	11.029(19)
D_{JK} /kHz	187.60(12)	207.51(13)
D_K /kHz	1032.05(26)	1034.33(28)
d_1 /kHz	-5.4103(38)	-4.0087(38)
d_2 /kHz	-1.7738(24)	-1.6706(27)
Sextic centifugal distortion constants[a]		
H_J /Hz	0.6(2)	-0.9(3)
H_{JK} /Hz	55.9(40)	89.7(41)
H_{KJ} /Hz	-560(20)	-600(20)
Nuclear quadrupole coupling constants		
χ_{aa} /MHz	-3.5854(12)	-3.6320(17)
$\Delta\chi$ /MHz	0.0478(19)	0.0224(30)
Quadrupole coupling centifugal distortion constants[b]		
$D_J^{\chi aa}$ /kHz	-1.80(67)	[c]
Spin-rotation coupling constants		
C_{aa} /kHz	-0.6(4)	[c]
C_{bb} /kHz	0.94(23)	[c]
C_{cc} /kHz	0.39(17)	[c]
Standard deviation of the fit		
σ /kHz	2.4	2.0

[a] Watson S reduction hamiltonian, I^R representation.
[b] See section 4.3.5 for definition of $D_J^{\chi aa}$. $D_K^{\chi aa}$, $D_K^{\Delta\chi}$ are not determined
[c] Not determined.

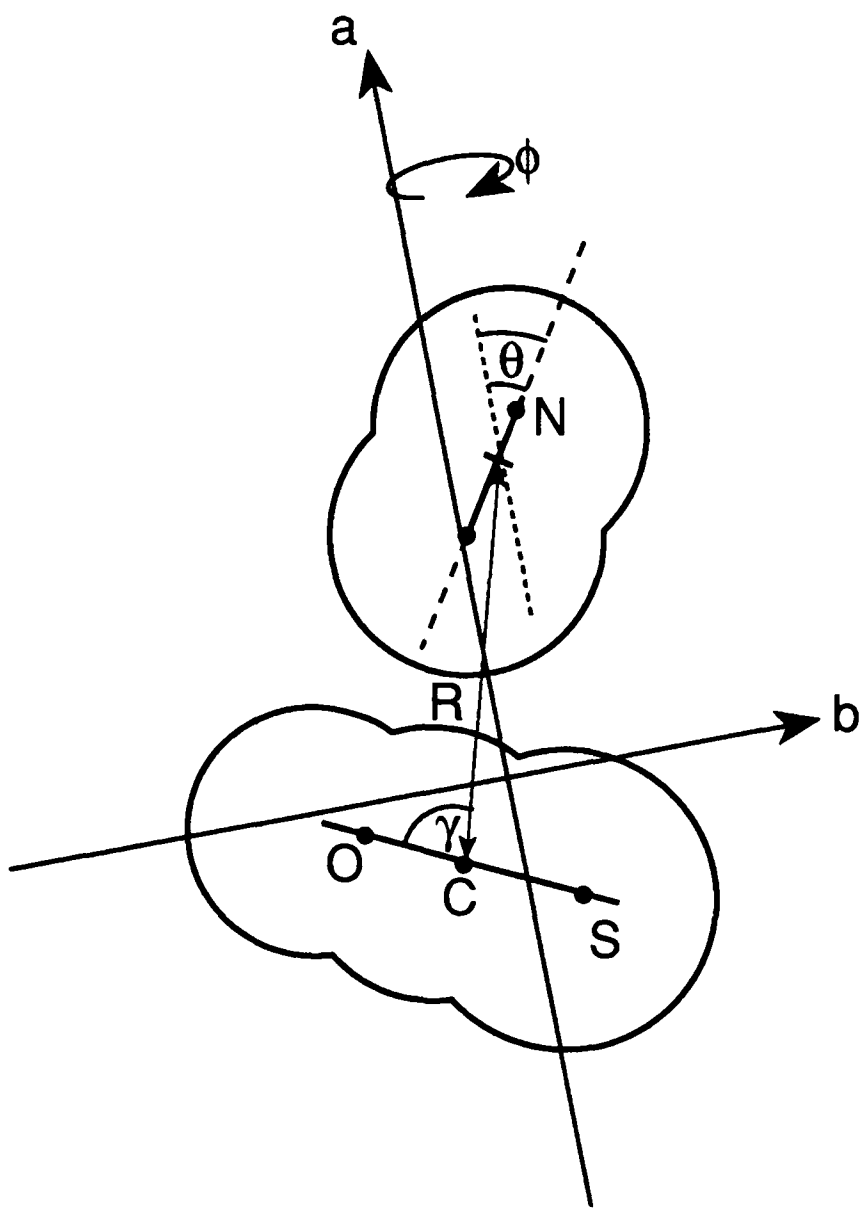

Figure 5.7a; Structural parameters for N_2-OCS

θ is the angle to the a-axis. ϕ is measured from the b axis. R joins the centres of mass.

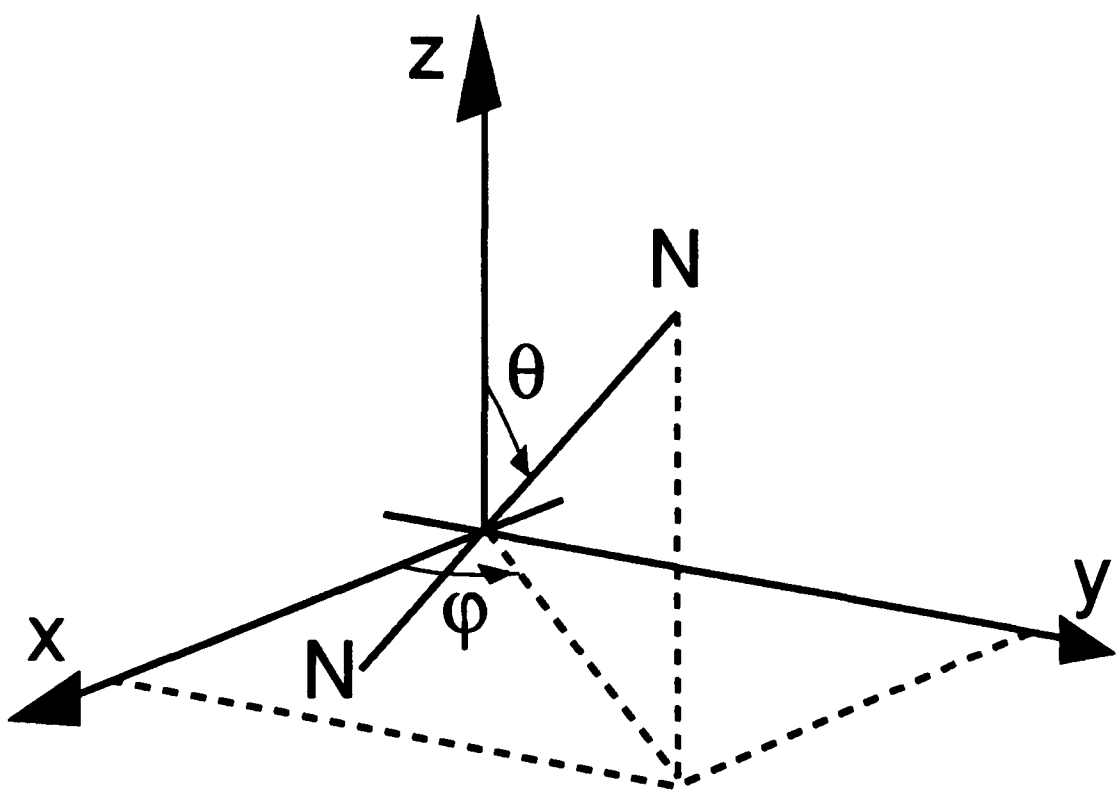

Figure 5.7b; N_2 angular orientation. z,x,y correspond to a,b,c in N_2-OCS.

5.3.1 Structure determination

The rotational constants and the quadrupole coupling constants can be used to deduce the effective structure of N_2-OCS in the ground vibrational state. Figure 5.7 shows the coordinate system employed to determine the N_2-OCS structure. It is assumed that the structures of the monomers are unaffected by complexation. For a planar molecule (in its equilibrium configuration), the inertial defect $\Delta_0 = I_c - I_b - I_a$ will be zero, where $I_{a,b,c}$ are moments of inertia. Deviations from zero arise as a result of using effective moments of inertia which include the effects of wide amplitude motions and Coriolis interactions between the rotations and low frequency bending modes. Generally, the in-plane vibration contribution is positive and larger than the negative out-of-plane contribution, as discussed by Fraser *et al.*[13] for Ar-CO_2. This is confirmed for N_2-OCS by the values of Δ_0, 3.877 u Å^2 for the symmetric and 3.312 u Å^2 for the antisymmetric N_2-OCS inertial defects, which are of the order of those observed for other planar nitrogen complexes N_2-N_2O[3] (Δ_0=2.00 amu Å^2) and N_2-CO_2[2] (Δ_0=2.44 u Å^2). In addition, the absence of observed c-type transitions indicates that the OCS lies close to, or in the ab plane. The small difference between the symmetric and antisymmetric inertial defects suggest a difference in vibrational contribution to internal motions although whether this arises from differences in the in-plane or out of plane effects is not given by the inertial defect.

The nuclear quadrupole coupling constants can be used to obtain information about the angular orientation of the nitrogen molecule relative to the inertial axis system. χ_{aa} can be used directly to deduce the vibrationally averaged angle, θ, between the nitrogen axis and the a inertial axis as in figure 5.7b. The projection of $\chi(N_2)$, the coupling constant of free nitrogen, onto the k inertial axis is given by

$$\chi_{kk} = \frac{1}{2}\left\langle 3\cos^2\theta_k - 1 \right\rangle \qquad (5.3)$$

- kk=a,b or c (as section 4.3.4, equation 4.25).
- The value of the coupling constant in free N_2 is taken as -5.39(5) MHz[6] for consistency with other published data[7,4].

Values for the symmetric and antisymmetric N_2-OCS angles are given in table 5.4. θ_{sym} is smaller than θ_{anti} as might be expected if the difference in A rotational constants is dominated by changes in the nitrogen orientation. For $\Delta\chi$, the projection is averaged over a simultaneous function of θ and ϕ such that $\langle\phi\rangle$ can not be evaluated directly.

The remaining two structural parameters in figure 5.7, R and γ, can be calculated using the derived rotational constants. It should be noted that the values of R and γ calculated in this way are the result of averaging over the zero point stretching motions and are not equilibrium values. R, the separation of the centres of mass of nitrogen and OCS in figure 5.7 can be calculated by assuming that the moments of inertia of the monomers are unchanged on complexation and using the out of plane moment of inertia I_C given by,

$$I_C = I_{N_2} + I_{OCS} + \mu R^2 \qquad (5.4)$$

- I_{OCS} is the moment of inertia of OCS (B_0(OCS) = 6081.49247(8) MHz[14], I_{OCS} = 83.1011 u Å^2)
- I_{N2} is the moment of inertia of nitrogen, ($B_0(N_2)$ = 59.64615(1) GHz[15], I_{N2} = 8.4733 u Å$_2$)
- $\mu = (m_{OCS}.m_{NN})/(m_{OCS}+m_{NN})$, is the reduced mass of an equivalent diatomic with point masses equal to OCS and N_2.

Values of R calculated for the symmetric and antisymmetric tunnelling state structures are given in table 5.4.

The angular dependence of the OCS, γ, is calculated by removing the contribution of nitrogen to each moment of inertia and then treating the problem as an atom-linear molecule system[16]. Since the averaged projections of the nitrogen quadrupole on to each inertial axis are known, new rotational constants A′,B′ and C′ are defined by subtracting projections of the nitrogen moment of inertia from the N_2-OCS moments of inertia. I_A', I_B' and I_C' are defined by,

$$I_k = I_k' + I_{N_2}\sin^2\theta_k \qquad (5.5)$$

where k= a,b or c and I_{N2} is the nitrogen moment of inertia. Using values for χ_{cc} of 1.7688 MHz for symmetric and 1.8048 MHz for antisymmetric states (calculated from corresponding χ_{aa} and $\Delta\chi$), $\sin^2\theta_c$ is obtained from equation 5.3. Adjusted moments of inertia for I_A' and I_C' are obtained from equation 5.5 and the problem becomes analogous to Ar-OCS where the argon mass is replaced by the mass of N_2. The OCS angle to the line joining the centres of mass(R) is then given by[15],

$$\sin\gamma = \frac{b_{OCS}}{A'}\left\{\frac{C'-A'}{C'-b_{OCS}}\right\}^{\frac{1}{2}} \qquad (5.6)$$

Although the structure is planar and hence only two rotational constants are independent, discrepancies arise due to the inertial defect. Of the three possible combinations of moments of inertia, I_C and I_A are chosen to minimize the effect of the motions of the nitrogen on the structure determination. The out of plane vibrational contribution is less than the in-plane contribution as indicated by the inertial defect and I_A is a less sensitive function of the nitrogen moment of inertia than I_B. Values of γ for the symmetric and antisymmetric constants are given in table 5.4.

Table 5.4; Effective structural parameters of N_2-OCS.

Parameter[a]	Symmetric	Antisymmetric
R /Å	3.9770	3.9815
θ /°	26.08	25.64
γ^c /°	69.89 (110.11)	69.92 (110.08)
$\phi^{b,c}$ /°	0.0 180.0	0.0 180.0

[a] Parameters defined in figure 5.4
[b] Constrained
[c] Two possible angles

The structural parameters and quadrupole constants indicate that the symmetric and antisymmetric states have slightly different averaged nitrogen orientations. Reasons for this can be related back to angular expectation values of the tunnelling wavefunctions, illustrated in figure 5.4. The symmetric tunnelling wavefunction (fig 5.4, ψ_+) is the sum of the librational basis functions and therefore has a finite probability for the orientation of N_2 at 90° to the minimum energy position. In contrast, the antisymmetric wavefunction has a node at this point and hence has a reduced probability of assuming angles approaching rotation of N_2 by 90°. This effect is manifested in the structure by the nitrogen in the antisymmetric state having a smaller vibrationally averaged angular expectation value indicated by the values of θ. As θ_s is larger, the nitrogen can adopt a more parallel, closer configuration with the OCS than the antisymmetric structure, which also accounts for the smaller centre of mass separation (R) deduced for the symmetric state. The deduced N_2 centre of mass (c.m.)-OCS c.m.-C angles, γ, also correspond to this model although little significance can be attributed to the small difference between γ_S and γ_A. Similar trends are observed in the centrifugal distortion constants. Most clearly illustrated is the effect on D_K where the increase in the angular momentum along the a axis and consequently the change in N_2 angle with respect to the a-axis is realized as a greater stiffness or bending force constant for the asymmetric van der Waals bend.

Without additional data from isotopically substituted N_2-OCS complexes, the structural analysis presented can not determine the absolute ϕ and γ angles. As a consequence, four possible structures can be proposed. Two structures corresponding to $\gamma=110°$ with the sulphur end of OCS tilted towards N_2 can be considered less likely on the basis of avoiding overlap of the estimated S and N van der Waals radii. With $\gamma=110°$, the N_2 centre of mass(c.m.)-S distance is 3.75 Å compared with the estimated sum of van der Waals radii of 3.7-3.9 Å and the 3.893(3)Å N_2 c.m.-SO_2 c.m. separation reported for N_2-SO_2[17]. γ is therefore expected to have the value 69.89° corresponding to a N_2 c.m.-S distance of 4.44Å . This result is also consistent with the structures of Ne-OCS ($\gamma=70.4(6)°$) and Ar-OCS ($\gamma=73.3(7)°$) where isotopic data[18] has been used to determined the absolute value of γ. There is no information available from the rotational constants to determine the nitrogen ϕ angle although the assumption of a symmetry plane confines ϕ to 0 or 180°. Similarly, the $\Delta\chi$ quadrupole coupling constant which is sensitive to ϕ is a periodic function over 180° (equations 4.25) and therefore does not distinguish the two values of ϕ.

5.3.2 The tunnelling potential

The symmetric and antisymmetric tunnelling states sample different parts of the angular potential experienced by the nitrogen molecule in the N_2-OCS complex. Since the nuclear quadrupole coupling constants are determined directly by the N_2 angular orientation and averaged motions within the complex, as discussed in section 4.3.4, they can be used to calculate the form of a parameterized angular potential describing the tunnelling motions.

A rotational hamiltonian accounting for internal rotation of the nitrogen molecule in a potential $V(R,\theta,\phi)$ due to a fixed orientation of OCS (parameters defined in figure 5.7) is given by,

$$H_{rot} = A'(J_a-j_a)^2+B'(J_b-j_b)^2+C'(J_c-j_c)^2+b_{N_2}j^2+V(R,\theta,\phi) \qquad (5.7)$$

- The hamiltonian refers to the body fixed inertial axis system of figure 5.3 defining the internal coordinates R,θ,γ and ϕ.
- $\mathbf{J}_{a,b,c}$ are components of the total angular momentum
- $\mathbf{j}_{a,b,c}$ are components of the angular momentum of the nitrogen molecule, $\mathbf{j}$, about the a,b,c principal inertial axes.
- A',B',C' are the rotational constants of the complex given in equation 5.5 and are functions of R,θ,γ and ϕ
- b_{N2}, the rotational constant of the nitrogen molecule, is 59.64615 GHz[15].

In the limit of a vanishingly small potential, $V(R,\theta,\phi)$, equation 5.7 becomes an expression for free rotating nitrogen within the N_2-OCS complex (OCS has fixed orientation). When the potential becomes large, the nitrogen couples strongly to the intermolecular axis and equation 5.7 reduces to an effective semi-rigid rotor hamiltonian as has been used to fit the experimental data. To calculate the form of the tunnelling potential, the rotational hamiltonian can be simplified. By expanding equation 5.7, the rigid rotor hamiltonian of the complex (equation 3.1) can be separated out. Cross terms such as $\mathbf{J}_a\ \mathbf{j}_a$ describing the Coriolis interaction are assumed to be small and neglected. The remaining terms define the tunnelling hamiltonian,

$$H_{tunnel} = (Aj_a^2+Bj_b^2+Cj_c^2) + bj^2 + V(R,\theta,\phi) \tag{5.8}$$

To a first approximation, the contribution due to the first term, with products of expectation values of $\mathbf{j}$ about the inertial axes and rotational constants, is taken to be small compared with the second term and neglected.

The general potential $V(R,\theta,\phi)$ is written as a function of all the internal coordinates defined in figure 5.7. Using the Born-Oppenheimer angular radial separation method discussed by Holmgren *et al.*[19], the radial dependence (R) can be separated from the angular degrees of freedom. Small differences in the symmetric and antisymmetric tunnelling state intermolecular distances are observed, $\Delta R = 0.0045$ Å where $R_{av} = 3.979$ Å so the tunnelling motion is assumed to involve small changes in the intermolecular separation about the vibrationally averaged equilibrium separation. However, no radial potential information is available so a limiting condition of no radial motion is assumed. A further simplification is to neglect the tunnelling angular dependence on changes in the OCS angle, γ. The angular tunnelling potential $V(\theta,\phi)$ can then be conveniently expanded as a sum of renormalized spherical harmonics C_{lk} to simplify the form of potential matrix elements between the angular momentum eigenfunctions.

$$V(\theta,\phi) = \sum_{l,k} V_{lk}C_{lk}(\theta,\phi)$$
$$C_{lk}(\theta,\phi) = \left(\frac{4\pi}{(2l+1)}\right)^{\frac{1}{2}} Y_{lk}(\theta,\phi) \tag{5.9}$$

- Y_{lk} are the spherical harmonics (equivalent to normalized diatomic rotational wave functions).
- V_{lk} are potential coefficients to be determined using the experimentally determined nuclear quadrupole parameters. By symmetry, $V_{lk} = V_{l,-k}$

- The orientation of the nitrogen molecule with respect to the a axis is given by θ and rotation in the bc plane by ϕ from the b axis as in figure 5.7b
- k can take integer values between l and $-l$ where l is the order of the spherical harmonic.

The potential must reflect the cylindrical symmetry about the OCS axis which precludes l from assuming odd values. Rotation by 180° of C_{lk} where l is odd results in a change in sign although the energy of the system must remain indistinguishable and hence the contribution from odd l must be zero. This can be easily understood in the case of $l=1$ which has analogous angular form to p atomic orbitals. The potential has therefore assumed an angular form directly comparable with the quadrupole coupling constant projections in section 4.3.4, equation 4.25. The V_{00} term affects the total energy and is not determined by this calculation. V_{2k} terms have analogous angular dependencies to the quadrupole coupling constants and also to d atomic orbitals with varying factors. As a result, the four observed nuclear quadrupole coupling constants are used to fit the three potential terms V_{2k}. In general only the first few terms of a potential expansion are significant unless the potential is very anisotropic so further expansion in terms of l to V_{4k} and higher are neglected. The small value of $\Delta\chi$ indicates a high degree of isotropy in the ϕ coordinate.

The tunnelling hamiltonian given by equation 5.8 with the potential expressed according to equation 5.9 is evaluated by constructing a matrix using $|\, j,m \,\rangle$ rotational basis functions. The projection of nitrogen molecule angular momentum **j** onto the a inertial axis of the complex is labelled by the m quantum number. Matrix elements are given by[20],

$$\langle j'm' \mid bj^2 \mid j\ m \rangle + \sum_{lk} V_{lk} \langle j'm' \mid C_{lk} \mid j\ m \rangle =$$

$$bj(j+1)\delta_{j'j} + (-1)^{m'}\left[(2j'+1)(2j+1)\right]^{\frac{1}{2}} \begin{pmatrix} j' & l & j \\ -m' & k & m \end{pmatrix} \begin{pmatrix} j' & l & j \\ 0 & 0 & 0 \end{pmatrix} \tag{5.10}$$

- $\delta_{j'j}$ is the Kronecker delta.
- The product of three-j symbols (:::) is non zero only when k = m′-m and j′+j+l = even integer and satisfies the triangle conditions[20].
- V_{2k} terms mix states differing in j by ± 2 and m by 0, ± 1 and ± 2.

The hamiltonian matrix is diagonalized to obtain the energy levels and eigenvectors. The two lowest energy levels correspond to the symmetric and antisymmetric tunnelling states with the separation equal to the tunnelling frequency, ν_N.

Expectation values for the symmetric quadrupole coupling constants are calculated using the corresponding symmetric eigenvector (lowest energy) by,

$$\frac{\chi_{aa}^{sym}}{\chi_{N_2}} = \sum_{-m}^{m} a_m a_m \langle\, 0,m \mid C_{2,0} \mid 0,m \,\rangle$$

$$\frac{\Delta\chi^{sym}}{\chi_{N_2}} = \sqrt{\frac{3}{2}} \sum_{-m}^{m} a_{m\pm2} a_m \langle\, 0,m\pm2 \mid C_{2,2} + C_{2,-2} \mid 0,m \,\rangle \qquad (5.11)$$

$$\frac{\chi_{ab}^{sym}}{\chi_{N_2}} = \sqrt{\frac{3}{2}} \sum_{-m}^{m} a_{m\pm1} a_m \langle\, 0,m\pm1 \mid C_{2,-1} - C_{2,1} \mid 0,m \,\rangle$$

a_m are the eigenvector coefficients. An identical procedure using the antisymmetric eigenvector gives the antisymmetric tunnelling state quadrupole coupling constants. Using a computer program to carry out a least squares fitting procedure, the $V_{2,0}$, $V_{2,1}$ and $V_{2,2}$ potential parameters have been fitted to the symmetric and antisymmetric quadrupole coupling constants (table 5.3). The basis set must include enough functions to achieve reasonable convergence of the eigenvalues. Convergence of the angular expectation values to within the experimental standard deviation was achieved with a set with basis functions $|j\ m\rangle$ in j up to 10. The results of the least squares fit of χ_{aa}, $\Delta\chi$ and χ_{ab} to the three parameter potential are given in table 5.5. Residuals are given in appendix II. χ_{ab} was down weighted by a factor of 100 with respect to the better determined, least squares values of χ_{aa} and $\Delta\chi$ which were weighted according to standard deviation.

Table 5.5; Least squares fitted potential parameters

Parameter	
V_{20} / cm^{-1}	-28.47(24)
V_{21} / cm^{-1}	1.93(36)
V_{22} / cm^{-1}	2.05(55)
ν_N / MHz	2983

Numbers in parenthesis are correspond to one standard deviation

Discussion.

The potential coefficients, $V_{2,k}$ are coefficients of angular functions which are analogous to the d atomic orbitals, as discussed in section 4.3.4. This allows the contribution of each angular function to be easily visualized. $V_{2,0}$ determines the N_2 projection along the a-inertial axis and is the main contribution to the barrier to rotation. Therefore, $V_{2,0}$ gives the approximate value of the barrier to internal rotation of the nitrogen. This is modified by the $V_{2,1}$ angular function which projects the nitrogen between the a and b axes. The sign of χ_{ab}, with the same angular form as $V_{2,1}$, is not determined in the second order analysis (equation 5.2) of the perturbed 2_{02} hyperfine transitions and the sign of the potential parameter $V_{2,1}$ is also not determined. Isotopic substitution, for example with ^{18}OCS or $OC^{34}S$, would result in a rotation of the complex with respect to the a- and b-axes, changing the nitrogen projections. This would be sensitive to the sign of χ_{ab} provided a significant second order effect is maintained. Isotopic substitution of the N_2 would not be very informative. Replacement by $^{15}N_2$ gives no hyperfine structure and any comparison of tunnelling motions must presume a radial dependence of the potential which has been ignored in the analysis presented here. $V_{2,2}$ determines the anisotropy with respect to projections in the bc plane and shows only a small effect for N_2-OCS.

The microwave study of N_2-OCS has several advantages over the previous infra-red experiment[1]. The higher resolution of the microwave experiment, ~ 6kHz, compared with the infra-red, ~ 10 MHz allows the hyperfine effects to be resolved, providing the additional data necessary to determine the four structural parameters (figure 5.4). The tunnelling effects on the rotational constants are well resolved and may provide the reason for problems reported with fitting the infra-red data satisfactorily[1]. Given the differences in rotational constants, at values of J typical of the supersonic expansion, the infra-red lineshape may distort significantly as the lines due to the two symmetry transitions begin to resolve.

There are few reported spectra which show comparable internal motions to the N_2 in N_2-OCS. Other than rare gas-molecule complexes, most complexes reported with tunnelling motions involve concerted or geared tunnelling motions, often accompanied by changes in the dipole moment operator parity, and with higher symmetry than in N_2-OCS. A similar treatment of hindered internal rotation of a molecule in a complex is reported by Hutson for Ar-H_2O[21]. A more extensive treatment of $(C_2H_2)_2$[22], which exhibits a geared tunnelling motion, has deduced a tunnelling frequency of 2.2 GHz and a barrier to the internal motion of ~ 33cm^{-1}.

References

[1]M. Baker, *Part II Thesis,* Oxford University, 1988.

[2]M. A. Walsh, T. R. Dyke, B. J. Howard, *J. Mol. Struct.*, **189**, 111 (1988).

[3]R. W. Randall, T. R. Dyke, B. J. Howard, *Faraday Diss. Chem. Soc.*, **86**, 21 (1988).

[4]W. Jäger, M. C. L. Gerry, *Chem. Phys. Lett.*, **196**, 274 (1992).

[5]A. C. Legon, P. W. Fowler, *Z. Naturforsch.*, **47a**, 367 (1991).

[6]T. A. Scott, *Phys. Rep. C,* **27**, 89 (1976).

[7]H. O. Leung, M. D. Marshall, R. D. Suenram, F. J. Lovas, *J. Chem. Phys.*, **90**, 700 (1989).

[8]G. T. Fraser, D. D. Nelson, K. I. Peterson, W. Klemperer, *J. Chem. Phys.*, **84**, 2473 (1986).

[9]F. J. Lovas, *J. Phys. Chem. Ref. Data,* **7**, 1445 (1978).

[10]A. D. Buckingham, P. W. Fowler, *Canad. J. Chem.*, **63**, 2018 (1985).

[11]S. Duxon. *Part II Thesis,* Oxford University 1990.

[12]C. H. Townes, A. L. Schawlow, *Microwave Spectroscopy,* Dover, New York, 1975.

[13]G. T. Fraser, A. S. Pine, R. D. Suenram, *J. Chem. Phys.*, **88**, 6157 (1988).

[14]A. G. Maki, *J. Phys. Chem. Ref. Data,* **3**, 221 (1974).

[15]K. P. Huber, G. Herzberg, *Molecular Spectra and Structure, Constants of Diatomic Molecules,* Van Nostrand, New York, 1979.

[16]G. D. Hayman, J. Hodge, B. J. Howard, J. S. Muenter, T. R. Dyke, *Chem. Phys. Lett.*, **118**, 12 (1985).

[17]Y. D. Juang, M. A. Walsh, A. K. Lewin, T. R. Dyke, *J. Chem. Phys.*, **97**, 832 (1992).

[18]F. J. Lovas, R. D. Suenram, *J. Chem. Phys.*, **87**, 2010 (1987).

[19]S. L. Holmgren, M. Waldman, W. Klemperer, J. Chem. Phys. **67**, 4414 (1977); *ibid.* **69**, 1661 (1978).

[20]R. N. Zare, *Angular Momentum,* Wiley Interscience, New York, p103, 1988.

[21]J. M. Hutson, *J. Chem. Phys.*, **92**, 157 (1990).

[22]G. T. Fraser, R. D. Suenram, F. J. Lovas, A. S. Pine, J. T. Hougen, W. J. Lafferty, J. S. Muenter, *J. Chem. Phys.*, **89**, 6028 (1988)

Chapter 6

The microwave spectrum of N_2-O_3 and N_2-SO_2

6.1 Introduction

The N_2-OCS study established that the nitrogen moiety was able to tunnel with an estimated frequency of ~3 GHz. It would be of interest to develop this type of behaviour further and study complexes of nitrogen where the partner to the nitrogen is non-linear and also demonstrates a propensity to undergo rotation-tunnelling. In addition to the many complexes of H_2O which show tunnelling effects as exemplified by N_2-H_2O[1], a number of SO_2 and a few O_3 complexes have spectra influenced by internal motions. This is largely due to the small moment of inertia about the monomer a-axis which for SO_2 (I_A = 8.315093 u Å^2, A = 60778.516 MHz)[2] is comparable to the N_2 moment of inertia (I_{N2} = 8.4729 u Å^2, A = 59646.15 MHz)[3], and considerably smaller for O_3 (I_A = 4.7438 amu Å^2, A = 106534.53 MHz)[2]. As a result, large amplitude motions about the corresponding axis in complexes may culminate in tunnelling motions. The tunnelling frequencies of Ar-O_3 and Ar-SO_2 have been measured directly in the microwave spectrum[4] to be 463 MHz and 975 MHz[5] respectively. The tunnelling potential in Ar-SO_2 has been modelled using infra-red data[6], giving a barrier to tunnelling of 80.32 cm^{-1}. A number of complexes of SO_2 have also been observed demonstrating simultaneous or geared tunnelling motions and internal rotation; $(SO_2)_2$[7] and H_2O-SO_2[8] complexes show geared tunnelling effects. Although the internal motions of C_2H_4-SO_2[9] are largely attributed to internal rotation of the C_2H_4, there is some isotopic evidence to suggest that SO_2 motions may also contribute.

Microwave studies of complexes of SO_2 with substituted amines[10] and HCN[11] have established that the HCN or amine symmetry axis aligns approximately 90° to the SO_2 plane with the nitrogen closest to the sulphur. This can be interpreted either as a result of the nitrogen behaving like a nucleophile and aligning with the electrophilic sulphur and necessarily implies a strong intermolecular bond, or in terms of weaker electrostatic interactions more appropriate to van der Waals complexes. The former model is quite reasonable in the case of the substituted amines where a charge transfer complex is formed. However, in neither study is there indication of SO_2 tunnelling which would appear as a tunnelling splitting directly measurable from the b or c-type spectrum. A recent infra-red and limited MBER study of N_2-SO_2 by Juang *et al.*[12] deduced a structure for

N_2-SO_2 analogous to that of HCN-SO_2. Rotational constants, one quadrupole coupling constant and approximate dipole moment projections for N_2-SO_2 were also given. No evidence of a tunnelling splitting was observed in the infra-red experiment which limits any possible tunnelling frequency to less than the 10 MHz experimental resolution. The MBER study was too limited to deduce any direct contribution of the SO_2 tunnelling frequency or centrifugal distortion effect of the nitrogen tunnelling motion on the rotational constants, which would lead to analogous grouping of the hyperfine transitions to those observed in the N_2-OCS complex.

Fewer complexes of ozone have been studied by microwave spectroscopy although several analogous ozone and SO_2 complexes show contrasting behaviour in internal motions and structure. In complexes with H_2O, the ozone complex[13] exhibits a concerted tunnelling motion where the O_3 and H_2O monomer planes are perpendicular. In contrast, the H_2O-SO_2 complex[8] has a structure with the monomers coplanar and no observable concerted tunnelling motions. This can be compared with the Ar-O_3 and Ar-SO_2 complexes where the Ar-O_3 complex has the lower tunnelling frequency, a result that is somewhat anomalous if similar internal motions and tunnelling potential are assumed for each complex. It is expected that the H_2O-O_3 complex provides the closest model to the internal motions of the N_2-O_3 and N_2-SO_2 complexes although much higher frequency motions will be associated with the H_2O. The N_2-O_3 complex is expected to be quite similar to N_2-SO_2 although probably with a weaker van der Waals interaction as a result of the smaller ozone dipole moment($\mu(O_3)$ 0.5324(24)D, $\mu(SO_2)$ 1.634(1) D)2.

6.2 Experimental

The apparatus described in chapter 2 employing an axial expansion was used to record the spectra of N_2-O_3 and N_2-SO_2 between 6 and 18 GHz. Ozone was prepared by flowing dried oxygen through a cold silent ac discharge apparatus and then condensed in a glass cold finger at -195 °C (liquid N_2) to give approximately 0.25ml samples of pure ozone. Conversion of oxygen to ozone was less than $\sim 10\%$ efficient so care was taken to avoid condensing oxygen during the preparation by continuously pumping with a rotary vacuum pump. In order to generate gas mixtures suitable for the experiment without decomposition of the ozone on metal surfaces, a glass and teflon gas line was used. A 5% mixture of N_2 in argon at 1.5 atmospheres was passed over the ozone sample maintained at -160 °C using an isopentane / liquid nitrogen slush bath. This provided a <20 torr partial vapour pressure of ozone[14] corresponding to a $\sim 2\%$ O_3/ 5% N_2 in argon mixture behind the 0.5mm solenoid nozzle.

N_2-O_3 spectra were collected using 250 μs gas pulses at a repetition rate of 30 Hz. C-type transitions were observed with adequate signal to noise on averaging 2500 free induction decays

Figure 6.1a; Antisymmetric $0_{00} -> 1_{10}$ transition of N_2-O_3.

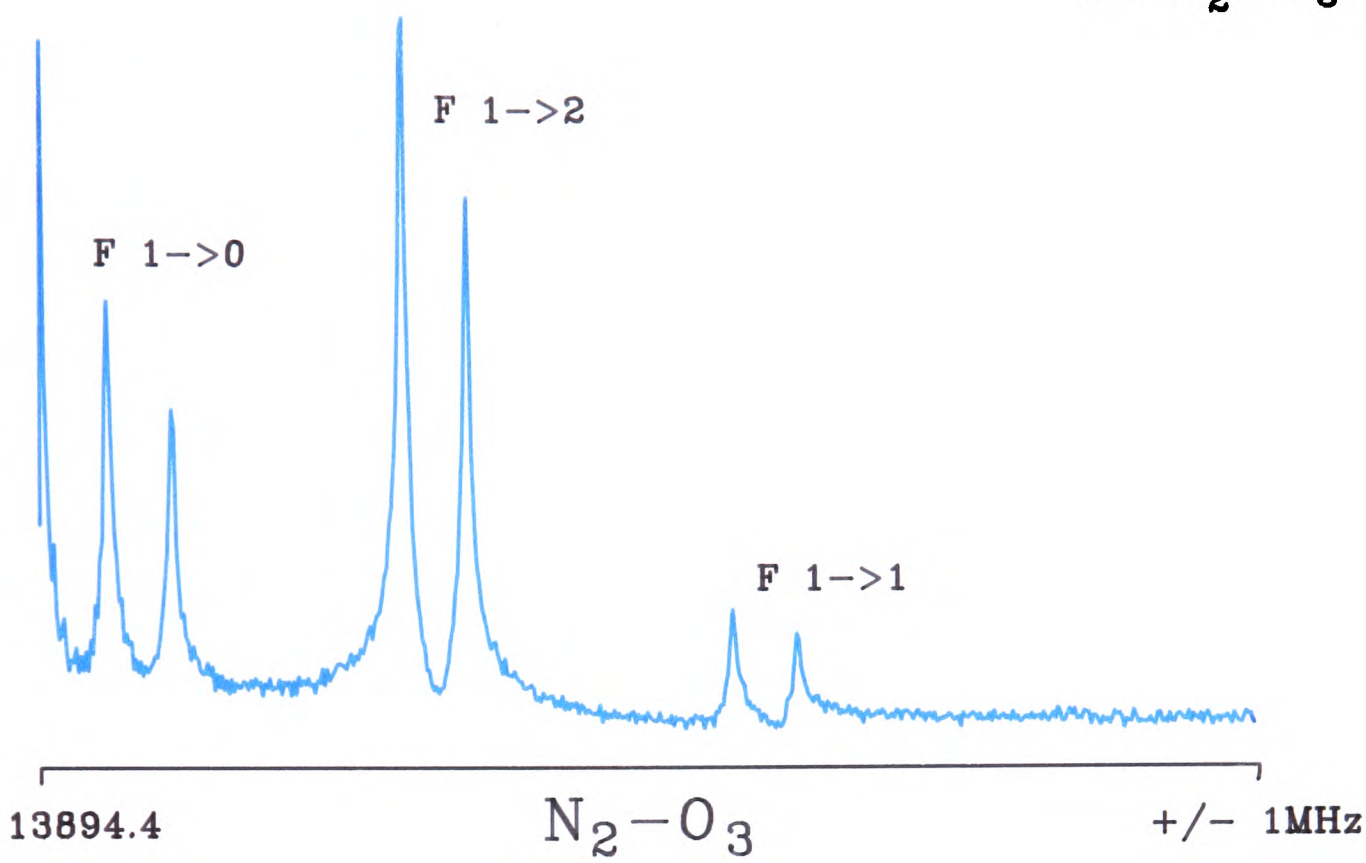

Figure 6.1b; $1_{01} -> 1_{11}$ transition of N_2-SO_2.

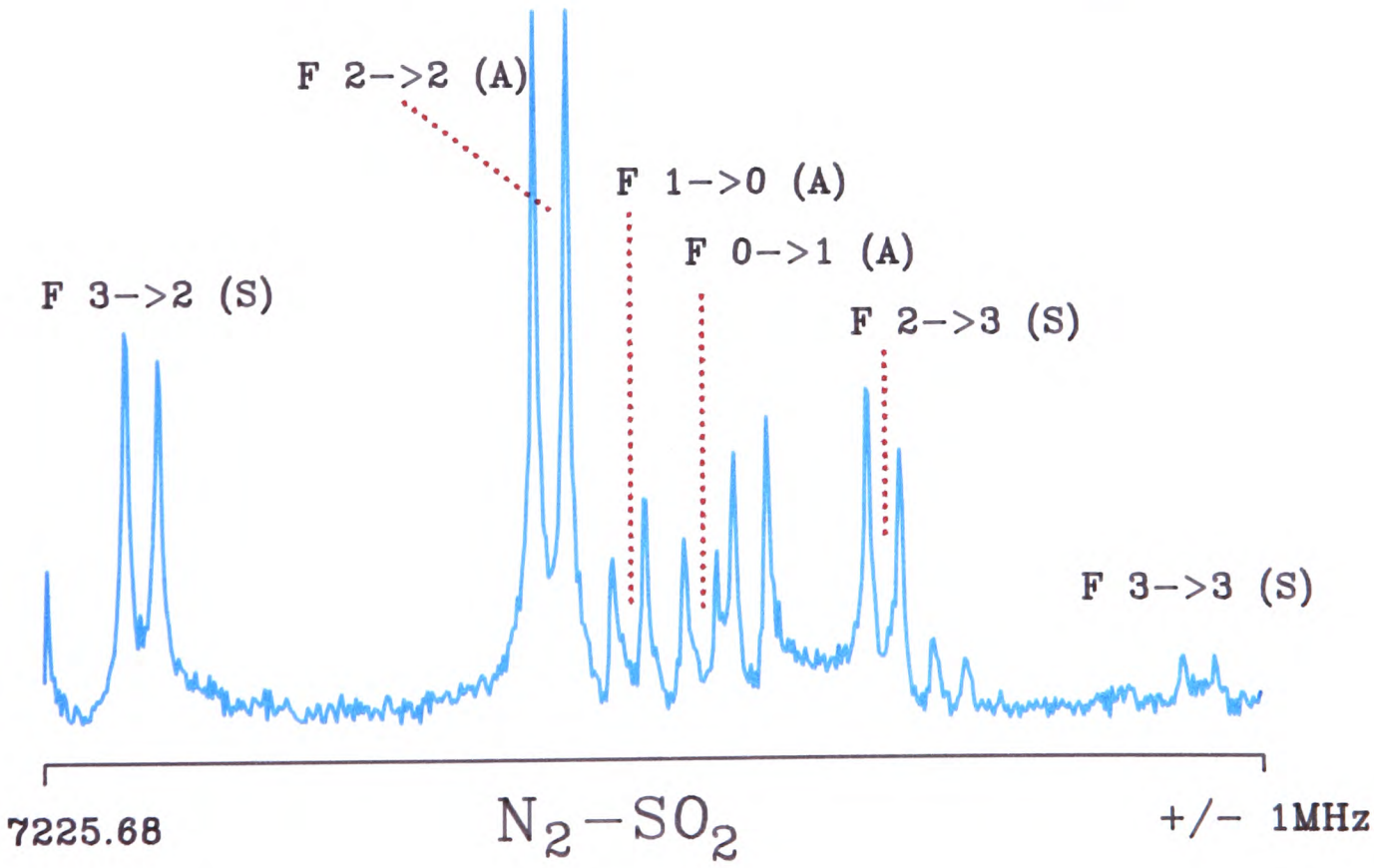

(FID); the weaker a-type transitions required averaging over approximately a factor of 10 more pulses (for the same pulse conditions). An example spectrum is given in figure 6.1.

Using the same nozzle pulse length and rate, N_2-SO_2 complexes were observed using a 1% SO_2 / 5% N_2 in argon expansion. c-type signals from this complex were very strong and observed easily on averaging 50 FIDs(see figure 6.1b) corresponding to a dipole moment $\sim$3 times larger than N_2-O_3. The much weaker a-type transitions have yet to be observed. According to the dipole measurement of Juang *et al.*[12] the a-axis projection of the SO_2 dipole moment in N_2-SO_2 is 0.0441(16) D. This is a reduction by a factor of 36 compared with the c-axis projection and consequently the pulse power must be increased by a similar factor (equation 2.13).

6.3 Spectral assignment

Searches for the N_2-O_3 spectrum were made on the basis of the Ar-O_3 structure with argon replaced by nitrogen. The proposed structure of N_2-O_3 is analogous to the structure of N_2-SO_2 which has been determined by infra-red spectroscopy. Dipole projections along the a and c axes are expected to be significant giving rise to a- and c-type transitions in the spectrum. The ac plane is assumed to be a plane of symmetry, therefore precluding b-type transitions. Both structures are illustrated in figures 6.2. A scan over 200 MHz around 8500 MHz was sufficient to find several transitions for N_2-O_3 with distinctive hyperfine patterns split into two groups associated with different rotational constants. This confirmed the equivalence of the nitrogen nuclei, resulting from the internal rotation of the N_2 molecule, and the assignment of the hyperfine transitions proceeded as described for N_2-OCS (section 5.3).

A similar procedure was followed for the N_2-SO_2 complex although in this case the groups of symmetric and antisymmetric hyperfine transitions were generally overlapping. In both the N_2-O_3 and N_2-SO_2 spectra, assignment of the rotational transitions were expected to be complicated by the O_3 or SO_2 tunnelling motion. With the parity change in the c-type dipole moment operator, resulting from SO_2/O_3 rotation-tunnelling motions, c-type transitions would cross the tunnelling symmetry and consequently the transition frequency would be modified by the tunnelling frequency (figure 6.4). In the case of a tunnelling frequency of $\sim$500 MHz which is of the order of the Ar-O_3 tunnelling frequency a large change in transition frequency would be observed. Initial assignments were made on the basis of the hyperfine patterns and a-type transitions which were unaffected by the O_3 or SO_2 tunnelling motion. However, it was subsequently found that most transitions were within 10 MHz of their predicted non-tunnelling positions for both N_2-O_3 and N_2-SO_2.

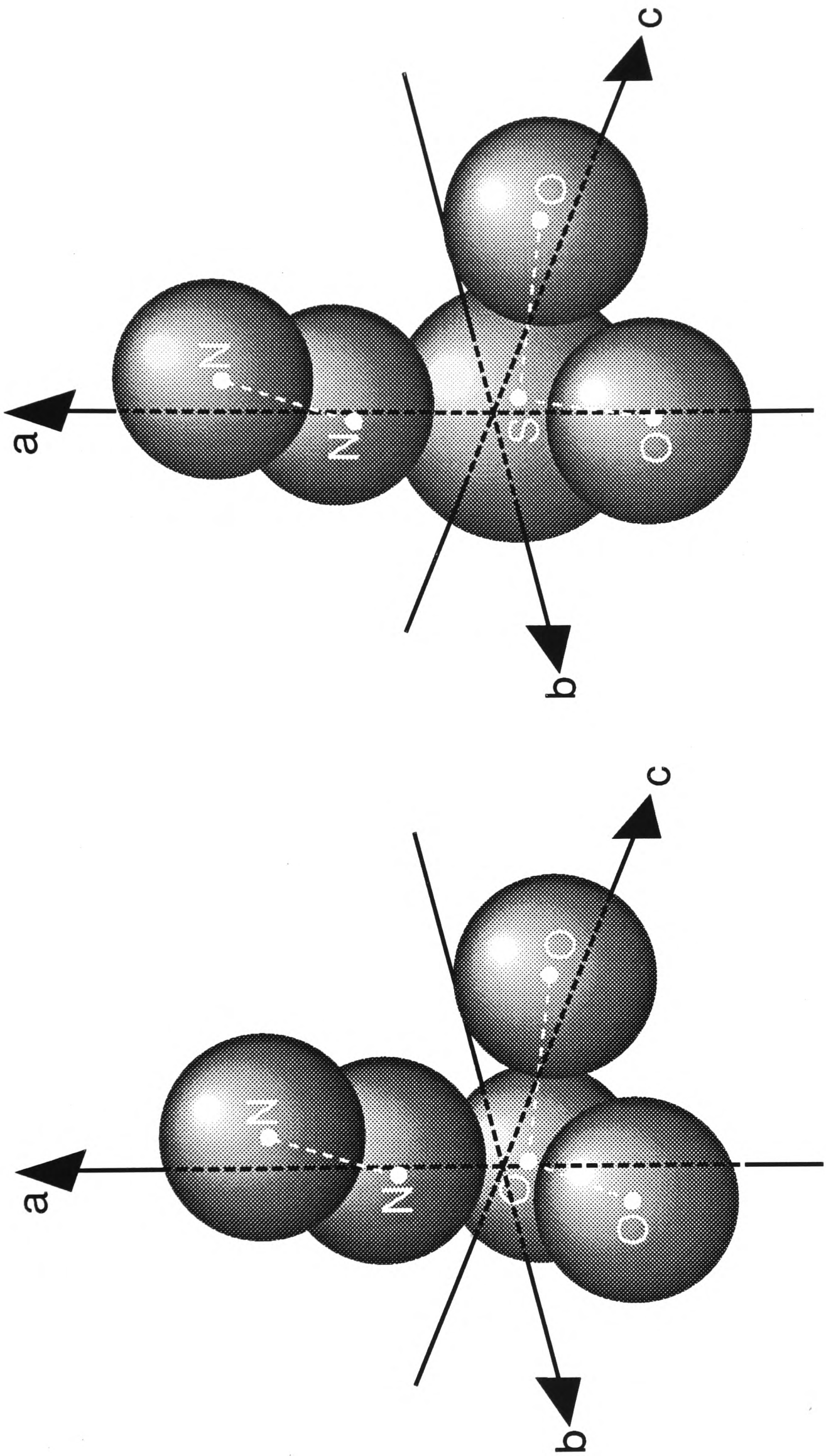

Figure 6.2; Billiard ball model of the N_2-O_3 and N_2-SO_2 structures in the principal inertial axis system. Spheres based on van der Waals radii (not to scale).

6.3.1 N_2 tunnelling and rotation-tunnelling motions of O_3 and SO_2

It has been demonstrated with the N_2-OCS spectrum that two sets of rotational constants are necessary to fit the observed features. The additional complexity on introducing tunnelling motion by the nitrogen partner might suggest that four sets of constants are required to account for distortion effects resulting from the two tunnelling motions in the case of N_2-O_3 or N_2-SO_2. However, symmetry will limit the rotational transitions possible and therefore limit the information available from the spectrum. The various possible tunnelling pathways may also differ considerably in their influence on the internal motions. Consequently the number of parameters required to fit the spectrum may be reduced.

With the proposed tunnelling motions of the nitrogen (section 5.3) and the rotation-tunnelling motion of the ozone or SO_2 moieties[5], four permutation states (ϕ_1-ϕ_4) of the nitrogen and oxygen nuclei are possible and these are illustrated in Figure 6.3a (axes z,x,y correspond to a,b,c). Tunnelling interconversions between these permutation states are listed in figure 6.3b with possible intermediates. Pathways involving the rotation-tunnelling of O_3 or SO_2 are expected to pass through intermediate configurations (a, b and c, fig 6.3b) with both the ab (zy) and ac (zx) planes as plane of symmetry, corresponding to C_{2h} symmetry. In this case, δ can assume values 0 or 180° and γ values 0, 90, 180 or 270°. Each tunnelling motion has an associated splitting frequency, ν_N with nitrogen rotation, ν_O with the O_3 or SO_2 (XO_2) tunnelling and ν_S with the simultaneous rotation-tunnelling of both N_2 and XO_2. These tunnelling frequencies are defined in the same way as for N_2-OCS, ie as interaction terms between states linked by tunnelling motion, such that the tunnelling energy levels are shifted $\pm \frac{1}{2}h\nu$ from degeneracy where ν is the tunnelling frequency. Since the transitions observed only involve low J and K_a, it is assumed that the J and K dependencies of the tunnelling frequencies are negligible so that ν_{tunnel} are constants. Figure 6.4 illustrates an approximate energy level diagram describing the effect of the tunnelling motions on the rotational levels. The N_2 tunnelling motion will give rise to a splitting of the degenerate N_2 librational levels in each rotational level (as described for N_2-OCS figure 5.6). In addition a second splitting due to the O_3 or SO_2 tunnelling motions will result in four tunnelling levels where the influence of spin statistics has yet to be included.

To calculate the tunnelling energy levels, an energy matrix in terms of the four permutation states (ϕ_1 to ϕ_4) can be written[15] to express the tunnelling splittings of the rotational energy. The energy matrix is given in equation 6.1. The energy matrix (equation 6.1) can be diagonalized by using symmetrized combinations of the basis functions, $\phi_{1\text{-}4}$, corresponding to the symmetrized tunnelling wavefunctions. This is most conveniently done in two steps.

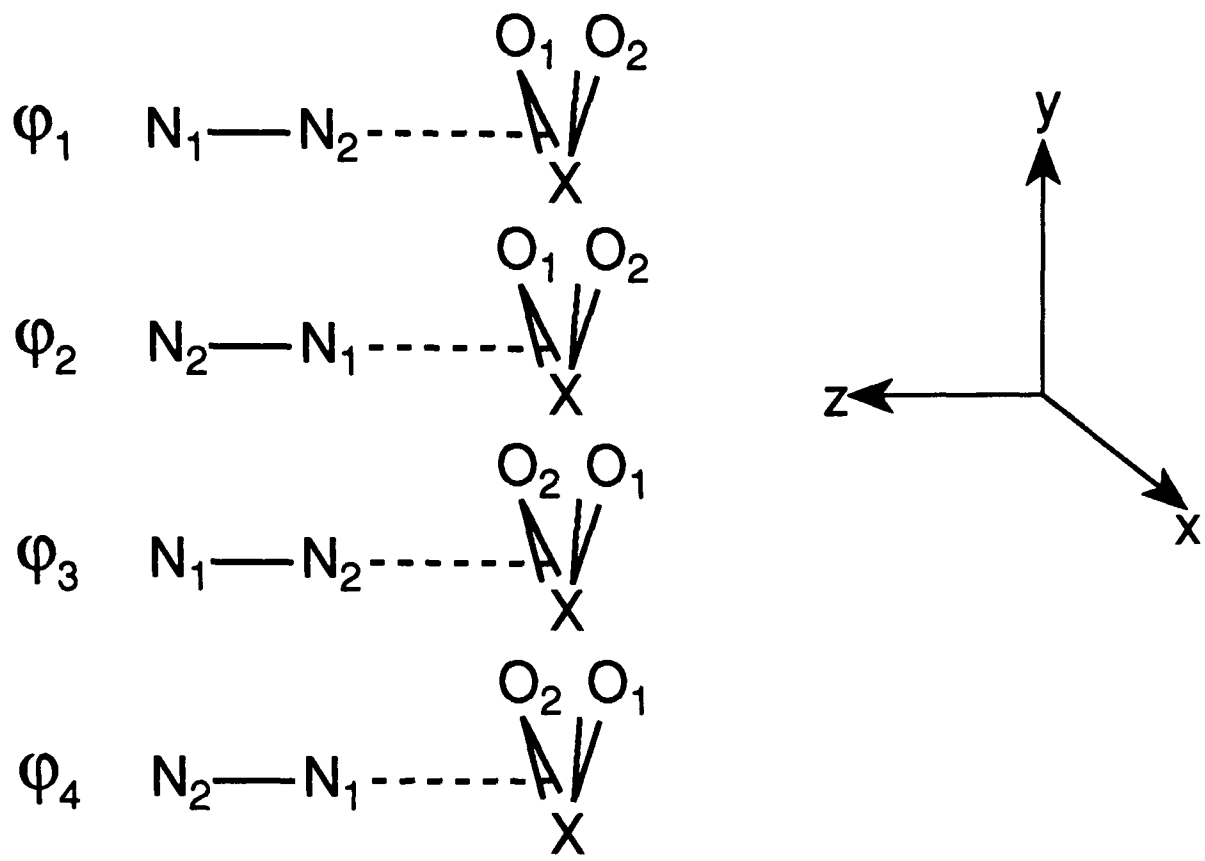

Figure 6.3a; Four permutation states of the oxygen and nitrogen nuclei in N_2-O_3 and N_2-SO_2. The axis system z,x,y correspond to a,b,c inertial axes.

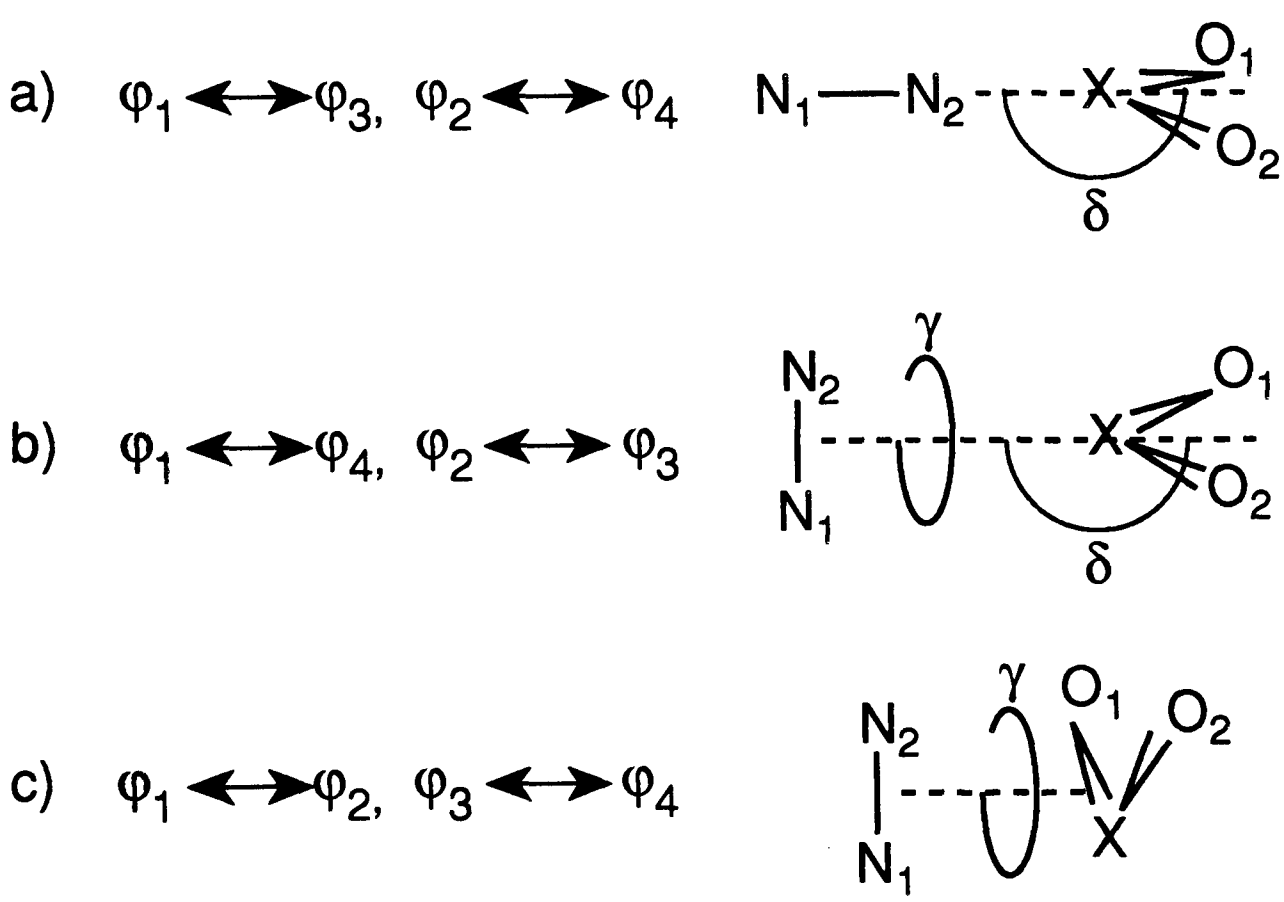

Figure 6.3b; Tunnelling interconversions between permutation states of N_2-O_3 and N_2-SO_2. The proposed intermediates do not include all possibilities.

Equation 6.1; Energy matrix for tunnelling motions in N_2-O_3 and N_2-SO_2

$$\begin{array}{c} \\ \phi_1 \\ \phi_2 \\ \phi_3 \\ \phi_4 \end{array} \begin{array}{c} \begin{array}{cccc} \phi_1 & \phi_2 & \phi_3 & \phi_4 \end{array} \\ \begin{vmatrix} E_{rot}-E & \Delta_N & \Delta_O & \Delta_S \\ \Delta_N & E_{rot}-E & \Delta_S & \Delta_O \\ \Delta_O & \Delta_S & E_{rot}-E & \Delta_N \\ \Delta_S & \Delta_O & \Delta_N & E_{rot}-E \end{vmatrix} \end{array} = 0 \qquad (6.1)$$

- E_{rot} is the energy of the rotational level.
- see figure 6.4 for definitions of $\phi_{1\text{-}4}$ and tunnelling pathways.
- $\Delta_{N,O,S} = -\frac{1}{2}h\nu_{N,O,S}$ where $\nu_{N,O,S}$ are the N_2, XO_2, and simultaneous tunnelling frequencies.

Table 6.1; Symmetrized tunnelling wavefunctions and associated energies for N_2-O_3 or N_2-SO_2.

Tunnelling wavefunction	label	energy	P_N	$P_O x(-1)^K$ K_{even}	K_{odd}	Stat. Wt. K_{even}	K_{odd}
$\sqrt{\frac{1}{2}}(\vartheta_A+\vartheta_C)$	+ +	$E_{rot}-\frac{1}{2}(\nu_N+\nu_O+\nu_S)$	S_N	S_O	(A_O)	6	0
$\sqrt{\frac{1}{2}}(\vartheta_A-\vartheta_C)$	+ −	$E_{rot}-\frac{1}{2}(\nu_N-\nu_O-\nu_S)$	S_N	(A_O)	S_O	0	6
$\sqrt{\frac{1}{2}}(\vartheta_B+\vartheta_D)$	− +	$E_{rot}+\frac{1}{2}(\nu_N-\nu_O+\nu_S)$	A_N	S_O	(A_O)	3	0
$\sqrt{\frac{1}{2}}(\vartheta_B-\vartheta_D)$	− −	$E_{rot}+\frac{1}{2}(\nu_N+\nu_O-\nu_S)$	A_N	(A_O)	S_O	0	3

- P_N permutation symmetry with exchange of nitrogen nuclei. (S - symmetric).
- P_O permutation symmetry with exchange of oxygen nuclei. (A - antisymmetric).
- Stat. Wt. is the product of nuclear spin statistical weights for nitrogen and oxygen.

Referring to figure 6.3, symmetric and antisymmetric functions with respect to the nitrogen tunnelling motion are defined by,

$$\begin{aligned} \vartheta_{\substack{A \\ B}} &= \frac{1}{\sqrt{2}}(\phi_1 \pm \phi_2) \\ \vartheta_{\substack{C \\ D}} &= \frac{1}{\sqrt{2}}(\phi_3 \pm \phi_4) \end{aligned} \qquad (6.2)$$

where $\vartheta_{a,c}$ are symmetric and labelled +, $\vartheta_{b,d}$ are antisymmetric and labelled −. Analogous symmetrized wavefunctions with respect to O_3 or SO_2 tunnelling can then be written in terms of $\vartheta_{a\text{-}d}$ with associated symmetry labelled + and −. The overall tunnelling symmetry is labelled with the nitrogen first, O_3/SO_2 second (as in figure 6.4). Table 6.1 shows the combined symmetrized tunnelling wavefunctions with their associated energies.

Having established a set of tunnelling wavefunctions, the effect of the nuclear spin statistics and rotation must be considered. Nitrogen tunnelling states (labelled +/−) combine with nitrogen nuclear spin states (labelled S_N, A_N) of the same symmetry to give symmetric states with a weight of 6 and antisymmetric states of weight 3 as discussed in section 5.3. This combination maintains the symmetry of the total wavefunction as symmetric, following the requirements of Bose-Einstein statistics. Similar arguments apply to exchange of oxygen nuclei which are spin 0 and therefore also require the total wavefunction to remain symmetric to permutation. With interchange of two nuclei of spin zero, only a symmetric spin wavefunction exists which combines with the symmetric combination of O_3/SO_2 tunnelling wavefunction (symmetry +/−) and rotational wavefunction. Since the permutation of the oxygen nuclei in O_3 and SO_2 is equivalent to tunnelling of O_3/SO_2 followed by rotation by 180° around the a-axis, the rotational wavefunction symmetry is determined by a $(-1)^{Ka}$ factor. Therefore, the O_3/SO_2 rotation is symmetric for even K_a and antisymmetric for odd K_a. The antisymmetric combination has a statistical weight of zero. This is illustrated in figure 6.4 where levels with zero weight are indicated as dashed lines.

Symmetry selection rules for a- and c-type transitions can be defined in terms of the notation given in figure 6.4 (table 6.1). The a-projection dipole moment operator does not change parity, therefore a-type transitions are between levels of the same tunnelling symmetry, ie $++ \longleftrightarrow ++$, $+- \longleftrightarrow +-$ (for S_NS_O levels), $-+ \longleftrightarrow -+$, $-- \longleftrightarrow --$ (for A_NS_O levels) as in figure 6.4. The c-projection dipole moment operator changes parity with tunnelling-rotation of the O_3 or SO_2, although there is no change associated with the nitrogen tunnelling motion. As a result, c-type transitions are between tunnelling states of the same symmetry with respect to N_2 but change the O_3 or SO_2 symmetry, ie $++ \longleftrightarrow +-$ (for S_NS_O levels), $-+ \longleftrightarrow --$ (for A_NS_O levels) as indicated in figure 6.4.

Using the energy expressions in table 6.1, the contributions made by the tunnelling frequencies to the transition frequencies can be deduced. It is apparent from figure 6.4 that the a-type transitions are not sensitive to any tunnelling splitting with both upper and lower levels having the same functional form in ν_N,ν_O and ν_S. Only centrifugal distortion of the tunnelling motion giving rise to different rotational constants for the S_NS_O and A_NS_O states will be evident. Expressions for the c-type transitions can be written using the expressions in table 6.1.

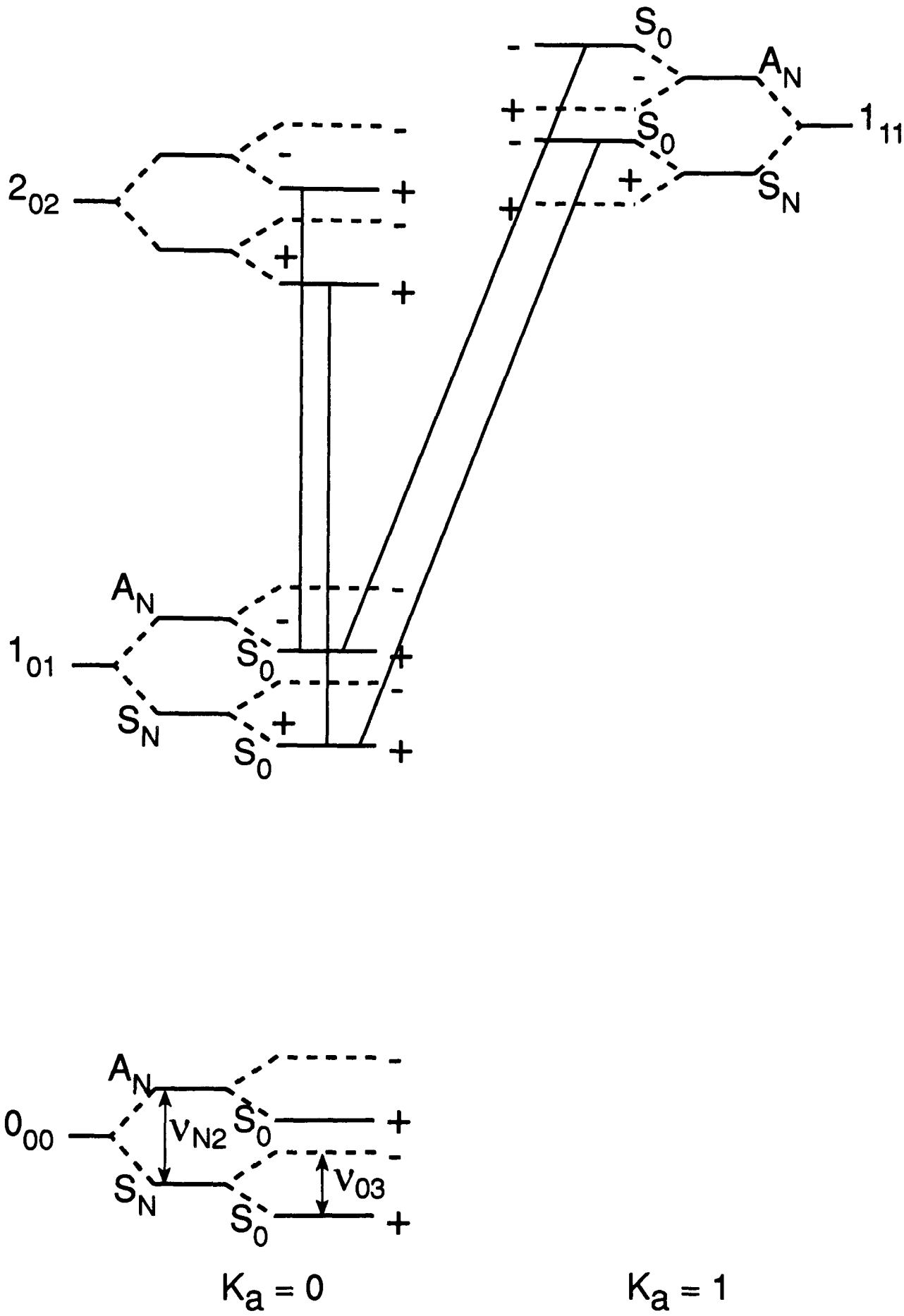

Figure 6.4; Energy level diagram for N_2-O_3 and N_2-SO_2 showing tunnelling splitting and allowed transitions. The N_2 splitting is indicated first, O_3/SO_2 second (not to scale). S_N/A_N and S_O refer to nuclear spin symmetry, +, − to tunnelling symmetry (see text).

Transition frequencies between S_NS_O levels, given by ν_{SS}, or A_NS_O, given by ν_{AS}, can be expressed for $K_a=0\rightarrow1$,

$$\begin{aligned} \nu_{SS} &= \nu_{rot}-\tfrac{1}{2}(\nu_N-\nu_O-\nu_S)+\tfrac{1}{2}(\nu_N+\nu_O+\nu_S) = \nu_{rot}+\nu_O+\nu_S = \nu_{rot}+\nu_{eff}^{SS} \\ \nu_{AS} &= \nu_{rot}-\tfrac{1}{2}(\nu_N-\nu_O+\nu_S)+\tfrac{1}{2}(\nu_O-\nu_N-\nu_S) = \nu_{rot}+\nu_O-\nu_S = \nu_{rot}+\nu_{eff}^{AS} \end{aligned} \qquad (6.3)$$

- ν_{rot} are rotational transitions in the absence ot tunnelling.
- $\nu_{eff}^{SS,AS}$ are effective tunnelling frequencies obtained from the c-type transition data, least squares fitting procedure (section 6.4.2)

Similar expressions where the effective tunnelling frequency $\nu_{eff}^{SS,AS}$ is subtracted from ν_{rot} are obtained for $K_a=1\rightarrow2$. Therefore, the tunnelling frequencies for the S_NS_O and A_NS_O c-type transitions have different dependencies on the simultaneous, ν_S, and O_3/SO_2, ν_O tunnelling frequencies. In addition, the tunnelling frequency of nitrogen can not be measured directly and the spectrum will only be sensitive to the difference in effective rotational constants resulting from distortion of the nitrogen tunnelling motion. By observing $\Delta K_a=0\rightarrow1$, $1\rightarrow2$ and $2\rightarrow3$ c-type, S_NS_O and A_NS_O transitions, enough information is available to decorrelate A and D_K, which determine the c-type transition energy, and ν_T the effective tunnelling frequency. From the small observed-calculated (with no ν_{eff}) frequency shifts for c-type transitions of N_2-O_3 and N_2-SO_2, the effective tunnelling frequency is expected to be 10 MHz or less which suggests that centrifugal distortion effects on the O_3 or SO_2 tunnelling motions are likely to be very small. As a result, the tunnelling features in the spectrum are expected to be fitted by two sets of rotational constants to account for centrifugal distortion the nitrogen tunnelling motion and two tunnelling frequencies, ν_O and ν_S. This may be reduced to one set in some of the rotational constants if ν_N is small.

6.4 Results and Analysis

The symmetric and antisymmetric N_2-O_3 and N_2-SO_2 spectra were fitted separately to the Watson S reduction hamiltonian (H_{rot}) given in equation 3.12 and the hyperfine hamiltonian (H_{hyperf}) defined in chapter 4. In order to account for the effect of tunnelling, a K_a dependent tunnelling term with an effective tunnelling frequency coefficient, ν_{eff} was included in the total hamiltonian (H), *i.e.*,

$$H = H_{rot} + H_{hyperf} - (-1)^{K_a}\,\nu_{eff} \qquad (6.4)$$

6.4.1 The N_2-O_3 spectrum

Twenty one rotational transitions consisting of 6 a-type and 15 c-type with K_a up to 2 were measured. 130 symmetric and 82 antisymmetric hyperfine transitions were assigned and are tabulated in appendix III. The same notation used for N_2-OCS to label the mixed nuclear spin levels is employed to distinguish the two F=J levels in each rotational level (section 5.3 and 4.3.3). As the observed c-type transitions involve ΔK_a of 0→1 and 1→2, only sufficient information is available to determine two constants from the three correlated parameters A,D_K and ν_{eff}, where ν_{eff} is the effective tunnelling frequency. A and D_K are chosen for inclusion in the fit although the values obtained are effective constants. Transitions involving ΔK_a 2→3 were either out of range of the spectrometer or too low in intensity. The result of the least squares fit of the symmetric and antisymmetric data to the Watson S reduction I^R rotational, quadrupole and spin-rotation hyperfine hamiltonians is given in table 6.2 and residuals are tabulated in appendix III.

It was found that the quality of the fit in both symmetric and antisymmetric cases was substantially improved with the exclusion of the $5_{15} \rightarrow 4_{23}$ transition. As a result, the $5_{15} \rightarrow 4_{23}$ transition has a systematic residual of 19kHz with the hyperfine components deviating from this value by within the experimental uncertainty. This indicates that the hyperfine pattern fits and the inadequacy in the calculated values is due to a rotational effect. Two possible effects may be considered giving rise to this effect. A Coriolis interaction could mix rotational levels of the same J and differing K in different vibrational levels. As the 5_{15} level contributes to other unperturbed transitions in the data set, this would require the interaction to affect the 4_{23} level. Since the effect is not observed for the other K doublet ($5_{14} \rightarrow 4_{22}$) or other lower or higher analogous transitions, possible mixing states in the excited vibrational state are 4_{14} or 4_{13} levels where the K splitting for K_a=1 can vary significantly between J levels. In the ground vibrational state, the splitting between 4_{14} and 4_{23} rotational levels is of the order of 1 cm^{-1} requiring the interacting vibrational frequency to be of this order corresponding to a very low force constant. A second possible effect may be due to the neglect of $h_{1,2,3}$ sextic centrifugal distortion terms. However, the d_2 contribution to the 4_{23} level is ~200 kHz so that the sextic contribution, which may be ~1/1000 of the d_2 contribution, is negligible. In addition, no effect is seen in any other similar transition involving both K doublets so precluding a contribution of the order of 19kHz from $h_{1,2,3}$.

The standard deviation of the fit corresponds approximately to the experimental uncertainty and shows a significant improvement on the standard deviation of the N_2-OCS fit where hyperfine discrepancies increased the value of σ_{fit}. The standard deviation of the asymmetric fit in particular is very small as a result of two factors. Firstly, the rotational constants of N_2-O_3 exclude the low J near-degeneracies observed for N_2-OCS and eliminate possible second order quadrupole effects. Secondly, most hyperfine transitions involve $\Delta F = \Delta J$, which are relatively insensitive to the hyperfine functional form.

Table 6.2; Rotational and hyperfine parameters for N_2-O_3.

Parameter	Symmetric	Antisymmetric
Rotational constants[a]		
A /MHz	11809.8255(5)	11785.4422(4)
B /MHz	2106.63670(13)	2106.58551(12)
C /MHz	1849.39374(27)	1849.31001(24)
Quartic centrifugal distortion constants[a]		
D_J /kHz	21.0408(9)	21.0816(79)
D_{JK} /kHz	261.654(89)	227.749(70)
D_K /kHz	3371.39(14)	-2560.72(14)
d_1 /kHz	-2.3259(58)	-2.3041(44)
d_2 /kHz	-6.381(76)	-6.801(58)
Sextic centifugal distortion constants[a]		
H_J /Hz	-1.53(24)	1.05(17)
H_{JK} /Hz	85.2(48)	-113.9(35)
H_{KJ} /Hz	3.2444(80)	-3.3936(79)
Nuclear quadrupole coupling constants		
χ_{aa} /MHz	-3.10466(63)	-3.1051(7)
$\Delta\chi$ /MHz	1.29149(90)	1.2898(12)
Spin-rotation coupling constants		
C_{aa} /kHz	0.41(23)	0.70(33)
C_{bb} /kHz	0.49(10)	0.47(12)
C_{cc} /kHz	0.301(85)	0.291(91)
Standard deviation of the fit		
σ_{fit} /kHz	1.3	1.0

[a] Watson S reduction hamiltonian, I^R representation.
[b] Numbers in parenthesis correspond to one standard deviation.

The near coincidence of the B and C symmetric and antisymmetric constants would appear to indicate a reduced centrifugal distortion of the N_2 tunnelling motion and consequently a lower N_2 tunnelling frequency, ν_N compared with N_2-OCS. The quadrupole coupling constants also confirm that the N_2 projections onto the inertial axes are the same in both the symmetric and antisymmetric states. In contrast, the large difference in the A and D_K (H_J,H_{JK} H_{KJ}) constants indicate the effective nature of these constants. From the definition of the centrifugal distortion constants (section 3.3), the sum of $D_J+D_{JK}+D_K$ must be positive, which is not the case for the antisymmetric due to the contribution made by the correlated tunnelling frequency. Similar effects are also expected to be translated into the sextic distortion constants.

Although A and D_K in table 6.2 are effective constants, some information on the component tunnelling splittings can be deduced from the two symmetry allowed transitions. From table 6.1 and figure 6.4, the frequency of the symmetric, S_NS_O $++ \longleftrightarrow +-(\nu_{SS})$ and antisymmetric A_NS_O $-+ \longleftrightarrow --(\nu_{AS})$ c-type transitions have different dependencies on the tunnelling frequencies. The effective tunnelling frequencies, given by equation 6.3, indicate that the spectrum is sensitive to the frequency of the simultaneous N_2 and O_3 tunnelling motion, ν_S but that the O_3 tunnelling frequency dependency is the same for both transitions. The values of ν_S and ν_O can be estimated by equating the contributions made by the effective constants A and D_K with the true rotational constants and tunnelling frequency contributions. For transitions involving the symmetric nitrogen tunnelling state, S_NS_O, the following expressions can be derived from equation 6.4,

$$A+\nu_O+\nu_S-D_K = A^{eff}-D_K^{eff} \qquad \Delta K_a=0\rightarrow1$$

$$3A-\nu_O-\nu_S-15D_K = 3A^{eff}-15D_K^{eff} \qquad \Delta K_a=1\rightarrow2 \qquad (6.5)$$

$$hence \quad \frac{1}{3}(\nu_O+\nu_S)+D_K = D_K^{eff}$$

- Coefficients of A and D_K calculated from equation 3.13.
- A^{eff} and D^{eff} are the fitted constants in table 6.2, A and D_K are the uncorrelated Watson S reduction parameters.

In the same way, an analogous equation for the antisymmetric nitrogen tunnelling state transitions gives,

$$\frac{1}{3}(\nu_O-\nu_S)+D_K = D_k^{eff} \qquad (6.6)$$

If the difference ($D_K(S)$-$D_K(A)$) is taken to be negligible so that $D_K^{eff}(S_NS_O)$-$D_K^{eff}(A_NS_O) = 2\nu_S/3$, equations 6.5 and 6.6 give an upper value of 8.898 MHz for ν_S. An upper limit for ν_O, when D_K is ~-250 kHz so that $D_J+D_{JK}+D_K \sim 0$, is 1.98 MHz and the lower limit, when $\nu_O = 0$ MHz, gives D_K of 405.3 kHz. Values of the Watson S reduction, A rotational constant with the tunnelling contribution removed can also be estimated. For $\nu_O = 1.98$ MHz, $A_S = 11795.3215$, $A_A = 11784.6662$ MHz and for $\nu_O = 0$ MHz, $A_S = 11797.9622$ MHz, $A_A = 11797.3062$ MHz.

6.4.2 The N_2-SO_2 spectrum

The work presented here represents a preliminary microwave study of N_2-SO_2. A-type transitions have yet to be observed although the P, Q and R c-type transitions measured provide enough information to decorrelate the Watson S reduction I^R parameters defined in section 3.3. 60 antisymmetric and 110 symmetric hyperfine transitions have been measured. In contrast to the N_2-O_3 spectrum (section 6.4.1), transitions involving levels with K_a up to 3 have been observed allowing A, D_K and ν_{eff} (effective tunnelling frequency) to be decorrelated and hence the tunnelling frequency can be measured directly from the spectrum. The result of the least squares fitting procedure to the rotational and hyperfine hamiltonian parameters defined in sections 3.3 and 4.3.3 is given in table 6.3. Observed transitions and residuals from the fitting procedure are given in appendix IV.

The effective tunnelling frequencies obtained from the symmetric and antisymmetric fits are combinations of the SO_2 and simultaneous tunnelling frequencies, ν_O and ν_S as described in equation 6.3. The negative value of the antisymmetric tunnelling constant indicates that the simultaneous tunnelling frequency is the predominant tunnelling motion. From the values of the symmetric and antisymmetric ν_{eff} (table 6.3) and equation 6.3, ν_S=172.65 kHz and ν_O=25.1 kHz. In addition, the very small differences between the symmetric and antisymmetric rotational constants would appear to indicate that centrifugal distortion of the nitrogen tunnelling motion is small, implying a small N_2 tunnelling frequency for N_2-SO_2 compared with N_2-OCS.

6.4.3 Structure determination

In order to describe the structure of N_2-O_3 or N_2-SO_2, five structural parameters can be defined relative to an axis system Z, X, Y where the Z axis passes through the N_2 and O_3/SO_2 centres of mass. Four angles and the separation of the centres of mass (c.m.), R, are illustrated in figure 6.5. An implicit assumption is that the monomer structures are unperturbed on complexation so that moments of inertia of the monomers[2] can be used. These are given in table 6.3.

Table 6.3; Rotational and hyperfine parameters for N_2-SO_2.

Parameter	Symmetric	Antisymmetric
Rotational constants[a]		
A /MHz	8860.86771(87)	8860.85854(76)
B /MHz	1635.32599(25)	1635.32587(16)
C /MHz	1441.74918(21)	1441.74826(17)
Quartic centrifugal distortion constants[a]		
D_J /kHz	10.796(5)	10.7816(46)
D_{JK} /kHz	329.404(73)	329.264(56)
D_K /kHz	-251.28(21)	-253.21(21)
d_1 /kHz	-1.3179(37)	-1.3265(11)
d_2 /kHz	-0.66243(52)	-0.66117(31)
Sextic centifugal distortion constants[a]		
H_J /Hz	[c]	[c]
H_{JK} /Hz	-25.6(25)	-6.9(27)
H_{KJ} /Hz	232.7(77)	169.5(61)
Nuclear quadrupole coupling constants		
χ_{aa} /MHz	-3.63124(75)	-3.62847(99)
$\Delta\chi$ /MHz	0.9264(13)	0.9289(18)
Spin-rotation coupling constants		
C_{aa} /kHz	0.47(30)	0.50(35)
C_{bb} /kHz	0.61(16)	0.97(20)
C_{cc} /kHz	0.20(11)	0.46(15)
Tunnelling frequency		
ν_{eff} /kHz	185.20(52)	-161.42(50)
Standard deviation of the fit		
σ_{fit} /kHz	1.8	1.5

[a] Watson S reduction hamiltonian, I^R representation.
[b] Numbers in parenthesis correspond to one standard deviation.
[c] Not well determined, excluded from the fit.

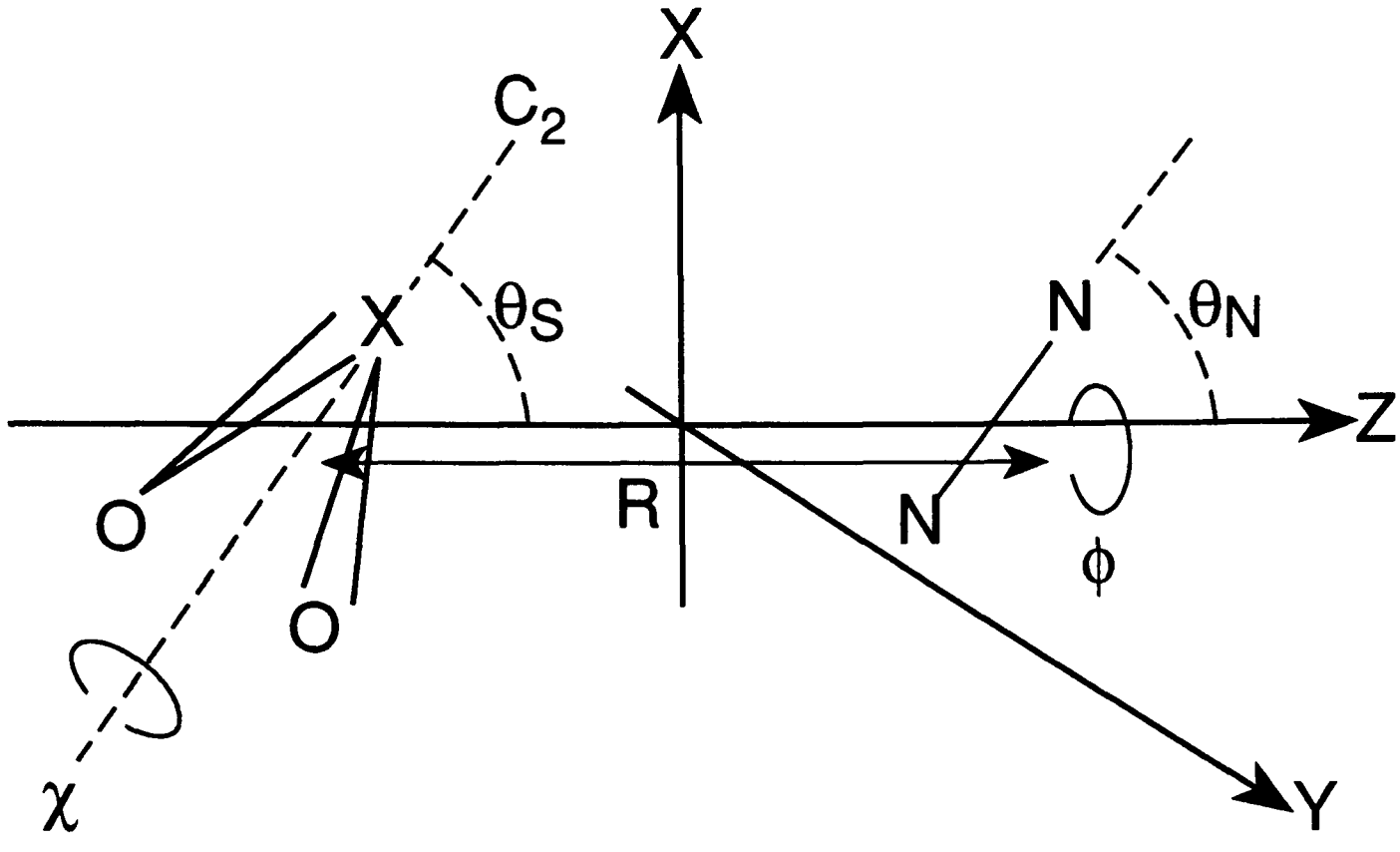

Figure 6.5a; Structural parameters for N_2-O_3 and N_2-SO_2.

R (and Z) join the centres of mass, χ is the angle of rotation about the monomer C_2 axis relative to the out of plane axis. Z, Y, X correspond approximately to a, b, c principal inertial axes.

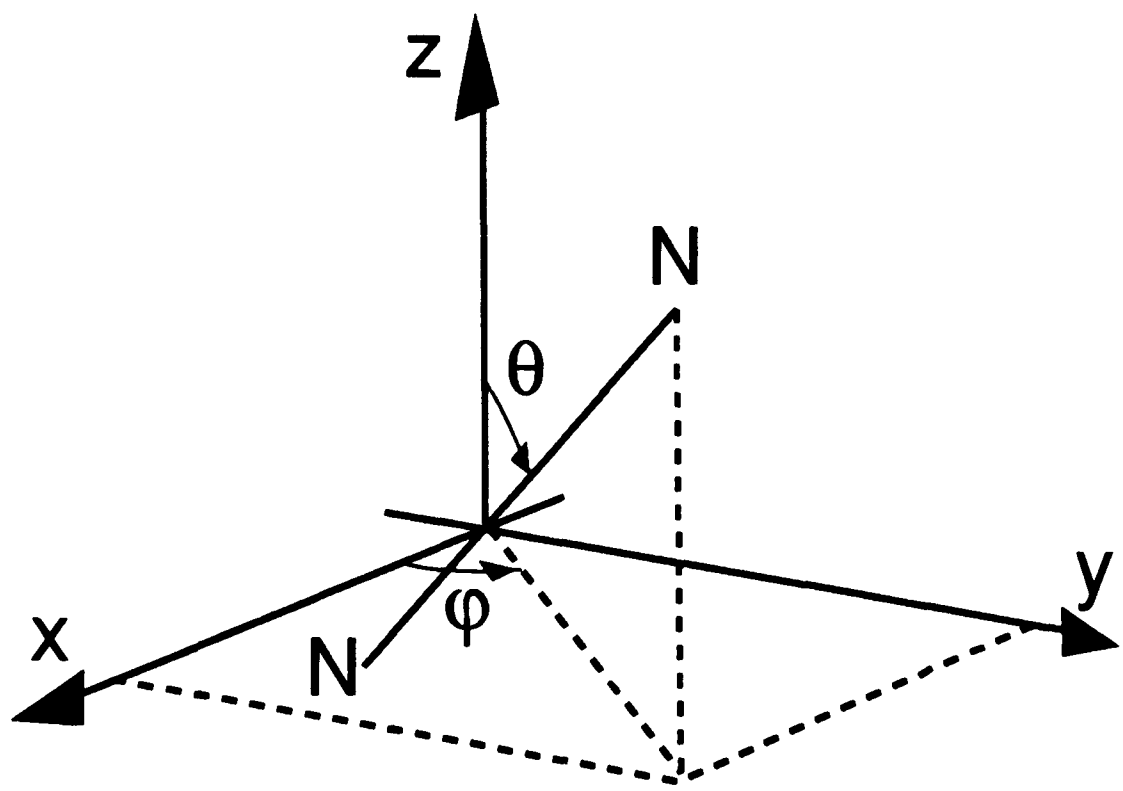

Figure 6.5b; N_2 angular orientation. z,y,x correspond to a,b,c in N_2-XO_2. θ is the angle between the N_2 and a-inertial axes (θ_N between N_2 and Z axis). φ measured from the c-axis.

The nitrogen orientation in figure 6.5a is described by two angles, θ_N (relative to the axis joining the centres of mass) and ϕ. It is more convenient to use the inertial axis system to describe the N_2 orientation and employ the quadrupole coupling constant analysis as described for N_2-OCS (section 5.3.1) to determine the vibrationally averaged N_2 projection angle, θ_k, with respect to the k-inertial axis (k=a,b,c) given by,

$$\langle \cos^2\theta_k \rangle = \frac{1}{3}\left(\frac{2\chi_{kk}}{\chi_{N_2}} + 1\right) \qquad (6.7)$$

Figure 6.5b illustrates the inertial axis projection angles used to define the nitrogen orientation. The Z,X,Y axes correspond to the a,c,b-inertial axes. The angle of N_2 to the dimer a-inertial axis, θ, for N_2-O_3 and N_2-SO_2 are given in table 6.5. The value of $\Delta\chi$ indicates for both N_2-O_3 and N_2-SO_2 a larger averaged projection of the quadrupole moment along the c-axis than the b-axis (N_2-O_3 θ_c=61.94°, θ_b=75.65°; N_2-SO_2 θ_c=65.95°, θ_b=76.887°). This gives an indication that the large amplitude motions of the nitrogen are more confined to the ac plane suggesting that the N_2 tunnelling pathway in the ac plane is more favourable than in the ab plane (figure 6.2). The b planar moment of inertia, $P_{bb}=\frac{1}{2}(I_{aa}+I_{cc}-I_{bb})$ of the complex is very close to the monomer I_{bb} moment of inertia in both N_2-O_3 and N_2-SO_2. This indicates that the moment of inertia out of the ac plane of the complex is almost totally due to O_3/SO_2 confining the N_2 to the ac plane in the equilibrium structure. In addition, with the absence of b-type transitions and using the infra-red analysis of the N_2-SO_2 structure[12], the ac inertial plane is assumed to be a plane of symmetry so that the equilibrium value of ϕ can take the value 0 or 180° (defined in figure 6.5b)). However, there is no information in the rotational or quadrupole constants to distinguish these two configurations.

Analysis of the rotational constants to obtain the three remaining structural parameters is most conveniently achieved by reducing the structure to an equivalent atom-non linear molecule model. Following the analysis described for N_2-OCS, the contribution of the nitrogen moment of inertia (I_{N2}=8.4733 u Å^2)^2 to each moment of inertia of the complex can be removed to define new moments of inertia corresponding to an atom-O_3/SO_2 structure where the atom has the mass of N_2. The modified moments of inertia, I'_k, are given by

$$I'_k = I_k - I_{N_2}\sin^2\theta_k \qquad (6.8)$$

where k=a,b or c and θ_k is given by equation 6.7. Values for the modified moments of inertia are given in table 6.4. For the N_2-O_3 complex, the tunnelling frequency contribution to the A rotational constants must also be removed. Since the effective tunnelling frequency is not determined, a range of structural parameter values are determined corresponding to the possible tunnelling frequency limits.

Expressions for the inertial matrix in the Z,X,Y coordinate system defined in figure 6.5a can be written in terms of projections of the O_3 or SO_2 monomer moments of inertia and a pseudo-diatomic moment of inertia, $I_{pd} = \mu_{pd}R^2$, based on the masses of N_2 and O_3/SO_2 (to give reduced mass μ_{pd}) and the centre of mass separation, R. The modified moments of inertia I'_{aa}, I'_{bb},I'_{cc} can be obtained by diagonalizing the Z, X, Y axis system (figure 6.5) inertial matrix. To obtain expressions for the Z, X, Y inertial matrix elements of the complex in terms of projections of monomer moments of inertia, two transformations of the O_3/SO_2 monomer must be considered before including the pseudo-diatomic contribution. These transformations correspond to a rotation of the monomer inertial axis system by i) the χ angle and then ii) the θ_s angle, analogous to Euler angle transformations[16]. In the principal axis system of O_3 or SO_2, the moment of inertia matrix has only diagonal elements I_a, I_b and I_c (table 6.4). The principal axis system of the monomer must be rotated by χ about the monomer b axis to an intermediate axis system, z,x,y where the b and z axes are collinear. This transformation can be written in matrix form as,

$$\boldsymbol{I'} = \boldsymbol{s}\,\boldsymbol{I}\,\boldsymbol{s}^{-1}$$

$$\begin{pmatrix} I_{xx} & I_{xy} & 0 \\ I_{yx} & I_{yy} & 0 \\ 0 & 0 & I_b \end{pmatrix} = \begin{pmatrix} \cos\chi & \sin\chi & 0 \\ -\sin\chi & \cos\chi & 0 \\ 0 & 0 & 1 \end{pmatrix} \begin{pmatrix} I_a & 0 & 0 \\ 0 & I_c & 0 \\ 0 & 0 & I_b \end{pmatrix} \begin{pmatrix} \cos\chi & -\sin\chi & 0 \\ \sin\chi & \cos\chi & 0 \\ 0 & 0 & 1 \end{pmatrix} \tag{6.9}$$

The intermediate axis system z,x,y is rotated by θ about the y axis to transform the x and z axis to the X and Z of figure 6.5a This transformation can be written as

$$\begin{pmatrix} I_{XX} & I_{XY} & I_{XZ} \\ I_{YX} & I_{YY} & I_{YZ} \\ I_{ZX} & I_{ZY} & I_{ZZ} \end{pmatrix} = \begin{pmatrix} \cos\theta_s & 0 & \sin\theta_s \\ 0 & 1 & 0 \\ -\sin\theta_s & 0 & \cos\theta_s \end{pmatrix} \begin{pmatrix} I_{xx} & I_{xy} & 0 \\ I_{yx} & I_{yy} & 0 \\ 0 & 0 & I_b \end{pmatrix} \begin{pmatrix} \cos\theta_s & 0 & -\sin\theta_s \\ 0 & 1 & 0 \\ \sin\theta_s & 0 & \cos\theta_s \end{pmatrix} \tag{6.10}$$

These two transformations give potentially nine matrix elements. However, a simplification can be made by assuming that the averaged value of χ is close to zero allowing the I_{XY} and I_{YX} products of inertia to be neglected. By adding the pseudo-diatomic term μR^2 to the I_{XX} and I_{YY} moments of inertia derived from equations 6.9 and 6.10, the expressions for the inertial matrix of the complex, in the Z,X,Y (figure 6.5a) axis system, are given by

$$
\begin{aligned}
I_{ZZ} &= (I_c\cos^2\chi + I_a\sin^2\chi)\cos^2\theta_s + I_b\sin^2\theta_s \\
I_{YY} &= \mu R^2 + (I_c\sin^2\chi + I_a\cos^2\chi) \\
I_{XX} &= \mu R^2 + (I_c\cos^2\chi + I_a\sin^2\chi)\cos^2\theta_s + I_b\sin^2\theta \\
I_{XY} &= I_{YZ} = 0 \\
I_{XZ} &= (I_b - I_c\cos^2\chi - I_a\sin^2\chi)\sin\theta\cos\theta
\end{aligned}
\qquad (6.11)
$$

It should be noted that two assumptions have been made. The first is that terms involving products such as $\langle\cos_2\chi\sin_2\theta\rangle$, where vibrational averaging takes place over the entire function, can be treated as separable, effectively with averaging over each function separately. The second assumption made is that rotational constants and moments of inertia can be treated in the same way as for the equilibrium structure. Since the effective constants include the effects of vibrational averaging, this is equivalent to assuming for example $\langle 1/\sin^2\theta\rangle^{-1} \approx \langle\sin^2\theta\rangle$. These assumptions are reasonable in the limit of small amplitude motions.

To obtain R, θ_s and χ from the expressions in equations 6.11, it is convenient to iteratively calculate the parameters by initially assuming $\sin\theta_s \sim 0$. This allows the off-diagonal term, I_{XZ} to be neglected with the result that the remaining terms become expressions for the principal moments of inertia. As a result, an expression in χ can be derived,

$$
I_{XX} + I_{ZZ} - I_{YY} = I'_{cc} + I'_{aa} - I'_{bb} = I_b + (I_c - I_a)\cos 2\chi \qquad (6.12)
$$

- $I_{a,b,c}$ are monomer moments of inertia.
- $I'_{aa,bb,cc}$ are moments of inertia of the dimer with the nitrogen contribution removed (table 6.4).

From equation 6.11, values of χ, representing the rms vibrationally averaged value of the angle, can be derived from I_{XX}-I_{YY}+I_{ZZ} = I_b+(I_c-I_a)cos2χ. This expression is relatively insensitive to the effects of the off-diagonal I_{XZ} term, which will move I_{XX} up and I_{ZZ} down symmetrically with no influence on I_{YY}. Substituting values for χ into the expression for $I_{YY} \equiv I'_{bb}$, gives values for R, the centres of mass separation. Substitution into the expression for $I_{ZZ} \equiv I'_{aa}$ gives values of θ_s. All calculated structural parameters are given in table 6.5.

Table 6.4; Moments of inertia.

Monomer/dimer	I_{aa} / u Å^2	I_{bb} / u Å^2	I_{cc} / u Å^2
O_3[a]	4.7437	37.8589	42.7038
modified symmetric N_2-O_3[b]	40.4411[c] 40.4506[d]	231.9460	266.6688
modified antisym. N_2-O_3[b]	40.4440[c] 40.4536[d]	231.9517	266.6811
SO_2[a]	8.3151	48.9807	57.4317
modified symmetric N_2-SO_2[b]	55.1891	301.0016	343.4674
modified antisym. N_2-SO_2	55.1867	301.0028	343.4706

[a] Data from reference 2.
[b] Reduced mass of N_2-O_3 = 17.68459 u, N_2-SO_2 = 19.47770 u
[c] Modified I_{aa} for ν_O=0 MHz, ν_S=8.898 MHz.
[d] Modified I_{aa} for ν_O= 1.98 MHz, ν_S=8.898 MHz.

Table 6.5; Structural parameters for N_2-O_3 and N_2-SO_2.

Parameter	N_2-O_3		N_2-SO_2	
	symmetric	antisym.	symmetric	antisym.
R /Å	3.582		3.875	
θ /°	32.118(6)	32.114(6)	27.810(6)	27.84(2)
ϕ[a] /°	0,180		0,180	
χ /°	5.31(2)	5.27(2)	3.848	3.850
θ_s /°	49.16, 130.84(4)	49.46, 130.54(4)	60.29, 119.71	60.27, 119.73

[a] angle measured in the bc plane from the c axis.

The value of χ which is the rms angle of the monomer undergoing a low frequency bending motion, appears to be rather small although for N_2-SO_2 χ is within the limits anticipated by Juang *et al.*[12]. However, χ is found to be quite sensitive to changes in the Y planar moment of inertia $2P_Y = I_{XX}-I_{YY}+I_{ZZ}$ which is very close to the I_b moments of inertia of the monomer for N_2-O_3 and N_2-SO_2. As a result, the model structure may be quite sensitive to the assumptions made earlier.

The different structural parameter values for the symmetric and antisymmetric constants are too small to attribute the cause to any significant tunnelling effect. The values obtained for N_2-SO_2 are similar to those obtained by Juang *et al.*[12] However, it should be noted that their reported rotational constants differ by $\sim$15 MHz for A and $\sim$ -15 MHz for B and C from the constants reported here which will affect the parameters significantly.

6.5 Discussion

The tunnelling frequencies extracted for the simultaneous and O_3/SO_2 motions are effective constants with contributions from potentially several distinguishable motions within the symmetry limitations imposed by the analysis in section 6.3.1.

A tunnelling pathway not included in the analysis is the O_3/SO_2 rotation-tunnelling motion involving rotation of the monomer about its b-inertial axis, giving an intermediate configuration with the O_3/SO_2 plane coincident with the complex ac plane. This motion does not result in a reversal of the c-type dipole moment operator. With no change in parity, transitions correponding to this motion are not observed in the a- or c-type spectra.

It is likely that the tunnelling pathways of the O_3 and SO_2 moieties are analogous to those in other complexes such as Ar-O_3[4] and Ar-SO_2[5], although a DMA calculation by Juang *et al.* demonstrates that the N_2-SO_2 potential is much more anisotropic than for Ar-O_3. where the planar intermediate configuration has been shown to position the sulphur or central oxygen furthest away from the argon, corresponding to the smallest reduced mass for the motion[4,5]. By this argument, the rates for the other tunnelling pathways of O_3 and SO_2 are likely to be small, allowing the plethora of associated concerted, geared and antigeared motions with the N_2 to be ignored.

The remaining simultaneous tunnelling motions may involve the N_2 monomer rotating in or out of the ac plane of the complex and either geared or antigeared to the O_3/SO_2 motion. However, there is no information in the spectrum to distinguish the motion direction. The sum of each of these contributions gives the effective simultaneous tunnelling frequency. $(D_2CO)_2$ provides an example of a complex where geared and antigeared tunnelling frequencies have been deduced as a result of non-zero nuclear spin statistics for energy levels of both participating monomers. The analogous

spectrum of (H_2CO) is sensitive only to the difference of the two tunnelling motions. A similar study in N_2-O_3/SO_2 would require $^{17}O(I=5/2)$ isotopic substitution at the terminal oxygen positions.

The large positive value of the $\Delta\chi$ quadrupole constants indicates that the large amplitude motions of the N_2 are more confined to the ac inertial plane with the N_2-SO_2 potential more anisotropic than for N_2-O_3. The N_2 tunnelling frequency can only be probed by the centifugal distortion of the tunnelling motion effect on rotational and quadrupole parameters. If the N_2-OCS tunnelling frequency is scaled with the splitting between symmetric and antisymmetric B rotational constants then, disregarding any other effects, a rough ν_N of $\sim$16 MHz is obtained for N_2-O_3 and $\sim$350 kHz for N_2-SO_2. This correlates with the concerted tunnelling motion and may be due exclusively to this motion. However, a lower limit can be placed on the frequency of the nitrogen tunnelling motion by the requirement that effects in the spectrum resulting from the nitrogen nuclei becoming inequivalent are less than the experimental measurement uncertainty. These effects can be considered in terms of a more complete expression for the hyperfine energy in terms of a hamiltonian including a symmetric (or sum) hyperfine hamiltonian as derived in chapter 4 and antisymmetric (or difference) hamiltonian as described by Altman *et al.*[17] for N_2-HCl. A rough second order estimate of the contribution of the antisymmetric hamiltonian can be obtained by assuming a matrix element connecting the tunnelling states of about ⅓ and an asymmetry splitting between the inequivalent nitrogen nuclei of $<$250 kHz[18]. For effects of $\sim$1.0 kHz (equivalent to the experimental uncertainty) ν_N should be 7 MHz or more. Since the observed hyperfine is fitted quite well by the (symmetric) hamiltonian describe in section 4.3.3, this would suggest the nitrogen tunnelling frequency is greater than this estimate in both N_2-O_3 and N_2-SO_2 complexes.

Comparison between the structures of several complexes of O_3 and SO_2 can be made. O_3-C_2H_4[19] and O_3-C_2H_2[20] show tunnelling effects associated with the rotation of the C_2H_4 and C_2H_2. The tunnelling frequency associated with the rotation of the C_2H_4 moiety in C_2H_4-O_3 is estimated as 10 MHz. However, the difference in structure between the O_3 and SO_2 complexes is quite pronounced. Both O_3 and SO_2 monomers are approximately coplanar with C_2H_4 but with opposite tilt such that the sulphur of SO_2 is closer to the C_2H_4[9](C_2H_2[21]) than the terminal oxygens. The reverse is observed in the ozone complex. This behaviour correlates with the difference in the angle to the intermolecular axis (θ_S, figure 6.5) between N_2-O_3 and N_2-SO_2 estimated from the dipole moment projections ($\theta_S(O_3)\sim$ 70°, $\theta_S(SO_2)\sim$90°[12]). O_3-H_2O[13] and SO_2-H_2O[8] are more extreme examples with the two stuctures quite different.

References

[1]H. O. Leung, M. D. Marshall, R. D. Suenram, F. J. Lovas, *J. Chem. Phys.*, **90**, 700 (1989).

[2]F. J. Lovas, *J. Phys. Chem. Ref. Data*, **7**, 1445 (1978).

[3]K. H. Huber, G. Herzberg, *Molecular Spectra and Structure, Constants of Diatomics*, Van Nostrand, New York, 1979.

[4]J. S. Muenter, R. L. DeLeon, A. Yokozeki, *Faraday. Discuss. Chem. Soc.*, **73**, 63 (1982).

[5]L. H. Coudert, K. Matsumura, F. J. Lovas, *J. Mol. Spectrosc.*, **147**, 46 (1991).

[6]A. K. Lewin, M. A. Walsh, T. R. Dyke, *J. Mol. Spectrosc.*, **151**, 334 (1992).

[7]A. Taleb-Bendiab, K. W. Hillig II, R. Kuczkowski, *J. Chem. Phys.*, **94**, 6956 (1991).

[8]K. Matsumura, F. J. Lovas, R. D. Suenram, *J. Chem. Phys.*, **91**, 5887 (1989).

[9]A. M. Andrews, A. Taleb-Bendiab, M. S. Labarge, K. W. Hillig II, R. L. Kuczkowski, *J. Chem. Phys.*, **93**, 7030 (1990).

[10]A. Taleb-Bendiab, K. W. Hillig II, R. L. Kuczkowski, *J. Chem. Phys.*, **97**, 2996 (1992).

[11]E. J. Goodwin, A. C. Legon, *J. Chem. Phys.*, **85**, 6828 (1986).

[12]Y. D. Juang, M. A. Walsh, A. K. Lewin, T. R. Dyke, *J. Chem. Phys.*, **97**, 832 (1992).

[13]J. Z. Gillies, C. W. Gillies, R. D. Suenram, F. J. Lovas, T. Schmidt, D. Cremer, *J. Mol. Spectrosc.*, **146**, 493 (1991).

[14]R. C. Weast, *CRC Handbook of Chemistry and Physics*, CRC Press, Cleveland, 1974.

[15]F. J. Lovas, R. D. Suenram, L. H. Coudert, T. A. Blake, K. J. Grant, S. E. Novick, *J. Chem. Phys.*, **92**, 891 (1990).

[16]E. B. Wilson, JR, J. C. Decius, P. C. Cross, *Molecular Vibrations*, McGraw-Hill, New York, 1955; Appendix 1.

[17]R. S. Altman, M. D. Marshall, W. Klemperer, *J. Chem. Phys.*, **79**, 57 (1983).

[18]A. C. Legon, P. W. Fowler, *Z. Naturforsch.*, **47a**, 367 (1991).

[19]C. W. Gillies, J. Z. Gillies, R. D. Suenram, F. J. Lovas, E. Kraka, D. Cremer, *J. Am. Chem. Soc.*, **113**, 2412 (1991).

[20]J. Z. Gillies, C. W. Gillies, K. Matsumura, R. D. Suenram, F. J. Lovas, *J. Am. Chem. Soc.*, **113**, 6408 (1991).

[21]A. M. Andrews, K. W. Hillig II, R. L Kuczkowski, A. C. Legon, N. W. Howard, *J. Chem. Phys.*, **94**, 6947 (1991).

Chapter 7

Laser ablation experiments

7.1 Introduction

There is considerable interest in extending the methods developed employing supersonic nozzles to transient and refractory molecules and complexes of these molecules. Nozzles provide high resolution and low rotational temperature spectra although with the challenge of producing sufficiently high number densities of transient molecules in the expansion to observe microwave spectra of complexes, small clusters and vibrationally excited states. A number of methods of production combined with nozzle arrangements have been reported. Thermal heating before and during the expansion has allowed the microwave spectrum of low vapour pressure complexes eg Hg-OCS[1] and thermolysis products, such as $CH_2=PCl$[2] to be measured. Electrical discharges have been applied to nozzles employing a number of different arrangements to produce involatile diatomics such as AgCl[3], radicals including SO[4] and excited vibrational states in complexes such as Ar-HCl[5]. Pulsed laser ablation has been extensively used in other areas of spectroscopy[6] and was recently applied to Fourier-Transform microwave spectroscopy by Suenram *et al.*[7] to study transition metal oxides.

A laser ablation system based on a Smalley type nozzle system using rods of material and similar to the Suenram design has been developed. Pulsed lasers provide very short pulses of energy with quite low cycle times which translate into lower number densities and longer experiments. In this respect, laser ablation only provides an advantage over electric discharge nozzles in the types of species produced and the initial temperature in the nozzle ($\sim$2000 K). The initial work described here sought to improve the sensitivity and resolution of the laser ablation technique by employing a supersonic expansion along the axis of the cavity with the advantages discussed in sections 2.2.1 and 2.2.3. Diatomic molecules were used as prototypes for development of the ablation technique. Although the rotational constants of diatomics molecules are well characterized[8], in a number of cases the nuclear quadrupole and magnetic dipole hyperfine structure is poorly resolved and provides a simple test of improvement in resolution.

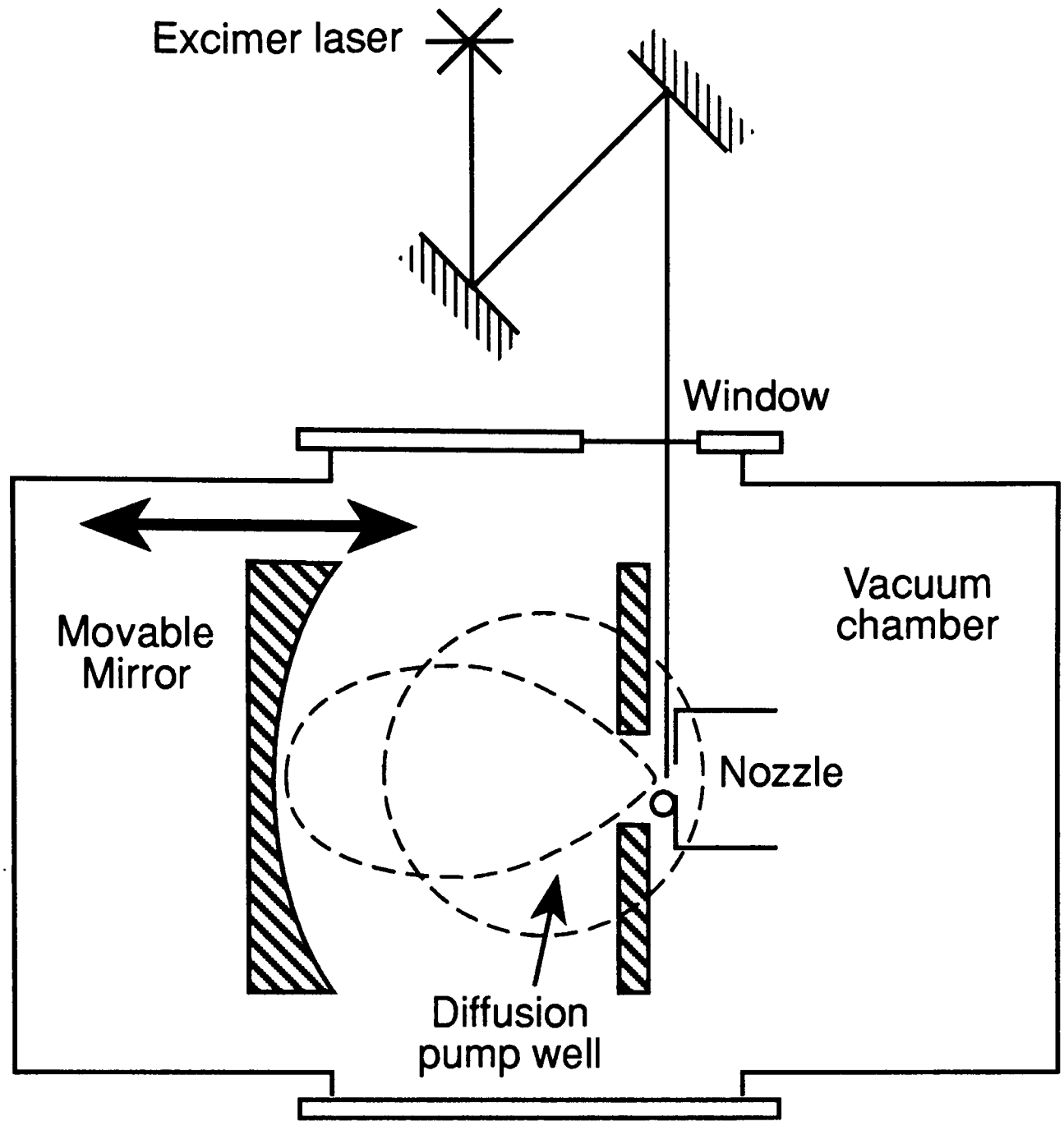

Figure 7.1a; Schematic diagram of the laser ablation experiment incorporating a hemispherical Fabry-Perot cavity.

i)

ii)

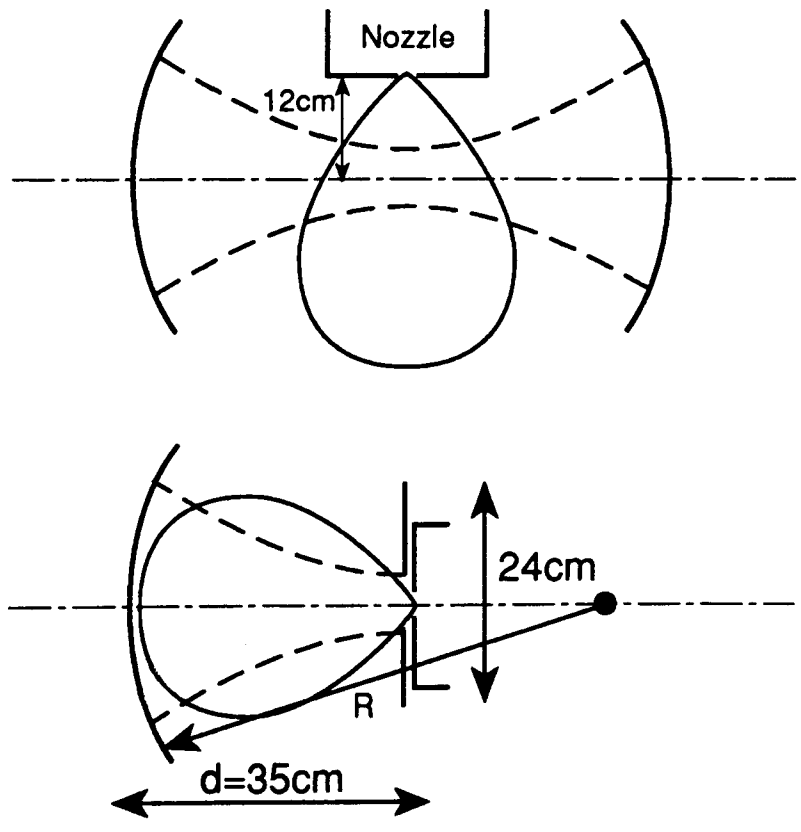

Figure 7.1b; Ablation configurations of the i) spherical cavity with perpendicular expansion (sample fixed to nozzle face plate) and ii) hemispherical Fabry-Perot cavity with parallel expansion.

7.2 Experimental development and results

7.2.1 Perpendicular expansion

Initial measurements used the experimental arrangement described in section 2.2.1 with a confocal Fabry-Perot cavity using two 50 cm radius of curvature mirrors. A LaserTechnics piezocrystal driven nozzle was mounted to give an expansion travelling at 90° to the cavity axis with the nozzle exit slightly within the volume between the mirrors (figure 7.1b). 20 ns duration pulses of laser light at 193 nm delivering 30-100 mJ of energy, generated using a Lambda Physik 200 ArF excimer laser, were introduced into the vacuum chamber through a quartz window. The beam direction was controlled using two mirrors and focused selectively in orthogonal planes using cylindrical lenses external to the vacuum chamber. This arrangement is illustrated in figure 7.1. Samples of AgCl, KCl and InF_3 were prepared by mixing powdered samples with water based wood glue and pressed to give tablets which were dried before use. The tablets were then glued to the nozzle face plate 1-2 mm from the nozzle exit so that the laser crossed the expansion before impinging on the sample. The rectangular profile laser beam was aligned and focussed to ablate material in the tablet parallel to the expansion axis. The laser pulses were timed to coincide with the centre of a 200μs argon gas pulse and signals were observed by setting the succeeding microwave pulse within a 50μs timing window. Although crude, this method produced single shot sensitivity with signal to noise of 50 for AgCl without the tablet appearing to interfere significantly with the expansion dynamics. A number of test results are given in table 7.1.

7.2.2 Rotating sample rod ablation nozzle; perpendicular expansion.

To enable an experiment involving a frequency search and extended ablation of the sample, an ablation nozzle of the type designed by Smalley *et al.*[9] was used. The design was based around a General Valve nozzle employing rods of material as illustrated in figure 7.3. By employing a drive mechanism the rods of material were rotated and translated through the nozzle presenting a new surface to the laser beam on each pulse. In figure 7.2, the gas flows along the z axis (of an arbitrary set of axes), the laser beam along the x axis and the rod translates along the y axis. The ablation process takes place in the throat of the 1 mm diameter nozzle, ~4mm from the nozzle exit. The entry hole for the laser in the nozzle throat is ½mm in diameter directly opposite the sample rod axis and at 90° to the nozzle axis to avoid affecting the gas flow. This arrangement was initially mounted to give an expansion perpendicular to the cavity axis.

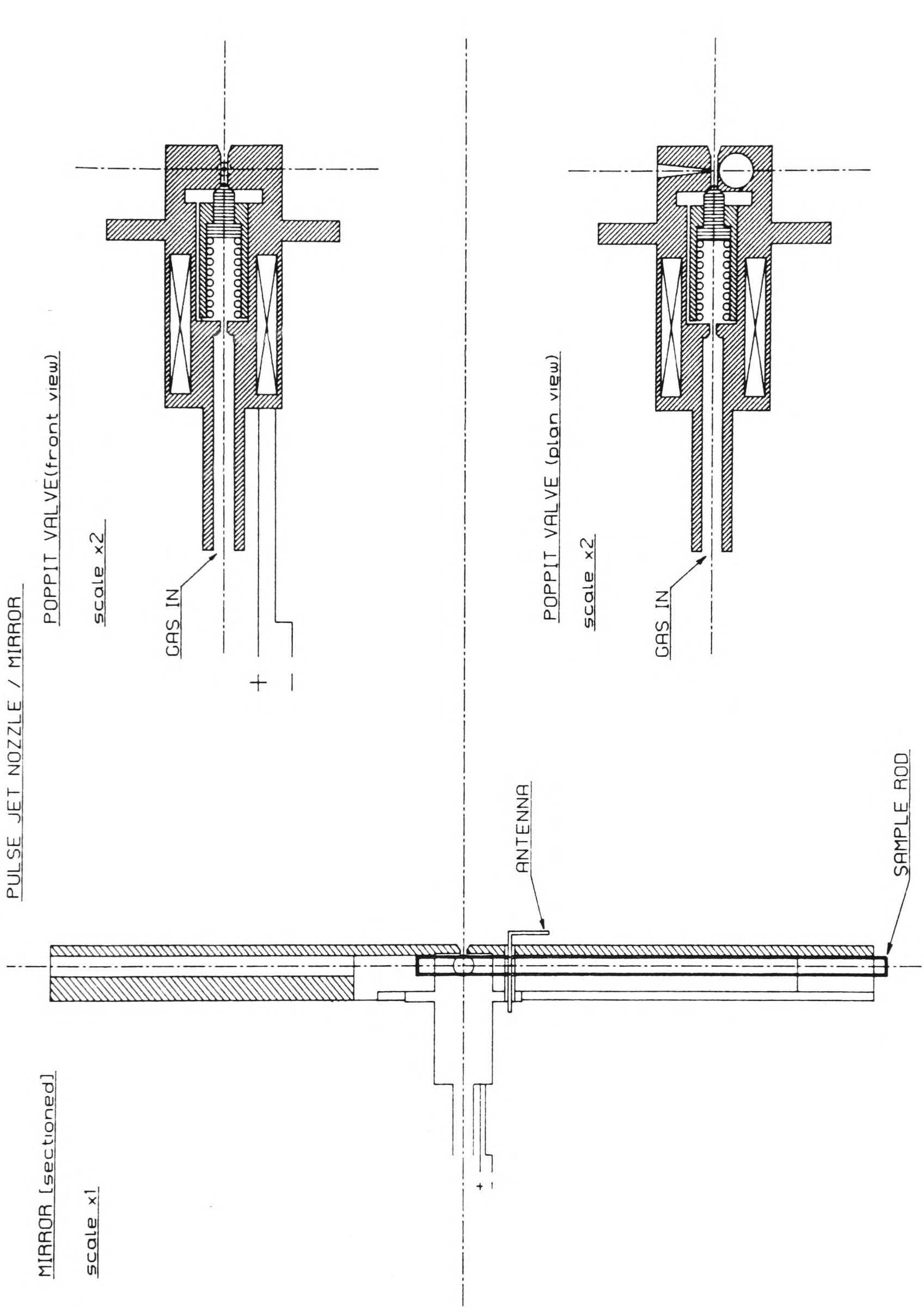

Figure 7.2; Rotating sample rod ablation nozzle and flat mirror arrangement for axial expansions of laser ablation products.

Table 7.1; Diatomic samples observed by laser ablation.

Molecule	**Precursor and preparation**	**Rotational transition**	**Comments/ observations**
AgCl	AgCl powder pressed on to mandrel	J=2-1 J=1-0	Several ^{35}Cl hyperfine transitions
KCl	KCl powder glued into tablet and rod.	J=2-1 J=1-0	Several ^{35}Cl hyperfine transitions
BaO	Pressed tablet of $Ba(OH)_2$ and glue.	J=1-0	^{138}Ba only
PbS	Glued rods of Pb and S, Pb foil and glued Pb powder rods with 3% OCS/Ar	J=1-0	ground and first excited vibrational levels ie ν=0 and 1.
InF	Tablet of InF_3 with glue	J=1-0	Several indium isomers
InCl	In foil rod 5% Cl_2/Ar	J=2-1	Several hyperfine lines observed
AlCl	Al rod, 5% Cl_2/Ar.	J=1-0	Weak.

Several results for diatomics employing the rod ablation apparatus are given in table 7.1 employing argon expansions with a backing pressure of 1 atm and a 10 Hz averaging rate. Cylindrical metal support rods (mandrels) supporting approximately 3 cm length, 1mm thickness of material were smoothed down to give 5mm diameter rods. Rod samples of AgCl and KCl were prepared from the powdered compound mixed with glue and pressed on to a steel supporting rod. A decrease in sensitivity from that observed using tablets of material was observed on ablating the rod and attributed to the smaller quantity of material ablated and high order clustering occurring in the nozzle exit channel. It was also expected that preparing the rod sample at higher pressures would improve the mechanical and ablation performance of the rods.

Several different methods to produce lead sulphide were tried. Mixing elemental sulphur and lead was found to give stronger signals than lead sulphide and observed easily on one pulse. This can be related to the relative melting points of lead (327°C), sulphur (113°C) and PbS (1114°C)[10]. A gas phase reaction between lead ablated from lead foil and OCS was found to reduce the signal strength by a factor of five. The first vibrationally excited state of PbS was also observed requiring 10000 more averages than the ground state for equivalent signal to noise.

7.2.3 Rotating sample rod ablation nozzle; axial expansion.

The rod drive was modified to mount behind a flat mirror producing the expansion along the cavity axis. A flat aluminium mirror was employed opposite a curved mirror with a 70 cm radius of curvature to halve the length of the Fabry-Perot cavity to ~35 cm (section 2.2.1, figure 2.2d). This was necessary to enable use of the laser window flange mounted centrally on the vacuum chamber. It also allowed the majority of the sample rod drive mechanism to be positioned in the diffusion pump well. The mirror design is illustrated in figure 7.2 and utilized the same sample rod nozzle, also in figure 7.2. Channels cut into the back surface of the flat mirror for the rod and laser beam, oriented at right angles, allowed the ablation process to occur 6mm from the nozzle exit. The exit channel in this arrangement was approximately 2mm longer than the previous transverse arrangement. Frequency tuning of the cavity was achieved by moving the curved mirror. The cavity bandwidth was approximately 1 MHz with the stepper motor driver providing tuning resolution of about 100 kHz per step. Microwave radiation was coupled in through the flat mirror using a coaxial dipole. To avoid possible mirror vibration associated with the General Valve and the rod drive mechanism, the flat mirror was quite firmly supported using a fixed support, the semi-rigid coaxial cable and the rod drive fitting.

The axial expansion ablation system was tested using lead sulphide. Improved resolution was obtained with line widths of 8 kHz although the sensitivity was about the same as the transverse expansion arrangement. Difficulties in obtaining identical ablation operating conditions and the increased exit channel length probably make comparisons unreliable. Since the use of an axial expansion laser ablation system has not been reported, CuCl was chosen for study since in previous measurements[11] the hyperfine has been poorly resolved with line widths of 400kHz (full width-half height) reported for low J transitions. An example spectrum is presented in figure 7.3. The hyperfine structure is due to perturbations resulting from the ^{35}Cl (I=3/2, $\chi(^{35}Cl)$=-32.1273(6) MHz) and ^{63}Cu (I=3/2, $\chi(^{63}Cu)$=16.1691(7)MHz) quadrupole moments[12]. Transition frequencies corresponding to those in figure 7.3 are given in table 7.2.

7.3 Discussion

A number of problems have been experienced with the arrangement described. The reduction in sensitivity when using the rod ablation system has been ascribed to higher complex formation and smaller quantities ablated. A similar conclusion based on mass spectroscopic data is reported by Haufler *et al.*[13] who describe a modified nozzle system to alleviate higher cluster formation. The success of the simplest ablation method described with the sample external to the nozzle suggests that this might provide a viable nozzle alternative although no practical method for prolonged ablation has yet been developed.

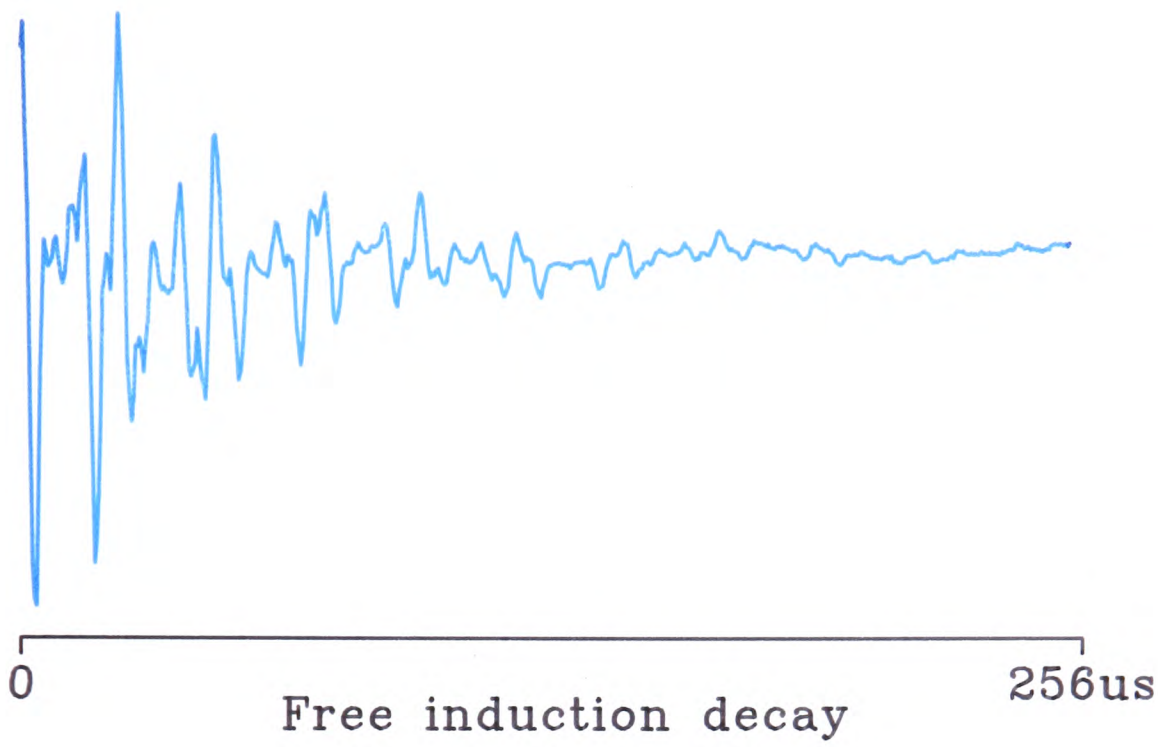

Figure 7.3; Spectrum of CuCl in an Ar expansion using the flat mirror ablation nozzle source.

Table 7.2; Microwave transition frequencies of $^{63}Cu^{35}Cl$ hyperfine around 10658.0 MHz.

J=1←0 transition		Frequency/MHz[b]
F(F_1')[a]	F"(F_1")[a]	
4(16)	3(16)	10657.9179
		10657.8770
2(12)	1(10)	10658.2196
		10658.2608
1(8)	0(4)	10657.2644
		10657.2242

[a] Coupling angular momenta according to $I_{Cu}+J=F_1$, $F_1+I_{Cl}=F$. F_1 quantum number convention reverse of Hoeft *et al.*[10]

[b] Doppler doublet frequencies. Transition frequency is given by the average of each pair.

Although suitable for photolysis, the excimer Laser at 193nm is not particularly suitable for ablation. In general the minimum energy output (30mJ) was in excess of that required. In the ablation process it is expected that following the initial removal of material from the sample surface, some proportion of the laser energy is absorbed by the gas phase molecule leading to dissociation and ionization. As a result several two body collision are required to reconstitute triatomics which may result in a number density too low to observe any transitions. This may in part explain the negative result in searching for transitions of $PbCl_2$ generated using solid $PbCl_2$ powder with glue and a 5% Cl_2/Ar expansion. Predictions were based on an electron diffraction structure[14].

The ablation technique has proven very successful in observing diatomic molecules. The dipole moments are in some cases very large, for example 5.70(15) D in the case of AgCl[15]. As a result, complexes with rare gases or nitrogen would be expected to be quite strongly bound and provide an interesting comparison with other rare gas complexes. In contrast, the electronic spectra of a number of rare gases- metal atom complexes with very low dipole moments have been reported[16]. The microwave spectrum of Hg-Ar[17] with a dipole moment estimated as $\ll$0.1D has been observed by FTMW so complexes with more refractory metals should prove to be a suitable challenge for the ablation experiment.

References

[1]M. Iida, Y Oshima, Y. Endo, *J. Chem. Phys.*, **94**, 6989 (1991).

[2]A. C. Legon, D. Stephenson, *J. Chem. Soc. Farad. Trans.*, **87**, 3325 (1991).

[3]C. Styger, M. C. L. Gerry, *Chem. Phys. Lett.*, **188**, 213 (1991).

[4]J. U. Grabow, N. Heineking, W. Stahl, *Z. Naturforsch.*, **46a**, 914 (1990).

[5]J. W. Bevan, A. C. Legon, C. A. Rego, J. Roach, *Chem. Phys. Lett.*, **198**, 347 (1992).

[6]T. C. Steimle, D. A. Fletcher, K. Y. Jung, C. T. Scurlock, *J. Chem. Phys.*, **97**, 2909 (1992).

[7]R. D. Suenram, G. T. Fraser, F. J. Lovas, *J. Mol. Spectrosc.*, **148**, 114 (1991); R. D. Suenram, F. J. Lovas, G. T. Fraser, K. Matsumura, *J. Chem. Phys.*, **92**, 4724 (1990).

[8]K. P.. Huber, G. Herzberg, *Molecular Spectra and Molecular Structure*, **Vol. 4**, Van Nostrand, New York, 1979.

[9]D. E. Powers, S. G. Hansen, M. E. Geusic, A. C. Pulu, J. B. Hopkins, T. G. Dietz, M. A. Duncan, P. R. R. Langridge-Smith, R. E. Smalley, *J. Phys. Chem.*, **86**, 2557 (1982).

[10]R. C. Weast (Ed.) *CRC Handbook of Chemistry and Physics*, 55th Edition, CRC Press, Cleveland, 1974.

[11]E. Tiemann, J. Hoeft, *Z. Naturforsch.*, **32a**, 1477 (1977).

[12]R. Low, T. D. Varberg, J.P.Connelly, A. R. Auty, J. M. Brown, B. J. Howard. In preparation (1993).

[13]R. E. Haufler, L. S. Wang, L. P. F. Chibante, C. Jin, J. Conceicao, Y. Chai, R. E. Smalley, *Chem. Phys. Lett.*, **179**, 449 (1991)

[14]M. W. Lister, L. E. Sutton, *Trans. Farad. Soc.*, **37**, 406 (1941).

[15]F. J. Lovas, E. Tiemann, *J. Phys. Chem. Ref. Data*, **3**, 609 (1974).

[16]M. J. McQuaid, J. L. Gole, M. C. Heaven, *J. Chem. Phys.*, **92**, 2733 (1990).

[17]Y. Ohshima, M. Iida, Y. Endo, *J. Chem. Phys.*, **92**, 3990 (1990).

Appendix I

Transition frequencies for Ar_2-OCS isotopomers

Table I.1; Observed rotational transition frequencies for Ar_2-OCS. Residuals were calculated using Watson S reduction parameters fitted to the data. Unweighted averages of multiple observations are given.

Ar_2-OCS Transitions		Observed	Observed-
$J'K_a'K_c'$	$J''K_a''K_c''$	Frequency/MHz[a]	Calculated/kHz
3 1 2	2 0 2	7516.1557	-0.9
3 2 1	2 1 1	7458.8167	-0.7
3 2 2	2 1 2	7708.9054	-1.5
3 3 0	2 2 0	7901.2191	-1.1
3 3 1	2 2 1	8028.4370	-1.5
4 1 3	3 0 3	10137.6445	1.7
4 2 3	3 1 3	10193.4428	-1.0
4 2 2	3 1 2	9930.3470	-0.1
4 3 2	3 2 2	10320.3778	-1.0
4 3 1	3 2 1	10031.4074	-0.2
4 4 1	3 3 1	10747.8617	-0.1
4 4 0	3 3 0	10668.3796	-0.3
5 1 4	4 0 4	12716.3166	3.0
5 2 4	4 1 4	12727.7844	3.4
5 2 3	4 1 3	12568.4392	0.1
5 3 3	4 2 3	12739.9607	-1.6
5 3 2	4 2 2	12373.0649	1.1
5 4 2	4 3 2	12964.4796	0.9
5 4 1	4 3 1	12692.5780	0.2
5 5 1	4 4 1	13485.5474	2.1
5 5 0	4 4 0	13447.1914	-0.2
6 1 5	5 0 5	15274.0642	-1.2
6 2 5	5 1 5	15276.0351	-0.9
6 2 4	5 1 4	15197.0784	-1.6
6 3 4	5 2 4	15245.1644	-4.4
6 3 3	5 2 3	14945.4901	0.2
6 4 3	5 3 3	15307.8236	0.3
6 4 2	5 3 2	14883.3310	-1.9
6 5 2	5 4 2	15642.6218	2.8
6 5 1	5 4 1	15441.4773	3.6

Ar_2-OCS Transitions		Observed	Observed-
$J'K'_aK'_c$	$J''K''_aK''_c$	Frequency/MHz[a]	Calculated/kHz
6 6 1	5 5 1	16233.8834	-1.8
6 6 0	5 5 0	16217.9793	-1.9
7 1 6	6 0 6	17825.9465	-0.2
7 2 6	6 1 6	17826.2522	1.2
7 2 5	6 1 5	17776.4280	0.0
7 3 5	6 2 5	17786.7606	-0.4
7 3 4	6 2 4	17622.6783	4.0
7 4 4	6 3 4	17763.7990	-3.6
7 4 3	6 3 3	17323.8380	0.5
7 5 3	6 4 3	17907.8842	-1.7
7 5 2	6 4 2	17486.7657	-0.9
7 6 2	6 5 2	18350.5344	2.0
4 0 4	3 0 3	6730.1938	-0.4
4 1 4	3 1 3	6721.8190	-0.8
4 1 3	3 1 2	7813.1039	-0.3
4 2 3	3 2 2	7632.0966	1.0
5 0 5	4 0 4	8282.9618	0.4
5 1 5	4 1 4	8281.6755	-1.2
5 1 4	4 1 3	9308.8651	0.1
6 0 6	5 0 5	9838.7578	-0.1
6 1 6	5 1 5	9838.5819	0.8
6 1 5	5 1 4	10840.7133	0.1
7 0 7	6 0 6	11394.8839[b]	7.5
7 1 7	6 1 6	11394.8456[b]	-8.0
7 1 6	6 1 5	12390.6396	0.4
7 2 6	6 2 5	12388.7965	0.3
8 0 8	7 0 7	12950.8194[c]	2.8
8 1 8	7 1 7	12950.8194[c]	0.0
4 1 4	4 0 4	1.485[d]	-2.4
6 2 5	6 1 5	2.173[d]	-0.3
8 3 6	8 2 6	2.233[d]	-2.7
5 5 0	5 5 1	25.237[d]	-0.3
6 5 1	6 5 2	216.855[d]	-0.1

[a] Transverse expansion, experimental uncertainty in the line positions is 2 kHz.

[b] Broad line shape. Uncertainty increased to 4 kHz.

[d] Weighted 1/10. MBER measurements from K. Leopold, *Ph.D. Thesis,* Harvard University, 1983.

Table I.2; Observed rotational transition frequencies for Ar_2-$OC^{34}S$. Residuals were calculated using Watson S reduction parameters fitted to the data. Unweighted averages of multiple observations are given.

Ar_2-$OC^{34}S$ Transitions		Observed	Observed-
$J'K_a'K_c'$	$J''K_a''K_c''$	Frequency/MHz	Calculated/kHz
3 1 2	2 0 2	7368.4532[a]	-1.6
3 2 2	2 1 2	7607.6204[a]	0.2
3 2 1	2 1 1	7333.1598[a]	0.0
3 3 1	2 2 1	7971.6671	0.9
3 3 0	2 2 0	7846.3593	-1.1
4 1 3	3 0 3	9958.34665	0.0
4 2 3	3 1 3	10038.2634	-0.1
4 2 2	3 1 2	9729.8947	0.4
4 3 2	3 2 2	10197.3580	0.0
4 3 1	3 2 1	9891.7134	-0.2
4 4 1	3 3 1	10681.9307	0.0
4 4 0	3 3 0	10611.7985	0.0
5 1 4	4 0 4	12507.8015	1.2
5 2 4	4 1 4	12526.7071[a]	-3.7
5 2 3	4 1 3	12315.8058	0.7
5 3 3	4 2 3	12551.8321	-0.4
5 3 2	4 2 2	12140.4696	1.1
5 4 2	4 3 2	12828.0264	0.7
5 4 1	4 3 1	12561.6962	0.5
5 5 1	4 4 1	13412.3129	1.2
5 5 0	4 4 0	13382.0621	1.1
6 1 5	5 0 5	15030.40085	0.5
6 2 5	5 1 5	15034.1221	0.0
6 2 4	5 1 4	14923.6429	1.1
6 3 4	5 2 4	15001.07825	-0.9
6 3 3	5 2 3	14625.93245	0.1
6 4 3	5 3 3	15096.3754	-1.3
6 4 2	5 3 2	14643.1152	-1.7
6 5 1	5 4 1	15323.9278	4.1
6 6 1	5 5 1	16153.2560	-1.3
6 6 0	5 5 0	16141.9747	-0.5

Ar_2-$OC^{34}S$ Transitions		Observed	Observed-
$J'K_a'K_c'$	$J''K_a''K_c''$	Frequency/MHz	Calculated/kHz
4 1 3	3 1 2	7711.1272[b]	0.3
4 2 2	3 2 1	8521.3158[b]	0.2
5 0 5	4 0 4	8163.2458[b]	0.3
5 1 4	4 1 3	9183.7733[b]	-0.6
5 2 4	4 2 3	9110.8585[b]	-0.1

[a] Recorded using a transverse expansion. Weighted ¼ according to an experimental uncertainty of 2kHz, the remainder weighted 1 for an uncertainty of 1kHz.

[b] Data provided by Y. Xu and M. C. L. Gerry. (Y. Xu, M.C.L. Gerry, J. P. Connelly, B. J. Howard, *J. Chem. Phys.*, **98**, 2735 (1993)).

Appendix II

Transition frequencies for N_2-OCS

Table II.1; Observed rotational and hyperfine transition frequencies for the symmetric tunnelling/symmetric nuclear spin states of N_2-OCS. Residuals were calculated using the Watson S reduction hamiltonian (section 3.3) and hyperfine hamiltonian described in sections 4.3.3 and 4.4. Unweighted averages of multiple observations are given. The labelling scheme, I=+/- defined in section 4.3.3 for distinguishing the mixed I=0 and I=2 states is used interchangeably with I=0(-) and I=2(+) for F=J levels and indicated as subscripts.

Symmetric N_2-OCS Transition		Hyperfine	Observed	Observed-
$J'K_a'K_c'$	$J''K_a''K_c''$	F'I'-F''I''	Frequency/MHz	Calculated/kHz
1 1 1	0 0 0	$1\ 0_-$-1 0	8306.5117	-0.1
		$1\ 2_+$-1 0	8308.2559	-0.6
		2 2-1 0	8308.3383	0.5
		3 2-2 0	8307.5209	0.5
2 1 2	1 0 1	1 2-1 0_-	10873.2133	-0.6
		3 2-3 2	10874.2536	-2.7
		2 2_+-1 2_+	10875.4431	-3.1
		2 0_--1 0_-	10873.3523	-1.7
		3 2-2 2	10875.8710	-0.1
		4 2-3 2	10875.0166	0.6
		1 2-1 2_+	10876.6622	5.1
		2 2_+-2 2	10875.6044	-1.5
		1 2-2 2	10876.8234	6.5
3 1 3	2 0 2	1 2-0 2	13292.7890	-0.3
		2 2-1 2	13292.9518[a]	-0.3
		3 2_+-2 2_+	13293.8204	-3.2
		3 0_--2 0_-	13293.1370[a]	-0.8
		4 2-3 2	13293.8772[a]	1.5
		5 2-4 2	13293.4464	1.0
		3 2_+-3 2_+	13293.2926[a]	-4.1
		2 2-2 2_+	13295.3406	5.5
		3 0_--3 2	13295.3091[a]	6.1
		4 2-4 2	13292.3294	-3.8
		2 2-2 0_-	13292.6415[a]	-1.6

Symmetric N_2-OCS Transition		Hyperfine	Observed	Observed-
$J'K_a'K_c'$	$J''K_a''K_c''$	F'I'-F''I''	Frequency/MHz	Calculated/kHz
4 1 4	3 0 3	2 2-1 2	15578.7733	0.7
		3 2-2 2	15578.8726	-0.5
		$4\ 2_+$-$3\ 2_+$	15579.3392	-1.6
		$4\ 0_-$-$3\ 0_-$	15578.9216	1.4
		5 2-4 2	15579.3273	-1.0
		6 2-5 2	15579.0776	1.9
		2 2-2 2	15579.8479	5.6
		3 2-3 2_+	15580.9056	7.3
		3 2-3 0_-	15578.2097	0.4
		$4\ 2_+$-4 2	15578.5566	-3.9
		$4\ 0_-$-4 2	15580.8363	7.4
		5 2-5 2	15577.8337	-3.6
5 0 5	4 1 4	3 2-2 2	9914.0544	1.4
		4 2-3 2	9913.8426	0.5
		$5\ 2_+$-$4\ 2_+$	9913.6756	0.8
		$5\ 0_-$-$4\ 0_-$	9914.0696	0.1
		6 2-5 2	9913.8884	0.1
		7 2-6 2	9914.0856	-1.7
		$5\ 2_+$-5 2	9912.9053	-1.8
		6 2-6 2	9912.6464	-3.6
6 0 6	5 1 5	5 2-4 2	13183.1998	1.9
		$6\ 2_+$-$5\ 2_+$	13183.1028	1.0
		7 2-6 2	13183.2496	-0.3
		8 2-7 2	13183.3736	-0.8
		$6\ 0_-$-$5\ 0_-$	13183.3537	-1.5
2 1 1	2 0 2	$2\ 0_-$-$2\ 0_-$	6056.8997[a]	2.9
		3 2-3 2	6057.9485[a]	1.5
		4 2-4 2	6057.1826	0.3
3 1 2	3 0 3	1 2-1 2	6557.2410	2.5
		$3\ 2_+$-$3\ 2_+$	6557.9823	-2.6
		$3\ 0_-$-$3\ 0_-$	6557.3400	1.9
		4 2-4 2	6557.7968	-0.9
		5 2-5 2	6557.4409	1.0
		4 2-5 2	6556.3019	-4.8
		2 2-2 2	6557.4977	1.2
		2 2-1 2	6556.4242	-2.5

Symmetric N_2-OCS Transition		Hyperfine	Observed	Observed-
$J'K_a'K_c'$	$J''K_a''K_c''$	F'I'-F''I''	Frequency/MHz	Calculated/kHz
4 1 3	4 0 4	2 2-2 2	7265.7841	3.8
		3 2-3 2	7265.9405	1.3
		4 2_+-4 2_+	7266.1924	-2.3
		4 0_--4 0_-	7265.8270	2.5
		5 2-5 2	7266.0688	-1.2
		6 2-6 2	7265.8705	1.7
		6 2-5 2	7267.3330	3.9
		3 2-4 2_+	7267.7848	9.7
		5 2-6 2	7264.6055	-4.2
		3 2-2 2	7264.7940	-2.9
		4 2-3 2	7264.3482[b]	-10.8
2 2 0	2 1 1	2 2_+-2 2_+	16299.0428	-2.1
		2 0_--2 0_-	16294.9201	0.5
		3 2-3 2	16298.2347	-1.1
		4 2-4 2	16295.9194	1.4
		3 2-2 2_+	16298.5089	0.5
		4 2-3 2	16296.7039	4.9
		2 2_+-3 2	16298.7692	-3.1
2 2 1	2 1 2	2 2_+-2 2_+	17205.4810[b]	-1.4
		2 0_--2 0_-	17201.3921[b]	2.4
		3 2-3 2	17204.6801[b]	0.1
		4 2-4 2	17202.3837[b]	2.3
		1 2-2 2_+	17203.0294[b]	7.8
		3 2-2 2_+	17204.9475[b]	2.4
		3 2-2 0_-	17203.5887[b]	-5.4
		4 2-3 2	17203.1469[b]	5.9
		2 2_+-3 2	17205.2147[b]	-2.6
		3 2-4 2	17203.9166[b]	-3.8
3 2 1	3 1 2	1 2-1 2	15891.2035	0.4
		2 2-2 2	15892.0104	-1.2
		3 2_+-3 2_+	15893.5357	-6.8
		3 0_--3 0_-	15891.5125	1.8
		4 2-4 2	15892.9497	-3.5
		5 2-5 2	15891.8291	1.9

Symmetric N_2-OCS Transition		Hyperfine	Observed	Observed-
$J'K_a'K_c'$	$J''K_a''K_c''$	F'I'-F''I''	Frequency/MHz	Calculated/kHz
3 2 2	3 1 3	2 2-2 2	17666.4680	0.2
		$3\ 2_+$-$3\ 2_+$	17667.9746	-5.9
		$3\ 0_-$-$3\ 0_-$	17665.9788	4.1
		4 2-4 2	17667.3966	-2.6
		5 2-5 2	17666.2910	2.3
		1 2-1 2	17665.6735	4.6
4 2 2	4 1 3	2 2-2 2	15416.0634	2.2
		3 2-3 2	15416.5769	-0.5
		$4\ 2_+$-$4\ 2_+$	15417.3998	-7.0
		$4\ 0_-$-$4\ 0_-$	15416.2023	3.6
		5 2-5 2	15416.9952	-2.7
		6 2-6 2	15416.3424	3.9
		5 2-$4\ 2_+$	15417.7797	1.2
4 2 3	4 1 4	2 2-2 2	18288.0391	5.1
		3 2-3 2	18288.5441	0.8
		$4\ 2_+$-$4\ 2_+$	18289.3539	-8.2
		$4\ 0_-$-$4\ 0_-$	18288.1754	3.5
		5 2-5 2	18288.9558	-4.2
		6 2-6 2	18288.3133	1.8
3 0 3	2 0 2	$3\ 2_+$-$2\ 2_+$	8572.6626	-0.5
		5 2-4 2	8572.8618	-0.1
		4 2-3 2	8572.9154[a]	-1.1
		2 2-$2\ 0_-$	8571.9970[a]	0.4
		$3\ 2_+$-3 2	8572.1348[a]	-1.4
		2 2-1 2	8572.3061[a]	0.3
		$3\ 0_-$-$2\ 0_-$	8572.6594[a]	-0.8
4 0 4	3 0 3	3 2-2 2	11370.9334	-0.3
		$4\ 2_+$-$3\ 2_+$	11371.1228	-0.4
		$4\ 0_-$-$3\ 0_-$	11371.1088	0.3
		6 2-5 2	11371.2176	0.0
		5 2-4 2	11371.2474	-0.9
		2 2-1 2	11371.0066	0.3

Symmetric N_2-OCS Transition		Hyperfine	Observed	Observed-
$J'K_a'K_c'$	$J''K_a''K_c''$	F'I'-F''I''	Frequency/MHz	Calculated/kHz
3 1 3	2 1 2	3 0$_-$-2 0$_-$	8155.2276	0.0
		5 2-4 2	8155.2426	0.6
		2 2-1 2	8154.8722	-0.6
		4 2-3 2	8154.8889	-0.5
		3 2_+-2 2_+	8154.5711	-1.4
4 1 3	3 1 2	4 2_+-3 2_+	12079.3313	-1.7
		3 2-2 2	12079.3765	0.0
		5 2-4 2	12079.5201	-0.5
		4 0$_-$-3 0$_-$	12079.5965	1.6
		6 2-5 2	12079.6471	0.6
		2 2-1 2	12079.5524	4.3
4 1 4	3 1 3	4 2_+-3 2_+	10858.1790	-1.3
		5 2-4 2	10858.3663	0.2
		6 2-5 2	10858.4932	0.9
		3 2-2 2	10858.2269	0.1
		4 0$_-$-3 0$_-$	10858.4433	0.6
5 1 5	4 1 4	4 2-3 2	13549.7169	0.4
		3 2-2 2	13549.8119	1.2
		6 2-5 2	13549.8335	-2.1
		7 2-6 2	13549.8909	-0.8
		5 0$_-$-4 0	13549.8522	1.8

[a] Perturbed hyperfine level due to the accidental near degeneracy of the 1_{10} and 2_{02} rotational levels. Second order quadrupole hyperfine correction included in order to fit the transition (see section 5.3).

[b] Poor/weak transition weighted ¼. General experimental uncertainty ~ 1 kHz

Table II.2; Observed rotational and hyperfine transition frequencies for the antisymmetric tunnelling/antisymmetric nuclear spin states of N_2-OCS. Residuals were calculated using the Watson S reduction hamiltonian (section 3.3) and hyperfine hamiltonian described in section 4.3.3 and 4.4. Unweighted averages of multiple observations are given.

Antisymmetric N_2-OCS Transition		Hyperfine	Observed	observed-
$J'K_a'K_c'$	$J''K_a''K_c''$	F'I'-F''I''	Frequency/MHz	Calculated/kHz
1 1 1	0 0 0	1 1 - 1 1	8305.7427	-1.1
		2 1 - 1 1	8306.2913	-0.3
		0 1 - 1 1	8307.1123	-1.7
2 1 2	1 0 1	1 1 - 0 1	10870.5434	-0.7
		2 1 - 1 1	10868.7229	1.0
		3 1 - 2 1	10869.2305	-0.9
		2 1 - 2 1	10869.8132	1.4
3 1 3	2 0 2	2 1 - 1 1	13285.4147	0.9
		3 1 - 2 1	13284.8225	2.3
		4 1 - 3 1	13285.0816	-0.8
		2 1 - 2 1	13283.5953	-3.4
		3 1 - 3 1	13285.9892	2.8
4 1 4	3 0 3	3 1 - 2 1	15569.7887	-0.8
		4 1 - 3 1	15569.4796	2.5
		5 1 - 4 1	15569.6363	-0.4
		3 1 - 3 1	15568.1546	-4.1
5 0 5	4 1 4	4 1 - 3 1	9859.5080	1.2
		6 1 - 5 1	9859.4917	0.0
		5 1 - 4 1	9859.6893	-1.5
6 0 6	5 1 5	5 1 - 4 1	13121.1837	0.9
		7 1 - 6 1	13121.1663	0.3
		6 1 - 5 1	13121.2957	-1.3
2 1 1	2 0 2	1 1 - 1 1	6056.4023	-0.9
		2 1 - 2 1	6055.5026	1.1
		3 1 - 3 1	6056.0804	-0.2

Antisymmetric N_2-OCS Transition		Hyperfine	Observed	observed-
$J'K_a'K_c'$	$J''K_a''K_c''$	F′I′-F″I″	Frequency/MHz	Calculated/kHz
3 1 2	3 0 3	2 1 - 2 1	6549.1560	-2.5
		3 1 - 3 1	6548.7592	1.1
		4 1 - 4 1	6549.0529	-1.2
		3 1 - 2 1	6550.3924	3.6
		3 1 - 4 1	6549.9675	2.3
4 1 3	4 0 4	3 1 - 3 1	7247.0750	-2.0
		4 1 - 4 1	7246.8560	1.9
		5 1 - 5 1	7247.0297	-1.2
2 2 0	2 1 1	1 1 - 1 1	16318.2379	0.0
		2 1 - 2 1	16315.5101	-0.6
		3 1 - 3 1	16317.2632	0.5
		2 1 - 1 1	16316.4285	4.4
		3 1 - 2 1	16316.6731	-2.5
		2 1 - 3 1	16316.0998	1.9
2 2 1	2 1 2	1 1 - 1 1	17213.0311	-1.2
		2 1 - 2 1	17210.3110	-1.6
		3 1 - 3 1	17212.0597	0.1
		2 1 - 1 1	17211.2199	3.8
		3 1 - 2 1	17211.4763	-2.8
		2 1 - 3 1	17210.8944	1.3
3 2 1	3 1 2	2 1 - 2 1	15917.0145	-2.7
		3 1 - 3 1	15915.7950	3.3
		4 1 - 4 1	15916.6978	-0.9
3 2 2	3 1 3	2 1 - 2 1	17669.3384	-3.2
		3 1 - 3 1	17668.1232	3.3
		4 1 - 4 1	17669.0230	-0.7
4 2 2	4 1 3	3 1 - 3 1	15444.7309	-3.1
		4 1 - 4 1	15444.0427	4.7
		5 1 - 5 1	15444.5894	-1.7

Antisymmetric N_2-OCS Transition		Hyperfine	Observed	observed-
$J'K_a'K_c'$	$J''K_a''K_c''$	F'I'-F''I''	Frequency/MHz	Calculated/kHz
4 2 3	4 1 4	3 1 - 3 1	18282.4023	-3.8
		4 1 - 4 1	18281.7149	5.2
		5 1 - 5 1	18282.2618	-0.9
3 0 3	2 0 2	4 1 - 3 1	8549.1060	-0.9
		3 1 - 2 1	8549.1485	0.7
		2 1 - 1 1	8549.3340	1.9
4 0 4	3 0 3	5 1 - 4 1	11341.5065	0.3
		4 1 - 3 1	11341.5305	0.0
		3 1 - 2 1	11341.6114	-0.3
3 1 3	2 1 2	2 1 - 1 1	8135.9863	-0.2
		4 1 - 3 1	8135.9797	-1.2
		3 1 - 2 1	8136.3047	0.2
4 1 3	3 1 2	5 1 - 4 1	12039.4833	0.4
		3 1 - 2 1	12039.5293	-1.0
		4 1 - 3 1	12039.6273	0.7
4 1 4	3 1 3	5 1 - 4 1	10833.6606	-0.6
		3 1 - 2 1	10833.7093	1.5
		4 1 - 3 1	10833.8044	-0.3
5 1 5	4 1 4	6 1 - 5 1	13519.8936	0.9
		4 1 - 3 1	13519.9326	0.2
		5 1 - 4 1	13519.9706	-0.1

Experimental measurement uncertainty ~ 1kHz.

Table II.3 Fit of the quadrupole constants of N_2-OCS using a three parameter potential (section 5.3.2)

Quadrupole constant[a]	Observed x 10^{-3} [b]	Obs−Calc x 10^{-3}	weight [c]
$\frac{\chi_{aa}}{\chi_{N_2}}$ (*symmetric*)	665.19(22)	0.95	1.0
$\sqrt{\frac{2}{3}}\frac{\Delta\chi}{\chi_{N_2}}$ (*symmetric*)	−6.60(35)	−0.64	0.4
$\frac{\chi_{aa}}{\chi_{N_2}}$ (*antisymmetric*)	673.84(32)	−2.5	0.5
$\sqrt{\frac{2}{3}}\frac{\Delta\chi}{\chi_{N_2}}$ (*antisymmetric*)	−3.39(56)	1.7	0.16
$\sqrt{\frac{2}{3}}\frac{\chi_{ab}}{\chi_{N_2}}$ (*symmetric*)	85.4	−2.1	0.01

[a] Quadrupole coupling constant normalized to give angular form as in equation 5.11. χ_{N2} = -5.39 MHz (T. A. Scott, *Phys. Rep. C*, 89 (1976)).
[b] Obtained from least squares fit of spectral data.
[c] Weighted according to standard deviations.

Appendix III

Transition frequencies of N_2-O_3

Table III.1; Observed rotational and hyperfine transition frequencies for the symmetric tunnelling/symmetric nuclear spin states of N_2-O_3. Residuals were calculated using the Watson S reduction hamiltonian (section 3.3) and hyperfine hamiltonian described in sections 4.3.3 and 4.4. Unweighted averages of multiple observations are given. The labelling scheme, I=+/− defined in section 4.3.3 for distinguishing the mixed I=0 and I=2 states is used interchangeably with I=0(−) and I=2(+) for F=J level and indicated by subscripts.

Symmetric N_2-O_3 Transition		Hyperfine	Observed	Observed−
$J'\ K_a'\ K_c'$	$J''\ K_a''\ K_c''$	$F'I'-F''I''$	Frequency/MHz	Calculated/kHz
1 1 0	0 0 0	1 0_--0 0	13911.8900	3.2
		3 2-2 2	13912.3924	1.3
		1 2_+-2 2	13912.7569	0.2
		2 2-2 2	13912.7967	-1.0
2 1 1	1 0 1	2 0_--1 0_-	18122.7479	1.3
		3 2-3 2	18123.1168	-3.4
		4 2-3 2	18124.0636	-0.4
		2 2_+-2 2	18124.1858	-3.3
		3 2-2 2	18124.5160	-2.5
		1 2-1 2_+	18125.5555	0.2
5 0 5	4 1 3	3 2-2 2	8498.4012	0.2
		4 2-3 2	8498.4588	0.3
		5 0_--4 0_-	8498.4770	0.4
		7 2−6 2	8498.5546	0.2
		6 2-5 2	8498.6873	-0.8
		5 2_+-4 2_+	8498.6961	0.9
7 0 7	6 1 5	5 2-4 2	14600.4842	0.3
		7 0_--6 0_-	14600.5447	1.1
		9 2-8 2	14600.6055	1.9
		6 2-5 2	14600.6782	-0.8
		8 2-7 2	14600.8581	-0.6
		7 2_+-6 2_+	14601.0041	-2.1

Symmetric N_2-O_3 Transition		Hyperfine	Observed	Observed-
J′ K_a' K_c'	J″ K_a'' K_c''	F′I′-F″I″	Frequency/MHz	Calculated/kHz
1 1 1	1 0 1	3 2-3 2	9698.7805	0.6
		1 0_--2 2	9698.9562	-0.8
		2 2-3 2	9699.7698	1.9
		1 0_--1 2_+	9698.8166	-1.8
		3 2-2 2	9700.1795	1.3
2 1 2	2 0 2	1 2-0 2	9444.8471	-0.3
		2 2_+-1 2	9444.9987	0.0
		2 0_--2 0_-	9445.4494	1.3
		3 2-4 2	9445.4624	0.4
		4 2-4 2	9445.8523	0.3
		2 2_+-3 2	9446.6496	-0.9
		3 2-3 2	9446.7872	0.6
		2 2_+-2 2_+	9447.1116	-1.2
		4 2-3 2	9447.1779	1.3
		3 2-2 2_+	9447.2484	-0.5
		1 2-2 2_+	9447.7346	1.8
3 1 3	3 0 3	3 2_+-2 2	9074.9733	-3.9
		2 2-1 2	9075.0102	-0.9
		4 2-5 2	9075.1339	-1.2
		1 2-1 2	9075.5139	0.3
		3 0_--3 0_-	9075.6730	0.5
		5 2-5 2	9075.8364	0.6
		2 2-2 2	9075.9285	0.1
		4 2-4 2	9076.4126	0.4
		3 2_+-3 2_+	9076.7137	-0.3
4 1 4	4 0 4	4 0_--4 0_-	8600.2793	1.1
		6 2-6 2	8600.3712	1.1
		3 2-3 2	8600.5236	0.1
		5 2-5 2	8600.7984	0.3
		4 2_+-4 2_+	8601.0630	-0.5
		3 2-4 2_+	8602.0883[a]	3.9
		6 2-5 2	8601.6010[a]	-9.0

Symmetric N_2-O_3 Transition		Hyperfine	Observed	Observed-
J′ K_a' K_c'	J″ K_a'' K_c''	F′I′-F″I″	Frequency/MHz	Calculated/kHz
5 1 5	5 0 5	3 2-3 2	8034.6242	1.6
		5 0-5 0	8034.6842	1.8
		7 2-7 2	8034.7437	1.1
		4 2-4 2	8034.9087	0.5
		6 2-6 2	8035.0892	0.1
		5 2_+-5 2_+	8035.3250	-0.7
6 1 6	6 0 6	4 2-4 2	7397.5290	-0.5
		6 0-6 0	7397.5707	-1.2
		8 2-8 2	7397.6150	0.3
		7 2-7 2	7397.9048	-2.0
		6 2_+-6 2_+	7398.1157	-3.5
3 2 1	4 1 3	1 2-2 2	12371.6118	-0.4
		3 0-4 0	12371.8907	-0.2
		5 2-6 2	12372.1718	-1.0
		2 2-3 2	12372.6486	-0.9
		4 2-5 2	12373.4909	-2.0
		3 2_+-4 2_+	12374.3112	-2.4
3 2 2	4 1 4	1 2-2 2	14917.1096	2.2
		3 0-4 0	14917.2813	1.7
		5 2-6 2	14917.4549	1.1
		2 2-3 2	14917.7450	1.6
		4 2-5 2	14918.2635	-0.2
		3 2_+-4 2_+	14918.7658	-0.5
4 2 2	5 1 4	2 2-3 2	7842.9745	1.0
		4 0-5 0	7843.0985	1.2
		6 2-7 2	7843.2220	0.5
		3 2-4 2	7843.6882	0.6
		5 2-6 2	7844.0612	-1.0
		4 2_+-5 2_+	7844.6691	-1.2

Symmetric N_2-O_3 Transition		Hyperfine	Observed	Observed-
J′ K_a' K_c'	J″ K_a'' K_c''	F′I′-F″I″	Frequency/MHz	Calculated/kHz
4 2 3	5 1 5	2 2-3 2	11621.0023[b]	21.7
		$4\ 2_+$-$5\ 2_+$	11621.7095[b]	22.8
		5 2-6 2	11621.4361[b]	21.6
		3 2-4 2	11621.3130[b]	22.2
		6 2-7 2	11621.0857[b]	22.9
		$4\ 0_-$-$5\ 0_-$	11621.0434[b]	21.5
5 2 4	6 1 6	7 2-8 2	8463.5789	0.5
		$5\ 0_-$-$6\ 0_-$	8463.5789	-0.4
		3 2-4 2	8463.5789	-0.8
		6 2-7 2	8463.7116	0.8
		4 2-5 2	8463.7116	-1.0
		$5\ 2_+$-$6\ 2_+$	8463.8406	0.0
2 0 2	1 0 1	4 2-3 2	7906.4684	2.6
		3 2-2 2	7906.5414	1.9
		3 2-3 2	7905.1422	1.0
		$2\ 0_-$-$1\ 0_-$	7905.3154	2.2
3 0 3	2 0 2	4 2-4 2	11844.4180	-0.2
		$3\ 0_-$-$2\ 0_-$	11845.4857	1.7
		$3\ 2_+$-$2\ 2_+$	11845.5375	0.9
		5 2-4 2	11845.6965	1.2
		4 2-3 2	11845.7432	0.5
2 1 1	1 1 0	2 2-2 2	8166.2491	-1.5
		$2\ 2_+$-$1\ 2_+$	8166.2909	-0.7
		3 2-2 2	8166.5801	0.1
		3 2-3 2	8166.9843	-2.3
		4 2-3 2	8167.9317	1.3
		$2\ 0_-$-$1\ 0_-$	8168.8399	-0.3
3 1 3	2 1 2	$3\ 2_+$-$2\ 2_+$	11475.1360	-1.9
		4 2-3 2	11475.3689	0.5
		2 2-1 2	11475.4702	1.1
		5 2-4 2	11475.6812	2.1
		$3\ 0_-$-$2\ 0_-$	11475.7092	0.7
		1 2-1 2	11475.9722	0.6

Symmetric N_2-O_3 Transition		Hyperfine	Observed	Observed-
J′ K_a' K_c'	J″ K_a'' K_c''	F′I′-F″I″	Frequency/MHz	Calculated/kHz
3 1 2	2 1 1	$3\ 2_+$-3 2	12245.9305	-1.3
		$3\ 2_+$-$2\ 2_+$	12246.2605	-0.7
		4 2-3 2	12246.5804	0.0
		3 0_--2 0_-	12246.8182	0.0
		5 2-4 2	12246.8767	1.0
4 1 4	3 1 3	$4\ 2_+$-$3\ 2_+$	15292.6822	-2.3
		3 2-2 2	15292.7580	4.0
		5 2-4 2	15292.8199	-1.3
		2 2-1 2	15292.8757[a]	-11.1
		4 0_--3 0_-	15292.9085	0.4
		6 2-5 2	15292.9326	0.2

[a] 3kHz experimental uncertainty. All other transitions have ~ 1kHz experimental uncertainty.

[b] Not included in the fit. See discussion in section 6.3.1.

Table III.2; Observed rotational and hyperfine transition frequencies for the antisymmetric tunnelling/symmetric nuclear spin states of N_2-O_3. Residuals were calculated using the Watson S reduction hamiltonian (section 3.3) and hyperfine hamiltonian described in sections 4.3.3 and 4.4. Unweighted averages of multiple observations are given.

Antisymmetric N_2-O_3 Transition		Hyperfine	Observed	Observed-
$J'\ K_a'\ K_c'$	$J''\ K_a''\ K_c''$	$F'I'$-$F''I''$	Frequency/MHz	Calculated/kHz
1 1 0	0 0 0	1 1-1 1	13893.8047	0.1
		2 1-1 1	12894.0771	-1.1
		0 1-1 1	13894.4817	-3.2
2 1 1	1 0 1	2 1-1 1	18105.3862	2.0
		3 1-2 1	18105.6102	0.1
		2 1-2 1	18106.3161	1.2
		1 1-0 1	18106.6130	-0.7
5 0 5	4 1 3	5 1-4 1	8515.5013	-0.8
		6 1-5 1	8515.5838	-0.7
		4 1-3 1	8515.6603	-0.5
6 0 6	5 1 4	6 1-5 1	11672.3230	1.2
		7 1-6 1	11672.4783	0.7
		5 1-4 1	11672.5451	0.1
7 0 7	6 1 5	7 1-6 1	14616.5460	1.1
		8 1-7 1	14616.7501	-1.5
		6 1-5 1	14616.8114	-0.1
1 1 1	1 0 1	1 1-1 1	9679.6385	0.4
		2 1-1 1	9680.2980	-0.4
		1 1-2 1	9680.5694	0.5
		2 1-2 1	9681.2290	-0.1
		0 1-1 1	9681.2855	-0.2
		1 1-0 1	9681.9676	0.2

Antisymmetric N_2-O_3 Transition		Hyperfine	Observed	Observed-
$J'\ K_a'\ K_c'$	$J''\ K_a''\ K_c''$	$F'I'$-$F''I''$	Frequency/MHz	Calculated/kHz
2 1 2	2 0 2	1 1-2 1	9426.8893	0.5
		3 1-2 1	9427.0530	0.2
		2 1-2 1	9427.3432	-0.1
		3 1-3 1	9428.0441	0.1
		2 1-3 1	9428.3346	0.0
		1 1-1 1	9428.4348	1.6
		2 1-1 1	9428.8887	0.8
3 1 3	3 0 3	2 1-3 1	9056.7955	-1.1
		3 1-3 1	9057.5529	-0.1
		4 1-4 1	9058.0139	0.2
		2 1-2 1	9058.1751	0.0
		3 1-4 1	9058.5729	1.2
		3 1-2 1	9058.9322	0.7
4 1 4	4 0 4	3 1-4 1	8581.4224	2.1
		5 1-4 1	8581.6005	-1.1
		4 1-4 1	8582.2750	-0.1
		5 1-5 1	8582.6310	-0.2
		3 1-3 1	8582.7225	-0.5
		4 1-3 1	8583.5752	1.6
5 1 5	5 0 5	5 1-5 1	8016.8480	-0.4
		6 1-6 1	8017.1439	-0.7
		4 1-4 1	8017.2045	-0.8
6 1 6	6 0 6	5 1-5 1	7380.2424	0.1
		6 1-6 1	7379.9449	0.9
		7 1-7 1	7380.1991	0.2
3 2 1	4 1 3	3 1-4 1	12388.0840	1.7
		4 1-5 1	12389.1825	0.4
		2 1-3 1	12389.4636	-0.5
3 2 2	4 1 4	3 1-4 1	14933.7954	0.7
		4 1-4 1	14933.7954	-1.3
		4 1-5 1	14934.4686	-1.6
		2 1-3 1	14934.6418	-1.8
		3 1-3 1	14934.6418	-3.3

J' K_a' K_c'	J'' K_a'' K_c''	Hyperfine $F'I'$-$F''I''$	Observed Frequency/MHz	Observed-Calculated/kHz
4 2 2	5 1 4	4 1-5 1	7859.0889	0.3
		5 1-6 1	7859.8203	-0.6
		3 1-4 1	7859.9465	-0.4
4 2 3	5 1 5	4 1-5 1	11637.5291[a]	-15.5
		5 1-6 1	11637.8401[a]	-18.5
		3 1-4 1	11637.8830[a]	-16.7
5 2 4	6 1 6	5 1-6 1	8480.0411	0.8
		6 1-7 1	8480.1695	-0.6
		4 1-5 1	8480.1695	0.1
3 0 3	2 0 2	2 1-2 1	11843.8277	-1.0
		4 1-3 1	11845.1792	-0.5
		3 1-2 1	11845.2067	-0.5
		2 1-1 1	11845.3728	-0.3
2 1 1	1 1 0	1 1-0 1	8166.3880	1.2
		1 1-1 1	8167.0685	1.6
		3 1-2 1	8167.1880	-0.2
		2 1-1 1	8168.1663	-0.2
3 1 3	2 1 2	2 1-1 1	11475.1148	-0.2
		4 1-3 1	11475.1486	-0.8
		3 1-2 1	11475.4171	0.3
3 1 2	2 1 1	4 1-3 1	12246.4027	0.0
		2 1-1 1	12246.4485	0.5
		3 1-2 1	12246.6856	0.3
4 1 4	3 1 3	5 1-4 1	15292.4056	0.5
		3 1-2 1	15292.4249	-1.8
		4 1-3 1	15292.5220	1.4

[a] Not included in the fit, see discussion in section 6.3.1. Experimental measurement uncertainty 1kHz.

Appendix IV

Transition frequencies for N_2-SO_2

Table IV.1; Observed rotational and hyperfine transition frequencies for the symmetric tunnelling/symmetric nuclear spin states of N_2-SO_2. Residuals were calculated using the Watson S reduction hamiltonian (section 3.3) and hyperfine hamiltonian described in sections 4.3.3 and 4.4. Unweighted averages of multiple observations are given. The labelling scheme, I=+/- defined in section 4.3.3 for distinguishing the mixed I=0 and I=2 states, is used interchangeably with I=0(-) and I=2(+) for F=J levels and indicated by subscripts.

Symmetric N_2-SO_2 transition		Hyperfine	Observed	Observed-
$J'K'_aK'_c$	$J''K''_aK''_c$	F'I'-F''I''	Frequency/MHz	Calculated/kHz
1 1 0	0 0 0	2 2-1 0	10496.3955	-1.4
		1 2_+-1 0	10496.3340	-1.7
		3 2-2 0	10495.7894	-0.6
		1 0_--1 0	10495.0395	1.5
2 1 1	1 0 1	3 2-3 2	13763.8977	-2.0
		2 0_--1 0_-	13763.2840	0.7
		4 2-3 2	13764.8788	0.4
		2 2_+-1 2_+	13765.0299	-1.3
		3 2-2 2	13765.5347	-0.2
5 0 5	4 1 3	4 2-3 2	6972.8468	0.6
		3 2-2 2	6972.8863	-2.3
		5 2_+-4 2_+	6972.9461	-3.4
		5 0_--4 0_-	6972.9523	4.6
		7 2-6 2	6973.0106	1.4
		6 2-5 2	6973.0287	0.8
6 0 6	5 1 4	7 2-6 2	9450.8929	0.3
		6 2_+-5 2_+	9450.8998	2.0
		8 2-7 2	9450.7940	0.4
		6 0_--5 0_-	9450.7394	0.6
		5 2-4 2	9450.7276	-1.2
		4 2-3 2	9450.6841	-1.0

Symmetric N_2-SO_2 transition		Hyperfine	Observed	Observed-
$J'K_a'K_c'$	$J''K_a''K_c''$	F′I′-F″I″	Frequency/MHz	Calculated/kHz
7 0 7	6 1 5	7 0-6 0	11768.6900	-5.3
		9 2-8 2	11768.7438	0.3
		6 2-5 2	11768.7514	3.7
		8 2-7 2	11768.8939	0.8
		7 2_+-6 2_+	11768.9560	-0.1
8 0 8	7 1 6	10 2-9 2	13910.5517	-0.3
		7 2-6 2	13910.6148[a]	6.7
		9 2-8 2	13910.7372	-0.8
		8 2_+-7 2_+	13910.8415	-2.9
		6 2-5 2	13910.4648	-2.4
		8 0-7 0	13910.5083	-1.1
9 0 9	8 1 7	7 2-6 2	15860.7841	-0.7
		9 0-8 0	15860.8230	0.5
		11 2-10 2	15860.8619	1.3
		8 2-7 2	15860.9472	-10.5
		9 2_+-8 2_+	15861.2146	-1.2
1 1 1	1 0 1	3 2-3 2	7224.7337	-0.3
		2 2-3 2	7225.7598	1.3
		1 2_+-1 2_+	7227.1304	1.2
		2 2-1 2_+	7227.2320	0.4
		1 2_+-2 2	7227.2936	2.3
		2 2-2 2	7227.3954	1.6
		3 2-2 2	7226.3692	-0.1
2 1 2	2 0 2	2 2_+-1 2	7032.8180	-0.4
		1 2-0 2	7032.8381	-1.8
		2 0-2 0	7033.5695	3.1
		4 2-4 2	7033.9857	-0.1
		0 2-1 2	7034.0820	0.3
		2 2_+-3 2	7034.7536	-0.9
		3 2-3 2	7034.9568	-0.3
		4 2-3 2	7035.5384	0.3
		1 2-2 2_+	7036.2229	1.1

Symmetric N_2-SO_2 transition		Hyperfine	Observed	Observed-
$J'K_a'K_c'$	$J''K_a''K_c''$	F'I'-F''I''	Frequency/MHz	Calculated/kHz
3 1 3	3 0 3	4 2-5 2	6753.9040	-0.7
		2 2-1 2	6753.8574	-1.0
		3 2_+-2 2	6753.6526	-4.1
		5 2-5 2	6754.8457	-0.7
		4 2-4 2	6755.4059	-0.1
		2 2-2 2	6754.9361	-0.9
		1 2-1 2	6754.5332	-1.3
		3 0_--3 0_-	6754.6891	0.8
4 1 4	4 0 4	4 0_--4 0_-	6396.0938	1.2
		6 2-6 2	6396.1750	-1.3
		5 2-5 2	6396.5705	1.4
		4 2_+-4 2_+	6396.8132	0.5
		3 2-3 2	6396.3188	1.0
		6 2-5 2	6397.6437	3.7
		2 2-3 2	6397.1595	2.7
2 2 1	3 1 3	2 0_--3 0_-	13317.6807	1.7
		1 2-2 2	13318.3794	0.0
		4 2-5 2	13318.6182	0.0
		4 2-4 2	13319.5625	2.7
		2 2_+-2 2	13320.8658	-3.7
		3 2-4 2	13321.1144	0.1
		3 2-3 2_+	13321.6081	1.0
		2 2_+-3 2_+	13322.1487	-1.0
2 2 0	3 1 2	2 0_--3 0_-	12160.1880	-0.8
		1 2-2 2	12161.0598	-0.7
		4 2-5 2	12161.2325	-1.3
		2 2_+-3 2_+	12165.3454	-1.7
		3 2-3 2_+	12164.8071	0.7
		3 2-4 2	12164.1103	-0.8
3 2 2	4 1 4	3 2_+-4 2_+	10634.4505	-1.6
		3 2_+-3 2	10633.1049	1.2
		5 2-6 2	10632.7224	2.1
		4 2-5 2	10633.7884	-0.6

Symmetric N_2-SO_2 transition		Hyperfine	Observed	Observed-
$J'K_a'K_c'$	$J''K_a''K_c''$	F′I′-F″I″	Frequency/MHz	Calculated/kHz
3 2 1	4 1 3	4 2-5 2	8718.6127	-0.4
		2 2-3 2	8717.6954	-0.1
		5 2-6 2	8717.1790	0.8
		3 0-4 0	8716.8728	1.3
		1 2-2 2	8716.5696	1.0
5 3 2	6 2 4	4 2-5 2	17929.3599	-2.3
		7 2-8 2	17928.8315	1.3
		5 0-6 0	17928.7010	3.3
		6 2-7 2	17929.7591	-1.9
6 3 3	7 2 5	$6\ 2_+$-$7\ 2_+$	14684.6792[a]	-8.1
		7 2-8 2	14684.1591	-4.3
		8 2-9 2	14683.4980	0.1
		6 0-7 0	14683.4256	1.5
		4 2-5 2	14683.3527	2.3
6 3 4	7 2 6	7 2-8 2	15152.4682	-3.4
		4 2-5 2	15151.7448	2.1
		6 0-7 0	15151.8102	1.9
		8 2-9 2	15151.8734	-0.6
		$6\ 2_+$-$7\ 2_+$	15152.9367	-7.4

Experimental measurement uncertainty ~ 1kHz.
[a] Weight ¼.

Table IV.2; Observed rotational and hyperfine transition frequencies for the antisymmetric tunnelling/antisymmetric nuclear spin states of N_2-SO_2. Residuals were calculated using the Watson S reduction hamiltonian (section 3.3) and hyperfine hamiltonian described in section 4.3.3 and 4.4. Unweighted averages of multiple observations are given.

Antisymmetric N_2-SO_2 Transition		Hyperfine	Observed	Observed-
$J'K_a'K_c'$	$J''K_a''K_c''$	F'I'-F''I''	Frequency/MHz	Calculated/kHz
1 1 0	0 0 0	1 1-1 1	10495.2315	-0.1
		2 1-1 1	10495.6368	--1.0
		0 1-1 1	10496.2417	-1.3
2 1 1	1 0 1	2 1-1 1	13764.2234	0.6
		3 1-2 1	13764.5788	-1.1
		2 1-2 1	13765.3112	1.2
		1 1-0 1	13765.8041	0.1
3 1 2	2 0 2	2 1-2 1	17128.9353	-1.1
		3 1-2 1	17130.3705	0.0
		4 1-3 1	17130.4718	-1.3
		2 1-1 1	17130.7459	0.5
		3 1-3 1	17131.5322	1.9
5 0 5	4 1 3	6 1-5 1	6973.3000	1.4
		5 1-4 1	6973.3164	-0.2
		4 1-3 1	6973.3592	0.0
6 0 6	5 1 4	6 1-5 1	9451.0966	0.4
		7 1-6 1	9451.1560	0.8
		5 1-4 1	9451.2090	-1.8
7 0 7	6 1 5	7 1-6 1	11769.0433	0.4
		8 1-7 1	11769.1551	0.8
		6 1-5 1	11769.2010	-3.0
8 0 8	7 1 6	8 1-7 1	13910.8412	1.3
		9 1-8 1	13910.9992	0.0
		7 1-6 1	13911.0323[a]	-12.0

Antisymmetric N_2-SO_2 Transition		Hyperfine	Observed	Observed-
$J'K_a'K_c'$	$J''K_a''K_c''$	F′I′-F″I″	Frequency/MHz	Calculated/kHz
9 0 9	8 1 7	9 1-8 1	15861.1581	-1.1
		10 1-9 1	15861.3366	-2.1
		8 1-7 1	15861.3833	3.1
1 1 1	1 0 1	1 1-1 1	7223.4954	0.3
		2 1-1 1	7224.1788	-0.8
		1 1-2 1	7224.5834	1.2
		2 1-2 1	7225.2665	-0.1
		0 1-1 1	7225.2028	-0.8
2 1 2	2 0 2	1 1-2 1	7032.7124	-2.1
		3 1-2 1	7032.9564	-1.9
		2 1-2 1	7033.3903	-0.2
		1 1-1 1	7034.5253	1.7
		2 1-3 1	7034.5526	2.2
		3 1-3 1	7034.1186	0.4
2 2 0	3 1 2	2 1-3 1	12160.9316	1.5
		1 1-2 1	12164.1704	-0.3
		3 1-4 1	12163.1513	0.2
2 2 1	3 1 3	2 1-3 1	13318.3903	-0.9
		2 1-2 1	13319.4074	0.7
		3 1-3 1	13319.5625	3.3
		1 1-2 1	13321.2182	-1.6
		3 1-4 1	13320.3065	-1.5
3 2 1	4 1 3	2 1-3 1	8718.7888	-1.9
		4 1-5 1	8718.4815	0.0
		3 1-4 1	8717.2889	0.9
3 2 2	4 1 4	4 1-5 1	10633.7791	0.3
		2 1-3 1	10634.0077	-1.2
		3 1-4 1	10632.8914	1.3
5 3 2	6 2 4	6 1-7 1	17929.1874	-1.6
		5 1-6 1	17928.3754	1.5
		4 1-5 1	17929.3245	0.0

Antisymmetric N_2-SO_2 Transition		Hyperfine	Observed	Observed-
$J'K_a'K_c'$	$J''K_a''K_c''$	F′I′-F″I″	Frequency/MHz	Calculated/kHz
6 3 3	7 2 5	5 1-6 1	14683.7689	1.9
		7 1-8 1	14683.6873	-2.5
		6 1-7 1	14683.0936	0.6
6 3 4	7 2 6	6 1-7 1	15151.4764	1.6
		7 1-8 1	15152.0102	-1.6

Experimental measurement uncertainty ~ 1kHz.
[a] Not included in the fit.